ANNÉE 2017

UNIVERSITÉ DE RENNES 1

FAKULTA ELEKTROTECHNICKÁ ZÁPADOČESKÉ UNIVERZITY V PLZNI

UNIVERSITE BRETAGNE LOIRE

THÈSE / UNIVERSITÉ DE RENNES 1
sous le sceau de l'Université Bretagne Loire

En Cotutelle Internationale avec
l'Université de Bohême de l'Ouest, République tchèque

pour le grade de

DOCTEUR DE L'UNIVERSITÉ DE RENNES 1

Mention : Électronique

École doctorale MATISSE

présentée par

Denys Nikolayev

préparée à l'IETR – UMR CNRS 6164
Institut d'Électronique et de Télécommunications de Rennes
Université de Rennes 1

Miniature Antennas for Biomedical Applications

Soutenance prévue à Rennes
le 19 Septembre 2017

devant le jury composé de :

Thierry MONÉDIÈRE
Professeur à l'Université de Limoges – XLIM / *rapporteur*

Christophe DELAVEAUD
Docteur ingénieur, HDR à CEA Leti / *rapporteur*

Anja SKRIVERVIK
Professeur à l'École polytech. fédérale de Lausanne / *examinateur*

Konstantina NIKITA
Professeur à l'Univ. polytech. nationale d'Athènes / *examinateur*

Ronan SAULEAU
Professeur à l'Université de Rennes 1 – IETR / *directeur de thèse*

Maxim ZHADOBOV
Chercheur CNRS, HDR à l'IETR / *co-directeur de thèse*

Pavel KARBAN
Docent à l'Univ. de Bohême de l'Ouest / *co-directeur de thèse*

Fabrice VERJUS
Président de la société BodyCap / *examinateur*

Acknowledgment

This work was supported by the BodyCap Company (www.bodycap-medical.com), the French Ministry of Foreign Affairs and International Development through Eiffel Scholarship, the CNRS/DGA through the PEPS program, the Ministry of Education, Youth and Sports of the Czech Republic under the RICE – New Technologies and Concepts for Smart Industrial Systems, project No. LO1607.

Résumé

La télémétrie biomédicale et l'interfaçage neuronal à base de dispositifs miniatures et autonomes sans fil constituent de nouvelles applications en émergence. Elles visent à répondre à de nombreux enjeux y compris dans les domaines de la santé, du sport et bien être, ou encore de la sécurité au travail et de la défense. Parmi les applications typiques de biotélémétrie, nous pouvons citer le monitoring de certains paramètres physiologiques : température corporelle, pression artérielle, rythme cardiaque, taux de glucose et d'anticorps, détection d'agents chimiques, etc. En ce qui concerne l'interfaçage neuronal, il permet de restaurer les informations sensorielles, d'aider à la réadaptation des amputés, des personnes atteintes de paralysie ou des patients atteints de maladies neurodégénératives.

L'objectif principal de cette thèse est de contribuer au développement de dispositifs électroniques miniaturisés et communicants (dispositifs biomédicaux implantables ou *in-body*) pour le monitoring, en continu, de variables physiologiques (température, pH, glucose, rythme cardiaque, etc.) d'humains ainsi que d'animaux. Ces dispositifs innovants nécessitent un système de communication fiable avec un équipement de mesure/contrôle. Plus particulièrement, il s'agit d'analyser le milieu de propagation à l'intérieur des tissus biologiques et de développer des antennes miniatures innovantes ainsi que des méthodes pour leur analyse et leur caractérisation.

L'un des plus grands défis dans conception de tels systèmes miniatures repose sur la transmission efficace et robuste d'énergie électromagnétique à travers de corps humain. Ceci permet de communiquer des données acquis avec des portées suffisantes ainsi que de recharger des dispositifs sans fil à l'intérieur du corps. Actuellement le verrou majeur concerne le rendement des antennes miniatures. Les effets des propriétés spécifiques des milieux biologiques (forte hétérogénéité, dispersion, pertes très élevées) et les contraintes de miniaturisation et d'intégration dans des dispositifs *in-body* induisent de très faibles efficacités d'antennes. Par conséquent, la portée des systèmes existants est limitée à quelques dizaines de centimètres. Cela rend inefficaces les dispositifs autonomes pour la biotélémétrie et inapplicable aux communications sans fil pour l'interfaçage neuronal.

Tout d'abord, en étudiant les méthodes de réduction de couplage électromagnétique avec les tissus biologiques, nous avons remarqué que les antennes microrubans à bande passante étroite et chargées d'un superstrat à haute permittivité (proche de celle des tissus biologiques) peuvent accroitre leur rendement de manière considérable. Lors de ces études, nous avons également établi une nouvelle méthode de détection des propriétés électromagnétiques in vivo avec l'objectif d'utiliser cette information pour les applications diagnostiques.

Puis, des outils spécifiques d'optimisation ont été développés en collaboration avec le Département de Théorie d'Ingénierie Électrique de l'Université de Bohème de

l'Ouest (Pilsen, République tchèque). Ces outils sont indispensables pour l'analyse des composants de systèmes antennaires complexes : le code Hermes2D/3D implémenté dans Agros2D (CAO interne du laboratoire KTE de l'Université de Bohème de l'Ouest, www.agros2d.org) utilise des méthodes entièrement adaptatives (notamment *hp*-FEM et *hp*-DG) pour la résolution de problèmes multiphysiques fortement couplés. Cette approche permet de réduire la complexité d'optimisation des antennes *in-body* jusqu'un seul dégrée de liberté accélérant de la manière significative le progrès dans le domaine de télémétrie biomédicale.

En se basant sur ces résultats, la limite fondamentale de rendement des antennes pour les applications *in-body* a été définie ; les liens entre cette limite et la taille de l'antenne, sa fréquence de fonctionnement, la polarisation et les matériaux utilisés (dont hypothétiques) ont été quantifiés pour la première fois. Ce travail fondamental a d'abord pour objectif l'optimisation des performances de l'antenne actuelle de la capsule e-Celsius de l'entreprise BodyCAP pour accroître la portée de la gélule, en prenant en compte les caractéristiques des matériaux avec lesquels elle est fabriquée et le milieu de propagation que constituent les tissus biologiques. Dans cette étape on inclut également la fabrication des prototypes de gélules télémétriques ainsi que leurs mesures d'impédance. L'antenne optimisée a une portée effective trois fois plus importante que celle actuelle tout en occupant le même volume et présentant des caractéristiques uniques entre terme de robustesse contre la désadaptation à cause de la variation des paramètres de milieu biologique. Ainsi, nous avons développé une nouvelle méthode de conception des antennes capsules implants. L'antenne démonstrateur (utilisant les matériaux hypothétiques ; permettant d'accroitre la portée jusqu'aux deux fois comparée aux homologues de la même taille) et la nouvelle procédure d'optimisation hybride analytique–numérique ont été proposés.

En utilisant ces principes de conception, nous avons développé et caractérisé une antenne à 434 MHz adaptée à une large gamme d'applications *in-body*. Des dimensions ultra-miniatures, une robustesse et un rendement accrus (par rapport aux homologues) permettent de l'utiliser à la fois pour des applications des capsules à implanter et à avaler. Cette antenne peut également être considérée pour la biotélémétrie animale puisque les propriétés électromagnétiques de certains tissus animaux peuvent différer de celles des humains, et la robustesse de l'antenne réduit partiellement la désadaptation d'impédance.

Enfin, en développant davantage les méthodes de conception et d'optimisation, nous avons conçu une antenne double-bande. Ayant la même robustesse que son équivalent actuel mono-bande, elle présente également un rendement encore plus élevé, permettant ainsi de fonctionner au-delà de 10 m. La caractéristique double-bande permet de concevoir les dispositifs *in-body* rechargeables sans fil dans le corps. L'alimentation sans fil, par nature non invasive, n'induit aucun risque d'infection et ne nécessite pas d'intervention chirurgicale afin de remplacer les piles ; sa durée de vie est quasi illimitée. Les antennes proposées contribuent au développement ultérieur d'une nouvelle génération de dispositifs miniatures *in-body* qui impliquent une intégration complexe et dense des capteurs, de la logique et de l'alimentation.

Les travaux de cette thèse s'inscrivent dans le cadre d'une cotutelle entre l'institut d'électronique et de télécommunications de Rennes (IETR – UMR CNRS 6164) et le Département de Théorie d'Ingénierie Electrique (KTE) de l'Université de Bohème de l'Ouest (Pilsen, République tchèque) avec un partenaire industriel français (BodyCap – www.bodycap-medical.com).

Plan de la thèse

Le manuscrit est organisé de la manière suivante.

Le **Chapitre 1** présente le domaine de la biotémétrie *in-body*. Après avoir identifié le contexte et les objectifs de la thèse, les solutions d'antenne existantes pour les applications capsules sont étudiées en détail.

Le **Chapitre 2** se concentre sur l'environnement biologique et les méthodes pour prendre en compte de ses effets sur l'antenne. Nous commençons par modéliser le tissu pour les cas à implanter et à avaler puis nous procédons au développement de fantômes numériques et physiques. Tout d'abord, nous développons deux fantômes bidimensionnels vectoriels : un fantôme de cerveau humain normal et un fantôme de la région abdominale humaine (torse). Ensuite, nous proposons une méthodologie pour obtenir les propriétés électromagnétiques d'intérêt à une fréquence donnée en utilisant la conception factorielle. Enfin, nous décrivons le fantôme physique sphérique pour la caractérisation du champ lointain de l'antenne avec une combinaison de techniques de découplage d'antenne du câble d'alimentation.

Le **Chapitre 3** concerne l'étude des mécanismes de propagation dans le corps humain et permet de déduire les conditions de fréquence et de rayonnement optimales pour les dispositifs *in-body*. Nous évaluons la dépendance du rendement sur la fréquence de fonctionnement, la profondeur d'implantation de la source et sa polarisation. Le problème formulé utilise des fantômes homogènes et hétérogènes avec un réalisme anatomique croissant du modèle : 1) milieux infinis avec une limite planaire entre demi-espaces homogènes et 2) hétérogènes ; 3) fantômes gastro-intestinaux stratifiés et 4) fantômes anatomiquement réalistes. Pour résoudre la formulation de façon globale, nous utilisons le code interne Agros2D mettant en œuvre une méthode d'éléments finis intégralement *hp*-adaptatif (*hp*-FEM). La résolution du problème formulé avec un solveur commercial permet de valider les résultats avec une vérification supplémentaire à l'aide de la méthode FDTD (finite-difference time-domain, le code Meep).

Le **Chapitre 4** présente l'antenne utilisée par le partenaire industriel BodyCap Company pour sa capsule e-Celsius. Comme la performance de l'antenne initiale est inconnue, nous avons d'abord effectué la rétro-ingénierie, puis les études paramétriques afin d'améliorer la portée et la robustesse sous des contraintes strictes d'intégration et des matérielles. Le modèle théorique développé permet de dimensionner l'antenne pour la fréquence de résonance donnée tout en tenant compte de l'effet de chargement des matériaux de la capsule et des tissus biologiques. Les mécanismes de couplage antenne–corps sont analysés et la solution proposée permet d'améliorer le gain d'antenne de 11 dBi (la portée est plus que triplée). Le circuit d'adaptation existant et le balun sont également optimisés pour l'application donnée réduisant sa taille de onze à sept éléments discrets et priorisant les performances TX.

Le **Chapitre 5** va au-delà des contraintes imposées dans le chapitre précédent et une antenne miniature, efficace et polyvalente adaptée aux applications *in-body* est proposée. La fréquence de fonctionnement est la bande ISM 434 MHz. L'antenne est synthétisée en utilisant une méthode analytique–numérique hybride et optimisée pour fonctionner dans une capsule céramique biocompatible de taille 17 mm$\times\varnothing$7 mm. L'antenne microruban, à bande étroite, est chargée par un superstrat de haute permittivité fabriqué en alumine. De cette façon, le couplage antenne–corps est réduit de manière significative, ce qui permet d'améliorer la robustesse (en termes d'adaptation) et l'efficacité de rayonnement de l'antenne. L'antenne ainsi conçue

reste bien adaptée ($|S_{11}| < -10$ dB) pour une large gamme des tissus. La bande passante de 17 MHz (soit 4% en valeur relative) est suffisante pour un fonctionnement en tant qu'antenne capsule ou antenne implant. Les performances du rayonnement sont caractérisées par la technique d'illumination directe utilisant une alimentation par fibre optique. Le gain réalisé mesuré (valeur maximale -19,6 dBi) dépasse les homologues d'au moins 3 dBi.

Le **Chapitre 6** propose une antenne à double bande 434 MHz et 2,45 GHz également robuste contre la détérioration de l'impédance causée par des propriétés électromagnétiques variables de l'environnement biologique. L'impédance d'entrée est de 50 Ω pour les deux fréquences de fonctionnement. Une telle antenne peut intégrer la transmission de données et la fonctionnalité de transfert de puissance sans fil. La conception proposée occupe 2,6% du volume dans la capsule de 28 mm×⌀9 mm. La forte robustesse de cette antenne permet de l'utiliser pour les applications à avaler ainsi qu'à implanter. Comme pour l'antenne précédente, nous caractérisons le rayonnement avec la technique d'illumination directe en utilisant une alimentation par fibre optique. Le gain réalisé de la capsule dépasse les solutions existantes de 434 MHz d'environ 9 dBi et les 2,45 GHz-environ d'environ 3 dBi. Enfin, dans la deuxième partie du Chapitre 6, nous parlons de l'application d'antennes *in-body* pour la détection in vivo des propriétés EM. Avec la méthodologie proposée, un dispositif interne peut utiliser la même antenne pour la communication de données et pour la détection de l'environnement. La méthode est basée sur les mesures du signal réfléchi dû à la désadaptation de l'antenne, qui dépend des tissus environnants. À partir de l'amplitude mesurée et de la phase du signal réfléchi, nous pouvons évaluer l'impédance complexe de l'antenne et, si nécessaire, les propriétés EM du milieu environnant.

Le manuscrit se termine par une **Conclusion** qui résume les principaux résultats et contributions, ainsi que les travaux futurs et perspectives.

La thèse contient trois annexes. L'**Annexe A** examine l'algorithme automatique d'adaptation de maille d'Agros2D. L'**Annexe B** fournit la validation du modèle numérique proposé au Chapitre 4 pour estimer l'impédance d'une ligne de transmission TEM arbitraire et hétérogène. Enfin, l'**Annexe C** décrit le circuit d'adaptation et le balun pour l'antenne optimisée de la capsule BodyCap e-Celsius présentée au Chapitre 4.

Abstract

EMERGING wireless biotelemetry using miniature implantable, ingestible or injectable (in-body) devices allows continuously monitor and yield human or animal physiological parameters while maintaining mobility and quality of life. Recent advances in microelectromechanical systems and microfluidics—along with ongoing miniaturization of electronics—have empowered numerous innovations in biotelemetry devices, creating new applications in medicine, clinical research, wellness, and defense. Among the typical applications, I can mention, for example, the monitoring of physiological variables: body temperature, blood pressure, heart rate, detection of antibodies, chemical, or biological agents.

Biotelemetry devices require a reliable communication system: robust, efficient, and versatile. Improving the transmission range of miniature in-body devices remains a major challenge: for the time being, they are able to operate only up to a few meters. Among the main issues to face are low radiation efficiencies ($< 0.1\%$), antenna impedance detuning, and strong coupling to lossy and dispersive biological tissues. Thus, the main goal of the thesis is to conduct a multi-disciplinary study on development, optimization and characterization of antennas for in-body biotelemetry devices.

After state-of-the-art and the context, I start with the development on both physical and numerical approaches to account for the effect of human tissues on the antenna. I propose the methodology to achieve given electromagnetic properties at a given frequency based on the full factorial experiment and surface response optimization. In addition, I describe the spherical physical phantom for the far-field characterization along with a combination of feed decoupling techniques.

I proceed by reviewing the trough-body propagation mechanisms and deriving the optimal frequency for the in-body devices. I formulate the problem using four phantoms (homogeneous and heterogeneous) and perform full-wave analysis using an in-house *hp*-FEM code Agros 2D.

Next, I study the existing antenna used by the BodyCap Company for its e-Celsius® capsule and the ways on how to improve its operating range and robustness under strict integration and material constraints. The mechanisms of antenna–body coupling are analyzed and the found solution improves the antenna IEEE gain by 11 dBi (the operating range is at least tripled). The existing matching circuit and balun are optimized too for the given application reducing its size from eleven to seven discrete elements.

In the following chapters, I continue studying the decoupling of antennas from a body using specific microstrip designs and dielectric loading via capsule shell. By applying the developed approaches, a high robustness and radiation efficiency can be achieved. At first, I develop a proof-of-concept antenna that demonstrates that the perfect matching (detuning immunity) is achievable for the operation within all

human tissues. Based on these results, I develop a miniature and versatile biotelemetry platform: a ($17 \times \varnothing 7$) mm alumina capsule containing a conformal 434 MHz antenna. The antenna is well matched to 50 Ω within the majority of human tissues and operates with an arbitrary device circuitry. Like this, one can use it "as is," applying it for a wide range of in-body applications.

Then, I develop a low profile conformal dual-band antenna operating in 434 MHz and 2.45 GHz bands. Such antenna can integrate both data transmission and wireless powering functionality increasing the available space inside an in-body device and increasing its scope of applications. Finally, I present the perspective developments including in-body sensing methodology.

The obtained results contributes to further development of a new generation of miniature in-body devices that involve complex and dense integration of sensors, logic, and power sources.

Keywords: antennas in lossy media, biotelemetry, computational phantoms, conformal antennas, electrically small antennas, finite element method, implantable antennas, in-body, ingestible antennas, ISM band, MedRadio band, microstrip antennas, miniature antennas, physical phantoms.

Contents

Résumé iii

Abstract vii

General Introduction 3
Outline of the Dissertation 5

1 In-Body Biotelemetry: Context and State-of-the-Art 11
1.1 Introduction 12
1.2 In-body Biotelemetry in Medicine and Clinical Research 13
1.3 Context, Objectives, and Goals 14
1.4 Capsule Antennas Overview 15
1.4.1 Wire Antennas 16
1.4.2 Planar Printed Antennas 17
1.4.3 Conformal Printed Antennas 19
1.5 Summary 26

2 Human Body Modeling in VHF–SHF Bands 35
2.1 Biological Environment of Capsule Antennas 36
2.1.1 Electromagnetic Properties of Tissues 36
2.1.2 Capsule Gastrointestinal Passage 37
2.1.3 Implantable Case 38
2.2 Computational Phantoms 38
2.2.1 Literature Review 39
2.2.2 2D Anatomically Realistic B-Rep Phantom 40
2.3 Physical Phantoms 41
2.3.1 Literature Review 41
2.3.2 Predictive Modeling of H_2O–$C_{12}H_{22}O_{11}$–NaCl Liquid Phantoms 42
2.4 Far-Field Characterization of In-Body Antennas 44
2.5 Summary 46

3 Radiation Efficiency of In-Body Devices 55
3.1 Introduction 56
3.2 Theory 57
3.2.1 Attenuation in Biological Tissues 57
3.2.2 Impedance Contrast and Mismatch Losses 59
3.2.3 Fundamental Limitations on Radiation Efficiency for Electrically Small Antennas 59
3.3 Problem Formulation 60

3.3.1 Numerical Model . . . 62
3.4 Results and Discussion . . . 63
3.4.1 Infinite Medium: Planar-Bounded Homogeneous Half-Space . 63
3.4.2 Infinite Medium: Planar-Bounded Layered Half-Space 66
3.4.3 Cylindrical Stratified Phantom . . . 66
3.4.4 Anatomical Torso Phantom . . . 69
3.5 Summary . . . 69

4 BodyCap e-Celsius® Antenna: Modeling and Optimization 77
4.1 Introduction . . . 78
4.2 Specifications and Material Constraints . . . 78
4.2.1 Characterization of Capsule Shell and Epoxy Filling 78
4.3 Theoretical Model . . . 79
4.4 Impedance Analysis . . . 81
4.4.1 Numerical Model . . . 81
4.5 Full-Wave Numerical Modeling . . . 82
4.5.1 Planar Model . . . 83
4.5.2 Conformal Model . . . 89
4.6 Antenna Feeding and Measurements . . . 90
4.6.1 Planar Antenna . . . 90
4.6.2 Conformal Antenna . . . 91
4.7 Influence of Capsule . . . 91
4.7.1 Capsule Measurements in Air, Water, and Phantoms 91
4.8 Antenna Optimization . . . 92
4.8.1 Optimized Design . . . 94
4.8.2 Performance . . . 95
4.8.3 Prototyping and Measurements . . . 96
4.9 Summary . . . 97

5 Miniature and Robust Antenna for In-Body Capsules 103
5.1 Introduction . . . 104
5.2 In-Body Antenna Environment . . . 104
5.2.1 Range of Tissue EM Properties . . . 105
5.3 Antenna Design . . . 106
5.3.1 Theoretical Considerations . . . 106
5.3.2 Approach Validation: Proof-of-Concept Antenna 107
5.3.3 Final Antenna Synthesis and Miniaturization 111
5.3.4 Material Choice and Capsule Weight Estimation 113
5.3.5 Capsule Size Constraints . . . 113
5.4 Full-Wave Numerical Analysis and Optimization . . . 114
5.4.1 Numerical Model . . . 114
5.4.2 Phantoms . . . 115
5.5 Fine-Tuning and Performance in Simplified Phantoms 116
5.6 Antenna Performance in Realistic Environment . . . 117
5.6.1 Robustness: Variation of Tissue EM Properties 117
5.6.2 Influence of Capsule Circuitry . . . 118
5.6.3 Application to Endoscopy . . . 119
5.6.4 Interference with Neighboring Devices . . . 120
5.6.5 Performance in Realistic Phantom . . . 121

5.6.6 Link Budget Calculation . . . 121
5.7 Prototyping and Measurements . . . 122
5.7.1 Prototype Manufacturing . . . 122
5.7.2 Phantoms . . . 123
5.7.3 Antenna Reflection Coefficient . . . 124
5.7.4 Radiation Performance . . . 124
5.8 Summary . . . 126

6 Dual-Band Capsule Antenna and *In Vivo* Sensing of EM Properties 133
6.1 Introduction . . . 134
6.2 Antenna Design . . . 134
6.2.1 Biological Tissue Environment . . . 134
6.2.2 Theoretical Considerations . . . 135
6.2.3 Antenna Synthesis . . . 135
6.2.4 Material Choice and Capsule Weight Estimation . . . 137
6.3 Dual-Band Capsule Antenna . . . 139
6.3.1 Numerical Modeling and Optimization . . . 139
6.3.2 Antenna Performance . . . 139
6.3.3 Prototyping and Measurements . . . 142
6.4 *In Vivo* Sensing of EM Properties . . . 144
6.4.1 Introduction . . . 144
6.4.2 Methodology Description . . . 145
6.4.3 Sensing Electromagnetic Properties via the Variation of Antenna Impedance . . . 146
6.5 Summary . . . 146

General Conclusion 153
Summary and Contributions . . . 153
Future Work and Perspectives . . . 157

Appendix A Automatic *hp*-Adaptivity 159

Appendix B Impedance Analysis of Transmission Line Cross-Sections: Model Validation 161

Appendix C Matching Circuit of e-Celsius® Antenna 163

About the Author 173

List of Publications 175

List of Figures

1.1 In-body biotelemetry. *left*: existing and potential applications; *right*: some examples of on- and off-body receivers. 12

1.2 Outline of an in-body capsule for biomedical telemetry. 13

1.3 BodyCap e-Celsius® is a miniature electronic pill that monitors and communicates wirelessly the intracorporal temperature. 15

1.4 Wire helical antenna (Kwak *et al.*, 2005): (a) dimensions, (b) reflection coefficient $|S_{11}|$, and (c) measured radiation pattern (norm. received power). © 2005 IEEE. 16

1.5 Multilayer printed planar antenna (Merli *et al.*, 2011): (a) design, (b) prototype, reflection coefficients $|S_{11}|$ ((c) MedRadio and (d) ISM), and (e) ISM radiation patterns (normalized). © 2010 IEEE. 18

1.6 Conformal microstrip meandered antenna (Psathas *et al.*, 2013): (a) design (mm) and (b) reflection coefficient $|S_{11}|$. © 2013 IEEE. 22

2.1 Electromagnefic properties (ε_r, σ) of GI tract and muscle tissues (data from Gabriel *et al.*). *left*: Real part of the relative permittivity ε_r of GI tract and muscle tissues.*right*: The conductivity σ of GI tract and muscle tissues 37

2.2 Two-dimensional B-Rep phantom of a normal human brain. *left*: Source MRI scan (simulated) of a head. *right*: Resulted polygonal phantom. 40

2.3 Liquid phantom characterization setup. *left*: DAK SPEAK kit setup. *right*: Temperature control of obtained liquids. 43

2.4 Measured and interpolated EM properties of the "Run 1" phantom with 40% of $C_{12}H_{22}O_{11}$ and 1% of NaCl. *left*: Real part of the relative permittivity $\varepsilon_r'(\omega)$. *right*: The conductivity $\sigma(\omega)$. 44

2.5 Spherical glass container for a tissue-equivalent liquid. *left*: Design and dimensions. *right*: Final design containing an AuT and fixed with Rohacell® IG foam ($\varepsilon_r = 1.05$, $\tan\delta = 0.0017$). 45

2.6 The measurement setup proposed for characterizing radiation performance of in-body antennas: 1) measurement antenna, 2) AuT in ⌀100 mm spherical phantom, 3) azimuth positioner, 4) optical fiber, 5) positioner control cables, 6) RF cables, 7) analog fiber optic link Enprobe LFA-3, 8) vector network analyzer R&S ZVA 24, 9) acquisition/control PC, and 10) positioner controller ORBIT/FR AL-4806-3C Opt. 1. 46

3.1 Main factors affecting in-body proparagion. (a) Dispersive EM properties of muscle and fat tissues derived using Eq. (2.2) interpolating experimental data obtained by Gabriel *et al.* (b) Penetration depths δ_p given by Eq. (3.4) into dispersive muscle and fat tissues modeled using Eq. (2.2). (c) Transmission coefficient T given by Eq. (3.5) of a normal-incident plane wave upon a planar infinite air–skin interface taking into account the dispersive skin EM properties modeled using Eq. (2.2). (d) The highest achievable radiation efficiencies η_{ub} given by Eq. (3.10) for several fractional bandwidths FBW $= f_0/\text{BW}$ considering VSWR $= 2$, assuming $a = 5$ mm, and taking the dispersive permittivity of muscle given by Eq. (2.2). 58

3.2 Definition of the Chu sphere circumscribing a capsule antenna used in this dissertation. 59

3.3 Two-dimensional (2D) model formulations used in the study (source regions not to scale, z-axis is out of plane). EM properties are according to Eq. (2.2). (a) A planar interface between two semi-infinite homogeneous half-spaces. $\Sigma_{\text{t}}\,(d < 0)$ with muscle-equivalent EM properties. (b) A planar stratified heterogeneous model as proposed by Poon *et al.*. $\Sigma_{\text{t}}\,(d < 0)$ contains muscle, fat, and skin layers. (c) Circular heterogeneous model (not to scale). $\Sigma_{\text{t}}\,(R < 90)$ contains muscle, fat, and skin layers. (d) Realistic model of a human abdominal region (nine tissues). (e) Magnetic dipole of a moment $\mathbf{m}$. 61

3.4 Absolute value of the relative residual power error for infinite planar-bounded half-space homogeneous medium. 63

3.5 Radiation efficiencies $\eta_{\text{rad}}\,(\omega) \equiv \min\,[\eta_{\text{idl}}, \eta_{\text{ub}}]$ in infinite planar-bounded media. (a) Orientation of magnetic dipole moment $\mathbf{m}$ strongly affects the efficiency (homogeneous half-space). (b) The 90° oriented magnetic dipole moment $\mathbf{m}$ (TM_z mode) compared to the out-of-plane magnetic current source (TE_z mode) at $d = 1$ cm implantation depth in homogeneous half-space medium. (c) The homogeneous half-space medium at $d = 1$ to 5 cm and (d) at $d = 6$ to 10 cm implantation depths. (e) The layered (skin–fat–muscle) half-space medium at $d = 1$ to 5 cm and (f) at $d = 6$ to 10 cm implantation depths. 64

3.6 Normalized **E**-field distributions at 1 cm depth in infinite planar-bounded homogeneous half-space medium [muscle-equivalent EM properties according to Eq. (2.2)] for (a) the magnetic current source (TE_z mode) and (b)–(c)–(d) the 90° oriented magnetic dipole (TM_z mode). The radiation efficiency peaks at 2.1 GHz (a)–(b) and 480 MHz (d) for both sources and drops at 1.3 GHz (c) due to constructive resonance in tissue that increases power absorption. 65

3.7 The optimal frequency in the infinite planar-bounded homogeneous half-space medium [dispersive EM properties of muscle according to Eq. (2.2)] follows the power law. 65

3.8 Normalized **E**-field distributions at 1 cm depth in the infinite planar-bounded layered half-space medium. The 90° oriented magnetic dipole moment $\mathbf{m}$ (TM_z mode) at (a) 780 MHz (maximum efficiency) and (b) 2.1 GHz. 66

3.9 Radiation efficiencies η_{rad} for the $R90$ mm cylindrical stratified phantom similar to the one used by Merli *et al.* and Chrissoulidis and Laheurte (4 mm skin-equivalent outer layer, 4 mm fat-equivalent intermediate layer, and $R82$ muscle-equivalent domain containing the source). Tissue EM properties of the layers are according to Eq. (2.2). (a) The 90° oriented magnetic dipole moment **m** (TM_z mode) source at $d = 1$ to 4 cm and (b) $d = 5$ to 9 cm implantation depths. (c) The out-of-plane magnetic current source (TE_z mode) at $d = 1$ to 4 cm and (d) $d = 5$ to 9 cm implantation depths. At $d = 9$ cm, the source is in the middle of the phantom. 67

3.10 Normalized **E**-field distributions at 110 MHz and 1 cm depth in the cylindrical stratified phantom. (a) The magnetic current source (TE_z mode). (b) The 90° oriented magnetic dipole moment **m** (TM_z mode). 67

3.11 Radiation efficiencies η_{rad} in the anatomical phantom at $d = 1$ to 20 cm implantation depths. (a)–(c) The 90° oriented magnetic dipole moment **m** (TM_z mode). (d)–(f) The out-of-plane magnetic current source (TE_z mode). 68

3.12 Normalized **E**-field distributions of a source at 1 cm depth (subcutaneous) in anatomical phantom. (a)–(d) The 90° oriented magnetic dipole moment **m** (TM_z mode). (e)–(h) The magnetic current source (TE_z mode). 68

3.13 Normalized **E**-field distributions of a source at 6 cm depth (stomach) in anatomical torso phantom at 480 MHz. (a) The 90° oriented magnetic dipole moment **m** (TM_z mode). (b) The magnetic current source (TE_z mode). 69

4.1 Reference antenna PCB layout and the initial stack-up. 78

4.2 The measurement set up for the material dielectric characterization: APC7 coaxial line connected to the network analyzer Keysight 8753ES. 79

4.3 Dielectric characterization results of the PVC capsule shell and bi-component epoxy filling. 79

4.4 Quarter-wave stepped impedance resonator equivalent transmission line model. 80

4.5 Final CST model with hexahedral mesh containing about 7×10^8 cells. 84

4.6 Adaptive mesh refinement study in CST MWS for min-DoF model: (a) S_{11} *vs.* passes, (b) mesh cells *vs.* passes, (c) solver time *vs.* passes, and (d) $\max(\Delta S)$ *vs.* passes. 84

4.7 Computational domain within the CST Microwave Studio using the rectangular homogeneous lossy phantom. 84

4.8 COMSOL model. The mesh contains 56 347 elements (54 433 tetrahedral and 1 914 prismatic ⇒ 1 096 983 DoF). 84

4.9 S_{11} magnitude and Z Smith chart for 2 mil (50.8 µm) substrate. . . . 85

4.10 Radiation pattern for surface PEC *vs.* volumetric copper platings. . . 86

4.11 Influence of the 50 MHz coil on the impedance of the antenna. 87

4.12 Model slice of the planar antenna considering the effects of the PVC shell and the epoxy capsule-filling. 87

4.13 The influence of the PVC shell and the epoxy filling on the resonant frequency f_{res} and the impedance Z_{ANT} of the antenna on a 50.8 µm substrate. 87
4.14 Antenna geometry and parametric dimensions. 88
4.15 The Pareto chart of effects of the antenna parametric dimensions on the input impedance Z_{ANT}. 88
4.16 The model of conformal capsule antenna inside a ⌀100 mm homogeneous phantom considering the PVC shell and epoxy filling. 89
4.17 Left: antenna on 50.4 µm polyimide substrate connected to 50 Ω semi-rigid coaxial cable. Right: Measurement set up using the Agilent PNA–X network analyzer (antenna in pure water). 90
4.18 Measurements for nine planar antennas in air *vs.* the numerical model: S_{11} and Z-Smith chart. 91
4.19 Two planar antennas in water *vs.* the model: the model, S_{11} and Z Smith chart. 91
4.20 Conformal antenna in the Rohacell IG 51 foam ($\varepsilon_r = 1.05$, $\tan\delta = 0.0003$). 92
4.21 Capsule preparation process for the impedance measurement: 1) to cut the PVC shell; 2) to insert the antenna and to measure the impedance; 3) to fix the connection with the epoxy resin for the mechanical rigidity and to re-measure the impedance; 4) to insert the capsule circuitry and to fill the capsule with the epoxy; 5) to measure the capsule impedance after 24 h (epoxy curing time). 92
4.22 Impedance characterization in phantoms. *left*: Phantom characterization using Agilent 85070C kit. *right*: $|S_{11}|$ and Z Smith chart measurement results of the antenna in the capsule in four environments (air, water, avg, and max. phantoms). 92
4.23 PCB stack-up with the variable substrate thickness. 93
4.24 Final PCB stack-up of the antenna PCB. 94
4.25 Geometry of the optimized hybrid microstrip-coplanar antenna. . . . 94
4.26 Conformal model of the optimized antenna taking into account the PCB stack-up, PVC shell and epoxy filling. *left*: Full capsule. *right*: Final mesh of the co-planar line. 95
4.27 y–z plane slice of the local SAR for an optimized antenna planar approximation. 95
4.28 Simulated 1g SAR (normalized by the radiated power P_{rad}) over the line in y–z plane 1 mm on top of the shell. 95
4.29 Initial proof-of-concept prototype of the optimized antenna on Rogers XT/duroid® 8000 substrate. *left*: Top and bottom views of the antenna connected to a 50 Ω semi-rigid coaxial cable. *right*: Magnified view of the co-planar line. 96
4.30 Final prototype of the optimized antenna on polyimide substrate. *left to right*: Connected antenna with and without circuitry, soldering connection, folding of the antenna inside of the capsule, and nine fully assembled antennas. 96

5.1 Proposed in-body capsule antenna. (a) Antenna within an alumina (Al_2O_3) capsule. (b) Capsule dimensions (mm) and antenna circumradius a. 105
5.2 Maximum achievable radiation efficiency of an arbitrary dielectric-loaded electrically small antenna with circumradius $a = 5.8$ mm operating at $f_0 = 434$ MHz with 2.5%, 5%, 10%, and 20% fractional bandwidths (FBW). 107
5.3 Proof-of-concept capsule antenna: (left) conformal design within the ($18 \times \varnothing 8$) mm capsule; (right) top and bottom views of the planar antenna geometry. 108
5.4 Reflection coefficient of the proof-of-concept antenna simulated in following environments: muscle-equivalent phantom, maximum phantom, 40% muscle phantom, and free space. 109
5.5 Proof-of-concept antenna prototype. (a) Photograph of the antenna printed on the 18 mm × 10 mm × 50 µm flexible substrate (Rogers ULTRALAM® 3850HT) and connected to a 50 Ω coaxial cable; (b) magnified view of the 0.2 mm microstrip line. 109
5.6 Measured and simulated reflection coefficients of three antenna prototypes in pure deionized water. 110
5.7 H-type half-wave microstrip stepped impedance resonator. 111
5.8 2D cross-section (not in scale) of the folded antenna inside the capsule within a circular phantom of radius R. 112
5.9 (a) Top and (b) bottom views of the antenna PCB and its dimensions (not in scale, mm) for ISM (433 to 434.8) MHz and MedRadio (401 to 406) MHz bands. 112
5.10 Antenna numerical analysis flowchart. 115
5.11 Impedance characteristics of the capsule antenna simulated in the homogeneous $\varnothing 100$ mm spherical phantom with muscle-equivalent ($\varepsilon = 56.9$, $\sigma = 0.81$ S·m^{-1}), highest ($\varepsilon = 77.3$, $\sigma = 2.26$ S·m^{-1}), and lowest (fat-equivalent, $\varepsilon = 11.6$, $\sigma = 0.08$ S·m^{-1}) EM properties. (a) Reflection coefficient $|S_{11}|$ and (b) antenna complex impedance Z_{ANT}. 116
5.12 (a) Simulated radiation pattern of the antenna at 434 MHz in $\varnothing 100$ mm spherical phantom with muscle-equivalent EM properties. (b) Locations of the capsule for the radiation performance evaluation in realistic phantom. (c) Azimuth and (d) elevation plane radiation patterns of the capsule simulated in the realistic phantom for four application scenarios. 117
5.13 Detuning immunity: reflection coefficient $|S_{11}|$ at $f_0 = 434$ MHz within the homogenous spheric phantom $\varnothing 100$ mm with $\varepsilon_r \in [10, 80]$ and $\sigma \in [0, 2.3]$ S·m^{-1}. White dotted contour denotes the $|S_{11}| = -10$ dB level. 118
5.14 Effect of capsule components on the antenna performance. (a) Perfect electric conductor capsule of the radius R modeling the device circuitry to analyze its effect on the antenna impedance. (b) Reflection coefficients $|S_{11}|$ of the antenna (muscle phantom) for the various radii R of the PEC capsule. 119

5.15 Application of the antenna to endoscopy. (a) Capsule antenna with a transparent cap. The PVC cap may be filled with either air or water. (b) Reflection coefficients $|S_{11}|$ of the antenna (average GI phantom) in the full alumina shell, with the cap filled with air or with water. . . 120
5.16 Influence of Other Devices in Proximity. (a) Numerical model. (b) Reflection coefficients $|S_{11}|$ of the antenna (muscle-equivalent phantom) for the various distances d to the PEC capsule. 120
5.17 Capsule antenna prototype. (a) Top and bottom views of the planar antenna soldered to a 50 Ω coaxial cable. (b) Antenna in the 0.5 mm thick alumina encapsulation. (c) Final assembly filled with pure water and sealed at both ends. 123
5.18 Measured and computed reflection coefficients of the antenna in phantoms with muscle-equivalent, maximum, and averaged GI EM properties. 124
5.19 Far-field characterization of the antenna. (a) The AuT mounted on the tower positioner and fed using an optical fiber. (b) Measured co-pol (vertical) radiation patterns of the AuT contained in the ⌀100 mm sphere filled the liquid with muscle-equivalent EM properties. 125

6.1 Antenna element geometry and parametric dimensions. 136
6.2 Array of two mirrored elements. 137
6.3 Proof-of-concept two-element antenna array prototype inside a (28 × ⌀9) mm capsule 138
6.4 Reflection coefficient $|S_{11}|$ of the antenna simulated in a ⌀100 mm spherical muscle-equivalent phantom using both time- (FIT) and frequency-domain (FEM) solvers of CST Microwave Studio® 2016. 140
6.5 Detuning immunity within the homogenous spheric phantom ⌀100 mm. *left:* Reflection coefficient $|S_{11}|$ at $f_0 = 434$ MHz with $\varepsilon_r \in [10, 80]$ and $\sigma \in [0, 2.3]$ S·m^{-1}. *right:* Reflection coefficient $|S_{11}|$ at $f_0 = 2.45$ GHz with $\varepsilon_r \in [5.5, 70]$ and $\sigma \in [0, 3.5]$ S·m^{-1}. 140
6.6 Co-pol (vertical polarization) radiation pattern of the antenna at 434 MHz simulated in the ⌀100 mm spherical muscle-equivalent phantom. 141
6.7 Co-pol (vertical polarization) radiation pattern of the antenna at 2.45 GHz simulated in the ⌀100 mm spherical muscle-equivalent phantom. 141
6.8 Antenna prototyping. (a) Printed and folded antenna with a microstrip feed. (b) Antenna inside a ⌀9 mm ceramic shell soldered to a semi-rigid coaxial cable and sealed at the bottom with epoxy. (c) Impedance characterization setup using spherical muscle-equivalent phantom. (d) Far-field characterization: the antenna in spherical muscle-equivalent phantom mounted on the tower positioner in an anechoic chamber. 142
6.9 $|S_{11}|$ of the antenna prototype in 434 MHz muscle-equivalent phantom. 143
6.10 $|S_{11}|$ of the antenna prototype in 2.45 GHz muscle-equivalent phantom. 143
6.11 Operation principle of the *in vivo* sensing of EM properties. 145
6.12 RF circuit implementation examples. *left*: Direct connection. *right*: A realization containing switches. 146

A.1 Possible types of automatic adaptivity implemented in Agros 2D. . . 159

B.1 Model geometry for 50Ω ISO 11452-5:2002 stripline for validation of the methodology. 162
B.2 Initial and solution meshes using *hp*-adaptivity. 162
B.3 Scalar potential and electric field distributions. 162
B.4 Error depends on the radius of computational domain for unshielded transmission lines. 162

C.1 Initial matching topology for direct tie configuration. 164
C.2 Optimized matching circuit topology for direct tie configuration. . . . 166
C.3 *S*-parameters of the circuit for the MCU in RX mode taking into account the TX. 167
C.4 Voltages at the RXp (P1) and RXn (P2) pins. The circuit takes into account TX as in previous Figure. 167
C.5 *S*-parameters of the non-optimized circuit for the MCU in TX mode taking into account the RX. 169
C.6 *S*-parameters of the optimized matching circuit for the MCU both in TX and RX modes. 169

List of Tables

1.1 Prototypes and commercial wireless gastrointestinal capsules 14
1.2 VHF–UHF Antennas for Ingestible Capsule Applications 25

2.1 Time-averaged dielectric properties of a human gastrointestinal tract at 434 MHz. 37
2.2 Tissue dielectric properties for the most common implantation sites. . 38
2.3 Full factorial experiment design (2^2) and measured EM properties at 434 MHz. 43

4.1 Plating approximation. Resonant frequency f_{res}, bandwidth at $S_{11} < -10$ dB and the antenna real impedance $\Re\left(Z_{\text{ANT}}\right)$ at f_{res} 86

5.1 Electromagnetic Properties of Biological Tissues at 434 MHz For Some Implantable (Top) and Ingestible (Bottom) Cases 105
5.2 Signal-to-Noise Ratios in Four in-Body Sites at 10 m Operating Distance for Free-Space, LOS, and NLOS Propagation 122
5.3 Phantoms Used for Measurements: EM Properties at 434 MHz and Concentrations for Water–Sucrose–NaCl Solutions 123
5.4 Design, Operating Frequency, Capsule Size, and Radiation Performance in the Given Phantom of Capsule Antennas Reported in Literature 126

6.1 Water–Sucrose–NaCl Phantoms Used for Measurements: EM Properties and Concentrations at 434 MHz and 2.45 MHz 142

General Introduction

IMPLANTABLE, ingestible and injectable (in-body) devices for biomedical telemetry (biotelemetry) can continuously monitor and yield human or animal physiological parameters while maintaining mobility and quality of life [1]–[3]. Recent advances in microelectromechanical systems and microfluidics—along with further miniaturization of electronics—have empowered numerous innovations in biotelemetry devices, creating new applications in medicine, clinical research, wellness, and defense. Apart from telemetering various diagnostic data (endoscopic imagery [4], temperature [5], pressure [6], pH [7], glucose levels [8], etc.), modern in-body applications include, but are not limited to: brain–machine interfaces and visual prosthesis, pacemakers and defibrillators, drug delivery and hyperthermia [9].

Naturally, in-body devices require an efficient and reliable way to communicate with an external monitor or controller (Figure 1.1). The most common solutions are radio frequency (RF) transmission, inductive coupling, and the human body communication method [10]. Each way has its own advantages and drawbacks. Yet, RF transmission in VHF–SHF bands yields the longest range and highest data transfer rates for in-body wireless devices.

In this frame, several antenna types have been reported in recent years. They can be divided into three groups: wire antennas [11], [12] planar printed antennas [13], and conformal printed antennas [14]–[18]. Various types of conformal designs have been already reported: loop antennas [17], dipoles [18], and various microstrip antennas [14]–[16]. A comprehensive review is given in Chapter 1.

Improving the transmission range of miniature in-body devices remains a major challenge (for the time being they are able to operate only up to a few meters). Among the main issues to face are low radiation efficiencies ($\eta < 0.1\%$), antenna impedance detuning, and strong coupling to lossy and dispersive biological tissues.

From electromagnetic (EM) point of view, the biological tissues can be considered as an isotropic, linear, heterogeneous, and dispersive medium. It contains water, free ions, dissolved, and insoluble matter. These ingredients along with the cellular anatomy define four dielectric relaxation regions, which contribute together to the permittivity and conductivity of the tissues. These EM properties must be taken into account as a *phantom* while designing the antennas [19]. One of the most common way to model the the EM spectrum of a tissue is by using the multiple Cole–Cole dispersion model [20]. A geometrical representation (by simple, complex, or compound shapes) of one or several tissues along with the corresponding EM properties assigned for each point of space together constitute a computational phantom. Physical phantoms (liquid, gel, solid, or hybrid) simulate biological tissues for the experimental characterization of in-body antennas both in terms or impedance and radiation efficiency.

The radiation efficiency of in-body antennas is mostly constrained by attenuation

and reflection losses [21] as well as by the required miniaturization of antennas that imposes fundamental limits on the maximum achievable radiation efficiency [22]. Detuning occurs since the antenna impedance strongly depends on EM properties of a surrounding environment that—in case of biological tissues—vary both in terms of permittivity and conductivity [23]. Ingestible antennas are more susceptive to impedance detuning than implantable ones as they must operate in a dynamically changing environment, i.e. through different gastrointestinal (GI) tract tissues. A straightforward approach to the problem is to design a wideband antenna with a bandwidth covering the expected detuning range, as reported in [17]. However, extending the bandwidth often implies sacrificing the radiation efficiency η, especially for electrically small antennas (ESA) [24].

The radiative far- or mid-field EM energy transfer from an in-body device to the surrounding free space (where a receiver is located) gives substantially better efficiency than near-field coupling in 10^6–10^7 Hz range [9], [25], [26]. For an ideal source, the radiation efficiency increases with frequency until reaching its maximum [25]. The frequencies around this maximum are hence optimal; they are inversely proportional to the implantation depth of the source. Maximizing the radiation efficiency for a given depth is therefore negotiating between the attenuation due to dielectric losses and the reflection (mismatch) losses caused by a high contrast between media.

Merli *et al.* [21] and Skrivervik [27] studied the effect of implantable device encapsulation on radiation efficiency and found that it improves with increasing permittivity of encapsulation. In addition, high permittivity and low loss superstrate contributes to the decoupling of the antenna from lossy tissues with varying EM properties [28]. Microstrip antenna designs [14]–[16] also help to decouple the antenna from tissues as the antenna geometry and substrate material mostly define its resonance [29]. In other words, the near field of the antenna is "squeezed" closer to its surface and therefore less dissipated in tissue.

With this in mind, we conjecture that by combining specific narrowband microstrip designs (provided sufficient decoupling from tissue to ensure impedance robustness) with dielectric loading, one can mitigate the attenuation loss, increase the total antenna efficiency, and, therefore, increase the operating range on in-body devices.

This dissertation will focus, at first, on theoretical studies of infinitesimal in-body sources and tissue models. Next, we will carry on to antenna solutions. The first studied antenna will be the one of BodyCap e-Celsius® capsule that we will reversely engineer and then optimize under strict material and integration constraints. After, we will design second (miniature) and third (dual-band) antennas based on the results of theoretical studies. Our objective will be to provide scientific community with small-footprint, efficient, 50 Ω-matched antennas to be used "as is" for arbitrary applications and implantation sites along with sensors, circuitry, and a microcontroller of choice. Finally, we will present a perspective methodology for *in vivo* wireless sensing of EM properties using the communication antenna of the in-body device.

The Ph.D. dissertation has been pursued under the joint supervision between the Institute of Electronics and Telecommunication of Rennes (IETR – UMR CNRS 6164, University of Rennes 1, France) and the Department of Theory of Electrical Engineering (KTE/FEL) of the University of West Bohemia in Pilsen. The industrial collaboration with the BodyCap Company (www.bodycap-medical.com)

defined the working program and study objectives.

Outline of the Dissertation

The manuscript is organized as follows.

Chapter 1 overviews the field of in-body biotelemetry. After identifying the context, objectives, and goals of the dissertation, I proceed to the comprehensive review of existing antenna solutions for capsule applications.

Chapter 2 focuses on the biological environment and methods to account for its effect of the antenna. I start by modeling the tissue for implantable and ingestible cases then proceed to the development of both computational and physical phantoms. First, I develop two two-dimensional boundary representation phantoms: a normal human brain and a human abdominal region (torso) phantom. Then, I propose the methodology to achieve given electromagnetic properties at a given frequency based on the full factorial experiment design. Finally, I describe the spherical physical phantom for the far-field characterization along with a combination of feed decoupling techniques.

Chapter 3 proceeds by reviewing the through-body propagation mechanisms and deriving the optimal frequency and radiation conditions for the in-body devices. I evaluate the radiation efficiency dependence on the operating frequency, implantation depth of a source, and its polarization. The formulated problem uses homo- and heterogeneous phantoms with increasing anatomical realism of the model: 1) infinite planar-bounded homogeneous and 2) layered half-space media, 3) stratified cylindrical and 4) anatomically realistic gastrointestinal phantom. To solve the full-wave formulation, I use the in-house code Agros2D implementing a fully *hp*-adaptive finite element method (*hp*-FEM). Solving the formulated problem with a commercial FEM-solver (COMSOL) validate the results along with an additional verification using the finite-difference time-domain (FDTD) method.

Chapter 4 presents the antenna used by BodyCap for its e-Celsius® capsule. As the performance of the initial antenna was unknown, I, at first, reverse-engineer the antenna and, second, study the ways on how to improve its operating range and robustness under strict integration and material constraints. The developed theoretical model allows dimensioning the antenna for a given resonance frequency whereas taking into account the loading effect of the capsule materials and biological tissues. The mechanisms of antenna–body coupling are analyzed, and the proposed solution improves the antenna gain by 11 dBi (the operating range is more than tripled). The existing matching circuit and balun are optimized too for the given application reducing its size from eleven to seven discrete elements and prioritizing TX performance.

Chapter 5 goes beyond the constraints imposed in previous chapter and proposes an ultra-miniature 434 MHz antenna immune to impedance detuning caused by varying EM properties of the surrounding biological environment. It is designed for a standard input impedance of 50 Ω. This allows using the antenna "as is" for a given in-body application in conjunction with a microcontroller or an RF circuit of choice. The antenna is synthesized and miniaturized using a hybrid analytical–numerical approach, then optimized to conform to the inner surface of a 17 mm long biocompatible encapsulation (7 mm diameter). The substrate is 50 µm thick. The capsule antenna is analyzed both in simplified and anatomically realistic heterogeneous phantoms. It remains matched at common implantation sites and through

the whole gastrointestinal tract. Enhanced robustness allows using the antenna for a wide range of in-body applications. Computed reflection coefficients and radiation performance show good agreement with measurements. The far-field radiation is characterized with the direct illumination technique using an analog fiber optic link. The realized gain (measured max. value –19.6 dBi) exceeds the counterparts by about 3 dBi.

Chapter 6 proposes a dual-band 434 MHz and 2.45 GHz antenna also immune to impedance detuning caused by varying EM properties of the surrounding biological environment. The input impedance is 50 Ω for both operating frequencies. Such antenna can integrate both data transmission and wireless power transfer functionality. The proposed design occupies 2.6% of the available volume inside of the 28 mm $\times\varnothing$ 9 mm capsule. High robustness allows using the antenna for both implantable and ingestible applications. We characterize the radiation with the direct illumination technique using an analog fiber optic link. The realized gain of the capsule exceeds the existing 434 MHz counterparts by about 9 dBi and the 2.45 GHz-ones by about 3 dBi. Finally, in the second part of Chapter 6, we talk about a potential application of in-body antennas to *in vivo* sensing of EM properties. With the proposed methodology, an in-body device can use the same antenna for data communication and for environment sensing. The method is based on measurements of the reflected signal due to antenna mismatch, which depends on surrounding tissues. From the measured amplitude and phase of the reflected signal, one can evaluate the complex impedance of the antenna and, if necessary, the EM properties of surrounding environment.

The main part finishes with **Conclusion** that summarizes the main findings and major contributions as well as identifies future work and perspectives.

The dissertation contains three **Appendices**. **Appendix A** reviews the automatic mesh adaptivity algorithm of Agros2D [30]. **Appendix B** provides the validation of the numerical model proposed in Chapter 4 for estimating impedance of an arbitrary and heterogeneous TEM transmission line. Finally, **Appendix C** describes the matching circuit and balun for the optimized antenna of BodyCap e-Celsius capsule® [5] reported in Chapter 4.

Bibliography

[1] K. S. Nikita, *Handbook of Biomedical Telemetry*. Hoboken, NJ: John Wiley & Sons, Jul. 2014.

[2] A. Kiourti and K. S. Nikita, "A review of in-body biotelemetry devices: Implantables, ingestibles, and injectables," *IEEE Transactions on Biomedical Engineering*, vol. 64, no. 7, pp. 1422–1430, 2017.

[3] M. Yuce and T. Dissanayake, "Easy-to-swallow wireless telemetry," *IEEE Microwave Magazine*, vol. 13, no. 6, pp. 90–101, Sep. 2012.

[4] G. Iddan, G. Meron, A. Glukhovsky, and P. Swain, "Wireless capsule endoscopy," *Nature*, vol. 405, no. 6785, pp. 417–417, May 2000.

[5] BodyCap Medical, *E-Celsius*. [Online]. Available: `http://www.bodycap-medical.com/`.

[6] E. Chow, A. Chlebowski, S. Chakraborty, W. Chappell, and P. Irazoqui, "Fully wireless implantable cardiovascular pressure monitor integrated with a medical stent," *IEEE Transactions on Biomedical Engineering*, vol. 57, no. 6, pp. 1487–1496, Jun. 2010.

[7] Given Imaging, *Bravo pH*. [Online]. Available: `http://www.givenimaging.com/en-int/Innovative-Solutions/Reflux-Monitoring/Bravo-pH/`.

[8] M. C. Shults, R. K. Rhodes, S. J. Updike, B. J. Gilligan, and W. N. Reining, "A telemetry-instrumentation system for monitoring multiple subcutaneously implanted glucose sensors," *IEEE Transactions on Biomedical Engineering*, vol. 41, no. 10, pp. 937–942, Oct. 1994.

[9] E. Chow, M. Morris, and P. Irazoqui, "Implantable RF medical devices: The benefits of high-speed communication and much greater communication distances in biomedical applications," *IEEE Microwave Magazine*, vol. 14, no. 4, pp. 64–73, Jun. 2013.

[10] C. H. Hyoung, S. W. Kang, J. H. Hwang, S. E. Kim, J. K. Kim, T. W. Kang, K. S. Kim, J. B. Kim, H. I. Park, I. G. Lim, K. H. PARK, and J. H. Shim, "Human body communication system and method," US20100274083 A1, Oct. 2010.

[11] S.-H. Lee and Y.-J. Yoon, "Fat arm spiral antenna for wideband capsule endoscope systems," in *2010 IEEE Radio and Wireless Symposium (RWS)*, New Orleans, LA, Jan. 2010, pp. 579–582.

[12] S.-I. Kwak, K. Chang, and Y.-J. Yoon, "The helical antenna for the capsule endoscope," in *2005 IEEE Antennas and Propagation Society International Symposium*, vol. 2B, Washington, DC, Jul. 2005, pp. 804–807.

[13] F. Merli, L. Bolomey, J. Zurcher, G. Corradini, E. Meurville, and A. Skrivervik, "Design, realization and measurements of a miniature antenna for implantable wireless communication systems," *IEEE Transactions on Antennas and Propagation*, vol. 59, no. 10, pp. 3544–3555, Oct. 2011.

[14] Y. Mahe, A. Chousseaud, M. Brunet, and B. Froppier, "New flexible medical compact antenna: Design and analysis," *International Journal of Antennas and Propagation*, vol. 2012, May 2012.

[15] K. A. Psathas, A. Kiourti, and K. S. Nikita, "A novel conformal antenna for ingestible capsule endoscopy in the MedRadio band," in *34th Progress in Electromagnetics Research Symposium (PIERS 2013)*, Stockholm, Sweden, Aug. 2013.

[16] X. Cheng, D. Senior, C. Kim, and Y.-K. Yoon, "A compact omnidirectional self-packaged patch antenna with complementary split-ring resonator loading for wireless endoscope applications," *IEEE Antennas and Wireless Propagation Letters*, vol. 10, pp. 1532–1535, 2011.

[17] R. Alrawashdeh, Y. Huang, M. Kod, and A. Sajak, "A broadband flexible implantable loop antenna with complementary split ring resonators," *IEEE Antennas and Wireless Propagation Letters*, vol. 14, pp. 1506–1509, 2015.

[18] L.-J. Xu, Y.-X. Guo, and W. Wu, "Bandwidth enhancement of an implantable antenna," *IEEE Antennas and Wireless Propagation Letters*, vol. 14, pp. 1510–1513, 2015.

[19] T. Karacolak, A. Hood, and E. Topsakal, "Design of a dual-band implantable antenna and development of skin mimicking gels for continuous glucose monitoring," *IEEE Transactions on Microwave Theory and Techniques*, vol. 56, no. 4, pp. 1001–1008, Apr. 2008.

[20] S. Gabriel, R. W. Lau, and C. Gabriel, "The dielectric properties of biological tissues: III. Parametric models for the dielectric spectrum of tissues," *Physics in Medicine and Biology*, vol. 41, pp. 2271–2293, Nov. 1996.

[21] F. Merli, B. Fuchs, J. R. Mosig, and A. K. Skrivervik, "The effect of insulating layers on the performance of implanted antennas," *IEEE Transactions on Antennas and Propagation*, vol. 59, no. 1, pp. 21–31, 2011.

[22] J. Volakis, C.-C. Chen, and K. Fujimoto, *Small Antennas: Miniaturization Techniques & Applications*. McGraw Hill Professional, Jun. 2010.

[23] C. Gabriel, "Dielectric properties of biological materials," in *Handbook of biological effects of electromagnetic fields. Bioengineering and biophysical aspects of electromagnetic fields*, F. S. Barnes and B. Greenebaum, Eds., 3rd ed., Boca Raton, FL: CRC Press, 2007, pp. 51–100.

[24] S. Best, "Bandwidth and the lower bound on Q for small wideband antennas," in *IEEE Antennas and Propagation Society International Symposium 2006*, Albuquerque, NM USA, Jul. 2006, pp. 647–650.

[25] A. S. Y. Poon, S. O'Driscoll, and T. H. Meng, "Optimal frequency for wireless power transmission into dispersive tissue," *IEEE Transactions on Antennas and Propagation*, vol. 58, no. 5, pp. 1739–1750, 2010.

[26] L. Chirwa, P. Hammond, S. Roy, and D. Cumming, "Electromagnetic radiation from ingested sources in the human intestine between 150 MHz and 1.2 GHz," *IEEE Transactions on Biomedical Engineering*, vol. 50, no. 4, pp. 484–492, Apr. 2003.

[27] A. K. Skrivervik, M. Bosiljevac, and Z. Sipus, "Propagation considerations for implantable antennas," in *11th European Conference on Antennas and Propagation (EuCAP 2017)*, Paris, France, Mar. 2017.

[28] A. Kiourti, J. Costa, C. Fernandes, and K. Nikita, "A broadband implantable and a dual-band on-body repeater antenna: Design and transmission performance," *IEEE Transactions on Antennas and Propagation*, vol. 62, no. 6, pp. 2899–2908, Jun. 2014.

[29] R. Waterhouse, *Microstrip Patch Antennas: A Designer's Guide*. New York, NY: Springer Science & Business Media, Feb. 2003.

[30] P. Karban, F. Mach, P. Kus, D. Panek, and I. Dolezel, "Numerical solution of coupled problems using code Agros2D," *Computing*, vol. 95, no. 1, pp. 381–408, 2013.

Chapter 1

In-Body Biotelemetry: Context and State-of-the-Art

Contents

1.1 Introduction 12
1.2 In-body Biotelemetry in Medicine and Clinical Research 13
1.3 Context, Objectives, and Goals 14
1.4 Capsule Antennas Overview 15
1.4.1 Wire Antennas 16
1.4.2 Planar Printed Antennas 17
1.4.3 Conformal Printed Antennas 19
1.5 Summary 26

1.1 Introduction

ELECTRONIC implants for biomedical applications came out in the '50s with the invention of the first pacemaker [1]. This healthcare innovation exposed the potential and revealed vast opportunities in the field of implantable electronic devices enabling new ways of diagnostics and treatment while maintaining a patient's mobility. In particular, Richard Feynman outlined the idea of in-body biotelemetry in his lecture "There's plenty of room at the bottom" [2].

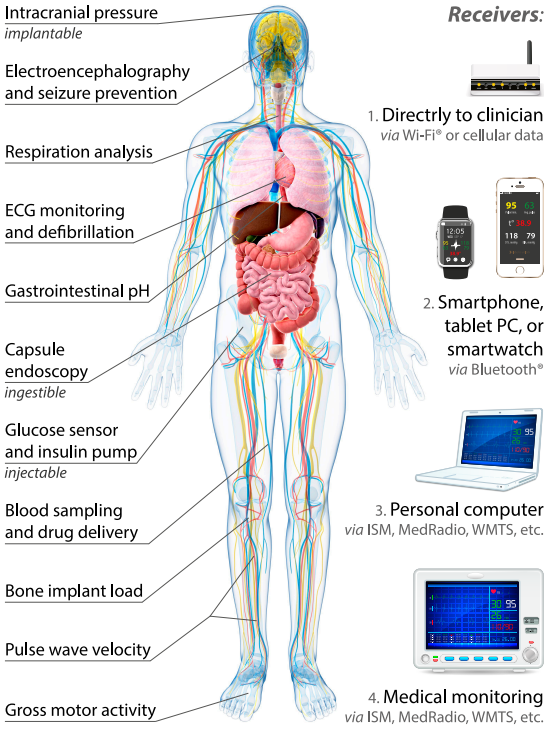

Fig. 1.1: In-body biotelemetry. *left*: existing and potential applications; *right*: some examples of on- and off-body receivers.

The first published statements about successful development of wireless ingestible capsules for diagnostic and research purposes appeared almost simultaneously in the Nature magazine in 1957 as a note by Zworykin and Farrar [3] and a letter from Mackay and Jacobson [4]. Zworykin's note reported the capsule that measures pressure variation inside a gastrointestinal (GI) tract. The capsule operated at frequencies around 1 MHz; more technical details were given later in [5]. Mackay *et al.* in their further works [6]–[8] proposed the capsules measuring pressure, temperature, and pH. These capsules operated at sub-megahertz frequencies. One of the first successful *in vivo* application of wireless telemetry implant was reported by Sines in 1960 [9]. The first US patent for the "Pill-type swallowable transmitter" appeared in 1964 [10]. In 1972, Watson *et al.* [11] reported a radiotelemetry capsule for pH profile measurement. The capsule operated in the 270–570 KHz range. Cáceres *et al.* [12] gave the first historical review of biomedical telemetry in the '60s. In the '70s, the first research appeared on implantable stimulation and control systems [13]. The period from 1970 to 1990, the implant systems matured. Biologists and field researchers used telemetry systems extensively both in laboratory and field research [14].

In the 2000s, advances in microelectromechanical systems and microfluidics—along with ongoing miniaturization of semiconductor electronics—empower numerous innovations in this field creating new applications in medicine, clinical research, wellness, and defense (Figure 1.1). Apart from telemetering various diagnostic data (for instance, endoscopic imagery [15], temperature [16], pressure [17], pH [18], glucose levels [19]), modern in-body applications include but are not limited to [20]–[23] brain–machine interfaces and visual prosthesis, pacemakers and defibrillators, drug delivery and hyperthermia. Emerging neural interfacing allows us studying the brain, restoring sensory function, and assisting in the rehabilitation of amputees, survivors of paralysis, and patients with neurodegenerative diseases [24], [25].

1.2 In-body Biotelemetry in Medicine and Clinical Research

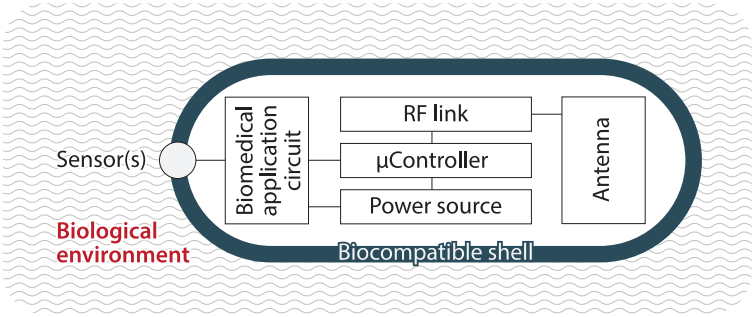

Fig. 1.2: Outline of an in-body capsule for biomedical telemetry.

Figure 1.2 shows a generic flowchart of a modern in-body wireless device. The devices use a wireless link to transmit biotelemetry data or to receive or modify operational and treatment instructions. The most common solutions are radio frequency (RF) transmission [26], inductive coupling [27], and human body communication method [28]. Each way has its own advantages and drawbacks. Yet, RF transmission in VHF–SHF[1] bands yields the longest range and highest data transfer rates for in-body wireless devices [29]. As for the power source, a multiband RF antenna can integrate both data transmission and wireless power transfer functionality increasing the available space inside an in-body device.

Wireless in-body devices for biomedical telemetry can be divided into three categories based on the way of insertion to the human body [23]: ingestible, implantable, and injectable.

Ingestible capsules are used primarily for wireless endoscopy or telemetry of various physiological parameters: e.g. temperature, pH and pressure [30], [31]. Potential future applications include the drug delivery [32] and surgery [33]. Some ingestible capsule antennas could be designed for both ingestible and subcutaneous/intraperitoneal implantable applications. It is useful for body temperature telemetry: the same capsule design can be used as ingestible for a human health monitoring or as implantable for a clinical research on animals. Table 1.1 lists the commercial ingestible systems and working prototypes available as for January 2017.

Implantable devices are widely used by clinicians and researchers to monitor health and to study normal and abnormal body functions [27]. These devices can measure and relay physiological signals (e.g., electrocardiogram, glucose levels, and blood pressure) to external equipment to be analyzed or to guide treatment. Implantable devices can also be used to record neural signals in brain–machine interfaces to control prostheses [34] or paralyzed limbs [35].

Injectable devices are implanted into the body by means of needles. For the moment, they are used mostly for the animal identification [36]. It is an emerging technology for the human use: Li *et al.* [37] reported a device for sensing and neurostimulation applications and Kim *et al.* [25] proposed a cellular-scale optoelectronics device with a broad application to biomedical science and engineering.

[1]Frequency bands as defined by ITU: very high frequency (VHF): 30–300 MHz, ultra high frequency (UHF): 300–3000 MHz, and super high frequency (SHF): 3–30 GHz

Table 1.1: Prototypes and commercial wireless gastrointestinal capsules

	Company	**Reference**	**Size** (mm)	f (MHz)	**Features**
Endoscopy	Given Imaging	PillCam SB 3	26.2×⌀11.4	434	2–6 fps, $\leqslant$ 8 h
		PillCam COLON 2	31.5×⌀11.6	434	4–35 fps, $\leqslant$ 8 h
		PillCam ESO 3	31.5×⌀11.6	434	35 fps, 30 min
	Chongqing	OMOM	28.3×⌀13	2400	0.5/2 fps, 7–9 h
	Olympus	Endocapsule 10	26×⌀11	434	2 fps, 12 h
	RF	Sayaka	23×⌀9	N/A	*Prot.*, 30 fps, WPT†
	IntroMedic	MiroCam MC1000-W	24.5×⌀10.8	~~Tx~~	HBC [28], 3 fps, 12 h
		MiroCam MC1000-WM	25.5×⌀10.8	Same + magnetic locomotion, 8 h	
	CapsoVision	CapsoCam SV-1	31×⌀11	~~Tx~~	20 fps, 15 h
Telemetry	BMedical	VitalSense	23×⌀8.7	40	$T°$, $\leqslant$ 10 days
	BodyCap	e-Celsius	17.7×⌀8.9	434	$T°$, $\approx$ 30 days
	Chongqing	OMOM pH	26×6 × 5.5	N/A	pH, $\approx$ 4 days
	Given Imaging	Bravo pH	25×6 × 5.5	434	pH, 2–4 days
		SmartPill	26×⌀13	434	$T°$, pH, P, $\geqslant$ 5 days
	HQ	CorTemp	22×⌀11	0.3	$T°$, 7–10 days
	Philips	IntelliCap	26×⌀11	N/A	*Prot.*, $T°$, pH, DD
	Remo	240	—	N/A	*Prot.*, $T°$, pH, P

~~Tx~~ – the capsule does not transmit data via radio waves; fps – frames per second; *Prot.* – prototype; $T°$ – temperature; P – pressure; DD – drug delivery.

† Wireless Power Transfer.

The comprehensive overviews of the modern in-body devices and applications from different perspectives are given in [21], [27], [31], [38], [39].

1.3 Context, Objectives, and Goals

The Ph.D. dissertation has been pursued under the joint supervision between the Institute of Electronics and Telecommunication of Rennes (IETR – UMR CNRS 6164, University of Rennes 1, France) and the Department of Theory of Electrical Engineering (KTE/FEL) of the University of West Bohemia in Pilsen. The industrial collaboration with the BodyCap Company (www.bodycap-medical.com) defined the working program and study objectives. BodyCap—located in Caen, France—develops, and commercializes miniature wireless electronic sensors and monitoring solutions. Specializing in wearable connected devices for physiological data monitoring, its high-tech products are used in medical, research, sport, and ergonomics areas. Having received medical device certifications ISO 13485 and ISO 9001, BodyCap designs products that comply with current European and worldwide standards and regulations.

The main objectives of the dissertation work are to 1) analyze the propagation within biological tissues; 2) optimize existing and develop new efficient, miniature and robust antennas for in-body capsule devices, and 3) improve methods for their analysis and characterization.

The initial goal of the research was to improve the existing antenna integrated into the BodyCap e-Celsius® capsule (Figure 1.3) in terms of radiation efficiency

Fig. 1.3: BodyCap e-Celsius® is a miniature electronic pill that monitors and communicates wirelessly the intracorporal temperature.

and matching robustness under strict material, integration, and size constraints. Thereby, I started with the state-of-the-art capsule antennas in their operational environment—human body—looking into major challenges of the design and ways to solve them. A new goal emerged: to understand the radiation mechanisms of an ideal in-body antenna and to formulate the optimal radiation conditions that maximize the radiation efficiency. Using the obtained knowledge, at first, I optimized the e-Celsius® antenna and, second, found means on how to further improve radiation performances and robustness unconstrained from the specifications of the e-Celsius® capsule. Having found the way, I set the final goals to fill-in gaps in state-of-the-art technology: 1) to design a universal, miniature, and robust in-body capsule antenna using widely accessible materials that can be applicable for both ingestible and a wide range of implantable applications. It must have a standard input impedance of 50 Ω so one can use it "as is" with a microcontroller, sensors, power sources, and RF circuits of choice; 2) to design a 50 Ω highly efficient and robust dual-band conformal antenna that allows both data and power transfers for a wide range of implantable and ingestible applications. Finally, I identify a way of using in-body antennas for simultaneous data transmission and sensing of surrounding tissues via its electromagnetic properties for diagnostic purposes.

1.4 Capsule Antennas Overview

At the frequencies lower than very high frequency (VHF) ($f_0 < 30$ MHz), wire induction links are used exclusively. As they operate in near field and show very low efficiencies [40], they are out of scope of this thesis. The comprehensive overview and design guidelines are given in [27, Ch. 5, 7].

VHF–UHF antennas fall into two categories: wire and printed. Reported wire antennas are either spiral or helical type, and printed antennas are either planar on a rigid printed circuit board (PCB) or conformal to the surface of a capsule. In this section, I review the VHF–UHF antennas for in-body applications, their performances along with the phantoms used, simulation methods, and characterization approaches. Table 1.2 on page 25 summarizes the published VHF–UHF band antennas for ingestible capsule applications.

1.4.1 Wire Antennas

Wire antennas for the ingestible capsules were the first published. They can be either helical or spiral with both circular and rectangular wire cross sections.

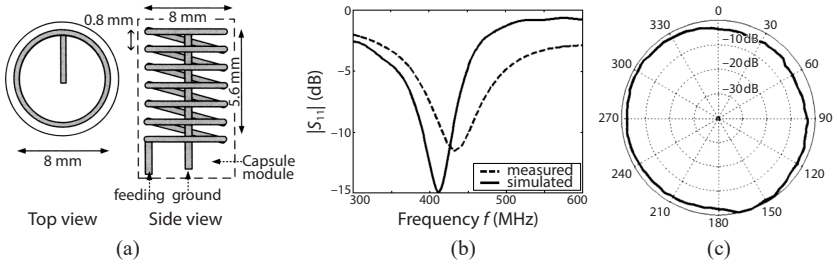

Fig. 1.4: Wire helical antenna (Kwak *et al.*, 2005): (a) dimensions, (b) reflection coefficient $|S_{11}|$, and (c) measured radiation pattern (norm. received power).

Kwak *et al.* [41] reported a helical antenna for a capsule endoscope (Figure 1.4). The size of the antenna is ($5.6 \times \varnothing 8$) mm. The antenna has a bandwidth of 410–442 MHz (32 MHz or 8%) for VSWR < 2 (or $|S_{11}| < -9.5$ dB) when measured in a liquid phantom ($\varepsilon_r = 56$, $\sigma = 0.8$ S·m^{-1}) in an $\varnothing 150$ mm cylindrical container. The authors used CST Microwave Studio® to simulate the antenna. The gain G and efficiency η were not reported.

Xu *et al.* [42]–[44] used a normal-mode helical antenna to study numerically (using FDTD implemented in Xfdtd®) the variations of radiation characteristics and SAR levels at 430, 800, 1200 and 2400 MHz due to the uncertainties of tissue dielectric properties. Four helical antennas were designed to fit the ($15 \times \varnothing 12$) mm capsule with 1 mm shell thickness. The wire is $\varnothing 1$ mm. The male and female phantoms reproduce the "Visible Human" anatomy data with the dielectric properties reported by Gabriel *et al.* [45]. The antenna was meshed with 1 mm^3 resolution and the tissue with 3 mm^3. The efficiencies η and gains G were not provided.

Rajagopalan and Rahmat-Samii [46] studied inverted conical helical antenna for a ($26 \times \varnothing 11$) mm capsule designed to operate within the Wireless Medical Telemetry Service (WMTS) 1.4 GHz band. The bandwidth was not reported, but according to the reflection coefficient, it is approximately 40 MHz (3%). The wire is $\varnothing 0.4$ mm and the pitch is 1 mm. The first loop is $\varnothing 1.5$ mm and increases by $\varnothing 2$ mm with each winding. The $\varnothing 9$ mm ground plane shields the antenna from the capsule circuitry. Additional $\varnothing 8$ mm metallic surface above the ground plane is used for the antenna tuning. The total antenna size is thus ($5.1 \times \varnothing 9$) mm. The authors report the radiation efficiency $\eta < 0.1\%$ and the simulated peak gain $G = -40$ dBi at 1.4 GHz. The antenna is linearly polarized. The tissue EM parameters were set as frequency dependent with the values $\varepsilon_r \in [53.55, 54.81]$ and $\sigma \in [0.98, 1.34]$ S·m^{-1} for 1–1.8 GHz. The permittivity of the capsule shell is $\varepsilon_r = 3.2$. For the antenna measurements, a tissue equivalent liquid phantom contained deionized water, sugar, salt and cellulose.

Lee *et al.* [47] proposed a conical spiral antenna for 450 MHz. Antenna has 101 MHz (or 22%) bandwidth for VSWR < 2 when measured in the liquid phantom with $\varepsilon_r = 56$, $\sigma = 0.83$ S·m^{-1} in a $\varnothing 300$ mm cylindrical container. Due to the conical structure, this antenna exhibits more broadband characteristics compared to the conventional narrowband spiral antennas and helical antennas mentioned

earlier. The antenna size is ($5 \times \varnothing 10$) mm. The authors used a 50 Ω coaxial cable to connect the antenna to a vector network analyzer for measurements and CST Microwave Studio® for simulations. The efficiency and gain were not reported.

Large-arm spiral antenna by Lee *et al.* [48], [49] uses flat wire and operates around 450 MHz with the $|S_{11}| < -10$ dB bandwidth from 76 MHz (17%) to 117 MHz (26%) depending on the antenna dimensions. The liquid phantom has $\varepsilon_r = 56.91$, $\sigma = 0.97$ S·m^{-1} and occupies a ⌀300 mm cylindrical container. The phantom consists of pure water, methanol, and sodium chloride. The 0.25 mm capsule shell has a relative permittivity $\varepsilon_r = 3.15$. The total antenna height h (including the ground plane) varies from 3 to 7 mm affecting the bandwidth; the diameter is ⌀10 mm. The 0.5 mm thick antenna arm width w varies from 2 to 4 mm: wider arms give more broadband characteristics. The total length of the arm—which defines the f_{res}—was experimentally found to be 90 mm ($\lambda/4$) for the antenna with the parameters $w = 4$ mm and $g = 1$ mm. The radiation efficiency η and the gain G were not given.

Dual spiral antenna for wireless endoscope is another development by Lee and Yoon [50]. The total antenna size is ($7 \times \varnothing 10$) mm. The antenna consists of two spirals: wire and printed on a PCB. The PCB is 1.574 mm thick with $\varepsilon_r = 2.5$. One feed line powers both spirals that are mounted above a ground plane. Two spirals have different overall length for enhancing the bandwidth (the printed one is longer than the wire one; the exact lengths were not reported). The authors reported a 411–600 MHz bandwidth for VSWR < 2 (189 MHz or 37.8%), when measured in a liquid phantom with $\varepsilon_r = 56$, $\sigma = 0.83$ S·m^{-1} in an ⌀300 mm cylindrical container. As for the previously mentioned antenna, the phantom consists of pure water, methanol, and sodium chloride. The radiation efficiency η and gain G were not reported.

Faerber and Desmulliez [51] reported a meander-shape wire antenna as well as its comparison to a small conformal helical antenna [52]. The antenna operates around $f_{\text{res}} = 586$ MHz ($FBW_{-10\text{dB}} = 47.4\%$) within a 100 mm^3 cubic phantom with the properties $\varepsilon_r = 52$, $\tan\delta = 0.246$. The reported gain is -26 dB. In free space, the $f_{\text{res}} = 5.1$ GHz. The ⌀0.4 mm wire is 58 mm long and is fixed within a layer of Loctite ($\varepsilon_r = 2.42$) to be fit on a ($25 \times \varnothing 10$) mm capsule. The authors used CST Microwave Studio® to analyze the antenna.

Wire antennas provide high achievable bandwidths and good efficiencies. However, they are voluminous and poorly integrable in a capsule device. Better integration and more technological manufacturing could be achieved with printed antennas.

1.4.2 Planar Printed Antennas

The first reported printed antenna for ingestible capsules was the spiral antenna on a rigid PCB reported by Kwak *et al.* [53]. The antenna bandwidth is comparable with wire antennas: 110 MHz or 24% (400–510 MHz for VSWR < 2) when measured in a liquid phantom with $\varepsilon_r = 56$, $\sigma = 0.8$ S·m^{-1} in an ⌀300 mm cylindrical container. The substrate is 3 mm thick (⌀10.5 mm) and has $\varepsilon_r = 2.17$. The $\lambda/4$ spiral trace width is 0.5 mm. The radiation efficiency η and gain G were not reported.

Xie *et al.* [54] reported a 2.45 GHz printed spiral antenna on a 3 mm thick F4BK335 substrate ($\varepsilon_r = 3.5$, $\tan\delta = 0.001$). A pin shortens the antenna. The reported bandwidth is 104 MHz (4%). The antenna lacks the omnidirectionality for

ingestible capsule applications. The phantom characteristics and radiation efficiency η were not reported. Another 2.45 GHz spiral antenna on a rigid PCB for capsule applications was reported by Zhao *et al.* [55]. The authors used the following phantom properties: $\varepsilon_r = 53.6$, $\sigma = 1.8$ S·m^{-1}. No dimensions were given along with the bandwidth, neither other performance indications as radiation pattern, gain and efficiency, nor the measurement data.

Huang *et al.* [56] proposed a microstrip four-arm spiral antenna for 914 MHz ISM band printed on a rigid 0.6 mm thick PCB with $\varepsilon_r = 6.1$. The antenna is narrowband (1.2% or 11 MHz bandwidth at $|S_{11}| < -10$ dB). The gain is approximately -46 dBi. A shortening strip contributes to the miniaturization; the total antenna size is $8.25 \times 8.25 \times 0.6$ mm^3. The capsule casing and circuitry were not taken into account in simulations. The antenna was analyzed using FDTD method inside a heterogeneous phantom (Visible Human, 25 distinct tissues). Adaptive mesh was used with the $0.25 \times 0.25 \times 0.3$ mm^3 resolution for the antenna and 5 mm^3 for the rest of the computational domain.

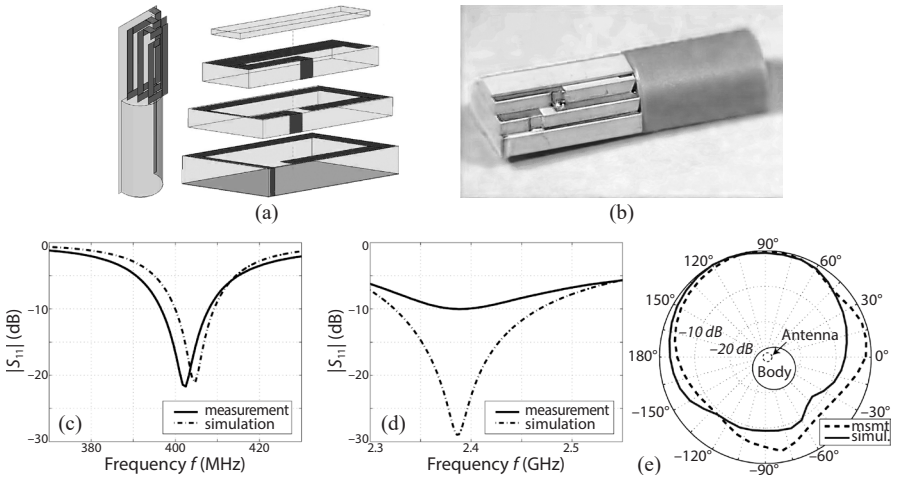

Fig. 1.5: Multilayer printed planar antenna (Merli *et al.*, 2011): (a) design, (b) prototype, reflection coefficients $|S_{11}|$ ((c) MedRadio and (d) ISM), and (e) ISM radiation patterns (normalized). © 2010 IEEE.

Merli *et al.* [57] reported the dual-band multilayered spiral antenna (Figure1.5) that operates in the 401–406 MHz MedRadio band and 2.4–2.5 GHz ISM band; the measured $|S_{11}| < -10$ dB bandwidths are 9.3 MHz (2.3%) and 145 MHz (6%), respectively, for MedRadio and ISM. The gains $G_{\text{MedRadio}} = -29.4$ dBi and $G_{\text{ISM}} = -17.7$ dBi, the directivities $D_{\text{MedRadio}} = 3.5$ dBi and $D_{\text{ISM}} = 4.4$ dBi, and the radiation efficiencies $\eta_{\text{MedRadio}} = 0.051\%$ and $\eta_{\text{ISM}} = 0.605\%$ within a liquid phantom in a ⌀80 mm cylindrical container. Unlike the previously mentioned phantoms, the capsule is displaced from the central axe. The measured parameters of the liquid phantoms are $\varepsilon_r = 57.36$, $\tan\delta = 0.580$ for the MedRadio band and $\varepsilon_r = 53.76$, $\tan\delta = 0.241$ for the ISM. The MedRadio phantom consists of (percent by weight): distilled water (51.3%), sugar (47.3%) and salt (1.4%). The ISM phantom is made of distilled water (73.2%), salt (1.4%) and DGBE (diethylene glycol butyl ether, 26.76%). Further analysis of the antenna was performed in SEMCAD X using the Duke phantom from the Virtual Family. The antenna size without the casing is $24.7 \times 8 \times 5.2$ mm^3. It fits inside the capsule of ($32.1 \times$ ⌀10) mm. The 0.8 mm shell is made of Polyetheretherketone (PEEK) ($\varepsilon_r \approx 3.5$). Antenna 35 µm copper layers

are printed on Rogers TMM® 10 substrate ($\varepsilon_r = 9.2$, $\tan\delta = 0.0022$) and united using 30 µm thick epoxy adhesive (MedRadio: $\varepsilon_r = 3$; ISM: $\varepsilon_r = 4$; $\tan\delta = 0.001$). The antenna was integrated into an in-body device and characterized *in vivo* [58].

Liu *et al.* [59] proposed a circularly polarized multilayer helical antenna for the ISM 2.4–2.48 GHz band. The bandwidth is 1.85–2.8 GHz (950 MHz or 41%) for $|S_{11}| < -10$ dB when simulated in a 100 mm^3 cubic phantom with $\varepsilon_r = 52.79$, $\sigma = 1.7$ S·m^{-1}. The peak gain is $G \approx -32$ dBi. The antenna consists of three layers interconnected by vias, each layer containing an open loop. The substrate is 1.27 mm Rogers RO3010 with $\varepsilon_r = 10.2$, $\tan\delta = 0.0022$. The total antenna footprint is $\pi \times 5.52 \times 3.81$ mm^3; it is designed to fit within the ($26 \times \varnothing 11$) mm capsule. The authors studied the sensitivity of the antenna by varying the phantom parameters; four tissues were used: muscle, stomach, small intestine, and colon. Ansys® HFSS™ was used to design and study the antenna within a homogeneous phantom and CST Microwave Studio® to study the antenna in a voxel phantom—Gustav from the CST Voxel Family—the antenna radiation, sensitivity and SAR.

Dissanayake *et al.* [60] reported a slot microstrip UWB antenna that operates at 3.5–4.5 GHz. The slot design is based on a magnetic dipole principle that is less affected by the near field perturbations caused by the varying dielectric parameters of the surrounding biological tissue. The antenna is printed on the capsule-shaped 1.27 mm Rogers TMM® 10i substrate ($\varepsilon_r = 9.8$, $\tan\delta = 0.002$). The total antenna size is $23.7 \times 8 \times 1.27$ mm^3, the capsule shell is 0.5 mm thick. The slot occupies half of the substrate, which is loaded with the glycerin. This contributes to the miniaturization as well as the impedance matching with the biological tissue. For the simulation in CST Microwave Studio®, various tissue parameters were used; the cylindrical computational phantom size is ($40 \times \varnothing 29$) mm. The proof-of-concept measurement used pork midloin tissue. The authors claim that the high permittivity dielectric loading of an antenna (ideally with ε_r equal to this of surrounding tissues) contributes to lower reflection coefficients, so that the wider band matching of the antenna could be achieved. The same antenna was used in the power absorption study by Thotahewa *et al.* [61]; Dissanayake *et al.* also reported the similar antenna design earlier [62].

Planar printed antennas perform well enough for the in-body capsule applications. They occupy less volume than wire antennas, they integrate easily with a capsule circuitry, and they are technological and inexpensive. However, their footprint is the critical drawback for capsule applications. Conformal printed antennas occupy negligibly small volume and they easily integrate within a capsule, yet they possess all the advantages of planar antennas, and could outperform them.

1.4.3 Conformal Printed Antennas

Izdebski *et al.* [63] reported a 1.4 GHz conformal chandelier meandered dipole antenna. The $|S_{11}| < -10$ dB bandwidth is about 136 MHz ($\approx 10\%$). The antenna is based on the offset meandered dipole design that permits better matching to 50 Ω than the balanced meandered dipole. The antenna conforms the capsule extremity. To validate the design and numerical models, the antenna was printed on a planar PCB (RT/duroid® 5880, $\varepsilon_r = 2.2$). The homogeneous phantom has cuboid shape with the sides $350 \times 350 \times 200$ mm^3 and the dielectric properties $\varepsilon_r = 58.8$, $\sigma = 0.84$ S·m^{-1} at $f_{\text{res}} = 1.4$ GHz. The capsule shell is 0.1 mm thick with $\varepsilon_r = 2.2$;

the antenna is printed on the interior surface. The final lengths of the antenna arms (i.e. tuned inside the phantom) are 25.2 mm for the shorter arm and 42 mm for the longer one. Numerical analysis of the influence of the batteries inside the capsule showed no critical effect on reflection coefficient. The simulation results for the cuboid phantom were verified by the simulation inside the Ansoft human body model. The radiation efficiency and gain inside the anatomically realistic Ansoft phantom are $\eta = 0.05\%$ and $G = -26$ dBi. The authors used the Finite element method (FEM) implemented in Ansys® HFSS™ to analyze the antenna. Similar antennas were also reported in [64], [65].

Cheng *et al.* [66] designed a 2.4 GHz (ISM band) conformal patch antenna loaded with the complementary split-ring resonator (CSRR). The reported gain is $G = -5.2$ dBi and radiation efficiency is $\eta = 21\%$ (both in air). No phantom was used for the simulation. For measurements, in addition to the air, a $75 \times 75 \times 50$ mm^3 sponge was used damped with 30 ml of water. The bandwidth was not reported, but according to the reflection coefficient it does not exceed 50 MHz ($< 2\%$ for $|S_{11}| < -10$ dB). The bending diameter is ⌀10 mm. The patch length is 10.5 mm (roughly $\lambda/10$) and the width could be varied for the impedance matching (consequently, the gap between the folded patch opposite edges will change). The 17 µm thick patch top layer is printed on the 0.254 mm (10 mil) RT/duroid® 5880 substrate with $\varepsilon_r = 2.2$, $\tan\delta = 0.0009$. Ground plane reduces the effect of a capsule circuitry on the antenna. The authors used the lumped element approximation along with Ansys® HFSS™ to analyze the antenna.

Kumagai *et al.* [67] reported a 430 MHz conformal helical antenna. The antenna was designed for wireless power transfer to in-body capsules. The $|S_{11}| < -10$ dB bandwidth is about 2.5 MHz (0.6%) according to the simulated reflection coefficient. The environment parameters (phantom) were not reported; conceivably it was air or vacuum according to the narrow bandwidth characteristic. Antenna conforms to a ($23 \times$ ⌀9.5) mm cylindrical volume. The trace is 0.4 mm wide and is fed symmetrically. One end of the antenna is open and the opposite end is shortened, thus the impedance match could be achieved. The power transfer to the antenna was analyzed using the antenna model in 20 mm air layer between two phantom layers: 15–35 mm the outer layer and 100 mm the inner layer. Both phantom layers are muscle equivalent with $\varepsilon_r = 56.9$, $\sigma = 0.81$ S·m^{-1}. The antenna was analyzed using the FDTD method.

Yun *et al.* [68] reported an UWB conformal meandered-loop antenna. The operation frequencies are 370–630 MHz (260 MHz or 52% VSWR < 2 bandwidth) when simulated in the phantom ($\varepsilon_r = 56.4$, $\sigma = 0.82$ S·m^{-1} at 500 MHz). ⌀300 mm cylindrical liquid phantom was used for the measurement; the ingredients were not reported. The full effective wavelength antenna is printed on the outer surface of the 0.5 mm capsule shell ($\varepsilon_r = 3.15$), maximizing the achievable Chu sphere radius, thus increasing the efficiency. The height of meanders and the gap between each could be used to tune the antenna. The total capsule size is ($24 \times$ ⌀11) mm. The copper layer is 18 µm thick. The prototype was printed on a 25.4 µm polyimide film and fixed on the outer surface of the capsule shell. The authors used CST Microwave Studio® to analyze the antenna. Kim *et al.* reported an *in vivo* measurement of the endoscope prototype using this antenna [69].

Mahe *et al.* [70] reported a conformal microstrip antenna for the 434 MHz ISM band. The antenna on a polyimide substrate ($\varepsilon_r = 3.4$) has a bandwidth about

50 MHz (or 12%) for $|S_{11}| < -10$ dB. The microstrip antenna design includes a ground plane, which implies antenna shielding and minimization of capsule circuitry effect on the radiation performance. Three miniaturization techniques were used: short circuiting, stepped impedance and meandering. The authors achieved 90% size reduction compared to the standard $\lambda/2$ patch antenna. The proposed analytical model permits to calculate the antenna dimensions for the desired f_{res} and miniaturization constraints to fit various capsules. Also, the model permits to shrink the numerical antenna tuning to one dimension (the length of meandered element). The proof-of-concept prototype was built on $18 \times 9 \times 1.58$ mm^3 FR4 substrate ($\varepsilon_r = 4.4$) with the 3×18 mm^2 first element size and 0.2×75 mm^2 the second. The maximum gain is $G = -33$ dBi. As for the quarter wave patch, the antenna input impedance depends on a feeding point with the maximum on the radiating edge and minimum near the short circuit. A flexible prototype was built on a 50 µm Pyralux® AP8525 substrate (polyimide, $\varepsilon_r = 3.4$), which conforms to a ($17 \times \varnothing 7$) mm capsule. The copper layer is 18 µm thick. The antenna was measured in a liquid phantom within a $\varnothing 200$ mm cylindrical container with $\varepsilon_r = 49.6$, $\sigma = 0.51$ S·m^{-1}. The effect of bending is insignificant. The authors used Ansys® HFSS™ to analyze the antenna.

Alrawashdeh *et al.* reported a range of conformal loop antennas. In [71], the authors reported a conformal U-shaped loop antenna covering both MedRadio 403 MHz and ISM 433 MHz bands. The antenna is UWB: 348–555 MHz or 207 MHz (46%) for VSWR < 2 when simulated inside a ($110 \times \varnothing 120$) mm homogeneous cylindrical phantom ($\varepsilon_r = 57.1$, $\sigma = 0.79$ S·m^{-1} at 404.4 MHz). In air, the antenna resonates at 4 GHz. The authors also compared a three-layer body model of the same size with a homogeneous phantom. The gain values are $G = -28.38$ dBi and $G = -28.95$ dBi, respectively, within the multilayer and homogeneous phantoms. The total antenna size conforms to the surface of the ($15 \times \varnothing 10$) mm cylinder. The 18 µm copper plating is approximated by Perfect electric conductor (PEC) for the model. The unfolded antenna electrical size is about $\lambda/3 \times \lambda/6$, including the 25.4 µm thick polyimide substrate. Another 17 µm polyimide layer was added above the antenna to insulate it from the tissue.

Further development with more meanders of the previous antenna was reported in [72]. The bandwidth is 327–530 MHz (203 MHz or 47%) for $|S_{11}| < -10$ dB when simulated in $180 \times 100 \times 50$ mm^3 elliptical cylinder phantom (human arm model) with $\varepsilon_r = 57$, $\sigma = 0.79$ S·m^{-1}. The reported gain is $G = -28.4$ dBi. Antenna conforms to the ($10 \times \varnothing 7$) mm cylinder. Another MedRadio conformal loop antenna by Alrawashdeh *et al.* [73] was designed for cylindrical knee implants. The $\varnothing 10$ mm antenna bending diameter is in the same range as for the GI capsules. The antenna resonates at 404 MHz with a bandwidth about 24 MHz (6%) when simulated in a ($444 \times \varnothing 130$) mm cylindrical multilayer phantom. The simulated gain is $G = -21$ dBi and the radiation efficiency is $\eta = 0.3\%$. It must be noted that the gain and the efficiency values are higher because of lower loss for this kind of implant application. The antenna is designed to be printed on a 20 µm polyimide substrate. The trace width is 1 mm and the separation distance varies from 1 to 3 mm. The radiation pattern is omnidirectional; however, the maximum gain is directed along the phantom. The transverse directivity would be preferable for the reported application.

Similar design of a conformal meandered loop antenna for the same application was proposed by Alrawashdeh *et al.* [74]. The bandwidth is 362–454 MHz (92 MHz

or 23%) for $|S_{11}| < -10$ dB when simulated in a multilayer cylindrical phantom: ⌀30 mm bone → 70 mm muscle layer → 4 mm fat layer → 2 mm skin layer. The simulated radiation efficiency is $\eta = 0.05\%$ and the gain is $G = -27.6$ dBi; as for the previous case, the values are higher because the environment is less lossy. The antenna conforms to the ($40 \times$ ⌀10) mm cylinder. The total radiator length is 137 mm (0.67λ) and the trace is 1 mm wide. In this study, the authors reported also the analysis of antenna detuning due to the variation of dielectric parameters of the surrounding tissue.

One more meandered loop antenna by Alrawashdeh *et al.* was reported in [75]. The antenna has one of the largest bandwidth among all reported capsule antennas due to high coupling to the tissue: 215–1000 MHz (785 MHz or 129%) for VSWR < 2 when simulated in the phantom ($\varepsilon_r = 56.4$, $\sigma = 0.82$ S·m^{-1} at 500 MHz). In free space, the antenna resonates around 3.1 GHz. The antenna is designed to conform the ($10 \times$ ⌀11) mm cylinder while printed on a 25.4 µm substrate with $\varepsilon_r = 3.5$ (presumably polyimide). The antenna trace is 0.5 mm width with 0.5 mm separation between meanders.

Alrawashdeh *et al.* also proposed a conformal loop antenna loaded with CSRR [76]. The antenna was designed to cover both MedRadio and ISM bands. The simulated and measured bandwidths are extremely large as for the previous design. The authors motivated using the CSRR to improve the impedance matching as well as to increase the antenna radiation efficiency η and gain G. The antenna was simulated using a homogeneous elliptic cylindrical muscle equivalent phantom ($180 \times 100 \times 50$ mm^3) as well as within a CST Katja voxel body model (43-year-old female, 62 kg). The simulated radiation efficiencies within the homogeneous phantom are 0.12%, 0.2%, 0.3%, 0.35%, and 0.53% and realized gains GR are -26, -25.1, -24, -21, and -15 dBi at 403, 433, 868, 915, and 2450 MHz, respectively. A prototype was manufactured and characterized in pork in terms of reflection coefficient. Antenna conforms to the ($15 \times$ ⌀10) mm cylinder and insulated with 0.2 mm shell. All mentioned antennas by Alrawashdeh *et al.* were analyzed using CST Microwave Studio®.

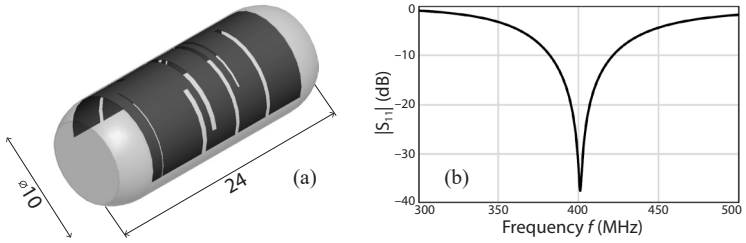

Fig. 1.6: Conformal microstrip meandered antenna (Psathas *et al.*, 2013): (a) design (mm) and (b) reflection coefficient $|S_{11}|$. © 2013 IEEE.

Psathas *et al.* [77] proposed a microstrip meandered antenna operating at 402 MHz (Figure 1.6). The $|S_{11}| < -10$ dB bandwidth is 39.95 MHz (9.9%) and the gain is $G = -29.64$ dBi when simulated in a homogeneous 100 mm^3 cubic phantom with $\varepsilon_r = 57$, $\sigma = 0.8$ S·m^{-1}. The antenna was printed on a $18 \times 18 \times 0.127$ mm^3 Rogers RT/duroid® 5880 substrate with $\varepsilon_r = 2.2$, $\tan\delta < 0.0009$ and conforms to ⌀10 mm cylinder. Superstrate layer is 0.1 mm polyethylene ($\varepsilon_r = 2.25$, $\tan\delta = 0.001$). Antenna miniaturization is achieved using shorting pin and meandering techniques, which permits to obtain dual-band characteristics

as well. The proposed feed is an L-shape coaxial probe. The antenna sensitivity to the environment variation was analyzed for four tissues [78]: esophagus, stomach, small and large intestines. The authors used FEM implemented in Ansys® HFSS™ to design the antenna; the mesh adaptivity was set-up to achieve 2% $|S_{11}|$ error.

J. C. Wang *et al.* [79] reported two conformal antennas based on a planar meander-line design. The first conformal antenna has a bandwidth of 306–529 MHz (223 MHz or 53%) for VSWR < 2 when simulated in the phantom having $\varepsilon_r = 56$, $\sigma = 0.8$ S·m^{-1}. However, there is a discrepancy between the reported values and reflection coefficient plot (roughly 150–950 MHz on the plot). The phantom has an elliptical cylinder shape with the dimensions $100\times150\times200$ mm^3. The conformal antenna was simulated with bending diameters ⌀10.6 mm (reported antenna results), ⌀14 mm, ⌀20 mm, and ⌀30 mm. The planar antenna size is 33×23 mm^2. The capsule shell has $\varepsilon_r = 4.4$. The authors analysed also the impact of a capsule shell with variable thickness: 0.5, 1.6, and 2.4 mm. The second antenna has a reported bandwidth of 330–894 MHz (564 MHz or 92%) for VSWR < 2 when simulated in the same phantom as for the first antenna. The same discrepancy as for the first antenna exists between written and plotted values: about 310–690 MHz on the plot. The conformal antenna was simulated with bending diameters ⌀4.8 mm (reported antenna results), ⌀10 *mm*, ⌀14 mm, ⌀20 mm, and ⌀30 mm. The planar antenna size is 18.2×15 mm^2. Efficiencies and gain were not reported for both antennas; however, authors claim the transmission for at least 15 cm from the body surface. The authors used CST Microwave Studio® to analyze the antenna.

Xu *et al.* [80] proposed an enhanced bandwidth dipole antenna for 401–406 MHz MedRadio band. The bandwidth is 358–516 or 158 MHz (36.1%) when simulated in a 180 mm^3 cubic phantom with $\varepsilon_r = 46.76$, $\sigma = 0.69$ S·m^{-1}. The capsule is located at the center of x–y-plane and 3 mm deep along the z-axis of the phantom. This phantom set-up is questionable for the suggested capsule application—endoscopy. The reported gain is $G = -37$ dBi and efficiency is about $\eta = 0.02\%$. The planar prototype was printed on 0.635 mm thick Rogers 3010 substrate ($\varepsilon_r = 10.2$, $\tan\delta = 0.0035$) and covered with the same material superstrate. The planar antenna was measured in the phantom containing sugar (56.18%), salt (2.33%) and deionised water. The measured dielectric characteristics of the phantom were not reported. The final antenna is optimized to be printed on the polyimide substrate ($\varepsilon_r = 3.5$, $\tan\delta = 0.008$) to conform the ($24 \times$ ⌀11) mm capsule. As the antenna is based on a dipole radiation principle, it does not have a ground plane (hence the mirror currents will affect the radiation efficiency).

Q. Wang *et al.* [81] proposed an UWB conformal trapezoid strip dielectric resonator antenna. The antenna bandwidth is 2–5 GHz (3 GHz or 86%) at $|S_{11}| < -10$ dB when simulated in a 200 mm^3 cubic homogeneous phantom with $\varepsilon_r = 51.5$, $\sigma = 3.2$ S·m^{-1} at 4 GHz. The maximum gain is $G = -24.2$ dBi. The permittivity of ⌀8 mm hemisphere is $\varepsilon_r = 3$ (presumably Polyvinylchloride (PVC)). It is designed to fit a ($26 \times$ ⌀11) mm capsule. The phantom for the measurement was prepared using the recipe from [82] containing $C_{12}H_{22}O_{11}$.

Morimoto *et al.* [83] proposed two UWB (3.4–4.8 GHz band) hemispherical capsule-conformal antennas: helical and loop. The -10 dB bandwidth begins at 3 GHz for the loop antenna and at 3.5 GHz for the helical. Antennas were simulated using the FDTD method inside a 50 mm^3 cubic phantom with $\varepsilon_r = 51.4$, $\sigma = 3.26$ S·m^{-1} at 4.1 GHz. The permittivity of ⌀8 mm hemisphere is $\varepsilon_r = 3$. The

antenna is covered with a 0.1 mm polyethylene shell ($\varepsilon_r = 2.2$). The maximum gains are $G_{\text{loop}} = -30$ dBi and $G_{\text{helical}} = -32$ dBi. The loop antenna has zeros in y–z-plane radiation pattern; both antennas are omnidirectional in x–y-plane. The authors manufactured a planar loop antenna to validate the model.

Suzan *et al.* [84] proposed an ultra-wideband loop antenna operating around 434 MHz mid-ISM band. The -10 dB bandwidth is 336–1080 MHz or 744 MHz (171%) when simulated in the $80 \times \varnothing 180$ mm cylindrical phantom with the muscle-equivalent properties, and the resonance frequency is 486 MHz. The simulated gain is -28 dBi. The effect of electronic components inside of the capsule was assessed using a 7.2-mm long PEC cylinder with a diameter varying from 7.5 to 9.5 mm. The antenna is printed on a flexible 100 µm substrate with $\varepsilon_r = 2.55$ to fit on the outer wall of the $(26 \times \varnothing 11)$ mm capsule covered by a 0.1 mm-thick biocompatible layer. The antenna was analyzed using CST Microwave Studio. The prototype was characterized in a muscle-equivalent liquid prepared using water–sugar–salt recipe. The antenna was characterized in terms of impedance using port extension technique [85] to avoid current leakage.

Table 1.2: VHF–UHF Antennas for Ingestible Capsule Applications

	Ref.	Antenna Type	Footprint	f_{central}, (MHz)	Bandwidth, (MHz)	(%)	Gain, (dBi)	η,* (%)	Phantom	Comments
Wire	[41]	Helical	$(5.6 \times \varnothing 8)$ mm	426	32	8	—	—	$\varepsilon_r = 56$, $\sigma = 0.8$ S/m	—
	[46]	Inv. conical helical	$(5.1 \times \varnothing 9)$ mm	1400	40	3	−40.0	< 0.1	$\varepsilon_r = 54.18$, $\sigma = 1.16$ S/m	Wire $\varnothing 0.4$ mm
	[47]	Conical spiral	$(5 \times \varnothing 10)$ mm	450	101	22	—	—	$\varepsilon_r = 56$, $\sigma = 0.83$ S/m	—
	[49]	Large arm spiral	$([3 \text{ to } 7] \times \varnothing 10)$ mm	450	76–117	17–26	—	—	$\varepsilon_r = 56.91$, $\sigma = 0.97$ S/m	90 mm arm length
	[48]	Dual spiral	$(7 \times \varnothing 10)$ mm	505	189	38	—	—	$\varepsilon_r = 56$, $\sigma = 0.83$ S/m	—
Planar PCB	[53]	Spiral	$(3 \times \varnothing 10.5)$ mm	455	110	24	—	—	$\varepsilon_r = 56$, $\sigma = 0.8$ S/m	Sub.: 3 mm, $\varepsilon_r = 2.17$
	[54]	Spiral	$(3 \times \varnothing 8.6)$ mm	2450	104	4	−0.17	—	Not reported	Sub.: 3 mm, $\varepsilon_r = 3.5$
	[55]	Spiral	—	2450	—		—	—	$\varepsilon_r = 53.6$, $\sigma = 1.8$ S/m	—
	[56]	Four arm spiral	$8.25^2 \times 0.6$ mm^3	915	11	1	−46.0	—	Visible human	Sub.: 0.6 mm, $\varepsilon_r = 6.1$
	[57]	Multilayered spiral	$24.7 \times 8 \times 5.2$ mm^3	403	9	2	−28.8	0.058	$\varepsilon_r = 43.5$, $\tan\delta = 0.799$	Sub.: $\varepsilon_r = 9.2$, $\tan\delta = 0.0022$
				2450	145	6	−18.5	0.530	$\varepsilon_r = 39.2$, $\tan\delta = 0.337$	
	[59]	Multilayered helical	$\pi \times 5.5^2 \times 3.81$ mm^3	2300	950	41	−32.0	—	$\varepsilon_r = 52.79$, $\sigma = 1.7$ S/m	Sub.: $\varepsilon_r = 10.2$, $\tan\delta = 0.0022$
	[60]	Microstrip slot	$23.7 \times 8 \times 1.27$ mm^3	3000	UWB		—	0.8–20	Variuos	Sub.: $\varepsilon_r = 9.8$, $\tan\delta = 0.002$
Conformal PCB	[63]	Mndr. asym. dipole	On $(26 \times \varnothing 11)$ mm	1400	136	10	−26.0	0.05	$\varepsilon_r = 58.8$, $\sigma = 0.84$ S/m	Shell: 0.1 mm, $\varepsilon_r = 2.2$
	[66]	Patch wth CSRR	10 mil substrate	2400	50	< 2	−5.2	0.21	None (air)	Sub.: $\varepsilon_r = 2.2$, $\tan\delta = 0.0009$
	[67]	Folded helical	On $(23 \times \varnothing 9.5)$ mm	430	< 3	< 1	—	—	Not reported	—
	[68]	Meandered loop	On $(24 \times \varnothing 11)$ mm	500	260	52	—	—	$\varepsilon_r = 56.4$, $\sigma = 0.82$ S/m	Shell: 0.5 mm, $\varepsilon_r = 3.15$
	[70]	Microstrip	2 mil substrate	434	50	12	−33.0	—	$\varepsilon_r = 49.6$, $\sigma = 0.51$ S/m	Sub.: $\varepsilon_r = 3.4$, $\tan\delta = 0.002$
	[71]	U-shaped loop	On $(15 \times \varnothing 10)$ mm	452	207	46	−28.95	—	$\varepsilon_r = 57.1$, $\sigma = 0.79$ S/m	—
	[72]	Meandered loop	On $(10 \times \varnothing 7)$ mm	429	203	47	−28.4	—	$\varepsilon_r = 57$, $\sigma = 0.79$ S/m	—
	[73]	Meandered loop	On $\varnothing 10$ mm cyl.	404	25	6	−21.0	0.30	Multilayer cylindrical	For knee implants
	[74]	Meandered loop	On $(40 \times \varnothing 10)$ mm	408	92	23	−27.6	0.05	Multilayer cylindrical	
	[75]	Meandered loop	On $(10 \times \varnothing 11)$ mm	608	785	129	—	—	$\varepsilon_r = 56.4$, $\sigma = 0.82$ S/m	—
	[77]	Mndr. microstrip	On $(18 \times \varnothing 10)$ mm	402	40	10	−29.64	—	$\varepsilon_r = 57$, $\sigma = 0.8$ S/m	Sub.: $\varepsilon_r = 2.2$; shell: $\varepsilon_r = 2.25$
	[79]	Meander-line	On $\varnothing 10.6$ mm cyl.	418	800	145	—	—	$\varepsilon_r = 56$, $\sigma = 0.8$ S/m	Discrepancies in reported bandwidth
			On $\varnothing 4.8$ mm cyl.	612	564	92	—	—		
	[80]	Mndr. asym. dipole	On $(24 \times \varnothing 11)$ mm	437	158	36	−37.0	0.02	$\varepsilon_r = 46.76$, $\sigma = 0.69$ S/m	
	[81]	Trapezoid strip DR	On $\varnothing 8$ mm hemisphr	3500	3000	86	−24.2	—	$\varepsilon_r = 51.5$, $\sigma = 3.2$ S/m	
	[83]	Helical DR	On $\varnothing 8$ mm hemisphr	3500	> 3000		−32.0	—	$\varepsilon_r = 51.4$, $\sigma = 3.26$ S/m	Hemisphere: $\varepsilon_r = 3$
		Loop DR					−30.0	—		

* Radiation efficiency (η)

1.5 Summary

Wireless biomedical telemetry enables continious monitoring of physiological parameters unaffecting the mobility of a patient: it allows one efficiently preventing, monitoring, and treating a disease timely. It relies on an efficient and reliable communication with an external monitor via a radio frequency link. Although alternatives to radio frequency transmission exist for wireless GI capsules (as, for instance, inductive links and Human body communication (HBC) method [28]), it is limited both in operational range and throughput. Wireless transmission in VHF–SHF bands yields the longest range and highest data transfer rates for ingestible wireless devices.

Modern VHF–SHF capsule antennas can be divided into wire, printed planar, and printed conformal. Wire antennas are easy to design and tune, they provide sufficient bandwidth, and, in helical implementation, they occupy a sufficiently large surface augmenting the fundamental bandwidth versus efficiency limits. Spiral antennas can have a ground plane sufficiently large to shield an antenna from a capsule circuitry. However, wire antennas are bulky, poorly integrable into a capsule design, and non-technological (i.e. expensive and poorly repeatable for mass production). Printed planar antennas are technological to manufacture and its spiral designs are less voluminous, but still lack the integrability. The bandwidth is comparable to wire antennas but it is harder to achieve the same Chu sphere radii, thus planar antennas are less efficient for a given bandwidth. Flexible substrates permit to minimize an antenna footprint within a capsule by conforming to the shell. In this way, we can increase the Chu sphere radius by making use of all available capsule surface, thus fending off the performance limits of ESAs [86], [87].

Therefore, theoretically achievable radiation efficiency η for a given bandwidth could be greater than for wire and planar antennas. Moreover, printed conformal antennas are technological and could be fully integrated into a circuit design; for instance, it could be printed on the same flexible PCB with electronics and rolled to fit into the capsule. Capsule circuitry affects more unshielded designs (e.g. meandered dipole and loop antennas). Conformal microstrip antennas, on the other hand, are less coupled to the circuitry because of a ground plane. It is convenient from a perspective of system design: once tuned, the antenna will maintain its characteristics when capsule circuitry or sensing units are revised.

Bibliography

[1] W. Greatbatch and C. Holmes, "History of implantable devices," *IEEE Engineering in Medicine and Biology Magazine*, vol. 10, no. 3, pp. 38–41, Sep. 1991.

[2] R. P. Feynman, "There's plenty of room at the bottom," *Engineering and Science*, vol. 23, no. 5, pp. 22–36, Feb. 1960.

[3] V. K. Zworykin and J. T. Farrar, "A 'Radio pill'," *Nature*, vol. 179, no. 4566, p. 898, 1957.

[4] R. S. Mackay and B. Jacobson, "Endoradiosonde," *Nature*, vol. 179, no. 4572, pp. 1239–1240, Jun. 1957.

[5] J. T. Farrar, V. K. Zworykin, and J. Baum, "Pressure-sensitive telemetering capsule for study of gastrointestinal motility," *Science*, vol. 126, no. 3280, pp. 975–976, Nov. 1957.

[6] R. S. Mackay and B. Jacobson, "Pill telemeters from digestive tract," *Electronics*, vol. 31, pp. 51–53, 1958.

[7] R. S. Mackay, "Radio telemetering from within the human body," *IRE Transactions on Medical Electronics*, vol. ME-6, no. 2, pp. 100–105, 1959.

[8] R. S. Mackay, "Endoradiosondes: Further notes," *IRE Transactions on Medical Electronics*, vol. ME-7, no. 2, pp. 67–73, Apr. 1960.

[9] J. O. Sines, "Permanent implants for heart rate and body temperature recording in the rat," *AMA Archives of General Psychiatry*, vol. 2, no. 2, pp. 182–183, Feb. 1960.

[10] M. Herbert, "Pill-type swallowable transmitter," US3144017 A, Aug. 1964.

[11] B. W. Watson, S. J. Meldrum, H. C. Riddle, R. L. Brown, and G. E. Sladen, "pH profile of gut as measured by radiotelemetry capsule.," *British Medical Journal*, vol. 2, no. 5805, pp. 104–106, Apr. 1972.

[12] C. A. Cáceres, *Biomedical telemetry*. Academic Press, 1965.

[13] W. H. Ko and P. X.-L. Feng, "Biomedical implantable systems – history, design, and trends," in *Implantable Bioelectronics*, E. Katz, Ed., Weinheim, Germany: Wiley-VCH Verlag GmbH & Co. KGaA, 2014, pp. 381–410.

[14] C. J. Amlaner and D. W. Macdonald, Eds., *A handbook on biotelemetry and radio tracking*. Oxford, UK: Pergamon Press, 1979.

[15] G. Iddan, G. Meron, A. Glukhovsky, and P. Swain, "Wireless capsule endoscopy," *Nature*, vol. 405, no. 6785, pp. 417–417, May 2000.

[16] BodyCap Medical, *E-Celsius*. [Online]. Available: `http://www.bodycap-medical.com/`.

[17] E. Chow, A. Chlebowski, S. Chakraborty, W. Chappell, and P. Irazoqui, "Fully wireless implantable cardiovascular pressure monitor integrated with a medical stent," *IEEE Transactions on Biomedical Engineering*, vol. 57, no. 6, pp. 1487–1496, Jun. 2010.

[18] Given Imaging, *Bravo pH*. [Online]. Available: `http://www.givenimaging.com/en-int/Innovative-Solutions/Reflux-Monitoring/Bravo-pH/`.

[19] M. C. Shults, R. K. Rhodes, S. J. Updike, B. J. Gilligan, and W. N. Reining, "A telemetry-instrumentation system for monitoring multiple subcutaneously implanted glucose sensors," *IEEE Transactions on Biomedical Engineering*, vol. 41, no. 10, pp. 937–942, Oct. 1994.

[20] T. F. Budinger, "Biomonitoring with wireless communications," *Annual Review of Biomedical Engineering*, vol. 5, pp. 383–412, 2003.

[21] A. Kiourti, K. A. Psathas, and K. S. Nikita, "Implantable and ingestible medical devices with wireless telemetry functionalities: A review of current status and challenges," *Bioelectromagnetics*, vol. 35, no. 1, pp. 1–15, Jan. 2014.

[22] R. Bashirullah, "Wireless implants," *IEEE Microwave Magazine*, vol. 11, no. 7, S14–S23, Dec. 2010.

[23] A. Kiourti and K. S. Nikita, "A review of in-body biotelemetry devices: Implantables, ingestibles, and injectables," *IEEE Transactions on Biomedical Engineering*, vol. 64, no. 7, pp. 1422–1430, 2017.

[24] J. S. Ho, Y. Tanabe, S. M. Iyer, A. J. Christensen, L. Grosenick, K. Deisseroth, S. L. Delp, and A. S. Y. Poon, "Self-tracking energy transfer for neural stimulation in untethered mice," *Physical Review Applied*, vol. 4, no. 2, p. 024 001, 2015.

[25] T. Kim, J. G. McCall, Y. H. Jung, X. Huang, E. R. Siuda, Y. Li, J. Song, Y. M. Song, H. A. Pao, R.-H. Kim, C. Lu, S. D. Lee, I.-S. Song, G. Shin, R. Al-Hasani, S. Kim, M. P. Tan, Y. Huang, F. G. Omenetto, J. A. Rogers, and M. R. Bruchas, "Injectable, cellular-scale optoelectronics with applications for wireless optogenetics," *Science*, vol. 340, no. 6129, pp. 211–216, 2013.

[26] E. Chow, M. Morris, and P. Irazoqui, "Implantable RF medical devices: The benefits of high-speed communication and much greater communication distances in biomedical applications," *IEEE Microwave Magazine*, vol. 14, no. 4, pp. 64–73, Jun. 2013.

[27] K. S. Nikita, *Handbook of Biomedical Telemetry*. Hoboken, NJ: John Wiley & Sons, Jul. 2014.

[28] C. H. Hyoung, S. W. Kang, J. H. Hwang, S. E. Kim, J. K. Kim, T. W. Kang, K. S. Kim, J. B. Kim, H. I. Park, I. G. Lim, K. H. PARK, and J. H. Shim, "Human body communication system and method," US20100274083 A1, Oct. 2010.

[29] F. Merli and A. Skrivervik, "Design and measurement considerations for implantable antennas for telemetry applications," in *4th European Conference on Antennas and Propagation (EuCAP 2010)*, Barcelona, Spain, Apr. 2010, pp. 1–5.

[30] C. McCaffrey, O. Chevalerias, C. O'Mathuna, and K. Twomey, "Swallowable-capsule technology," *IEEE Pervasive Computing*, vol. 7, no. 1, pp. 23–29, Jan. 2008.

[31] M. Yuce and T. Dissanayake, "Easy-to-swallow wireless telemetry," *IEEE Microwave Magazine*, vol. 13, no. 6, pp. 90–101, Sep. 2012.

[32] F. Munoz, G. Alici, and W. Li, "A review of drug delivery systems for capsule endoscopy," *Advanced Drug Delivery Reviews*, vol. 71, pp. 77–85, 2013.

[33] J. L. Toennies, G. Tortora, M. Simi, P. Valdastri, and R. J. Webster, "Swallowable medical devices for diagnosis and surgery: The state of the art," *Proceedings of the Institution of Mechanical Engineers, Part C: Journal of Mechanical Engineering Science*, vol. 224, no. 7, pp. 1397–1414, Jul. 2010.

[34] C. T. Moritz, S. I. Perlmutter, and E. E. Fetz, "Direct control of paralysed muscles by cortical neurons," *Nature*, vol. 456, no. 7222, pp. 639–642, Dec. 2008.

[35] M. Velliste, S. Perel, M. C. Spalding, A. S. Whitford, and A. B. Schwartz, "Cortical control of a prosthetic arm for self-feeding," *Nature*, vol. 453, no. 7198, pp. 1098–1101, Jun. 2008.

[36] P. R. Troyk, "Injectable electronic identification, monitoring, and stimulation systems," *Annual Review of Biomedical Engineering*, vol. 1, no. 1, pp. 177–209, 1999.

[37] X. Li, W. A. Serdijn, W. Zheng, Y. Tian, and B. Zhang, "The injectable neurostimulator: An emerging therapeutic device," *Trends in Biotechnology*, vol. 33, no. 7, pp. 388–394, Jul. 2015.

[38] E. Katz, *Implantable Bioelectronics*. John Wiley & Sons, Feb. 2014.

[39] D. Nikolayev, M. Zhadobov, R. Sauleau, and P. Karban, "Antennas for ingestible capsule telemetry," in *Advances in body-centric wireless communication: Applications and state-of-the-Art*, London, UK: IET, 2016, pp. 143–186.

[40] A. S. Y. Poon, S. O'Driscoll, and T. H. Meng, "Optimal frequency for wireless power transmission into dispersive tissue," *IEEE Transactions on Antennas and Propagation*, vol. 58, no. 5, pp. 1739–1750, 2010.

[41] S.-I. Kwak, K. Chang, and Y.-J. Yoon, "The helical antenna for the capsule endoscope," in *2005 IEEE Antennas and Propagation Society International Symposium*, vol. 2B, Washington, DC, Jul. 2005, pp. 804–807.

[42] L. Xu, M.-H. Meng, H. Ren, and Y. Chan, "Radiation characteristics of ingestible wireless devices in human intestine following radio frequency exposure at 430, 800, 1200, and 2400 MHz," *IEEE Transactions on Antennas and Propagation*, vol. 57, no. 8, pp. 2418–2428, Aug. 2009.

[43] L. Xu, M.-H. Meng, and Y. Chan, "Effects of dielectric parameters of human body on radiation characteristics of ingestible wireless device at operating frequency of 430 MHz," *IEEE Transactions on Biomedical Engineering*, vol. 56, no. 8, pp. 2083–2094, Aug. 2009.

[44] L. Xu, M.-H. Meng, and C. Hu, "Effects of dielectric values of human body on specific absorption rate following 430, 800, and 1200 MHz RF exposure to ingestible wireless device," *IEEE Transactions on Information Technology in Biomedicine*, vol. 14, no. 1, pp. 52–59, Jan. 2010.

[45] S. Gabriel, R. W. Lau, and C. Gabriel, "The dielectric properties of biological tissues: II. Measurements in the frequency range 10 Hz to 20 GHz," *Physics in Medicine and Biology*, vol. 41, pp. 2251–2269, Nov. 1996.

[46] H. Rajagopalan and Y. Rahmat-Samii, "Wireless medical telemetry characterization for ingestible capsule antenna designs," *IEEE Antennas and Wireless Propagation Letters*, vol. 11, pp. 1679–1682, 2012.

[47] S.-H. Lee, K. Chang, K. J. Kim, and Y.-J. Yoon, "A conical spiral antenna for wideband capsule endoscope system," in *IEEE Antennas and Propagation Society International Symposium, 2008. AP-S 2008*, San Diego, CA, Jul. 2008, pp. 1–4.

[48] S.-H. Lee and Y.-J. Yoon, "Fat arm spiral antenna for wideband capsule endoscope systems," in *2010 IEEE Radio and Wireless Symposium (RWS)*, New Orleans, LA, Jan. 2010, pp. 579–582.

[49] S.-H. Lee, J. Lee, Y. J. Yoon, S. Park, Changyul-Cheon, K. Kim, and S. Nam, "A wideband spiral antenna for ingestible capsule endoscope systems: Experimental results in a human phantom and a pig," *IEEE Transactions on Biomedical Engineering*, vol. 58, no. 6, pp. 1734–1741, Jun. 2011.

[50] S.-H. Lee and Y.-J. Yoon, "A dual spiral antenna for ultra-wideband capsule endoscope system," in *International Workshop on Antenna Technology: Small Antennas and Novel Metamaterials, 2008. iWAT 2008*, Chiba, Mar. 2008, pp. 227–230.

[51] J. Faerber and M. P. Y. Desmulliez, "Conformal meander shaped antenna for biotelemetry in endoscopic capsules," in *2015 Loughborough Antennas Propagation Conference (LAPC)*, Nov. 2015, pp. 1–4.

[52] J. Faerber, G. Cummins, and M. P. Y. Desmulliez, "Design of conformai wideband antennas for capsule endoscopy within a body tissue environment," in *2016 46th European Microwave Conference (EuMC)*, Oct. 2016, pp. 1223–1226.

[53] S.-I. Kwak, K. Chang, and Y.-J. Yoon, "Ultra-wide band spiral shaped small antenna for the biomedical telemetry," in *Microwave Conference Proceedings, 2005. APMC 2005. Asia-Pacific Conference Proceedings*, vol. 1, Suzhou, China, Dec. 2005.

[54] X. Xie, G. Li, B. Chi, X. Yu, C. Zhang, and Z. Wang, "Micro-system design for wireless endoscopy system," in *27th Annual International Conference IEEE-EMBS 2005*, Shanghai, China, Jan. 2005, pp. 7135–7138.

[55] D. Zhao, X. Hou, X. Wang, and C. Peng, "Miniaturization design of the antenna for wireless capsule endoscope," in *2010 4th International Conference on Bioinformatics and Biomedical Engineering (iCBBE)*, Chengdu, China, Jun. 2010, pp. 1–4.

[56] B. Huang, G. Yan, and P. Zan, "Design of ingested small microstrip antenna for radiotelemetry capsules," *Electronics Letters*, vol. 43, no. 22, pp. 1–2, Oct. 2007.

[57] F. Merli, L. Bolomey, J. Zurcher, G. Corradini, E. Meurville, and A. Skrivervik, "Design, realization and measurements of a miniature antenna for implantable wireless communication systems," *IEEE Transactions on Antennas and Propagation*, vol. 59, no. 10, pp. 3544–3555, Oct. 2011.

[58] F. Merli, L. Bolomey, F. Gorostidi, B. Fuchs, J. Zurcher, Y. Barrandon, E. Meurville, J. Mosig, and A. Skrivervik, "Example of data telemetry for biomedical applications: An in vivo experiment," *IEEE Antennas and Wireless Propagation Letters*, vol. 11, pp. 1650–1654, 2012.

[59] C. Liu, Y.-X. Guo, and S. Xiao, "Circularly polarized helical antenna for ISM-band ingestible capsule endoscope systems," *IEEE Transactions on Antennas and Propagation*, vol. 62, no. 12, pp. 6027–6039, Dec. 2014.

[60] T. Dissanayake, K. Esselle, and M. Yuce, "Dielectric Loaded Impedance Matching for Wideband Implanted Antennas," *IEEE Transactions on Microwave Theory and Techniques*, vol. 57, no. 10, pp. 2480–2487, Oct. 2009.

[61] K. Thotahewa, J.-M. Redoute, and M. Yuce, "Electromagnetic power absorption of the human abdomen from IR-UWB based wireless capsule endoscopy devices," in *2013 IEEE International Conference on Ultra-Wideband (ICUWB)*, Sydney, NSW, Sep. 2013, pp. 79–84.

[62] T. Dissanayake, M. Yuce, and C. Ho, "Design and Evaluation of a Compact Antenna for Implant-to-Air UWB Communication," *IEEE Antennas and Wireless Propagation Letters*, vol. 8, pp. 153–156, 2009.

[63] P. Izdebski, H. Rajagopalan, and Y. Rahmat-Samii, "Conformal ingestible capsule antenna: A novel chandelier meandered design," *IEEE Transactions on Antennas and Propagation*, vol. 57, no. 4, pp. 900–909, Apr. 2009.

[64] H. Rajagopalan, P. Izdebski, and Y. Rahmat-Samii, "A miniaturized ingestible antenna for capsule medical imaging system," in *IEEE Antennas and Propagation Society International Symposium, 2009*, Charleston, SC, Jun. 2009, pp. 1–4.

[65] H. Rajagopalan and Y. Rahmat-Samii, "Novel ingestible capsule antenna designs for medical monitoring and diagnostics," in *4^{th} European Conference on Antennas and Propagation (EuCAP 2010)*, Barcelona, Spain, Apr. 2010, pp. 1–5.

[66] X. Cheng, D. Senior, C. Kim, and Y.-K. Yoon, "A compact omnidirectional self-packaged patch antenna with complementary split-ring resonator loading for wireless endoscope applications," *IEEE Antennas and Wireless Propagation Letters*, vol. 10, pp. 1532–1535, 2011.

[67] T. Kumagai, K. Saito, M. Takahashi, and K. Ito, "A 430mhz band receiving antenna for microwave power transmission to capsular endoscope," in *General Assembly and Scientific Symposium, 2011 XXXth URSI*, Istanbul, Turkey, Aug. 2011, pp. 1–4.

[68] S. Yun, K. Kim, and S. Nam, "Outer-Wall Loop Antenna for Ultrawideband Capsule Endoscope System," *IEEE Antennas and Wireless Propagation Letters*, vol. 9, pp. 1135–1138, 2010.

[69] K. Kim, S. Yun, S. Lee, S. Nam, Y. J. Yoon, and Changyul-Cheon, "A design of a high-speed and high-efficiency capsule endoscopy system," *IEEE Transactions on Biomedical Engineering*, vol. 59, no. 4, pp. 1005–1011, Apr. 2012.

[70] Y. Mahe, A. Chousseaud, M. Brunet, and B. Froppier, "New flexible medical compact antenna: Design and analysis," *International Journal of Antennas and Propagation*, vol. 2012, May 2012.

[71] R. Alrawashdeh, Y. Huang, and P. Cao, "A conformal U-shaped loop antenna for biomedical applications," in *7th European Conference on Antennas and Propagation (EuCAP 2013)*, Gothenburg, Sweden, Apr. 2013, pp. 157–160.

[72] R. Alrawashdeh, Y. Huang, and P. Cao, "Flexible meandered loop antenna for implants in MedRadio and ISM bands," *Electronics Letters*, vol. 49, no. 24, pp. 1515–1517, Nov. 2013.

[73] R. Alrawashdeh, Y. Huang, and P. Cao, "A flexible loop antenna for total knee replacement implants in the MedRadio band," in *Antennas and Propagation Conference (LAPC), 2013 Loughborough*, Nov. 2013, pp. 225–228.

[74] R. Alrawashdeh, Y. Huang, and A. A. B. Sajak, "A flexible loop antenna for biomedical bone implants," in *The 8th European Conference on Antennas and Propagation (EuCAP 2014)*, Hague, Netherlands, Apr. 2014, pp. 999–1002.

[75] R. Alrawashdeh, Y. Huang, P. Cao, and E. Lim, "A new small conformal antenna for capsule endoscopy," in *7th European Conference on Antennas and Propagation (EuCAP 2013)*, Gothenburg, Sweden, Apr. 2013, pp. 220–223.

[76] R. Alrawashdeh, Y. Huang, M. Kod, and A. Sajak, "A broadband flexible implantable loop antenna with complementary split ring resonators," *IEEE Antennas and Wireless Propagation Letters*, vol. 14, pp. 1506–1509, 2015.

[77] K. A. Psathas, A. Kiourti, and K. S. Nikita, "A novel conformal antenna for ingestible capsule endoscopy in the MedRadio band," in *34th Progress in Electromagnetics Research Symposium (PIERS 2013)*, Stockholm, Sweden, Aug. 2013.

[78] K. Psathas, A. Keliris, A. Kiourti, and K. Nikita, "Operation of ingestible antennas along the gastrointestinal tract: Detuning and performance," in *2013 IEEE 13th International Conference on Bioinformatics and Bioengineering (BIBE)*, Chania, Grece, Nov. 2013, pp. 1–4.

[79] Q. Wang, K. Wolf, and D. Plettemeier, "An UWB capsule endoscope antenna design for biomedical communications," in *1rd International Symposium on Applied Sciences in Biomedical and Communication Technologies (ISABEL 2010)*, Rome, Italy, Nov. 2010, pp. 1–6.

[80] L.-J. Xu, Y.-X. Guo, and W. Wu, "Bandwidth enhancement of an implantable antenna," *IEEE Antennas and Wireless Propagation Letters*, vol. 14, pp. 1510–1513, 2015.

[81] J. C. Wang, E. G. Lim, Z. Wang, Y. Huang, T. Tillo, M. Zhang, and R. Alrawashdeh, "UWB planar antennas for wireless capsule endoscopy," in *2013 International Workshop on Antenna Technology (iWAT)*, Karlsruhe, Germany, Mar. 2013, pp. 340–343.

[82] J. Zhou, D. Hara, and T. Kobayashi, "Development of ultra wideband electromagnetic phantoms for antennas and propagation studies," in *First European Conference on Antennas and Propagation (EuCAP 2006)*, Nice, France, Nov. 2006, pp. 1–6.

[83] Y. Morimoto, D. Anzai, and J. Wang, "Design of ultra wide-band low-band implant antennas for capsule endoscope application," in *2013 7th International Symposium on Medical Information and Communication Technology (ISMICT)*, Tokyo, Japan, Mar. 2013, pp. 61–65.

[84] M. M. Suzan, K. Haneda, C. Icheln, A. Khatun, and K. Takizawa, "An ultra-wideband conformal loop antenna for ingestible capsule endoscope system," in *10th European Conference on Antennas and Propagation (EuCAP 2016)*, Davos, Switzerland, Apr. 2016, pp. 1–5.

[85] X. Qing, C. K. Goh, and Z. N. Chen, "Impedance characterization of RFID tag antennas and application in tag co-design," *IEEE Transactions on Microwave Theory and Techniques*, vol. 57, no. 5, pp. 1268–1274, May 2009.

[86] J. Volakis, C.-C. Chen, and K. Fujimoto, *Small Antennas: Miniaturization Techniques & Applications*. McGraw Hill Professional, Jun. 2010.

[87] A. Karlsson, "Physical limitations of antennas in a lossy medium," *IEEE Transactions on Antennas and Propagation*, vol. 52, no. 8, pp. 2027–2033, Aug. 2004.

Chapter 2

Human Body Modeling in VHF–SHF Bands

Contents

2.1 Biological Environment of Capsule Antennas 36

2.1.1 Electromagnetic Properties of Tissues 36

2.1.2 Capsule Gastrointestinal Passage 37

2.1.3 Implantable Case 38

2.2 Computational Phantoms 38

2.2.1 Literature Review 39

2.2.2 2D Anatomically Realistic B-Rep Phantom 40

2.3 Physical Phantoms 41

2.3.1 Literature Review 41

2.3.2 Predictive Modeling of H_2O–$C_{12}H_{22}O_{11}$–NaCl Liquid Phantoms 42

2.4 Far-Field Characterization of In-Body Antennas 44

2.5 Summary 46

2.1 Biological Environment of Capsule Antennas

From EM point of view, body tissues can be considered as an isotropic, linear, heterogeneous, and dispersive medium. It contains water, free ions, dissolved and insoluble matter. The electromagnetic spectrum of the tissue is characterized by three main relaxation regions accounting for ($\boldsymbol{\alpha}$) ionic diffusion, ($\boldsymbol{\beta}$) capacitive charging of cellular membranes and intercellular bodies, and ($\boldsymbol{\gamma}$) dipolar polarization of water in tissues. Another fourth minor dispersion ($\boldsymbol{\delta}$) can also appear in some protein solutions [1].

2.1.1 Electromagnetic Properties of Tissues

These relaxation regions contribute together to the complex permittivity of tissues

$$\hat{\varepsilon}(\omega) = \varepsilon'(\omega) - j\varepsilon''(\omega) = \varepsilon'(\omega) - j\sigma(\omega)/\omega\varepsilon_0, \tag{2.1}$$

where $\varepsilon' = \varepsilon_r(\mathbf{r},\omega)\,\varepsilon_0$ is the permittivity ($\mathrm{F{\cdot}m^{-1}}$), $\sigma(\mathbf{r},\omega)$ is the conductivity ($\mathrm{S{\cdot}m^{-1}}$), $\mathbf{r}$ is the position vector, $\omega = 2\pi f$ is the angular frequency ($\mathrm{rad{\cdot}s^{-1}}$), and f is the frequency (Hz).

Many representations exist for complex frequency-dispersive permittivities [2]. One of the most common way to model the the EM spectrum of a tissue is by using the multiple Cole–Cole dispersion model [3]: one for each of four relaxation regions $\boldsymbol{\alpha}$, $\boldsymbol{\beta}$, $\boldsymbol{\gamma}$, and $\boldsymbol{\delta}$ [4]–[6]:

$$\hat{\varepsilon}(\omega) = \varepsilon_\infty + \sum_{n=1}^{4} \frac{\varepsilon_s - \varepsilon_\infty}{1 + (j\omega\tau_n)^{(1-\alpha_n)}} + \frac{\sigma_i}{j\omega\varepsilon_0}, \tag{2.2}$$

where τ_n are the relaxation times (s), ε_∞ is the infinite permittivity when $\omega\tau \gg 1$, ε_s is the static permittivity ($\omega\tau \ll 1$), σ_i is the ionic conductivity, and α_n are the measures of the dispersion broadening.

Besides, we should also note that one can use Kramers–Kronig formulas [7], [8] to determine $\varepsilon_r'(\omega) = \varepsilon'(\omega)/\varepsilon_0$ and $\varepsilon_r''(\omega) = \varepsilon''(\omega)/\varepsilon_0$ uniquely when either ε_r' or ε_r'' is known over the given frequency range. The Kramers–Kronig formulas are given by [9, p. 334]

$$\varepsilon_r'(\omega_0) = 1 + \frac{2}{\pi} P \int_0^\infty \frac{\omega\varepsilon_r''(\omega_0)}{\omega^2 - \omega_0^2}\mathrm{d}\omega \tag{2.3}$$

and

$$\varepsilon_r''(\omega_0) = -\frac{2\omega_0}{\pi} P \int_0^\infty \frac{[\varepsilon_r'(\omega) - 1]}{\omega^2 - \omega_0^2}\mathrm{d}\omega, \tag{2.4}$$

where P stands for the principal part of the complex integral [9, p. 333] and ω_0 is the constant angular frequency where the permittivity is evaluated.

Eqs 2.3 and 2.4 are the most commonly used versions of the Kramers–Kronig relations [10]. These expressions show that the value of either part of the permittivity $\hat{\varepsilon}(\omega)$ at one given frequency ω_0 depends on the values of the other part over the entire frequency range.

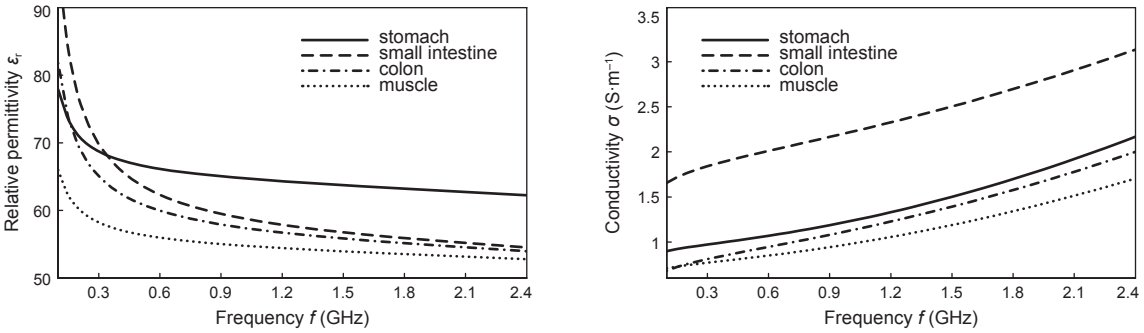

Fig. 2.1: Electromagnefic properties (ε_r, σ) of gastrointestinal tract and muscle tissues (data from Gabriel *et al.* [4]–[6]). *left*: Real part of the relative permittivity $\varepsilon_r'(\omega)$. *right*: The conductivity $\sigma(\omega)$.

2.1.2 Capsule Gastrointestinal Passage

Ingestible capsule antennas must efficiently transmit from a gastrointestinal tract. Antenna performances strongly depend on dielectric parameters of the environment [11]. These properties must be taken into account as a phantom[1] while designing the antennas. Let us overview the passage of a capsule through GI tract indicating the measured electromagnetic properties at 434 MHz for each organ (data from Gabriel *et al.* [4]–[6], Fig. 2.1).

Table 2.1: Time-averaged dielectric properties of a human gastrointestinal tract at 434 MHz.

	Time (min)	**Time** (%)	ε_r	σ (S·m^{-1})
Stomach	180	10.53	67.2	1.01
Small Intestine	228	13.33	65.3	1.92
Large Intestine	1302	76.14	62.0	0.87
Time-average			**63.0**	**1.02**

After swallowing, a capsule passes through oesophagus to stomach; the typical transit time is a few seconds and the dielectric parameters are $\varepsilon_r = 67.2$, $\sigma = 1.01$ S·m^{-1} for both. In stomach, the capsule was found to spend in average 33 min for a person without a gastric retention [12]; Worsøe *et al.* indicane a duration from 35.5 min to 57.5 min [13]. Rao *et al.* [14] reported the 3 h gastric empty time for a healthy person. The substantial differences in observed duration are explained by different experimental protocols, i.e. various patient preparation and diet.

These data do not take into account the typical contents of the GI tract that have not been measured yet. However, it is an accurate approach for the phantom design when the antenna is robust enough.

Later, the capsule leaves stomach by duodenum and proceeds to small bowel ($\varepsilon_r = 65.3$, $\sigma = 1.92$ S·m^{-1}). Ben-soussan *et al.* [12] report the average transition time is around 212 min for the patients without the gastric retention and Worsøe *et al.* [13] indicate the range from 260.5 min to 275 min. Rao *et al.* [14] report the average time of 228 min. After caecum is reached, the capsule begins the passage through colon ($\varepsilon_r = 62.0$, $\sigma = 0.87$ S·m^{-1}), which lasts in average 21.7 h

[1]Environment with tissue-equivalent electromagnetic properties.

for a healthy person and 46.7 h for a constipated one [14]. After passing colon, the capsule exits the body by rectum.

Permittivity and conductivity of adjacent tissues (Fig. 2.1) affect the antenna impedance and resonance frequency. As the values change during the capsule passage, antenna detunes. By properly averaging the environmental EM properties and matching the antenna for the obtained ones, we can improve the antenna performance over time. One way to do it is to calculate appropriate time-averaged properties of human GI tract. Table 2.1 shows an example of this derivation for the dielectric properties at 434 MHz using the transition duration data from [14].

2.1.3 Implantable Case

As stated in Chapter 1, in some cases it is useful to design a capsule antenna to operate in both ingestible and implantable scenarios. If so, we must consider the tissue dielectric properties at the implantation site. Table 2.2 lists the parameters (according to Gabriel *et al.* [4]–[6]) for the most common implantation sites at MedRadio and ISM frequencies. If several tissues are adjacent to a capsule, their properties should be properly averaged.

Table 2.2: Tissue dielectric properties for the most common implantation sites.

Tissue	403 MHz		434 MHz		2.4 GHz	
	ε_r	σ	ε_r	σ	ε_r	σ
Skin	46.7	0.69	46.1	0.70	38.1	1.44
Muscle	57.1	0.80	56.9	0.81	52.8	1.71
Fat	11.6	0.08	11.6	0.08	10.8	0.26
Cortical Bone	13.1	0.09	13.1	0.09	11.4	0.39
Uterus	64.4	1.08	64.0	1.09	57.9	2.21

Conductivity σ is in $\mathrm{S{\cdot}m^{-1}}$

Impedance characteristics of the state-of-the-art antennas (Table 1.2) indicate that stratifying the phantom perturbs the reflection coefficient insignificantly. However, tissues in direct contact with the antenna (or its superstrate) strongly affect the antenna impedance. Hence, a homogeneous phantom is an appropriate approximation of the biological environment for the impedance analysis of in-body antennas. Likewise, a homogeneous physical phantom for antenna measurements could be fabricated using pure water, salt, sugar and an antibacterial agent (if long-term storage is required) [15, sect. 9.2.2.2].

2.2 Computational Phantoms

Computational (or numerical) phantoms are models of the human body used in computer-aided analysis. They could be conditionally divided into three generations: 1) stylized anthropomorphic phantoms, 2) voxel phantoms, 3) boundary representation (B-Rep) phantoms or CAD phantoms. B-Rep phantoms could be either polygonal or NURBS-based (non-uniform rational basis spline).

2.2.1 Literature Review

First Generation

First-generation computational phantoms came around in the '40s for ionized radiation research. These phantoms had simple geometric shapes—usually a sphere or a cylinder—and homogeneous properties. First heterogeneous phantoms imitated roughly the anatomical structure of a human body. An example is Shepp–Logan phantom [16] that is still widely employed in medical imaging. MIRD was the first stylized anthropomorphic phantom [17]; its variations are still used today too.

Homo- and heterogeneous *stylized* phantoms are ubiquitous for investigating the effect of tissue on in-body antenna parameters. Almost all antennas reviewed in Section 1.4 used such a phantom to evaluate antenna performances both in terms of impedance and radiation. The most common shapes are cubic (e.g. in [18]–[20]) and cylindrical ([21]–[26]). However, these shapes distort the intrinsic radiation pattern of the antenna [27], [28]. Spherical phantoms are thus preferable for the analysis of the antennas with undefined in-body position (for instance, ingestible) since spherical symmetry of the phantom conserves the intrinsic directivity D of the antenna.

Second Generation

Voxel phantoms were the first anatomically realistic models of human body. They are based on cadaver cryosection photos from Visible Human Project [29], CT (Computed Tomography), or MRI (Magnetic Resonance Imaging) scans. Comprehensive list of human voxel phantoms could be found in [30] and detailed overview is given in [31]. Voxel phantom development consists of three steps: 1) identifying tissues for every pixel on 2D raster images (photos, CT or MRI); 2) superposition of the sequence of segmented images into a 3D phantom; 3) assigning tissue properties to voxels. The volume of voxel is then defined as $V = Ah$ (m^3), where A is the pixel area and h is the thickness of a slice. Voxel phantoms quickly became popular in non-ionizing radiation studies since it is convenient to use it with FDTD (Finite-difference time-domain) method that is among the simplest methods to implement for the full wave solution of Maxwell's equations [32]. The main disadvantages of voxel phantoms are the impossibility to deform the geometry without considerable losses, "staircase effects" in the geometry [33] due to curved boundaries and rotations of planar ones, limited possibility for FDTD and FEM (finite element method) mesh space adaptivity, accordingly high computational costs and the order of grow $O\left(n^3\right)$.

The voxel phantoms are used mainly to estimate the radiation performances on in-body antennas in realistic application scenarios. For instance, Liu *et al.* [34] use a *Gustav* phantom from the CST Voxel Family (38-year-old female, 69 kg, resolution: $2.08 \times 2.08 \times 8$ mm) and Alrawashdeh *et al.* [26] employ the CST *Katja* voxel body model (43-year-old female, 62 kg, resolution: $1.775 \times 1.775 \times 4.84$ mm).

Third Generation

Boundary representation or *B-rep* phantoms—do not have all aforementionned drawbacks of voxel phantoms. Either polygonal mesh or NURBS approximate tissue boundaries so it could be easily scaled, deformed, or rotated without any accuracy

loss. The first versions were developed only in the 2000s (NCAT phantom [35]). The most prominent B-Rep phantoms used today for non-ionizing radiation are The Virtual Family group developed by Christ *et al.* [36] and its extension The Virtual Population by Gosselin *et al.* [37]. It includes models of independent anatomies including both sexes, with ages spanning from fetus to 84 years old and adult BMIs ranging from 21.7 to 36.2.

Polygonal mesh could be easily converted to NURBS and *vice versa* using various 3D CAD packages. Novel hybrid phantoms contain both NURBS and polygonal mesh, taking advantage of each technique according to the modeled full body tissue geometry and providing an easy simulation of subject movements, e.g. respiratory or walking. Nowadays research efforts are focused on the creation of new hybrid phantoms of the subjects of various ages and sexes for augmenting the statistical significance of simulation results.

Third generation phantoms are now implemented both in CST Microwave Studio® 2017 [38] (CST Female Visible Human Model "Nelly") and ANSYS® HFSS™ [39]. Izdebski *et al.* [40] used the latter to estimate the capsule antenna efficiency in realistic application scenarios.

2.2.2 2D Anatomically Realistic B-Rep Phantom

In order to study in-body propagation within realistic biological environment, I develop two two-dimensional (2D) phantoms: a normal human brain (used only for algorithm testing) and a human abdominal region (torso) phantom. 2D phantom approximation allows us significantly reducing the computation time of full-wave simulations and at the same time preserving the anatomical accuracy of the model.

The B-Rep phantom building process consists of the following steps: 1) acquiring the subject slices using MRI, CT, or cryosection photos; 2) segmenting of the images according to the tissue type using image processing algorithms; 3) vectorizing obtained closed segments using piecewise linear approximation or NURBS curves; 4) *for 3D phantoms*: constructing surfaces bounded by obtained loops using polygons or NURBS surfaces; 5) combining obtained closed surfaces (edges for 2D models) into a completed phantom; and 6) assigning appropriate tissue properties to the volumes enclosed by the surfaces.

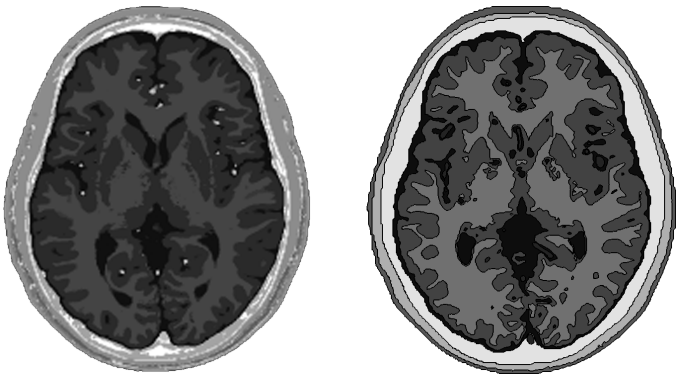

Fig. 2.2: Two-dimensional B-Rep phantom of a normal human brain. *left*: Source MRI scan (simulated) of a head. *right*: Resulted polygonal phantom.

For vectorization of the images, I develop a MATLAB script that, at first, reduces the color space from an arbitrary raster image to the indexed one (using `rgb2ind()`)

and then traces region boundaries (`bwboundaries()`). The code is tested on a head MRI scan of a normal brain from Aubert-Broche *et al.* [41]. This approach is more time-efficient since the tissues are already segmented within the generated scans. Now, the obtained boundaries can be converted to shapes using polygons or NURBS and combined to the final geometry (Fig. 2.2). Finally, phantom could be meshed using different types of adaptivity for achieving desired accuracy and performance.

Using the same methodology, I create a realistic model of a human abdominal region (torso). The source image of the slice is obtained from VHP Female College v2.2 [42]. Figure 3.3 shows the final geometry of the phantom used in the Section 3.4.4 to study in-body propagation within realistic biological environment.

2.3 Physical Phantoms

Physical phantoms are widely used for the experimental characterization of antennas both in terms or impedance and radiation. These phantoms are classified mainly based on the physical state of the phantom [15, Ch. 2], [43]: liquid, semisolid (gel), solid (dry). Only the first two are applied for in-body antennas. However, using a solid shell is common to contain the liquid and gel phantoms. If the EM properties of the shell are tissue-equivalent too (e.g. skin), this would be a hybrid phantom.

To achieve the given EM properties, the phantoms usually contain pure water (H_2O) as a base material. Sucrose is usually used to reduce the permittivity ε_r of the solution [44] (diacetin or diethylene glycol butyl ether (DGBE) at higher frequencies). To increase the conductivity in VHF–UHF bands, NaCl is usually used. Liquid phantom can be conveniently transformed to a gel using a solidifying agent such as, for instance, gelatin, agar [45], polysaccharide material TX-151 [46], or hydroxyethyl cellulose (HEC) [47].

2.3.1 Literature Review

Chou *et al.* [48] reported mixtures to simulate muscle tissue from 13.56 MHz to 2.45 GHz. The phantom contains H_2O, NaCl, and aluminum ($f \leq 100$ MHz) or polyethylene powder ($f > 100$ MHz). Hartsgrove *et al.* [47] developed formulas for simulating bone, lung, brain, and muscle tissue in the frequency range of 100 MHz to 1 GHz. Muscle- and brain-equivalent phantoms contained (apart from water–sucrose–NaCl) HEC and a bactericide. Lung phantom, in addition to aforementioned ingredients, contained $\varnothing$30–180 μm hollow silica micro-spheres that simulated alveoli in the human lung. The bone-equivalent material was presented in both solid and liquid versions. Watanabe *et al.* [49] used the same ingredients as for the previous muscle-equivalent phantom to develop liquid phantoms for SAR estimation at 144 MHz, 430 MHz, and 1.2 GHz. Ito *et al.* [46] developed a H_2O-based phantom for 300 MHz to 2.5 GHz range containing agar, polyethylene powder, NaCl, TX-151, and sodium azide NaN_3. The phantom simulates the EM properties of high-water-content tissues. Fukunaga *et al.* studied in [50] various phantoms containing H_2O, DGBE, NaCl, and ohter ingridients in 900 MHz to 2.45 GHz spectrum. In [51], the authors reported concentrations for water-based phantoms in 50 MHz to 2.45 GHz bands containing a nonion surfactant (polyoxyethylene sorbitan

monolaurat, TWEEN) and compared its temperature stability to glycol-containing phantoms.

Karacolak *et al.* [52] used agar-jellified H_2O–$C_{12}H_{22}O_{11}$–NaCl phantom to study a dual-band implantable antenna. The concentrations were given for MICS and ISM bands. Kanda *et al.* [53] showed that predition of EM parameters using either a linear or polynomial curve is possible for sugar- and DGBE-based formulations found in the IEEE 1528 Standard [54].

Just like the homogeneous computational phantoms, liquid physical phantoms are ubiquitous for experimentally studying the effect of biological tissues on in-body antenna performance. Most of the antennas reviewed in Section 1.4 use a liquid phantom to evaluate antenna performances both in terms of impedance and radiation. The majority of studies applied the H_2O–$C_{12}H_{22}O_{11}$–NaCl-based phantoms [19], [24], [52], [55]; Kiourti *et al.* replaced $C_{12}H_{22}O_{11}$ with glycerol. Liu *et al.* [34] used the DGBE-based formulation and Lee et al. [22] the methanol-based one.

Some authors reported the antenna characterization in animal tissues *ex vivo* as well, for instance, in pork [26]. Merli *et al.* [24], [56], Kim *et al.* [57] and Lee *et al.* [22] reported also an *in vivo* evaluation of the implantable capsule antenna.

Despite the large number of reported recipes and successful characterization ex vivo and in vivo, an easy-to-use closed-form prediction models for liquid phantoms are yet to be proposed. An ideal liquid phantom formulation should have following characteristics:

1. accurately predictable EM properties at a given frequency corresponding to these of a given biological environment (a tissue or an effective properties of two or more tissues);

2. easy-to-mix, homogeneous, non-flammable, and non-toxic solution;

3. ingredients accessible over-the-counter;

4. transparency is desired but not required.

A perfect candidate for such a phantom—corresponding to all aforementioned critera—is the well-studied water–sucrose–salt mixture [44].

2.3.2 Predictive Modeling of H_2O–$C_{12}H_{22}O_{11}$–NaCl Liquid Phantoms

Based on the results obtained by Kanda *et al.* [53], I develop a prediction model for the water–sucrose–salt (H_2O–$C_{12}H_{22}O_{11}$–NaCl) liquid phantoms to achieve given EM properties at a given frequency in 200 MHz to 1 GHz range. This model is necessary to simulate, for instance, the time-averaged gastrointestinal environment (see Section 2.1.2).

I use the full factorial experiment design [58, Ch. 5] to determine the initial concentrations (by weight) of $C_{12}H_{22}O_{11}$ and NaCl in H_2O. For $C_{12}H_{22}O_{11}$, the low value is 40% and the high one is 50%; for NaCl, 1% and 2%, respectively. The total weight of the initial phantoms is 200 g. The ingredients are weighted with 0.01 g accuracy (Kern precision balance EMB 2000-2 [59]).

To begin, I compare the dielectric properties (using SPEAG DAK kit [60]) of over-the-counter deionized water with a filtered one from IETR's clean room. The

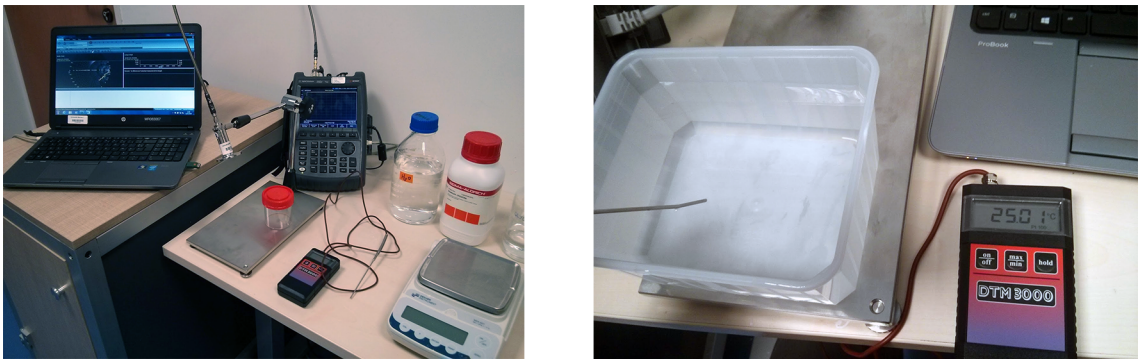

Fig. 2.3: Liquid phantom characterization setup. *left*: DAK SPEAK kit setup. *right*: Temperature control of obtained liquids.

results are in perfect agreement in 4 MHz to 3 GHz range (the operating range of DAK-12 probe). To prepare phantoms, I use pure NaCl (Sigma-Aldrich "BioXtra Sodium Chloride," S7653, $\geq$ 99.5%) and pure sucrose (Sigma-Aldrich "BioXtra Sucrose," S7903, $\geq$ 99.5%).

The four initial obtained phantoms are characterized using the SPEAG DAK kit [60] (Fig. 2.3 left) at 25 °C (Fig. 2.3 right). The experiment is repeated three times (each time new phantoms are prepared). The order of phantom preparation and measurement is randomized so that the unknown, unmeasurable, and uncontrollable disturbances cannot systematically affect the outcome. Finally, the obtained EM parameters are averaged. Table 2.3 shows the experiment design along with the average measured values of the four phantoms at 434 MHz.

Table 2.3: Full factorial experiment design (2^2) and measured EM properties at 434 MHz.

Run	NaCl (%)	$C_{12}H_{22}O_{11}$ (%)	ε_r	σ (S·m^{-1})
1	1	40	66.8	0.87
2	2	40	67.5	1.56
3	1	50	58.5	0.68
4	2	50	57.5	1.01

The EM properties in 200 MHz to 1 GHz range are interpolated using a method that gives the highest coefficient of determination (R^2) value. Fig. 2.4 shows the measured EM properties along with the interpolation curves for the Run 1. The R^2 values of ε_r, σ interpolations for the Runs 2–4 are of the same order ($R^2 \geq 0.99$).

Analysis of the results follows by least-squares modeling (using R [61]) considering the first-order interactions. The resulting expressions for the relative permittivity ε_r and conductivity σ are:

$$\begin{aligned} \varepsilon_r &= 62.575 - 0.075C_{\mathrm{NaCl}} - 4.575C_{\mathrm{C_{12}H_{22}O_{11}}} - 0.0425C_{\mathrm{NaCl}}C_{\mathrm{C_{12}H_{22}O_{11}}} \\ \sigma &= 1.03 + 0.255C_{\mathrm{NaCl}} - 0.185C_{\mathrm{C_{12}H_{22}O_{11}}} - 0.09C_{\mathrm{NaCl}}C_{\mathrm{C_{12}H_{22}O_{11}}} \end{aligned} \tag{2.5}$$

where C_{NaCl} and $C_{\mathrm{C_{12}H_{22}O_{11}}}$ are the coded values of NaCl and $C_{12}H_{22}O_{11}$ concentrations, respectively.

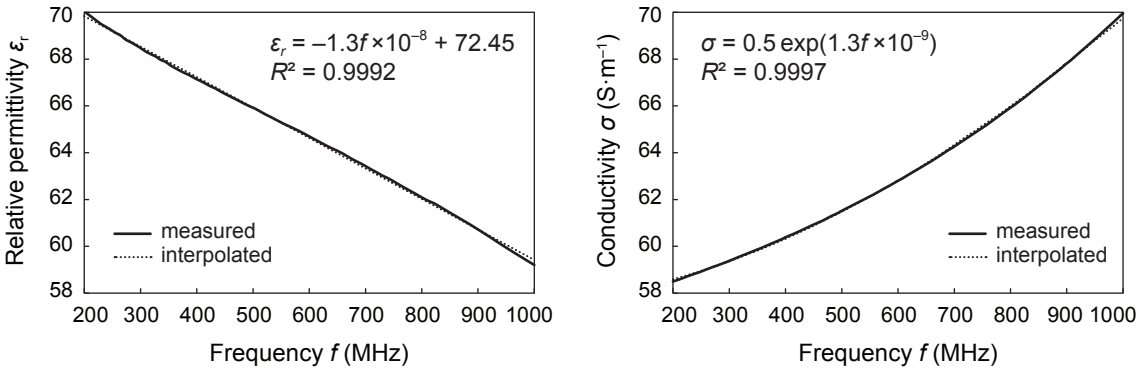

Fig. 2.4: Measured and interpolated EM properties of the "Run 1" phantom with 40% of $C_{12}H_{22}O_{11}$ and 1% of NaCl. *left*: Real part of the relative permittivity $\varepsilon'_r(\omega)$. *right*: The conductivity $\sigma(\omega)$.

The values are coded by transforming the scale of measurement for a factor [concentration (%)] so that the high value becomes +1 and the low value becomes −1. After coding all factors in a 2-level full factorial experiment, the design matrix has all orthogonal columns. Coding is a linear transformation of the original measurement scale. If the "high" value is C_h and the "low" value is C_l (in the original scale), then the scaling transformation takes any original C value and converts it to $C_{\text{coded}} = (C - a)/b$, where $a = (C_h + C_l)/2$ and $b = (C_h - C_l)/2$. Inversely, $C = bC_{\text{coded}} + a$.

The model (2.5) allows accurately estimating the EM properties in 200 MHz to 1 GHz range. With reservation, one can apply the model for an extended frequency range (within about 20% of the bound f_0) using extrapolated values.

The concentration prediction of the time-averaged gastrointestinal phantom at 434 MHz ($\varepsilon_r = 63.0$ and $\sigma = 1.02$ S·m^{-1}, see Section 2.1.2) using (2.5) is 1.45% of NaCl and 44.5% of $C_{12}H_{22}O_{11}$. Measuring this concentration gives the $\varepsilon_r = 63.8$ and $\sigma = 1.09$ S·m^{-1}.

The obtained EM properties predictions are sufficiently accurate for impedance and radiation characterization of robust in-body antennas. More precision may be required for calibration purposes. One can achieve higher prediction accuracy by refitting the model with new data points (to begin with, the EM properties for the phantom with 1.5% of NaCl of 45% of $C_{12}H_{22}O_{11}$) and introducing higher degree polynomial approximation.

Concerning the radiation characterization—as for the computational phantoms (Section 2.2.1)—spherical phantoms are preferable for the analysis of the antennas with undefined in-body position (for instance, ingestible) since spherical symmetry of the phantom conserves the intrinsic directivity D of the antenna. In addition, one has to apply an appropriate decoupling approach of the feeding cable from the antenna.

2.4 Far-Field Characterization of In-Body Antennas

Despite many reliable methods for impedance measurements, radiation characterization of both electrically and physically small antennas remains a major challenge. The antenna under test (AuT) couples strongly to a feeding cable that leads to

impaired measured data [62]. The current induced on the cable may affect the radiation pattern and matching, making difficult, if not impossible, to separate the antenna radiation from that of the cable. Different approaches allow minimizing this effect: baluns [63], differential feeding techniques [64], electrooptical converters [65], or measurements using a monostatic scattering characterization of an antenna [66]. For in-body antennas, the problem is more complicated as, in addition to these sources of error, the antenna has to be measured in a lossy phantom.

To evaluate experimentally in-body radiation performance of ingestible and implantable antennas, I submerge them in liquid phantoms with various EM properties depending on the target antenna application. The AuT is centered inside a glass spherical container filled with the liquid phantom. The spherical phantom preserves the intrinsic radiation pattern of the antenna whereas other shapes (e.g. cylindrical or cubic) may mislead about the antenna performance in terms of directivity D.

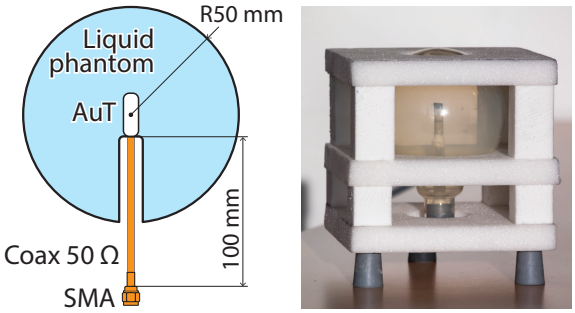

Fig. 2.5: Spherical glass container for a tissue-equivalent liquid. *left*: Design and dimensions. *right*: Final design containing an AuT and fixed with Rohacell® IG foam ($\varepsilon_r = 1.05$, $\tan\delta = 0.0017$).

The phantom diameter should be large enough to do not perturb the antenna impedance by the proximity of air. However, a too big phantom would strongly attenuate the signal reducing the signal-to-noise ratio and affecting the measurement accuracy. Hence, I have chosen to work with a ⌀100 mm phantom. A ⌀100 mm glass container is filled with the tissue-equivalent liquid, sealed with a rubber plug, and fixed using a Rohacell® IG foam ($\varepsilon_r = 1.05$, $\tan\delta = 0.0017$). The SMA connector locates outside of the sealed container easing the connection to measurement equipment. Figure 2.5 shows the phantom setup.

I characterize in-body antennas using the direct illumination far-field technique. Figure 2.6 depicts the measurement setup. A 50 Ω semi-rigid coaxial cable links the antenna to an SMA connector located outside the spherical phantom container. A silicone-sealed ⌀10 mm polyamide tube is fitted between the AuT and the connector to insulate the cable from the phantom. The vertically positioned AuT and its container constitute the device under test (DuT).

The DuT localizes at a distance from the measurement horn fulfilling the far-field criteria [27]. An electro-optical converter (enprobe LFA-3 [67]) feeds the DuT (Figure 2.6). In this way, an optical fiber replaces the RF cable inside an anechoic chamber thus minimizing the main source of signal impairment. The DuT is mounted and aligned on the tower positioner using foam blocks ($\varepsilon_r \approx 1.0$, $\tan\delta \approx 0.001$).

The estimation of the realized gain uses the gain substitution technique employing a reference antenna of a known gain (ETS-Lindgren Model 3164-06 [68], 300 MHz–6 GHz).

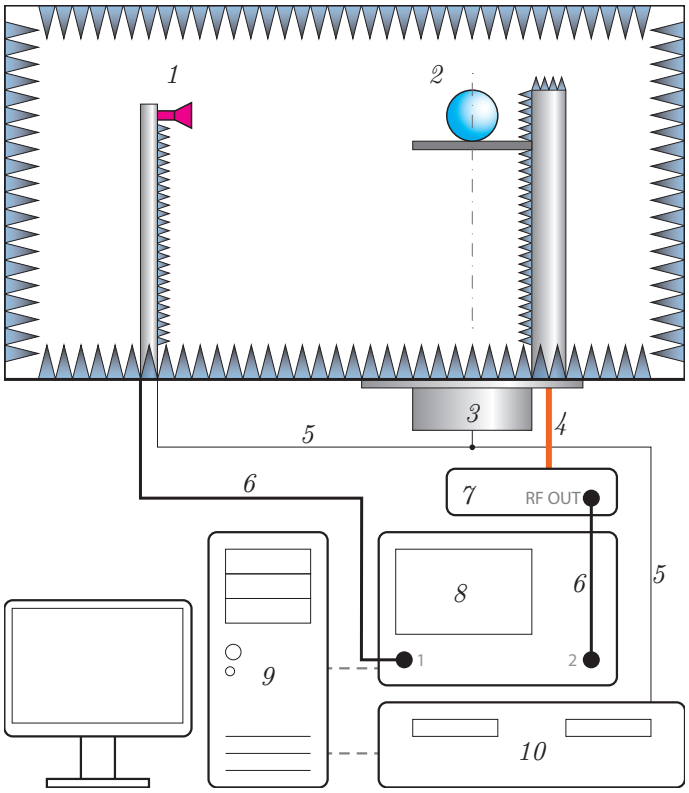

Fig. 2.6: The measurement setup proposed for characterizing radiation performance of in-body antennas: 1) measurement antenna, 2) AuT in ⌀100 mm spherical phantom, 3) azimuth positioner, 4) optical fiber, 5) positioner control cables, 6) RF cables, 7) analog fiber optic link Enprobe LFA-3, 8) vector network analyzer R&S ZVA 24, 9) acquisition/control PC, and 10) positioner controller ORBIT/FR AL-4806-3C Opt. 1.

2.5 Summary

Body tissues are heterogeneous and highly dispersive medium. The effective EM properties $\hat{\varepsilon}(\omega)$ of each individual tissue are characterized by four relaxation regions that can be accurately modeled using the multiple Cole–Cole dispersion. One must account for these properties while designing antennas for in-body applications. In particular, for ingestible applications—where the surrounding tissues vary in time—an averaging of the tissue EM properties is necessary. We proposed a time-averaging scheme based on the standard GI transition time reported in the literature.

A geometrical representation (by simple, complex, or compound shapes) of one or several tissues along with corresponding EM properties assigned for each point space constitute a computational phantom. According to the assigned EM properties, the phantoms can be homo- and heterogeneous. Stylized homogeneous phantoms are widely applied for in-body antenna design as they accurately represent the effect of tissues on antenna impedance and are computationally efficient. For simplified radiation studies, spherical shapes are preferable since spherical symmetry of the phantom conserves the intrinsic directivity D of the antenna. Realistic heterogeneous voxel and B-rep phantoms enable accurate estimation of radiation performance. However, using these phantoms is computationally expensive and thus time-consuming. B-rep phantoms support spatially adaptive meshing techniques (e.g. using triangles in two spatial dimensions or tetrahedrons in three dimensions) that not only reduces the

number of degrees of freedom but also better resolves thin tissue layers compared to the voxel phantoms. Even though the spatial adaptivity exists for grid-based methods (e.g. finite difference in time domain [69] or finite integration technique [70]), the fact that voxel phantoms are already pre-meshed with a given resolution limits the adaptivity advantages.

2D approximation of realistic heterogeneous phantoms allows one significantly reducing the computation time of full-wave simulations and at the same time preserving the anatomical accuracy of the model. In this chapter, we developed two two-dimensional (2D) B-rep phantoms: a normal human brain (used only for algorithm testing in this dissertation) and a human abdominal region (torso) phantom.

Liquid physical phantoms are widely used for the in-body antenna experimental characterization of impedance and of radiation. To achieve the given EM properties in UHF range, the phantoms usually contain pure water as a base material. Adding NaCl increases conductivity, and mixing in a non-polar component—as, for instance, sucrose, glycerol, or DGBE—reduces the permittivity. One can conveniently transform a liquid phantom to a gel one using solidifying agents. In this chapter, we developed a prediction model for the water–sucrose–salt liquid phantoms to achieve given EM properties at a given frequency in 200 MHz to 1 GHz range. The model is based on a full-factorial design considering the first order interactions and gives accurate predictions for impedance and radiation characterization of in-body antennas. Higher prediction accuracy is achievable by refitting the model with new data points and introducing higher degree polynomial approximation.

Far-field characterization of miniature in-body antennas inside physical phantoms faces many technical challenges. Using conventional techniques, the antenna under test couples strongly to a feeding cable that leads to impaired measured data. The approach and the phantom setup discussed in this chapter improves the measurement accuracy in two ways: (1) the spherical phantom preserve the intrinsic radiation pattern of an antenna; (2) replacing the majority of a feeding cable with an optical fiber as well as insulating the remaining part with air allow suppressing currents induced on the cable.

Bibliography

[1] C. Gabriel, "Dielectric properties of biological materials," in *Handbook of biological effects of electromagnetic fields. Bioengineering and biophysical aspects of electromagnetic fields*, F. S. Barnes and B. Greenebaum, Eds., 3rd ed., Boca Raton, FL: CRC Press, 2007, pp. 51–100.

[2] F. S. Barnes and B. Greenebaum, *Handbook of biological effects of electromagnetic fields. Bioengineering and biophysical aspects of electromagnetic fields*, 3rd ed. Boca Raton: CRC/Taylor & Francis, 2007.

[3] K. S. Cole and R. H. Cole, "Dispersion and absorption in dielectrics I. Alternating current characteristics," *The Journal of Chemical Physics*, vol. 9, no. 4, pp. 341–351, Apr. 1941.

[4] C. Gabriel, S. Gabriel, and E. Corthout, "The dielectric properties of biological tissues: I. Literature survey," *Physics in Medicine and Biology*, vol. 41, pp. 2231–2249, Nov. 1996, 11.

[5] S. Gabriel, R. W. Lau, and C. Gabriel, "The dielectric properties of biological tissues: II. Measurements in the frequency range 10 Hz to 20 GHz," *Physics in Medicine and Biology*, vol. 41, pp. 2251–2269, Nov. 1996.

[6] S. Gabriel, R. W. Lau, and C. Gabriel, "The dielectric properties of biological tissues: III. Parametric models for the dielectric spectrum of tissues," *Physics in Medicine and Biology*, vol. 41, pp. 2271–2293, Nov. 1996.

[7] H. A. Kramers, "La diffusion de la lumiere par les atomes," *Atti del Congresso Internationale dei Fisici, Como*, vol. 2, pp. 545–557, 1927.

[8] R. d. L. Kronig, "On the theory of dispersion of X-rays," *Journal of the Optical Society of America*, vol. 12, no. 6, pp. 547–557, Jun. 1926.

[9] J. D. Jackson, *Classical electrodynamics*, 3rd ed. Hoboken, NJ: John Wiley & Sons, 1999.

[10] M. M. Scott, G. L. Wilson, and J. A. Berrie, "Kramers-kronig analysis of RIF polymers and composites," *IEEE Antennas and Propagation Magazine*, vol. 47, no. 3, pp. 157–163, Jun. 2005.

[11] M. Yuce and T. Dissanayake, "Easy-to-swallow antenna and propagation," *IEEE Microwave Magazine*, vol. 14, no. 4, pp. 74–82, Jun. 2013.

[12] E. Ben-Soussan, G. Savoye, M. Antonietti, S. Ramirez, E. Lerebours, and P. Ducrotté, "Factors that affect gastric passage of video capsule," *Gastrointestinal Endoscopy*, vol. 62, no. 5, pp. 785–790, Nov. 2005.

[13] J. Worsøe, L. Fynne, T. Gregersen, V. Schlageter, L. A. Christensen, J. F. Dahlerup, N. J. Rijkhoff, S. Laurberg, and K. Krogh, "Gastric transit and small intestinal transit time and motility assessed by a magnet tracking system," *BMC Gastroenterology*, vol. 11, no. 145, pp. 1–10, 2011.

[14] S. S. C. Rao, B. Kuo, R. W. McCallum, W. D. Chey, J. K. DiBaise, W. L. Hasler, K. L. Koch, J. M. Lackner, C. Miller, R. Saad, J. R. Semler, M. D. Sitrin, G. E. Wilding, and H. P. Parkman, "Investigation of colonic and whole-gut transit with wireless motility capsule and radiopaque markers in constipation," *Clinical Gastroenterology and Hepatology*, vol. 7, no. 5, pp. 537–544, May 2009.

[15] P. S. Hall and Y. Hao, *Antennas and Propagation for Body-Centric Wireless Communications*, Second. Norwood, MA: Artech House, 2012.

[16] L. Shepp and B. Logan, "The Fourier reconstruction of a head section," *IEEE Transactions on Nuclear Science*, vol. 21, no. 3, pp. 21–43, 1974.

[17] H. L. Fisher Jr and W. S. Snyder, "Variation of dose delivered by 137cs as a function of body size from infancy to adulthood," *ORNL*, vol. 4007, pp. 221–228, 1966.

[18] K. A. Psathas, A. Kiourti, and K. S. Nikita, "A novel conformal antenna for ingestible capsule endoscopy in the MedRadio band," in *34th Progress in Electromagnetics Research Symposium (PIERS 2013)*, Stockholm, Sweden, Aug. 2013.

[19] L.-J. Xu, Y.-X. Guo, and W. Wu, "Bandwidth enhancement of an implantable antenna," *IEEE Antennas and Wireless Propagation Letters*, vol. 14, pp. 1510–1513, 2015.

[20] Q. Wang, K. Wolf, and D. Plettemeier, "An UWB capsule endoscope antenna design for biomedical communications," in *1rd International Symposium on Applied Sciences in Biomedical and Communication Technologies (ISABEL 2010)*, Rome, Italy, Nov. 2010, pp. 1–6.

[21] S.-I. Kwak, K. Chang, and Y.-J. Yoon, "The helical antenna for the capsule endoscope," in *2005 IEEE Antennas and Propagation Society International Symposium*, vol. 2B, Washington, DC, Jul. 2005, pp. 804–807.

[22] S.-H. Lee, J. Lee, Y. J. Yoon, S. Park, Changyul-Cheon, K. Kim, and S. Nam, "A wideband spiral antenna for ingestible capsule endoscope systems: Experimental results in a human phantom and a pig," *IEEE Transactions on Biomedical Engineering*, vol. 58, no. 6, pp. 1734–1741, Jun. 2011.

[23] Y. Mahe, A. Chousseaud, M. Brunet, and B. Froppier, "New flexible medical compact antenna: Design and analysis," *International Journal of Antennas and Propagation*, vol. 2012, May 2012.

[24] F. Merli, L. Bolomey, J. Zurcher, G. Corradini, E. Meurville, and A. Skrivervik, "Design, realization and measurements of a miniature antenna for implantable wireless communication systems," *IEEE Transactions on Antennas and Propagation*, vol. 59, no. 10, pp. 3544–3555, Oct. 2011.

[25] T. Dissanayake, K. Esselle, and M. Yuce, "Dielectric Loaded Impedance Matching for Wideband Implanted Antennas," *IEEE Transactions on Microwave Theory and Techniques*, vol. 57, no. 10, pp. 2480–2487, Oct. 2009.

[26] R. Alrawashdeh, Y. Huang, M. Kod, and A. Sajak, "A broadband flexible implantable loop antenna with complementary split ring resonators," *IEEE Antennas and Wireless Propagation Letters*, vol. 14, pp. 1506–1509, 2015.

[27] R. Moore, "Effects of a surrounding conducting medium on antenna analysis," *IEEE Transactions on Antennas and Propagation*, vol. 11, no. 3, pp. 216–225, May 1963.

[28] A. Karlsson, "Physical limitations of antennas in a lossy medium," *IEEE Transactions on Antennas and Propagation*, vol. 52, no. 8, pp. 2027–2033, Aug. 2004.

[29] M. Ackerman, "The Visible Human Project," *Proceedings of the IEEE*, vol. 86, no. 3, pp. 504–511, 1998.

[30] L. A. DeWerd and M. Kissick, *The Phantoms of Medical and Health Physics: Devices for Research and Development*. Springer Science & Business Media, Nov. 2013.

[31] H. Zaidi and X. G. Xu, "Computational anthropomorphic models of the human anatomy: The path to realistic Monte Carlo modeling in radiological sciences," *Annu. Rev. Biomed. Eng.*, vol. 9, pp. 471–500, 2007.

[32] K. S. Yee, "Numerical solution of initial boundary value problems involving Maxwell's equations in isotropic media," *IEEE Transactions on Antennas and Propagation*, vol. 14, pp. 302–307, 1966, 3.

[33] B. B. Beard, W. Kainz, T. Onishi, T. Iyama, S. Watanabe, O. Fujiwara, W. Jianqing, G. Bit-Babik, A. Faraone, J. Wiart, A. Christ, N. Kuster, L. Ae-Kyoung, H. Kroeze, M. Siegbahn, J. Keshvari, H. Abrishamkar, W. Simon, D. Manteuffel, and N. Nikoloski, "Comparisons of computed mobile phone induced SAR in the SAM phantom to that in anatomically correct models of the human head," *IEEE Transactions on Electromagnetic Compatibility*, vol. 48, pp. 397–407, 2006, 2.

[34] C. Liu, Y.-X. Guo, and S. Xiao, "Circularly polarized helical antenna for ISM-band ingestible capsule endoscope systems," *IEEE Transactions on Antennas and Propagation*, vol. 62, no. 12, pp. 6027–6039, Dec. 2014.

[35] W. P. Segars, "Development and application of the new dynamic NURBS-based Cardiac-Torso (NCAT) phantom," Ph.D. dissertation, University of North Carolina, Chapel Hill, 2001.

[36] A. Christ, W. Kainz, E. G. Hahn, K. Honegger, M. Zefferer, E. Neufeld, W. Rascher, R. Janka, W. Bautz, J. Chen, B. Kiefer, P. Schmitt, H.-P. Hollenbach, J. Shen, M. Oberle, D. Szczerba, A. Kam, J. W. Guag, and N. Kuster, "The Virtual Family—development of surface-based anatomical models of two adults and two children for dosimetric simulations," *Physics In Medicine And Biology*, vol. 55, N23–N38, Jan. 2010.

[37] M.-C. Gosselin, E. Neufeld, H. Moser, E. Huber, S. Farcito, L. Gerber, Maria Jedensjö, I. Hilber, F. D. Gennaro, B. Lloyd, E. Cherubini, D. Szczerba, Wolfgang Kainz, and N. Kuster, "Development of a new generation of high-resolution anatomical models for medical device evaluation: The Virtual Population 3.0," *Physics in Medicine & Biology*, vol. 59, no. 18, p. 5287, 2014.

[38] Computer Simulation Technology AG, *CST Microwave Studio*. [Online]. Available: `https://www.cst.com/Products/CSTMWS` (visited on 08/06/2016).

[39] ANSYS, Inc., *Ansys HFSS*. [Online]. Available: `http://www.ansys.com/products/electronics/ansys-hfss` (visited on 08/06/2016).

[40] P. Izdebski, H. Rajagopalan, and Y. Rahmat-Samii, "Conformal ingestible capsule antenna: A novel chandelier meandered design," *IEEE Transactions on Antennas and Propagation*, vol. 57, no. 4, pp. 900–909, Apr. 2009.

[41] B. Aubert-Broche, A. C. Evans, and L. Collins, "A new improved version of the realistic digital brain phantom," *NeuroImage*, vol. 32, pp. 138–145, Jan. 2006.

[42] S. N. Makarov, G. M. Noetscher, and A. Nazarian, "Triangular surface human body meshes for computational purposes," in *Low-Frequency Electromagnetic Modeling for Electrical and Biological Systems Using MATLAB*, Hoboken, NJ: John Wiley & Sons, Jun. 2015, pp. 89–130.

[43] K. Ito, "Human body phantoms for evaluation of wearable and implantable antennas," in *1nd European Conference on Antennas and Propagation (EuCAP 2007)*, Edinburgh, UK, Nov. 2007, pp. 1–6.

[44] C. G. Malmberg and A. A. Maryott, "Dielectric constants of aqueous solutions of dextrose and sucrose," *Journal of Research of the National Bureau of Standards*, vol. 45, no. 4, pp. 299–303, 1950.

[45] N. Chahat, M. Zhadobov, R. Sauleau, and S. I. Alekseev, "New method for determining dielectric properties of skin and phantoms at millimeter waves based on heating kinetics," *IEEE Transactions on Microwave Theory and Techniques*, vol. 60, no. 3, pp. 827–832, Mar. 2012.

[46] K. Ito, K. Furuya, Y. Okano, and L. Hamada, "Development and characteristics of a biological tissue-equivalent phantom for microwaves," *Electronics and Communications in Japan (Part I: Communications)*, vol. 84, no. 4, pp. 67–77, Apr. 2001.

[47] G. Hartsgrove, A. Kraszewski, and A. Surowiec, "Simulated biological materials for electromagnetic radiation absorption studies," *Bioelectromagnetics*, vol. 8, no. 1, pp. 29–36, Jan. 1987.

[48] C. K. Chou, G. W. Chen, A. W. Guy, and K. H. Luk, "Formulas for preparing phantom muscle tissue at various radiofrequencies," *Bioelectromagnetics*, vol. 5, no. 4, pp. 435–441, 1984.

[49] S. Watanabe, Y. Akiyama, R. Ishikawa, and Y. Yamanaka, "Tissue-equivalent liquid for experimental estimation of local SAR caused by hand-held amateur radio communication devices," *Proceedings of the 2000 International Symposium on Antennas and Propagation*, vol. 1, pp. 241–244, 2000.

[50] K. Fukunaga, S. Watanabe, and Y. Yamanaka, "Dielectric properties of tissue-equivalent liquids and their effects on specific absorption rate," *IEEE Transactions on Electromagnetic Compatibility*, vol. 46, no. 1, pp. 126–129, Feb. 2004.

[51] K. Fukunaga, S. Watanabe, H. Asou, and K. Sato, "Dielectric properties of non-toxic tissue-equivalent liquids for radiowave safety tests," in *2005 IEEE International Conference on Dielectric Liquids, 2005. ICDL 2005*, Jun. 2005, pp. 425–428.

[52] T. Karacolak, A. Hood, and E. Topsakal, "Design of a dual-band implantable antenna and development of skin mimicking gels for continuous glucose monitoring," *IEEE Transactions on Microwave Theory and Techniques*, vol. 56, no. 4, pp. 1001–1008, Apr. 2008.

[53] M. Kanda, M. Ballen, S. Salins, C.-K. Chou, and Q. Balzano, "Formulation and characterization of tissue equivalent liquids used for RF densitometry and dosimetry measurements," *IEEE Transactions on Microwave Theory and Techniques*, vol. 52, no. 8, pp. 2046–2056, Aug. 2004.

[54] IEEE, "IEEE Recommended Practice for Determining the Peak Spatial-Average Specific Absorption Rate (SAR) in the Human Head from Wireless Communications Devices: Measurement Techniques," Tech. Rep. IEEE Std 1528-2003, 2003, p. 120.

[55] H. Rajagopalan and Y. Rahmat-Samii, "Wireless medical telemetry characterization for ingestible capsule antenna designs," *IEEE Antennas and Wireless Propagation Letters*, vol. 11, pp. 1679–1682, 2012.

[56] F. Merli, L. Bolomey, F. Gorostidi, B. Fuchs, J. Zurcher, Y. Barrandon, E. Meurville, J. Mosig, and A. Skrivervik, "Example of data telemetry for biomedical applications: An in vivo experiment," *IEEE Antennas and Wireless Propagation Letters*, vol. 11, pp. 1650–1654, 2012.

[57] K. Kim, S. Yun, S. Lee, S. Nam, Y. J. Yoon, and Changyul-Cheon, "A design of a high-speed and high-efficiency capsule endoscopy system," *IEEE Transactions on Biomedical Engineering*, vol. 59, no. 4, pp. 1005–1011, Apr. 2012.

[58] G. E. P. Box, J. S. Hunter, and W. G. Hunter, *Statistics for Experimenters: Design, Innovation, and Discovery*, Second. Hoboken, N.J: Wiley-Interscience, May 2005.

[59] Kern & Sohn GmbH, *Precision balance EMB*. [Online]. Available: `https://www.kern-sohn.com/en/EMB/` (visited on 03/28/2017).

[60] Schmid & Partner Engineering AG, *Dielectric Assessment Kit*. [Online]. Available: `http://www.speag.com/products/dak/dielectric-measurements/` (visited on 08/06/2016).

[61] R Development Core Team, *R: A language and environment for statistical computing*, ISBN 3-900051-07-0, Vienna, Austria: R Foundation for Statistical Computing, 2008. [Online]. Available: `http://www.R-project.org`.

[62] L. Huitema, C. Delaveaud, and R. D'Errico, "Impedance and radiation measurement methodology for ultra miniature antennas," *IEEE Transactions on Antennas and Propagation*, vol. 62, no. 7, pp. 3463–3473, Jul. 2014.

[63] S. Pivnenko, J. Zhang, A. Khatun, T. Laitinen, and J. Carlsson, "Characterization of small antennas for hearing aids by several measurement techniques," in *Proceedings of the Fourth European Conference on Antennas and Propagation*, Barcelona, Spain, Apr. 2010, pp. 1–5.

[64] M. M. Suzan, K. Haneda, C. Icheln, A. Khatun, and K. Takizawa, "An ultra-wideband conformal loop antenna for ingestible capsule endoscope system," in *10th European Conference on Antennas and Propagation (EuCAP 2016)*, Davos, Switzerland, Apr. 2016, pp. 1–5.

[65] T. H. Loh, D. Cheadle, and L. Rosenfeld, "Radiation pattern measurement of a low-profile wearable antenna using an optical fibre and a solid anthropomorphic phantom," *Electronics*, vol. 3, no. 3, pp. 462–473, Aug. 2014.

[66] W. Wiesbeck and E. Heidrich, "Wide-band multiport antenna characterization by polarimetric RCS measurements," *IEEE Transactions on Antennas and Propagation*, vol. 46, no. 3, pp. 341–350, Mar. 1998.

[67] enprobe GmbH, *LFA-3 Analog fiber optic link*. [Online]. Available: `http://www.enprobe.de/products_FO-Links.htm` (visited on 07/02/2016).

[68] ETS-Lindgren, *3164-06 Open boundary quad-ridged horn*. [Online]. Available: `http://www.ets-lindgren.com/3164-06` (visited on 07/14/2016).

[69] M. J. White, M. F. Iskander, and Z. Huang, "Development of a multigrid FDTD code for three-dimensional applications," *IEEE Transactions on Antennas and Propagation*, vol. 45, no. 10, pp. 1512–1517, Oct. 1997.

[70] M. Clemens and T. Weiland, "Discrete electromagnetism with the finite integration technique," *Progress In Electromagnetics Research*, vol. 32, pp. 65–87, 2001.

Chapter 3

Radiation Efficiency of In-Body Devices

Contents

3.1 Introduction 56

3.2 Theory 57

3.2.1 Attenuation in Biological Tissues 57

3.2.2 Impedance Contrast and Mismatch Losses 59

3.2.3 Fundamental Limitations on Radiation Efficiency for Electrically Small Antennas 59

3.3 Problem Formulation 60

3.3.1 Numerical Model 62

3.4 Results and Discussion 63

3.4.1 Infinite Medium: Planar-Bounded Homogeneous Half-Space 63

3.4.2 Infinite Medium: Planar-Bounded Layered Half-Space . . 66

3.4.3 Cylindrical Stratified Phantom 66

3.4.4 Anatomical Torso Phantom 69

3.5 Summary 69

3.1 Introduction

MINIATURE implantable, ingestible, and injectable (in-body) wireless devices applied to biotelemetry and neural interfacing require efficient radiative electromagnetic (EM) energy transfer from lossy media to surrounding free space [1]. Typical biotelemetry applications include monitoring of physiological parameters, for instance: body temperature, blood pressure, heart rate, glucose and antibody levels. In addition, neural interfacing allows us studying the brain, restoring sensory function, and assisting in the rehabilitation of amputees, survivors of paralysis, and patients with neurodegenerative diseases [2], [3].

As Section 1.1 demonstrates, advances in microelectromechanical systems and microfluidics—along with ongoing miniaturization of semiconductor electronics—empower numerous innovations in this field creating new applications in medicine and clinical research. Wireless powering makes possible further miniaturizing in-body devices by removing bulky energy storage components [4]. In addition, it avoids surgery needed to replace the batteries and thus makes the lifespan of an implanted device almost unlimited. Kim *et al.* [4], [5] introduced a powering approach using mid-field (the region where the wavelength is comparable to the distance between an implant and transmitter) and achieved much higher power transfer efficiency than traditional inductively coupled systems. Using this approach, Agrawal *et al.* reported the conformal focusing system [6] that makes possible powering, for instance, of an ultra-miniature pacemaker [7].

Yet, improving the operating range of miniature in-body devices (the distance between a body and an external equipment) remains a major challenge: for the time being, they are able to operate only up to about a meter [8]. The major issues are low radiation efficiency ($\eta < 0.1\%$) and strong coupling to lossy dispersive biological tissues [1], [9]. Chirwa *et al.* studied numerically the radiation from an ingested normal-mode monofilar helix antenna in the human intestine between 150 MHz and 1.2 GHz and suggested that the maximum radiation occurs between 450 and 900 MHz [10], [11]. Poon *et al.* [12] showed that the optimal wireless power transfer to an in-body device from a small current loop can be achieved operating at GHz frequencies (mid-field region). A number of studies suggests that the optimal frequency exists as well for the energy transfer in far field from a body to surrounding free space [9]–[11], [13]–[15]. Considering dispersive properties of body tissues [16], attenuation, reflection losses, and efficiency limitations of electrically small antennas [17], we conjecture that the optimal frequencies exist in 10^8 Hz to 3×10^9 Hz range. The optimal frequency within this range depends on the type and depth of the source, its size, polarization, and bandwidth.

To derive the optimal frequency, we start by modeling the biological media as an infinite homogeneous half-space with dispersive muscle-equivalent EM properties bounded with a free space by a planar interface. Then, we stratify the infinite half-space medium by adding skin and subcutaneous fat layers. Next, we model human body as a stratified cylindrical domain. Finally, we analyze a heterogeneous realistic model of the human abdominal region. Using the formulated models, we establish the optimal operating frequencies for deep-body (for instance, ingestible; depth $d \gtrsim 3$ cm) and for subcutaneous applications ($d \lesssim 3$ cm). The interference induced by a standing surface wave plays an important role for the subcutaneous case. We also analyze the **E**-field polarization effect on the far-field power transfer efficiency by

exciting TE (arbitrary polarization of the **E**-field incident on the media interfaces) and TM modes (pure p-polarization—**E**-field along the plane of incidence) through the infinitesimal sources: a magnetic current and a magnetic dipole, respectively.

3.2 Theory

Figure 3.1(a) shows the EM properties of muscle and fat according to Eq. (2.2) based on experimental data obtained by Gabriel *et al.* [16]. For the majority of biological tissues, relative permittivity $\varepsilon_r(\omega)$ is inversely proportional to ω, and $\sigma(\omega)$ is directly proportional to ω.

An antenna forms a coupled system of accelerating charges with biological tissues. This system radiates to surrounding free space due to non-conserved current and charge in the localized region surrounding the antenna. The EM radiation mechanics can be understood in the context of the explicit symmetry breaking [18]. The inhomogeneous wave equation models the behavior of EM field from an arbitrary source. In terms of the time-harmonic (time variations of the form $e^{j\omega t}$) electric field $\mathbf{E}$ ($\mathrm{V{\cdot}m^{-1}}$), it is expressed as

$$\nabla^2\mathbf{E} = \nabla\times\mathbf{M}_i + j\omega\mu_0\mathbf{J}_i + \frac{1}{\varepsilon}\nabla q_{ev} + j\omega\mu_0\sigma\mathbf{E} - \omega^2\mu_0\varepsilon\mathbf{E}, \tag{3.1}$$

where $\mathbf{M}_i$ is the source magnetic current density ($\mathrm{V{\cdot}m^{-2}}$), $\mathbf{J}_i$ is the source electric current density ($\mathrm{A{\cdot}m^{-2}}$), and q_{ev} is the electric charge density ($\mathrm{C{\cdot}m^{-3}}$).

From the conservation-of-energy point of view (Poynting's theorem),

$$\overbrace{-\frac{1}{2}\left(\mathbf{H}^*\cdot\mathbf{M}_i + \mathbf{E}\cdot\mathbf{J}_i^*\right)}^{P_s} = \overbrace{\nabla\cdot\left(\frac{1}{2}\mathbf{E}\times\mathbf{H}^*\right)}^{P_e} + \underbrace{\frac{1}{2}\sigma|\mathbf{E}|^2}_{P_d} + \underbrace{j2\omega\left(\frac{1}{4}\mu_0|\mathbf{H}|^2 - \frac{1}{4}\varepsilon|\mathbf{E}|^2\right)}_{j2\omega(W_m - W_e)}, \tag{3.2}$$

where $\mathbf{H}$ is the magnetic field ($\mathrm{A{\cdot}m^{-1}}$), P_s is the supplied power (W), P_e is the exiting power (W), P_d is the dissipated power, and W_m and W_e are the time-average magnetic and electric energies, respectively.

Several frequency-dependent mechanisms affect the power transfer efficiency from a body to free space. The major are 1) the attenuation due to material (dielectric) losses, 2) the reflection (mismatch) losses due to impedance contrast, and 3) the physical limitations on the radiation efficiency of electrically small sources in lossy media [17]. Furthermore, the efficiency is affected by the resonance behavior of the body or its parts [19]–[21].

3.2.1 Attenuation in Biological Tissues

For a TEM wave in a lossy medium, the attenuation constant α ($\mathrm{Np{\cdot}m^{-1}}$) can be expressed as [22, p. 142]

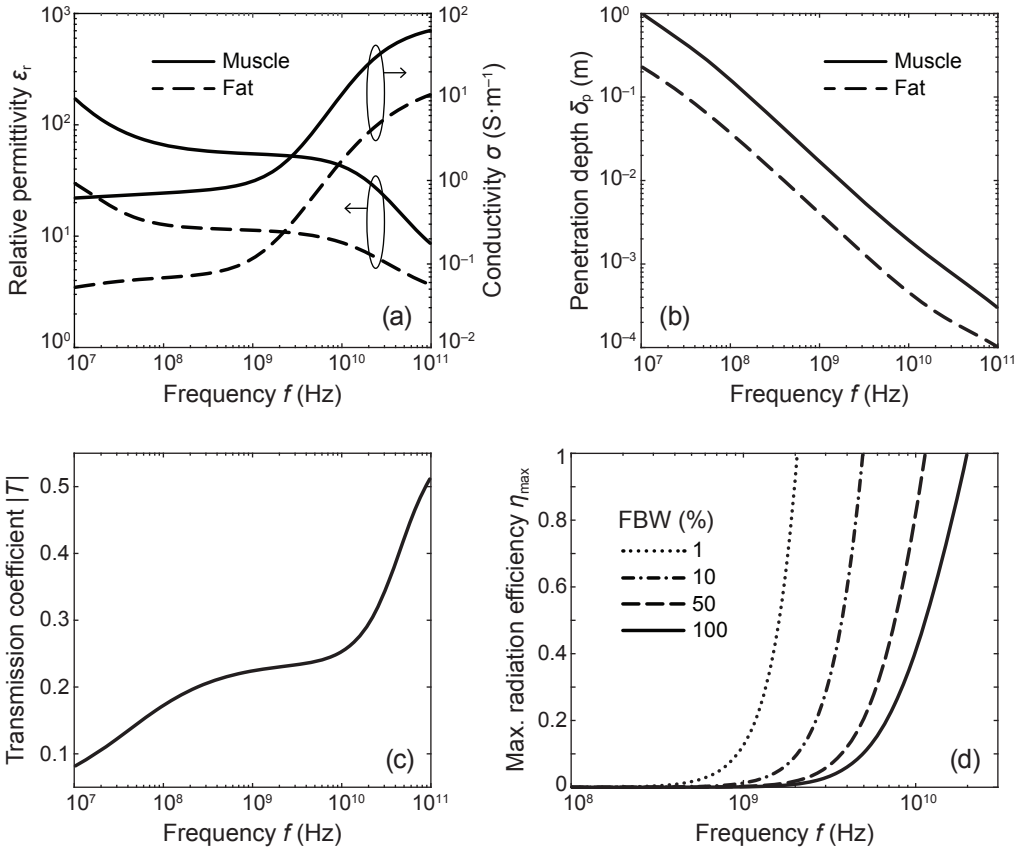

Fig. 3.1: Main factors affecting in-body proparagion. (a) Dispersive EM properties of muscle and fat tissues derived using Eq. (2.2) interpolating experimental data obtained by Gabriel *et al.* [16] (b) Penetration depths δ_p given by Eq. (3.4) into dispersive muscle and fat tissues modeled using Eq. (2.2). (c) Transmission coefficient T given by Eq. (3.5) of a normal-incident plane wave upon a planar infinite air–skin interface taking into account the dispersive skin EM properties modeled using Eq. (2.2). (d) The highest achievable radiation efficiencies η_{ub} given by Eq. (3.10) for several fractional bandwidths $\text{FBW} = f_0/\text{BW}$ considering $\text{VSWR} = 2$, assuming $a = 5$ mm, and taking the dispersive permittivity of muscle given by Eq. (2.2).

$$\alpha = \omega\sqrt{\mu_0\varepsilon\left(\omega\right)}\sqrt{\frac{1}{2}\left[\sqrt{1+\left(\frac{\sigma\left(\omega\right)}{\omega\varepsilon\left(\omega\right)}\right)^2}-1\right]}. \tag{3.3}$$

Characterizing the propagation loss using the penetration depth

$$\delta_p = {}^1\!/_\alpha \tag{3.4}$$

gives the depth (m) at which the amplitude of the fields falls by $1/e$ (about 37%) or the intensity by $1/e^2$ (14%).

Figure 3.1(b) shows the characteristic depth of penetration (3.4) in muscle and fat tissues taking into account dispersive properties (2.2) of the tissues. This mechanism prominently favors lower frequencies to maximize the transmission efficiency. Obviously, the attenuation losses depend on how deep the source is.

3.2.2 Impedance Contrast and Mismatch Losses

Rapid transitions in EM properties occur at the tissue–air interface as well as at the boundaries between tissues. The resulting impedance contrast at an interface deteriorates the through-body transmission due to reflections [23]. A high contrast arises, for instance, on a skin–air and muscle–fat interfaces [Figure 3.1(a)]. The transmission efficiency through these boundaries can be characterized using the transmission coefficient T defined as a ratio of transmitted electric field E_t to the incident E_i at an interface between two tissues $T = E_t/E_i$. For an interface between two given tissues, the transmission coefficient depends on the angle of incidence and polarization but generally rises with frequency for biological tissues [23]. This trend can be demonstrated qualitatively assuming the plane wave solution of (3.1) under normal incidence upon a planar interface $E_x(z) = E_0^+ e^{-j\beta z} + E_0^- e^{+j\beta z}$, where E_0 are the amplitudes of the incident and reflected traveling waves and β represents the phase constant (rad·m^{-1}). In this case, the transmission coefficient depends only on the wave impedance Z (Ω) of each media as [22, p. 175]

$$T = \frac{2Z_2}{Z_2 + Z_1}, \tag{3.5}$$

where

$$Z_i = \sqrt{\frac{j\omega\mu_0}{\sigma + j\omega\varepsilon}}, \quad i = 1, 2. \tag{3.6}$$

Figure 3.1(c) shows the transmission coefficient (3.5) for a normal-incident plane wave upon a planar air–skin interface taking into account dispersive properties (2.2) of skin. The lower is the frequency the higher are reflection loss. For oblique incidence, p-polarized **E** gives better transmission (with no reflection at Brewster's angle) than the **s**-polarized one. The plane-wave model, however, is inappropriate to quantify the reflection losses when a source is close to the interface, and the separation is usually much shorter than a wavelength [12]. On the other hand, a full-wave solution of (3.1) accounts for non-TEM wave propagation effects through the highly heterogeneous and dispersive medium with arbitrary angles of incidence and **E**-field polarization.

3.2.3 Fundamental Limitations on Radiation Efficiency for Electrically Small Antennas

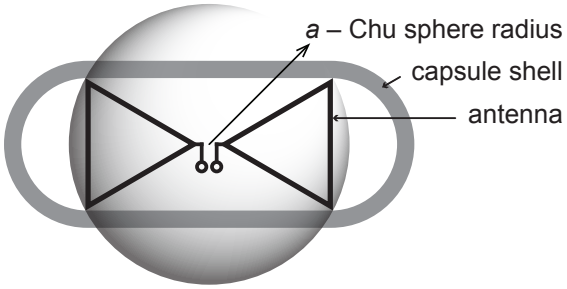

Fig. 3.2: Definition of the Chu sphere circumscribing a capsule antenna used in this dissertation.

By definition [24], an antenna is electrically small (ESA) when its electrical size satisfies

$$ka < 0.5, \tag{3.7}$$

where $k(\varepsilon) = 2\pi/\lambda$ is the wavenumber (m^{-1}), $\lambda(\varepsilon)$ represents the wavelength (m), and a denotes the radius of the minimum size sphere that circumscribes the antenna (also known as the Chu sphere on Figure 3.2).

The physical limitations of ESAs in terms of the quality factor Q were established by Chu [25] and re-examined by McLean [26]. This derivation is valid for an antenna in free space [27], [28]. To use it for an antenna radiating into lossy media of a fixed size [29], two assumptions have to be made. First, the currents induced in lossy tissues reradiate negligible energy. Second, assuming the antenna can be modeled by the Thevenin's equivalent circuit [30, p. 78], the loss resistance R_L accounts for the power dissipation in tissue. In this way, the lower bound on Q_{LB} is inversely proportional to the antenna electrical size ka as [31]

$$Q_{\mathrm{LB}} \approx \eta \left(\frac{1}{(ka)^3} + \frac{1}{ka} \right) \tag{3.8}$$

where η is the radiation efficiency of the antenna.

The fundamental lower bound of the quality factor Q is inversely proportional to the upper bound of the antenna bandwidth. Yaghjian and Best [32] expressed the antenna Q as a function of the bandwidth (BW) at a given voltage standing wave ratio (VSWR) level as

$$Q = \frac{\mathrm{VSWR} - 1}{\sqrt{\mathrm{VSWR}}} \frac{f_0}{\mathrm{BW}} \tag{3.9}$$

where f_0 if the central frequency.

Combing (3.8) and (3.9) gives the physical limitation of achievable (upper bound) radiation efficiency η_{ub} for a given bandwidth

$$\eta_{\mathrm{ub}} \approx \frac{\mathrm{VSWR} - 1}{\sqrt{\mathrm{VSWR}}} \frac{f_0}{\mathrm{BW}} \frac{[k(\varepsilon)\, a]^3}{[k(\varepsilon)\, a]^2 + 1} \tag{3.10}$$

Eq. (3.10) implies that the radiation efficiency must be sacrificed in order to achieve the bandwidth over the ESA limits. Figure 3.1(d) illustrates the highest achievable radiation efficiencies η_{ub} (3.10) for 1, 10, 50 and 100 percent fractional bandwidths FBW $= f_0/\mathrm{BW}$ for VSWR $= 2$ (FBW_2) assuming $a = 5$ mm (average radius for an in-body antenna) and the permittivity $\varepsilon'(\omega)$ as for the muscle. The physical limitations on achievable radiation efficiency for a given fractional bandwidth favor using higher operation frequencies to maximize the $\eta_{\mathrm{ub}}/\mathrm{FBW}_2$ ratio.

3.3 Problem Formulation

The aforementioned mechanisms define the radiation efficiency of a body-implanted device and thus its range of optimal operating frequencies. It requires a full-wave solution of Eq. (3.1) to accurately analyze the EM energy transfer from a source located in the dispersive heterogeneous media into surrounding free space. Assuming $\mathbf{E}(x, y, z) = \mathbf{E}(x, y)e^{ik_z z}$ where k_z is the out-of-plane wavenumber, the spatial dimensionality of the problem is reduced.

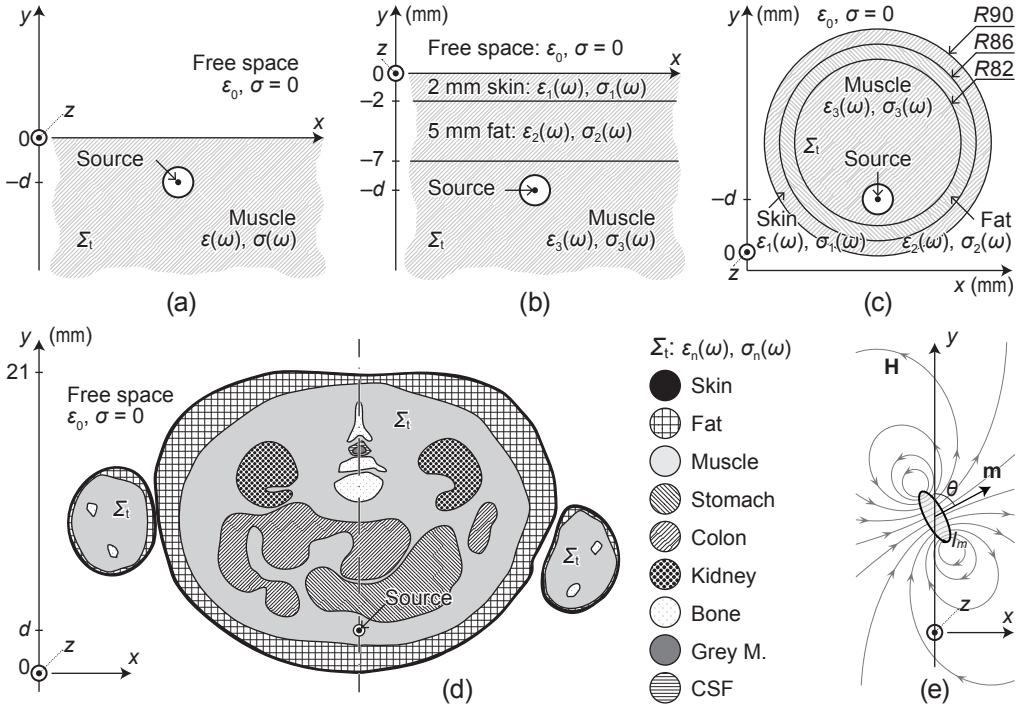

Fig. 3.3: Two-dimensional (2D) model formulations used in the study (source regions not to scale, z-axis is out of plane). EM properties are according to Eq. (2.2). (a) A planar interface between two semi-infinite homogeneous half-spaces. Σ_t ($d < 0$) with muscle-equivalent EM properties. (b) A planar stratified heterogeneous model as proposed by Poon *et al.* [12]. Σ_t ($d < 0$) contains muscle, fat, and skin layers. (c) Circular heterogeneous model (not to scale) similar to the one used in [33], [36]. Σ_t ($R < 90$) contains muscle, fat, and skin layers. (d) Realistic model of a human abdominal region (nine tissues). (e) Magnetic dipole of a moment $\mathbf{m}$.

We formulate the problem geometry increasing its complexity from a simple to anatomically realistic one (Figure 3.3). First, we consider a planar homogeneous medium consisting of two infinite half-spaces that represent a free space domain and lossy dispersive tissue domain Σ_t [Figure 3.3(a)]. Then, we study a planar layered medium by adding 2 mm skin and 5 mm fat layers to the Σ_t [as proposed in [12], Figure 3.3(b)]. Next, we model human body as a heterogeneous circular stratified domain Σ_t with the dimensions used in [33] [Figure 3.3(c)]. Finally, we analyze the heterogeneous realistic model of a human abdominal region [Figure 3.3(d)].

We consider magnetic sources as they give better efficiency in lossy dielectrics due to non-magnetic properties of biological tissue ($\mu \approx \mu_0$) [12], [15], [34]–[36]. Two source formulations have been studied: 1) a magnetic dipole of a moment $\mathbf{m}$ oriented at angles $\theta = 0°, 45°, 60°$, and $90°$ [Figure 3.3(e)] that excite TM_z mode of the first angular order (by convention, the dipole moment $\mathbf{m}$ aligns with the the y-axis at $0°$ and x-axis at $90°$); 2) out-of-plane magnetic current I_m that excite TE_z mode of zeroth angular order. In this way, both azimuthal and elevation modes of a dipole-like radiation pattern are considered as well diationas the arbitrary polarization (TE_z mode) and pure p-polarization (TM_z mode) of the $\mathbf{E}$-field incident on the media interfaces.

The elementary source is centered within a lossless ($\sigma = 0$ S·m^{-1}) ⌀4 mm area bounded by a closed contour C_S on which the supplied specific power P_s (W·m^{-1})

can be evaluated independently of the source formulation as

$$P_s = \oint_{C_S} \left(\frac{1}{2} \mathbf{E} \times \mathbf{H}^* \right) \cdot \mathrm{d}\mathbf{s}. \tag{3.11}$$

The exiting specific power P_e ($\mathrm{W \cdot m^{-1}}$) is evaluated on the contour C_{FF} located at the distance from the source satisfying the far-field criterion [37] as

$$P_e = \int_{C_{\mathrm{FF}}} \left(\frac{1}{2} \mathbf{E} \times \mathbf{H}^* \right) \cdot \mathrm{d}\mathbf{s}. \tag{3.12}$$

To verify the conservation-of-energy condition (3.2), the dissipated specific power P_d ($\mathrm{W \cdot m^{-1}}$) is evaluated over all lossy domains Σ_{t} as

$$P_d = \frac{1}{2} \iint_{\Sigma_{\mathrm{t}}} \sigma \left(\mathbf{r}, \omega \right) |\mathbf{E}|^2 \mathrm{d}x \, \mathrm{d}y. \tag{3.13}$$

The radiation efficiency of an ideal source (assuming limitation (3.10)

$$\eta_{\mathrm{idl}} \left(\omega \right) \equiv \frac{P_e}{P_s}. \tag{3.14}$$

Taking into account the maximum radiation efficiency limitations (3.10) of an ESA for a given BW and assuming the dissipation in tissues as an equivalent loss resistance of the antenna R_L (see Section 3.2.3), the (3.14) becomes

$$\eta_{\mathrm{rad}} \left(\omega \right) \equiv \min \left[\eta_{\mathrm{idl}}, \eta_{\mathrm{ub}} \right]. \tag{3.15}$$

For a realistic antenna, the total efficiency estimate includes also the reflection (mismatch) loss of the antenna as $\eta_{\mathrm{tot}} = \eta_{\mathrm{rad}} \left(1 - |\Gamma|^2 \right)$, where Γ is the reflection coefficient at the input terminals of the antenna. In this study, we consider perfectly matched sources ($\Gamma = 0$).

To enable comparative analysis of **E**-field distributions for given f, d, and source formulations, I normalize $\|\mathbf{E}\|$ by the supplied power P_s (3.11) and the intrinsic impedance of the media Z (3.6) surrounding the source as $\log_{10} \left(\|\mathbf{E}\| / \sqrt{Z P_s} \right)$.

3.3.1 Numerical Model

The formulated problem requires a numerical solution of the second-order linear partial differential equation (3.1). We use the *hp*-FEM method implemented into the in-house code Agros2D [38] as it gives more accurate representation of curved interfaces for the same mesh density compared, for instance, to FDTD. The automatic *hp*-adaptivity was set up to maintain the relative error $\Delta C / C \leqslant 1\%$. The description of the adaptivity algorithm is given in Appendix A. Curvilinear elements were used to accurately represent the circular geometry of the model boundaries (Figure B.1).

The results obtained for each geometry are validated using the FEM solver of COMSOL Multiphysics® 5.2 [39]. For the planar homogeneous half-space medium, we additionally verify the results using the FDTD method implemented in Meep [40]. The results agree within the $\delta \eta_{\mathrm{idl}} < 1\%$ tolerance for each studied frequency and depth.

The frequency range spans from 10^7 Hz to 10^{10} Hz and is discretized into 16 $\log_{10}$-spaced intervals. For the planar homogeneous and layered heterogeneous models, a circular perfectly matched layer (PML) truncates the study domain at the distance $2\lambda(\varepsilon_0)$ from the source to ensure that negligibly small power reaches the tissue–PML boundary. For the circular and realistic abdominal models, the distance to the PML is λ from the models. The exiting power P_e (3.12) is evaluated on the inner boundary of the PML. The Dirichlet boundary condition $\eta \times \mathbf{E} = 0$ (perfect electric conductor) is imposed the outside of the PML. The initial mesh contains first order elements with the maximum length $\lambda(\varepsilon)/4$ for each analyzed frequency. The automatic *hp*-adaptivity algorithm selectively refines specific elements and operates up to ninth polynomial order. The accuracy is set to maintain the total energy relative error below 0.5%.

Conservation of Energy

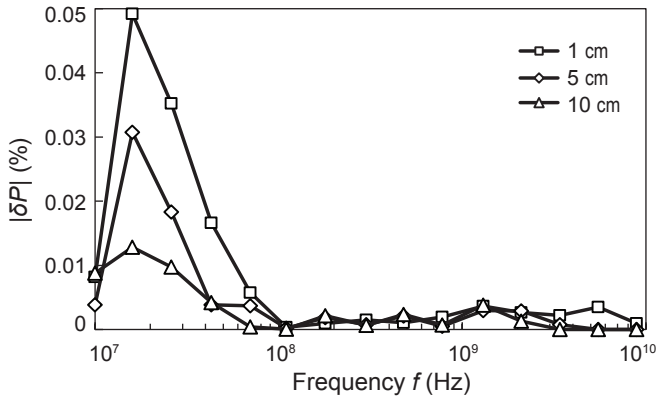

Fig. 3.4: Absolute value of the relative residual power error for infinite planar-bounded half-space homogeneous medium.

Conservation of energy (power balance) is one of the necessary conditions of the model validity. To verify this condition, we calculated the relative residual power error as $\delta P = (P_s - P_e - P_d)/P_s$ for every solution given here. According to the numerical model formulation, we consider the model valid when $\delta P < 0.5\%\ \forall \eta_{\text{idl}}(f, d)$. The planar model formulations give the highest error due to the PML-truncation of the half-space representing tissue. Figure 3.4 shows the relative residual power errors δP for the planar homogeneous medium. The maximum error $\max|\delta P| \ll 0.5\%$ at $d = 1$ cm, $f = 1.6 \times 10^7$ Hz.

3.4 Results and Discussion

3.4.1 Infinite Medium: Planar-Bounded Homogeneous Half-Space

We start with an arbitrary oriented magnetic dipole in the infinite homogeneous planar-bounded half-space with muscle-equivalent EM properties [Figure 3.1(a)]. Figure 3.5(a) shows the efficiencies η_{idl} for four dipole moment $\mathbf{m}$ orientations ($\theta = 0°, 45°, 60°$, and $90°$) at $d = 1$ cm. The efficiency strongly depends on θ and peaks about 2 GHz for all orientations. The extremely low efficiency at $\theta = 0°$ is

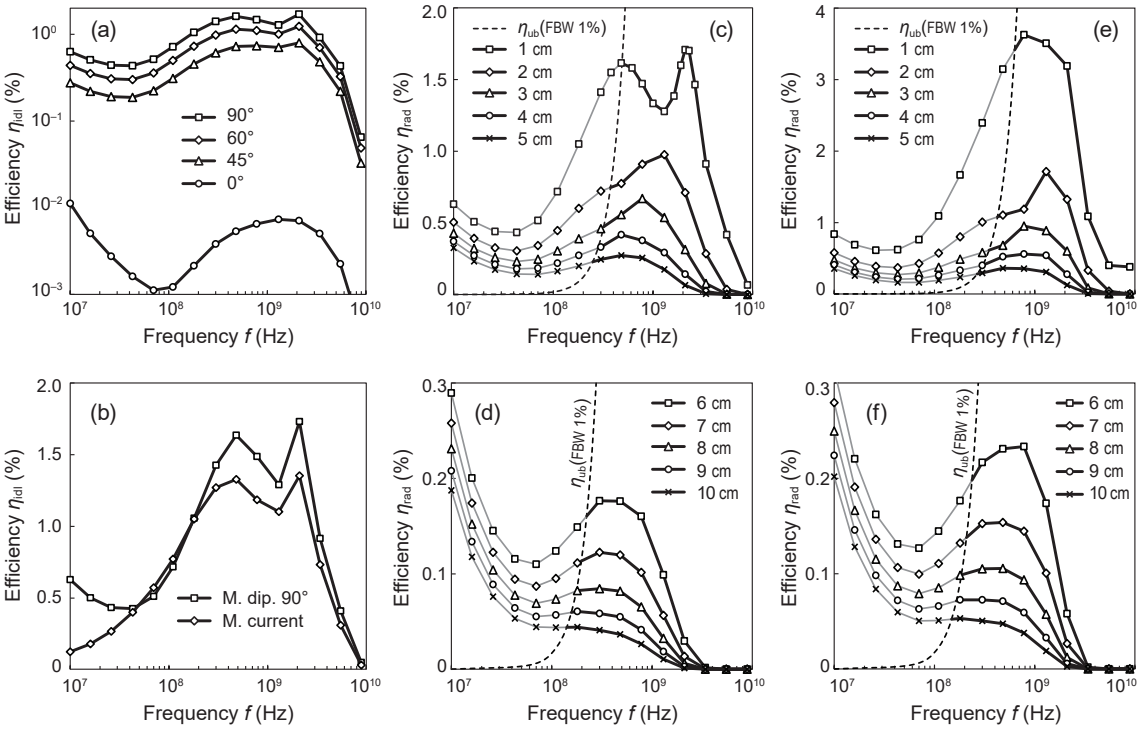

Fig. 3.5: Radiation efficiencies $\eta_{\text{rad}}(\omega) \equiv \min[\eta_{\text{idl}}, \eta_{\text{ub}}]$ in infinite planar-bounded media. (a) Orientation of magnetic dipole moment $\mathbf{m}$ strongly affects the efficiency (homogeneous half-space). (b) The 90° oriented magnetic dipole moment $\mathbf{m}$ (TM_z mode) compared to the out-of-plane magnetic current source (TE_z mode) at $d = 1$ cm implantation depth in homogeneous half-space medium. (c) The homogeneous half-space medium at $d = 1$ to 5 cm and (d) at $d = 6$ to 10 cm implantation depths. (e) The layered (skin–fat–muscle) half-space medium at $d = 1$ to 5 cm and (f) at $d = 6$ to 10 cm implantation depths.

due to the both radiation lobes of the dipole pointing towards the direction parallel to the infinite planar interface. The optimal frequency is invariant to the orientation of magnetic dipole moment $\mathbf{m}$. Therefore, for further studies we proceed with the $\theta = 90°$ alignment that gives the highest efficiency η_{idl} and thus minimizes the computational error. For the magnetic current source, the reduced overall efficiency is due to higher radiation isotropy [Figure 3.6(a)] compared to the one of the magnetic dipole source [Figure 3.6(b)]. The rising efficiency at the bottom part of the spectrum for the magnetic dipole [Figure 3.5(b)] is due to the full p-polarization of the TM_z mode with respect to the interface between two model half-spaces. The optimal frequency, however, stays invariant to the source formulation [Figure 3.5(b)].

The analysis in the infinite planar-bounded homogeneous half-space medium [Figure 3.5(c) and 3.5(d)] reveals that the optimal frequency range is inversely proportional to the depth of the source and follows the power law (Figure 3.7). At 1 cm depth [$\eta_{\text{idl}}(f)$ on Figure 3.5(c)], the radiation efficiency peaks at 480 MHz and 2.1 GHz but drops in-between at 1.3 GHz. At the global maximum [2.1 GHz, Figure 3.6(a) and 3.6(b)]), the destructive interference acts close to the Σ_{t} interface reducing the area of dissipated power independently of the source formulation. On the other hand, at the local minimum [1.3 GHz, Figure 3.6(c)], one can notice the enlarged back lobe [compared to the local maximum at 480 MHz, Figure 3.6(d)] as well as increased power absorption around zeros of the dipole radiation pattern

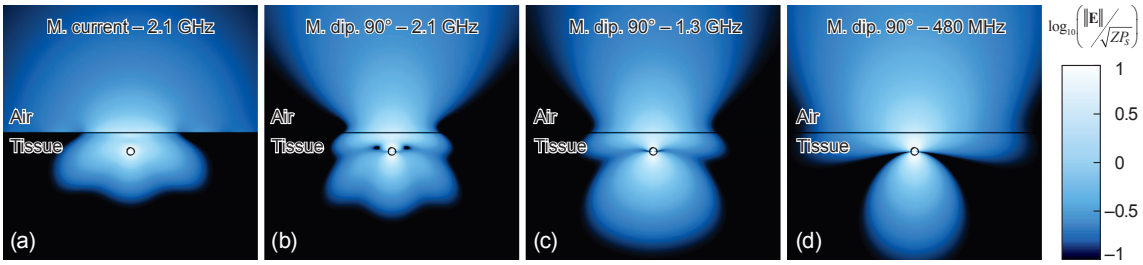

Fig. 3.6: Normalized **E**-field distributions at 1 cm depth in infinite planar-bounded homogeneous half-space medium [muscle-equivalent EM properties according to Eq. (2.2)] for (a) the magnetic current source (TE_z mode) and (b)–(c)–(d) the 90° oriented magnetic dipole (TM_z mode). The radiation efficiency peaks at 2.1 GHz (a)–(b) and 480 MHz (d) for both sources and drops at 1.3 GHz (c) due to constructive resonance in tissue that increases power absorption.

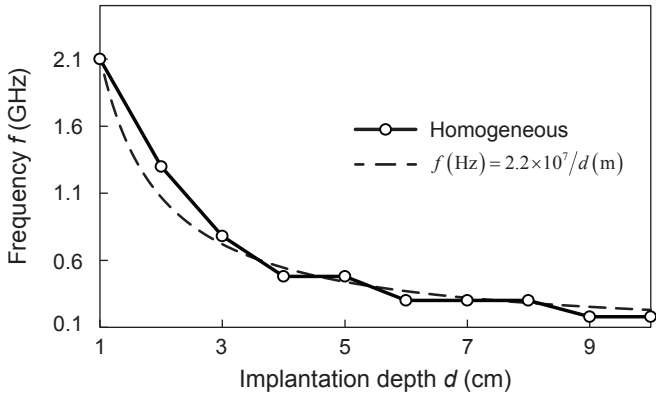

Fig. 3.7: The optimal frequency in the infinite planar-bounded homogeneous half-space medium [dispersive EM properties of muscle according to Eq. (2.2)] follows the power law.

(collinear with the the moment **m**). As the position of local minimum is invariant to the source formulation and the orientation of **m** (except for $\theta = 0°$ where the source does not radiate in the direction of the interface), the effect is due to the f/d relation and consequently to the interference with the standing surface wave appearing at the Σ_t interface. Christ *et al.* [41] reported a similar effect: reflections at the fat–muscle interface gave rise to a standing wave in subcutaneous fat increasing the specific absorption rate (SAR) by more than 3 dB.

For a deep (6–10 cm) implantation of the magnetic dipole [Figure 3.5(d)], the attenuation losses at higher frequencies overtake, the reflection losses diminish (due to the p-polarization of the TM_z mode), and the peak efficiency of ideal source η_idl (15) lies below 10 MHz. However, these efficiencies are unattainable for a reasonable bandwidth of a real source (e.g. $\mathrm{FBW}_2 > 1\%$). The practically achievable radiation efficiency η_rad (3.15) locates below $f < 1$ GHz range for deep implantations (Figure 3.7).

For the energy transfer from the infinite planar-bounded homogeneous half-space with muscle equivalent EM properties to surrounding free space, the maxima of radiation efficiency shifts from about 2 GHz for $d = 1$ cm down to below 200 MHz for $d = 10$ cm [Figure 3.7]. This frequency range is about two times lower than the one derived by Poon *et al.* [12] for the wireless power transfer in mid-field from an

on-body source region to an implant.

3.4.2 Infinite Medium: Planar-Bounded Layered Half-Space

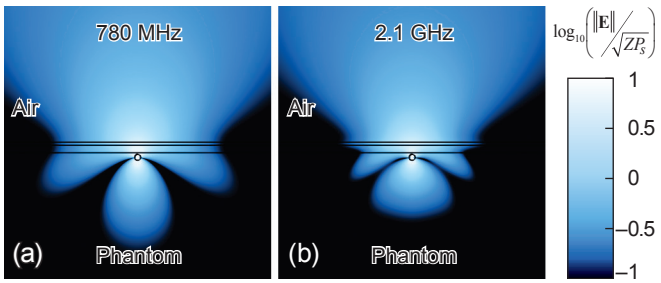

Fig. 3.8: Normalized **E**-field distributions at 1 cm depth in the infinite planar-bounded layered half-space medium. The 90° oriented magnetic dipole moment **m** (TM_z mode) at (a) 780 MHz (maximum efficiency) and (b) 2.1 GHz.

In this section, we study the effect of skin and subcutaneous fat layer on the optimal frequency. Figure 3.5(e) and 3.5(f) show the evolution of the efficiency peak for 1–10 cm implantation depths. Fat acts as a low loss matching layer, increasing the overall efficiency compared to the homogeneous half-space medium [Figure 3.5(c) and 3.5(d)] by up to a factor of two. At 1 cm, the peak around 2 GHz disappears shifting the optimal frequency down to below 1 GHz. Figure 3.8(a) shows the normalized **E**-field distribution at the global maximum of η_{rad} at 780 MHz. The destructive interference with the surface wave reduces the width of the dipole back lobe thus minimizing the power absorption at this frequency. On the other hand, at 2.1 GHz [Figure 3.8(b)] the back lobe is significantly wider. Albeit the destructive interference reduces the front lobe **E**-field in the fat layer (which is practically lossless), one can notice the higher intensity in the lossy skin (the uppermost) layer of the half-space Σ_{t}. The wide back lobe and the amplified intensity in the skin layer together contribute to the increased power dissipation at 2.1 GHz—the global optimum for the homogeneous half-space medium.

A sharp η_{idl} peak appears at about 1.3 GHz for 2 cm depth [Figure 3.5(e)] that increases the optimal frequency with the depth compared to $d = 1$ cm. Again, at this depth the observed resonance behavior plays a significant role, and for the shallow implantation ($d \leq 2$ cm) the optimal frequency does not follow the power law on Figure 3.7. However, the $f = 2.2 \times 10^7/d$ approximation is still valid for deeper implantation ($d = 2$ cm to 10 cm).

3.4.3 Cylindrical Stratified Phantom

Next, we model a human body as an infinitely-long three-tissue stratified cylinder (Figure 3.3c) with the same radii as for the spherical phantom used by Merli *et al.* [33] and Chrissoulidis and Laheurte [36]. Considering the magnetic dipole source (TM_z mode) at $d = 1$–4 cm [Figure 3.9(a)], the efficiency η_{idl} is about five times higher than the one for planar media due to the finite lossy domain Σ_{t}. The efficiency η_{idl} remains on its peak from 20 to 500 MHz for $d = 1$–3 cm. On the other hand, the magnetic current source [Figure 3.9(a)] gives the results similar to the magnetic dipole in the planar layered medium [cf. Figure 3.5(e)] with a clear peak near

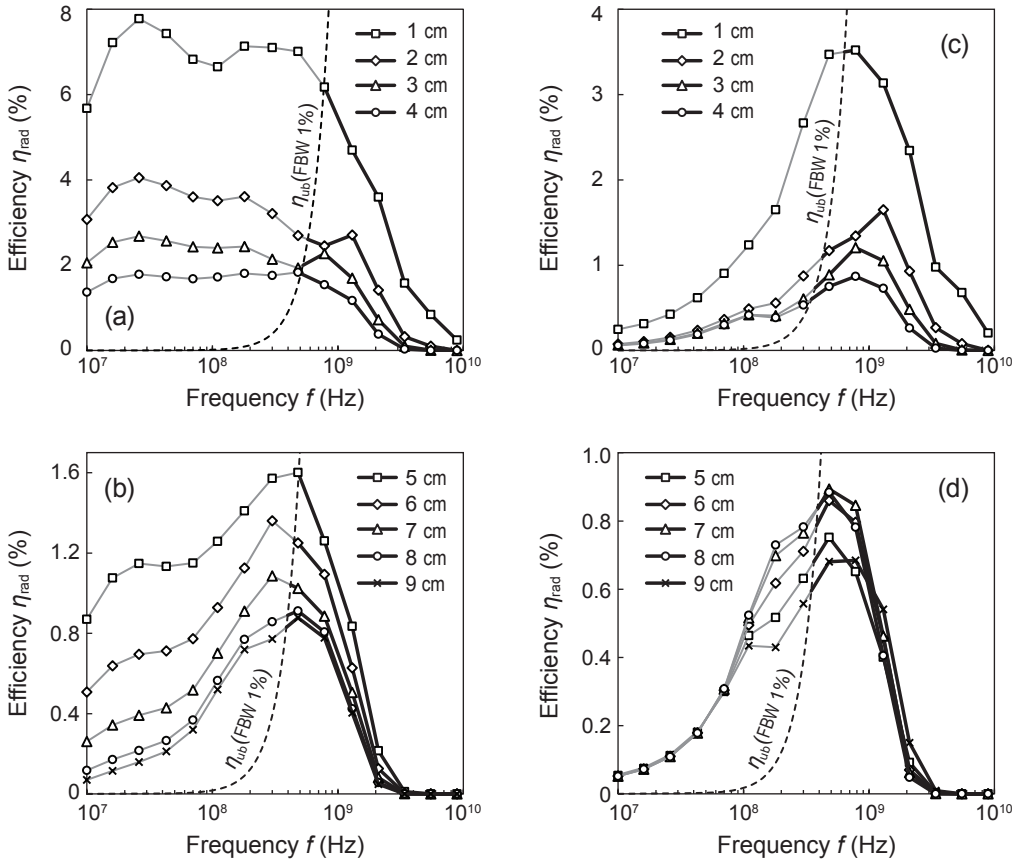

Fig. 3.9: Radiation efficiencies η_{rad} for the $R90$ mm cylindrical stratified phantom similar to the one used by Merli *et al.* [33] and Chrissoulidis and Laheurte [36] (4 mm skin-equivalent outer layer, 4 mm fat-equivalent intermediate layer, and $R82$ muscle-equivalent domain containing the source). Tissue EM properties of the layers are according to Eq. (2.2). (a) The 90° oriented magnetic dipole moment $\mathbf{m}$ (TM_z mode) source at $d = 1$ to 4 cm and (b) $d = 5$ to 9 cm implantation depths. (c) The out-of-plane magnetic current source (TE_z mode) at $d = 1$ to 4 cm and (d) $d = 5$ to 9 cm implantation depths. At $d = 9$ cm, the source is in the middle of the phantom.

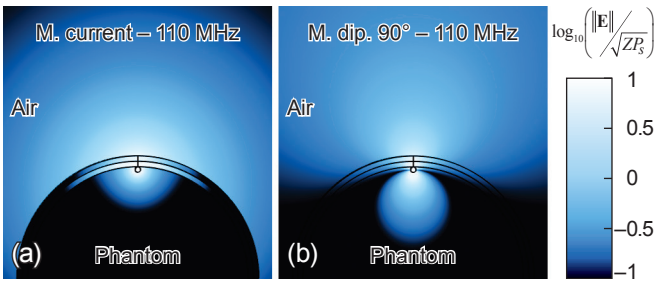

Fig. 3.10: Normalized **E**-field distributions at 110 MHz and 1 cm depth in the cylindrical stratified phantom. (a) The magnetic current source (TE_z mode). (b) The 90° oriented magnetic dipole moment $\mathbf{m}$ (TM_z mode).

1 GHz. For deeper implantations (d = 5–9 cm), the efficiency peaks roughly at about 0.5 GHz for both sources [Figure 3.9(b) and 3.9(d)].

Two sources behave differently for the shallow implantation as the reflection losses depend on the **E**-field polarization. The TE_z mode of the magnetic current source gives the arbitrary polarization of the **E**-field incident on the cylindrical

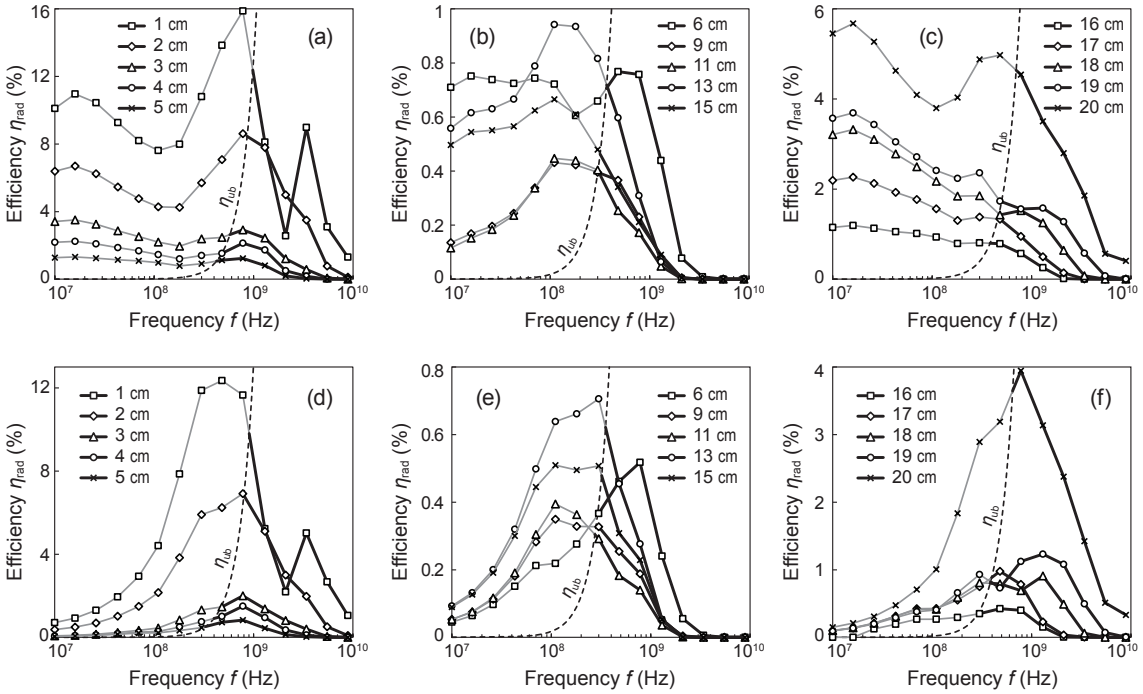

Fig. 3.11: Radiation efficiencies η_{rad} in the anatomical phantom at $d = 1$ to 20 cm implantation depths. (a)–(c) The 90° oriented magnetic dipole moment $\mathbf{m}$ (TM_z mode). (d)–(f) The out-of-plane magnetic current source (TE_z mode).

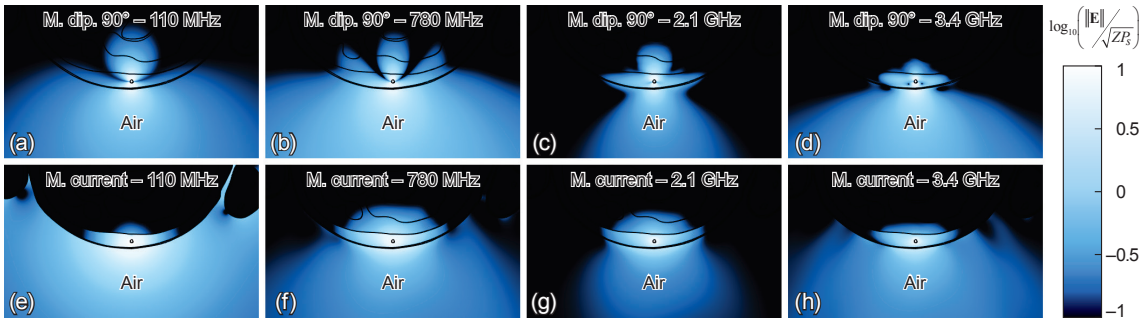

Fig. 3.12: Normalized **E**-field distributions of a source at 1 cm depth (subcutaneous) in anatomical phantom. (a)–(d) The 90° oriented magnetic dipole moment $\mathbf{m}$ (TM_z mode). (e)–(h) The magnetic current source (TE_z mode).

phantom boundary. On the other hand, the magnetic dipole excites TM_z mode. Hence, the **E**-field is p-polarized for all boundaries of the phantom. This results in lower reflection losses for all incidence angles and up to the full transmission at the Brewster's angle. The difference between the boundary fields excited by two sources is visible on the surface plots shown on Figure 3.10(a) and 3.10(b). The same, less pronounced, effect exists for the planar media at lower frequencies [Figure 3.5(b)] where the reflection losses are dominant. For the deeper implantation, the attenuation losses take over, and both sources give the similar optimal frequency range [Figure 3.9(b) and 3.9(d)].

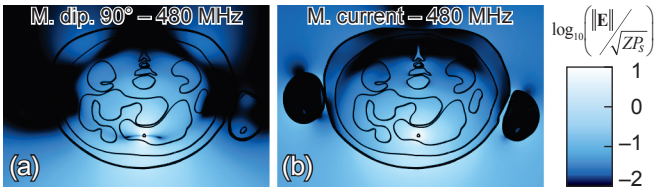

Fig. 3.13: Normalized **E**-field distributions of a source at 6 cm depth (stomach) in anatomical torso phantom at 480 MHz. (a) The 90° oriented magnetic dipole moment **m** (TM_z mode). (b) The magnetic current source (TE_z mode).

3.4.4 Anatomical Torso Phantom

Finally, with the understanding built on how the reflection and attenuation losses depend on the source formulation and affect propagation in the canonical models, we proceed to studies in the anatomical (abdominal) phantom [Figure 3.3(d)]. The implantation depth varies along the y-axis from 1 cm to 20 cm. At 20 cm, the source is again about 1 cm far from the skin–air interface.

Figure 3.11 shows the radiation efficiencies for both source formulations. The optimal frequency range for deep implantation ($d \gtrsim 2$ cm) is congruent with the canonical models (Figure 3.7). The same effect reveals at $f < 10^8$ Hz range, as for the cylindrical stratified phantom, of the increased efficiency of TM_z mode compared to TE_z. The **E**-field distributions for both sources at 10^8 Hz are given in Figure 3.12(a) and 3.12(e). For the magnetic current source, the **E**-field is contained in fat layer. Within the optimal frequency range, TM_z mode gives about 20% higher efficiency than TE_z mode for all implantation depths due both to higher directivity and lower reflection losses.

At 1 cm depth, the efficiency drop manifests at about 2.1 GHz in the optimal range independently of the excitation mode as for the planar homogeneous model [Figure 3.11(a) and 3.11(d), **E**-field distributions on Figure 3.12(c) and 3.12(g)]. The global efficiency maximum appears around 800 MHz [Figure 3.12(b) and (f)] and a local one at 3.4 GHz [Figure 3.12(d) and 3.12(h)]. The local minimum is at 2.1 GHz. The efficiency η_{idl} at 800 MHz exceeds the one at 2.1 GHz by about 6.5 times. As for the planar homogeneous model, the drop of the efficiency is due to the constructive interference with the standing surface wave that increases power absorption in tissue.

For the deep-body implantation [more than 2 cm from skin, Figure 3.11(b) and 3.11(e)], the radiation efficiency optimum spreads within 10^8–10^9 Hz range. Figure 3.13 shows the **E**-field distribution for magnetic dipole and current sources at 6 cm depth. The maximum **E**-field outside the phantom localizes where the attenuation path is shorter and contains less interfaces between tissues. The polarization visibly affects **E**-field distribution even though the peak achievable efficiency localizes within the same range for both sources.

3.5 Summary

The radiative far- or mid-field EM energy transfer from an in-body device to the surrounding free space (where a receiver is located) gives substantially better efficiency than near-field coupling in 10^6–10^7 Hz range. For an ideal source, the radiation efficiency increases with frequency until reaching its maximum. The frequencies around

this maximum are hence optimal; they are inversely proportional to the implantation depth of the source. Maximizing the efficiency for a given depth is negotiating between the attenuation due to dielectric losses and the reflection (mismatch) losses caused by high contrast between media. The optimal frequency of operation for deep implantation (for instance, ingestible; $d \gtrsim 3$) lies in 10^8–10^9 Hz range for all four model formulations and can be conveniently approximated as $f = 2.2 \times 10^7/d$. MedRadio 401 MHz and mid-ISM 434 MHz frequency bands belong to this range.

For subcutaneous applications ($d \lesssim 3$ cm), the interference effects induced by a standing surface wave play an important role. Within the optimal frequency range, the local max/min efficiency ratio reaches 6.5 times [Figure 3.11(a)] for the realistic case (torso phantom). The exact location of local minima and maxima depends on the implantation depth d as well as on skin and subcutaneous fat layers thickness. It is, however, invariant on the source formulation and thus on the polarization. Therefore, for a given subcutaneous device it is important to consider that the optimal frequency depends strongly on a subject and an implantation site. Adaptive frequency hopping within the optimal range may be used to maximize the efficiency for subcutaneous applications.

The magnetic dipole (intrinsic directivity $D = 1.5$) gives about 20% better efficiency than the isotropic magnetic current source ($D = 1$) for all implantation depths. Lower power dissipation in tissue may be achieved either by increasing the intrinsic antenna directivity to minimize the back lobe radiating inside the body (for the fixed position implants) or by beam steering (for the implants with undefined positions, e.g. ingestible). Both are applicable only to non-electrically-small antennas.

Full p-polarization of TM_z mode reduces the effect of reflection losses at the sub-10^8 Hz part of the spectrum. Hence, the radiation efficiency increases compared to TE_z mode. However, such efficiency is unrealizable in this frequency range as it implies the source must operate with inapplicably narrow bandwidth [Figure 3.1(d)]. Minimum realistic bandwidth $\mathrm{FBW}_2 = 1\%$ imposes the limitations on achievable efficiency within the lower part of the optimal frequency range (Figure 3.11). Yet, the estimate of achievable efficiency for a given bandwidth using (3.10) gives a conservative value due to the assumptions made (see Section 3.2.3). The real-world values would be less strict due to re-radiation of energy by currents induced in tissue. These "fringing" currents increase the electrical size of the antenna and therefore raise the physical limitations of achievable (upper bound) radiation efficiency η_{ub} for a given bandwidth (3.10).

These results establish the optimal frequency range and achievable radiation efficiencies for the far-field energy transfer from magnetic sources inside lossy tissues to surrounding free space. A cautionary remark: even though theoretically possible, a purely magnetic antenna has not been proposed yet. The near field **E**-component of a real-world antenna will unavoidably couple to the tissue leading to the increased power dissipation close to the implant. A high permittivity and low loss superstrate partially lessens this effect.

In this study, the established optimal frequency ranges relay on 2D problem formulations. Going beyond this approximation brings us up against more conditions to consider. Namely: 1) standing surface-wave interference behavior is more complex affecting the local minima and maxima of the radiation efficiency for shallow sources ($d \lesssim 3$ cm); 2) impure p-polarization of the TM_z mode incident on the

air–body interface; and 3) depending on application, slightly reduced attenuation losses due to finite z-dimensionality. These additional conditions do not influence the main findings of this study in terms of optimal frequency range. Nevertheless, they provide the opening point for further investigations on maximum achievable radiation efficiency.

With proper design of the in-body antennas—considering the depth of implantation, frequency of operation, radiation modes, polarization, and directivity—more than an order of magnitude improvement of radiation efficiency is feasible compared to existing autonomous body-implanted devices.

Bibliography

[1] A. Kiourti and K. S. Nikita, "A review of in-body biotelemetry devices: Implantables, ingestibles, and injectables," *IEEE Transactions on Biomedical Engineering*, vol. 64, no. 7, pp. 1422–1430, 2017.

[2] J. S. Ho, Y. Tanabe, S. M. Iyer, A. J. Christensen, L. Grosenick, K. Deisseroth, S. L. Delp, and A. S. Y. Poon, "Self-tracking energy transfer for neural stimulation in untethered mice," *Physical Review Applied*, vol. 4, no. 2, p. 024 001, 2015.

[3] T. Kim, J. G. McCall, Y. H. Jung, X. Huang, E. R. Siuda, Y. Li, J. Song, Y. M. Song, H. A. Pao, R.-H. Kim, C. Lu, S. D. Lee, I.-S. Song, G. Shin, R. Al-Hasani, S. Kim, M. P. Tan, Y. Huang, F. G. Omenetto, J. A. Rogers, and M. R. Bruchas, "Injectable, cellular-scale optoelectronics with applications for wireless optogenetics," *Science*, vol. 340, no. 6129, pp. 211–216, 2013.

[4] S. Kim, J. S. Ho, and A. S. Y. Poon, "Midfield wireless powering of subwavelength autonomous devices," *Physical Review Letters*, vol. 110, no. 20, p. 203 905, 2013.

[5] S. Kim, J. S. Ho, L. Y. Chen, and A. S. Y. Poon, "Wireless power transfer to a cardiac implant," *Applied Physics Letters*, vol. 101, no. 7, p. 073 701, 2012.

[6] D. R. Agrawal, Y. Tanabe, D. Weng, A. Ma, S. Hsu, S.-Y. Liao, Z. Zhen, Z.-Y. Zhu, C. Sun, Z. Dong, F. Yang, H. F. Tse, A. S. Y. Poon, and J. S. Ho, "Conformal phased surfaces for wireless powering of bioelectronic microdevices," *Nat. Biomed. Eng.*, vol. 1, p. 0043, 2017.

[7] J. S. Ho, A. J. Yeh, E. Neofytou, S. Kim, Y. Tanabe, B. Patlolla, R. E. Beygui, and A. S. Y. Poon, "Wireless power transfer to deep-tissue microimplants," *PNAS*, vol. 111, pp. 7974–7979, 2014.

[8] E. Chow, M. Morris, and P. Irazoqui, "Implantable RF medical devices: The benefits of high-speed communication and much greater communication distances in biomedical applications," *IEEE Microwave Magazine*, vol. 14, no. 4, pp. 64–73, Jun. 2013.

[9] A. K. Skrivervik, M. Bosiljevac, and Z. Sipus, "Propagation considerations for implantable antennas," in *11th European Conference on Antennas and Propagation (EuCAP 2017)*, Paris, France, Mar. 2017.

[10] L. Chirwa, P. Hammond, S. Roy, and D. Cumming, "Radiation from ingested wireless devices in biomedical telemetry bands," *Electronics Letters*, vol. 39, no. 2, pp. 178–179, Jan. 2003.

[11] L. Chirwa, P. Hammond, S. Roy, and D. Cumming, "Electromagnetic radiation from ingested sources in the human intestine between 150 MHz and 1.2 GHz," *IEEE Transactions on Biomedical Engineering*, vol. 50, no. 4, pp. 484–492, Apr. 2003.

[12] A. S. Y. Poon, S. O'Driscoll, and T. H. Meng, "Optimal frequency for wireless power transmission into dispersive tissue," *IEEE Transactions on Antennas and Propagation*, vol. 58, no. 5, pp. 1739–1750, 2010.

[13] L. Xu, M.-H. Meng, H. Ren, and Y. Chan, "Radiation characteristics of ingestible wireless devices in human intestine following radio frequency exposure at 430, 800, 1200, and 2400 MHz," *IEEE Transactions on Antennas and Propagation*, vol. 57, no. 8, pp. 2418–2428, Aug. 2009.

[14] L. Xu, M.-H. Meng, and C. Hu, "Effects of dielectric values of human body on specific absorption rate following 430, 800, and 1200 MHz RF exposure to ingestible wireless device," *IEEE Transactions on Information Technology in Biomedicine*, vol. 14, no. 1, pp. 52–59, Jan. 2010.

[15] F. Merli, L. Bolomey, J. Zurcher, G. Corradini, E. Meurville, and A. Skrivervik, "Design, realization and measurements of a miniature antenna for implantable wireless communication systems," *IEEE Transactions on Antennas and Propagation*, vol. 59, no. 10, pp. 3544–3555, Oct. 2011.

[16] S. Gabriel, R. W. Lau, and C. Gabriel, "The dielectric properties of biological tissues: II. Measurements in the frequency range 10 Hz to 20 GHz," *Physics in Medicine and Biology*, vol. 41, pp. 2251–2269, Nov. 1996.

[17] J. Volakis, C.-C. Chen, and K. Fujimoto, *Small Antennas: Miniaturization Techniques & Applications*. McGraw Hill Professional, Jun. 2010.

[18] D. Sinha and G. A. J. Amaratunga, "Electromagnetic radiation under explicit symmetry breaking," *Physical Review Letters*, vol. 114, no. 14, p. 147 701, 2015.

[19] A. Hirata, S. Kodera, J. Wang, and O. Fujiwara, "Dominant factors influencing whole-body average SAR due to far-field exposure in whole-body resonance frequency and GHz regions," *Bioelectromagnetics*, vol. 28, no. 6, pp. 484–487, 2007.

[20] A. Shapiro, R. Lutomirski, and H. Yura, "Induced fields and heating within a cranial structure irradiated by an electromagnetic plane wave," *IEEE Transactions on Microwave Theory and Techniques*, vol. 16, no. 2, pp. 187–196, 1968.

[21] H. N. Kritikos and H. P. Schwan, "Formation of hot spots in multilayer spheres," *IEEE Transactions on Biomedical Engineering*, vol. BME-23, pp. 168–172, 1976, 2.

[22] C. A. Balanis, *Advanced engineering electromagnetics*, 2nd ed. Hoboken, NJ: John Wiley & Sons, 2012.

[23] F. S. Barnes and B. Greenebaum, *Handbook of biological effects of electromagnetic fields. Bioengineering and biophysical aspects of electromagnetic fields*, 3rd ed. Boca Raton: CRC/Taylor & Francis, 2007.

[24] H. Wheeler, "Fundamental limitations of small antennas," *Proc. IRE*, vol. 35, no. 12, pp. 1479–1484, 1947.

[25] L. J. Chu, "Physical limitations of omni-directional antennas," *Journal of Applied Physics*, vol. 19, no. 12, pp. 1163–1175, 1948.

[26] J. S. McLean, "A re-examination of the fundamental limits on the radiation Q of electrically small antennas," *IEEE Transactions on Antennas and Propagation*, vol. 44, no. 5, pp. 672–676, 1996.

[27] F. Merli and A. Skrivervik, "Design and measurement considerations for implantable antennas for telemetry applications," in *4th European Conference on Antennas and Propagation (EuCAP 2010)*, Barcelona, Spain, Apr. 2010, pp. 1–5.

[28] A. K. Skrivervik and F. Merli, "Design strategies for implantable antennas," in *Antennas and Propagation Conference (LAPC), 2011 Loughborough*, Nov. 2011, pp. 1–5.

[29] A. Karlsson, "Physical limitations of antennas in a lossy medium," *IEEE Transactions on Antennas and Propagation*, vol. 52, no. 8, pp. 2027–2033, Aug. 2004.

[30] C. A. Balanis, *Antenna theory: analysis and design*, 4th ed. Hoboken, NJ: John Wiley & Sons, 2016.

[31] S. R. Best and A. D. Yaghjian, "The lower bounds on Q for lossy electric and magnetic dipole antennas," *IEEE Antennas and Wireless Propagation Letters*, vol. 3, no. 1, pp. 314–316, 2004.

[32] A. D. Yaghjian and S. R. Best, "Impedance, bandwidth, and Q of antennas," *IEEE Transactions on Antennas and Propagation*, vol. 53, no. 4, pp. 1298–1324, 2005.

[33] F. Merli, B. Fuchs, J. R. Mosig, and A. K. Skrivervik, "The effect of insulating layers on the performance of implanted antennas," *IEEE Transactions on Antennas and Propagation*, vol. 59, no. 1, pp. 21–31, 2011.

[34] S. Yun, K. Kim, and S. Nam, "Outer-Wall Loop Antenna for Ultrawideband Capsule Endoscope System," *IEEE Antennas and Wireless Propagation Letters*, vol. 9, pp. 1135–1138, 2010.

[35] R. Alrawashdeh, Y. Huang, M. Kod, and A. Sajak, "A broadband flexible implantable loop antenna with complementary split ring resonators," *IEEE Antennas and Wireless Propagation Letters*, vol. 14, pp. 1506–1509, 2015.

[36] D. P. Chrissoulidis and J. M. Laheurte, "Radiation from an encapsulated hertz dipole implanted in a human torso model," *IEEE Transactions on Antennas and Propagation*, vol. 64, no. 12, pp. 4984–4992, 2016.

[37] R. Moore, "Effects of a surrounding conducting medium on antenna analysis," *IEEE Transactions on Antennas and Propagation*, vol. 11, no. 3, pp. 216–225, May 1963.

[38] P. Karban, F. Mach, P. Kus, D. Panek, and I. Dolezel, "Numerical solution of coupled problems using code Agros2D," *Computing*, vol. 95, no. 1, pp. 381–408, 2013.

[39] COMSOL Inc., *COMSOL Multiphysics*. [Online]. Available: `https://www.comsol.com/` (visited on 03/28/2017).

[40] A. F. Oskooi, D. Roundy, M. Ibanescu, P. Bermel, J. D. Joannopoulos, and S. G. Johnson, "Meep: A flexible free-software package for electromagnetic simulations by the FDTD method," *Computer Physics Communications*, vol. 181, no. 3, pp. 687–702, 2010.

[41] A. Christ, T. Samaras, A. Klingenbock, and N. Kuster, "Characterization of the electromagnetic near-field absorption in layered biological tissue in the frequency range from 30 MHz to 6,000 MHz," *Physics in Medicine and Biology*, vol. 51, no. 19, pp. 4951–4965, 2006.

Chapter 4

BodyCap e-Celsius® Antenna: Modeling and Optimization

Contents

4.1 Introduction 78
4.2 Specifications and Material Constraints 78
4.2.1 Characterization of Capsule Shell and Epoxy Filling . . . 78
4.3 Theoretical Model 79
4.4 Impedance Analysis 81
4.4.1 Numerical Model 81
4.5 Full-Wave Numerical Modeling 82
4.5.1 Planar Model 83
4.5.2 Conformal Model 89
4.6 Antenna Feeding and Measurements 90
4.6.1 Planar Antenna 90
4.6.2 Conformal Antenna 91
4.7 Influence of Capsule 91
4.7.1 Capsule Measurements in Air, Water, and Phantoms . . . 91
4.8 Antenna Optimization 92
4.8.1 Optimized Design 94
4.8.2 Performance 95
4.8.3 Prototyping and Measurements 96
4.9 Summary 97

4.1 Introduction

The initial goal of this study is to improve the antenna of BodyCap e-Celsius® capsule [1] (Figure 1.3) in terms of radiation efficiency and matching robustness under strict material, integration, and size constraints.

Before proceeding with the optimization, the optimal numerical model must be found containing the least numerical degrees of freedom (DoF) while providing accurate results [2]. In this chapter, we 1) analyze theoretically and model numerically the reference antenna, 2) characterize the reference antenna in terms of impedance, 3) design, optimize, and characterize a new antenna.

4.2 Specifications and Material Constraints

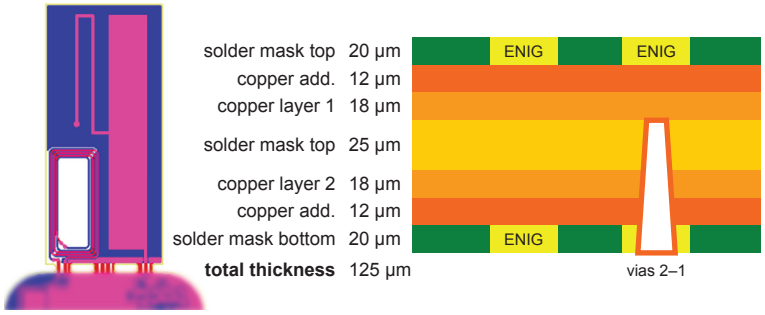

Fig. 4.1: Reference antenna PCB layout and the initial stack-up.

The reference antenna (Figure 4.1) is printed on a laminated 25.4 µm-thick polyimide substrate (DuPont Pyralux® AP: $\varepsilon_r = 3.4$, $\tan\delta = 0.003$). The capsule shell is 0.65 mm-thick and made of polyvinyl chloride (PVC, dielectric properties initially unknown). The capsule size is ($17.7 \times \varnothing 8.9$) mm. The antenna conforms to the inner surface of the capsule wrapping around the circuitry (printed on the same PCB) as in [3]. The free space within the capsule is filled with a bi-component epoxy resin (dielectric properties initially unknown).

The Silicon Labs SI 1014 microcontroller [4] connects to the antenna via a standard matching circuit from application notes (AN 427 [5] and AN 436 [6]). The antenna is fed using a microstrip line; the input impedance of the antenna is unknown. The 434 MHz antenna shares the PCB with a 50 MHz coil (Figure 4.1 left) that serves to wake up the capsule).

The optimized antenna must operate in mid-ISM 434 MHz frequency band (433.0 MHz to 434.79 MHz) and occupy the substrate and the capsule of the same dimensions. The thickness of the substrate, however, may be increased to 50.8 µm if necessary. The 50 MHz coil must remain unaltered as well as all capsule materials. From the electronics point of view, only the RF part (matching circuit and balun) of the circuitry can be modified.

4.2.1 Characterization of Capsule Shell and Epoxy Filling

We characterize the dielectric properties of PVC and bi-component epoxy in the 100 MHz to 6 GHz band using the transmission/reflection method [7, Ch. 4]. The

materials where milled into the 2 mm-thick washers (ext. ⌀7 mm ± 10 µm, int. ⌀3.04 mm ± 10 µm) and fitted within the APC-7 coaxial line connected to the network analyzer Keysight 8753ES. Figure 4.2 shows the measurement set up.

Fig. 4.2: The measurement set up for the material dielectric characterization: APC7 coaxial line connected to the network analyzer Keysight 8753ES.

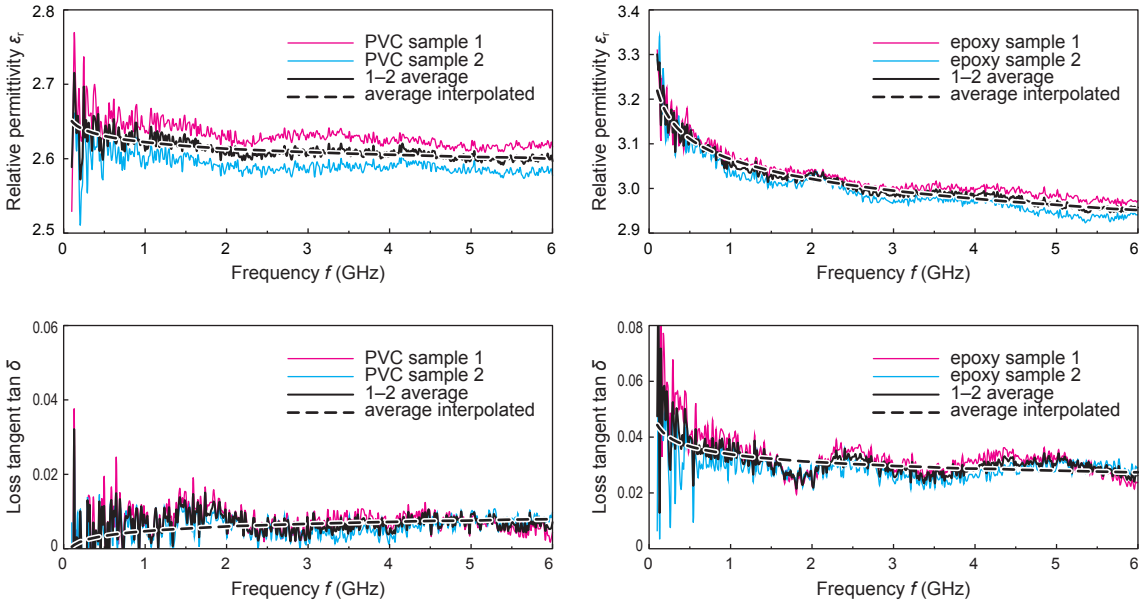

Fig. 4.3: Dielectric characterization results of the PVC capsule shell and bi-component epoxy filling.

Figure 4.3 shows the characterization results. For the shell, we used PVC with its measured dielectric properties $\varepsilon_r = 2.61$, $\tan\delta = 0.0029$ at 434 MHz. For the filling, it was a bi-composite epoxy resin with its measured properties $\varepsilon_r = 3.13$ and $\tan\delta = 0.0372$.

4.3 Theoretical Model

Patent No. WO2010119207 A1 [8] describes the operational principle of the initial antenna. Stepped-impedance resonator technique [9], [10] and meandering miniaturize the antenna. The operating frequency of the antenna depends on the characteristic impedance Z_c of each section of the stepped impedance resonator.

The characteristic impedance Z_c of any microstrip line depends on its geometry and dielectric properties of surrounding environment (substrate, superstrate, etc.). In our case, the width of microstrip lines is much larger than the substrate thickness (25.4 µm). So, the influence of fringing fields on Z_c is minor. In addition, a superstrate (represented here by a 0.65 mm PVC capsule shell) "squeezes" the fringing fields closer to the substrate and hence decouples the SiR from lossy biological tissues. As the capsule shell and substrate are practically lossless, and the biological tissue has minor influence on Z_c, we can consider the SiR as a lossless transmission line.

Quarter-wave stepped impedance resonator line consists of to connected transmission line elements: the first is open-circuited and the second is short-circuited (Figure 4.4).

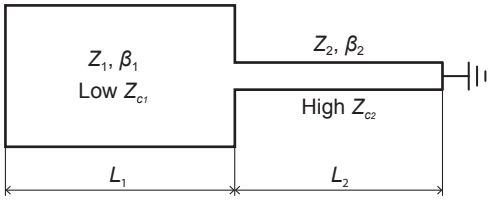

Fig. 4.4: Quarter-wave stepped impedance resonator equivalent transmission line model.

The input impedance Z_{in} of a lossless transmission line with the characteristic impedance Z_c depends on a distance l to the load Z_L [11, p. 59]:

$$Z_{\text{in}} = Z_c \frac{Z_L + jZ_c \tan \beta L}{Z_c + jZ_L \tan \beta L}, \tag{4.1}$$

where Z_c is the element characteristic impedance, Z_L stands for the load impedance, β denotes the phase constant and L is the element length.

Applying the equation (4.1) to both elements according to Mahe *et al.* [3], we obtain the resonance condition for the system on Figure 4.4:

$$\begin{cases} -Z_{c_1} + Z_{c_2} \cdot \tan(\beta_2 L_2) \cdot \tan(\beta_1 L_1) = 0 \\ -Z_{c_2} \cdot \tan(\beta_1 L_1) + Z_{c_1} \cdot \tan(\beta_2 L_2) \neq 0 \end{cases} \tag{4.2}$$

where β is the phase constant defined as

$$\beta_i = k_0 \sqrt{\varepsilon_r^{\text{eff}}}, \quad k_0 = \frac{2\pi}{v_0} f_{\text{res}} \quad \Rightarrow \quad \beta = \frac{2\pi}{c} f_{\text{res}} \sqrt{\varepsilon_r^{\text{eff}}}, \tag{4.3}$$

where f_{res} is the desired antenna resonance frequency, $\varepsilon_r^{\text{eff}}$ stands for the effective relative permittivity and $v_0 \approx 3 \times 10^8 \, (\text{m} \cdot \text{s}^{-1})$ is the speed of light in free space.

Eq. (4.2) relates the high-Z_c and low-Z_c lines geometry (via l and Z_c) and dielectric properties of the environment (via Z_c and β) to a resonant frequency f_{res} (when $\mathbb{I}\text{m}(Z_{\text{in}}) = 0$).

Effective relative permittivity $\varepsilon_r^{\text{eff}}$ is defined as relative permittivity of a homogeneous medium that equivalently replaces the heterogeneous medium [11, p. 148].

The characteristic impedance Z_c for an arbitrary transmission is defined as [11, p. 50]:

$$Z_c = \sqrt{\frac{R + j\omega L}{G + j\omega C}}, \tag{4.4}$$

which for the case with negligible losses reduces to

$$Z_c \approx \sqrt{\frac{L}{C}}, \tag{4.5}$$

where R is the resistance of the transmission line conductors, L is the self-inductance of the conductors, C is for the shunt capacitance, and G is the shunt conductance.

The inductance L and capacitance C (per unit length) may be represented through the phase velocity v_p. For any lossless TEM transmission cell, it can be written as [12, p. 457]

$$v_p = \frac{1}{\sqrt{LC}} = \frac{1}{\sqrt{\mu\varepsilon}} \;\Rightarrow\; \sqrt{L} = \frac{1}{v_p\sqrt{C}} = \sqrt{\frac{\mu\varepsilon}{C}}, \tag{4.6}$$

where L and C are inductance and capacitance per unit length, respectively.

After substituting (4.5) into (4.6), we obtain:

$$Z_c = \frac{\sqrt{\mu\varepsilon}}{C} = \frac{\sqrt{\mu_r\varepsilon_r}}{v_0 C}, \tag{4.7}$$

So, only the total capacitance per unit length C (*i.e.* including fringing fields) and effective relative permittivity $\varepsilon_r^{\text{eff}}$ of each element must be known in order to solve the equation (4.2) for the second element length.

As neither the capsule environment nor the biological tissues exhibit ferromagnetic properties, we can assume that $\mu_r^{\text{eff}} = 1$. The capacitance C could be determined either using the charge or the energy formulation, respectively:

$$C = \frac{Q}{V} \quad \text{or} \quad C = \frac{2W_e}{V^2}, \tag{4.8}$$

where Q is the charge, V stands for the electrical potential difference, and W_e is the total electrical energy stored in the system.

The relative permittivity $\varepsilon_r^{\text{eff}}$ can be evaluated by replacing the heterogeneous capsule environment by an equivalent homogeneous environment with the value of $\varepsilon_r^{\text{eff}}$ such that $C_{\text{heterogen}} = C_{\text{homogen}}$. The prior knowledge of (4.8) is thus required.

The closed-form solution—often approximate—relating the geometry of a transmission line to its impedance Z_c could be found only for simple geometries. For an arbitrary TEM transmission line, numerical solution is needed.

4.4 Impedance Analysis

4.4.1 Numerical Model

2D electrostatic problem formulation permits to analyze the characteristic impedance Z_c of an arbitrary TEM transmission line cross-section using the finite element method (FEM) [13]. The governing PDE can be written as:

$$-\nabla \cdot (\varepsilon \nabla \varphi) = \rho, \tag{4.9}$$

where φ is the sought-for electrostatic potential, and ρ is the charge density.

The study domain of the radius R circumscribes the cross-section of the structure (Figure B.1). In order to accurately estimate the capacitance per unit length C, the radius R must be large enough. We have iteratively chosen $R = 4$ cm.
The boundary conditions could be defined as

$$\begin{cases} \varphi = 1 & \text{on the conductor(s)} \\ \varphi = 0 & \text{on the ground plane} \end{cases} \tag{4.10}$$

and zero charge (Neumann) condition is imposed on the domain outer boundaries encircled by R:

$$\sigma_q = D_n = \varepsilon \frac{\partial \varphi}{\partial n_0} = 0 \tag{4.11}$$

where σ_q is the surface charge density.

The standard finite element procedure follows. Firstly, we set up the weak formulation of the problem (4.9) defined in Ω [14]:

$$\int_\Omega \varepsilon \nabla\varphi \cdot \nabla v \, \mathrm{d}S = \rho \int_\Omega v \, \mathrm{d}S \qquad \forall\ \varphi, v \in H_0^1(\Omega),\ \rho \in L^2(\Omega), \tag{4.12}$$

where v is the test function.

The weak formulation, along with the defined finite element piecewise-polynomial space $V_{h,p}(\Omega_h), \Omega_h \backsim \Omega$, together constitute a discrete finite element problem with N linear algebraic equations. In the matrix form:

$$\mathbf{A}\mathbf{x} = \mathbf{b}, \tag{4.13}$$

where $\mathbf{A} \in \mathbb{R}^{N \times N}$ is the "stiffness" matrix, $\mathbf{x} \in \mathbb{R}^N$ the vector of unknowns, and $\mathbf{b} \in \mathbb{R}^N$ the "load" vector.

After the assembly of the martices, the problem can be solved iteratively using the fully adaptive higher-order finite element method (*hp*-FEM) [14], which is implemented in our in-house software Agros2D [15]. Adaptivity overview is given in Appendix A.

To validate the method, we simulate a 50 Ω standard stripline with the dimensions according to the ISO 11452-5:2002 [16].The result converge to a 50.5Ω that represents the 1% error, which corresponds to the tolerance set for the automatic *hp*-adaptivity. The validation details are given in Appendix B

Now, the full wave model of the antenna must be created in order to verify the theoretical model, study the antenna parameters, and for the desired frequency (434 MHz in our case). The latter can be done using the one dimensional parametric optimization for the L_1 or L_2 parameters (Figure 4.4).

4.5 Full-Wave Numerical Modeling

Before proceeding with the full wave antenna modeling, an appropriate method must be chosen along with its implementation. The chosen antenna type (Figure 4.14) possesses the following features that cannot be neglected: 1) thin substrate $h \ll (L, W)$, 2) thin ($\sim 30\,\mu\mathrm{m}$) volumetric plating with $h_{\mathrm{sub}} \sim h_{\mathrm{met}}$, 3) lossy and dispersive medium, 4) finite ground plane effects.

Given the antenna features, we considered the following modeling environments and methods:

Ansys® HFSS™ R.15 [17]: finite element method (FEM), discontinuous Galerkin method in time domain (DGTD)

COMSOL® 4.4 RF Module [18] FEM (FD and transient)

CST Microwave Studio® 2014 [19]: finite integration in time domain (FI-TD), FEM, and transmission-line matrix method (TLM)

FEKO® 6.3 [20]: FEM and FDTD

SEMCAD–X® [21]: FDTD

The method of moment (MoM) and multilevel fast multipole method (MLFMM) implemented in Ansys HFSS-IE, CST Microwave Studio and FEKO were not considered as the structure is electrically resonant, thin volumetric plating layers must be modeled, and substrate and ground plane effects are significant.

After evaluating the listed codes, the CST Microwave Studio FI-TD method [22] was chosen to model the planar antenna, as it has the highest performance using the GPU. CST Microwave Studio FD was chosen to analyze the conformal antenna as it supports the curvilinear element approximation and h-adaptivity.

4.5.1 Planar Model

Up-to-date antenna (Figure 4.14) was modelled in CST Microwave Studio 2014 Time Domain (TD) environment (finite integration technique [22], hexahedral meshing). The results were confirmed using the COMSOL 4.4 RF Module (finite element method [14], hybrid tetrahedral–hexahedral meshing) for the surface PEC plating type (Figure 4.8). The adaptive mesh refinement (Figs. 4.5, 4.6) and the sweep over the distance to PML provide the S_{11} error tolerance about 2%.

CST TD solver uses the finite integration technique based on the finite volume discretisation in $\mathbf{R}^3$ for the Maxwell's equations in their integral form onto a dual grid cell complex [22]. PML boundaries were used to truncate the calculation domain at the distance 14 mm from the model edges for the homogeneous phantom environment; the distance was chosen iteratively increasing by 50% the distance model–PML to assure the variation of $f_{\mathrm{res}}\,(\min|S_{11}|)$ inferior 1% between each iteration. Both surface and volumetric lossy plating types use surface impedance boundary conditions. Thus, the mesh cells inside the plating are ignored.

The antenna is immersed in a lossy medium, the dielectric parameters are those of averaged biological tissue used for the antenna initial design in [8] $\varepsilon_r = 49.6$, $\sigma = 0.51$ S·m^{-1} (Figure 4.7).

All models were computed on a single node (2 × Xeon® E5-2643, 128 GB RAM) using 2 × NVIDIA® TESLA™ C2075 GPU.

Copper Plating Approximation

Along with the volumetric copper (Cu), we considered three basic plating approximation types: PEC surface, PEC volume, and Cu surface as well as hybrid types such as surface Cu for the ground layer and volumetric Cu for the antenna layer. The Cu conductivity is $\sigma = 5.96 \times 10^7$ S·m^{-1}.

For every plating type the simulation was run at least for three substrate (PI) thicknesses: (1, 2 and 3) mil, which are accordingly (25.4, 50.8 and 76.2) µm. The

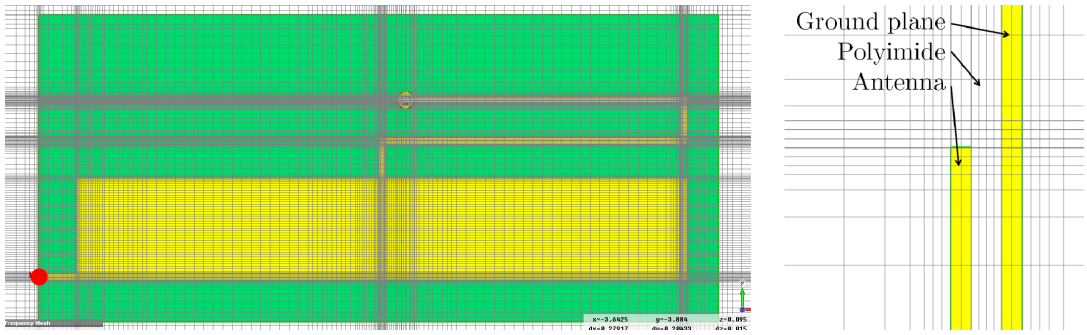

Fig. 4.5: Final CST model with hexahedral mesh containing about 7×10^8 cells.

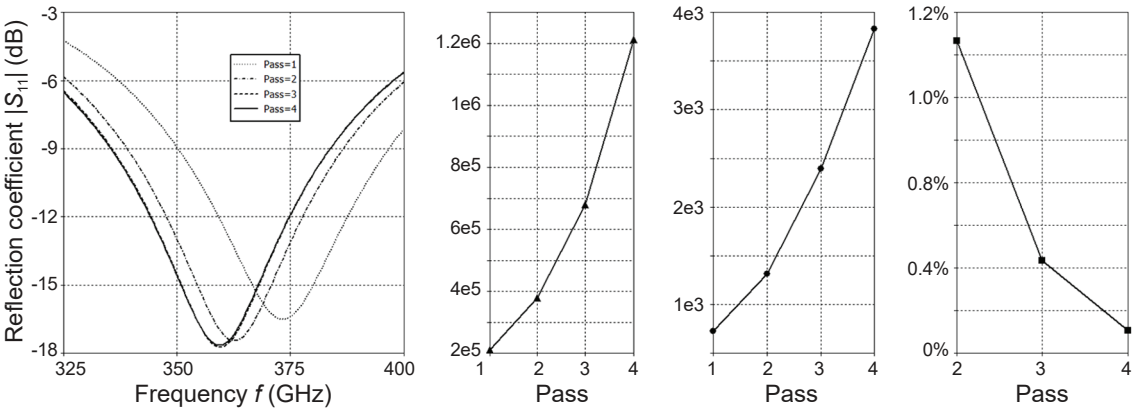

Fig. 4.6: Adaptive mesh refinement study in CST MWS for min-DoF model: (a) S_{11} *vs.* passes, (b) mesh cells *vs.* passes, (c) solver time *vs.* passes, and (d) max (ΔS) *vs.* passes.

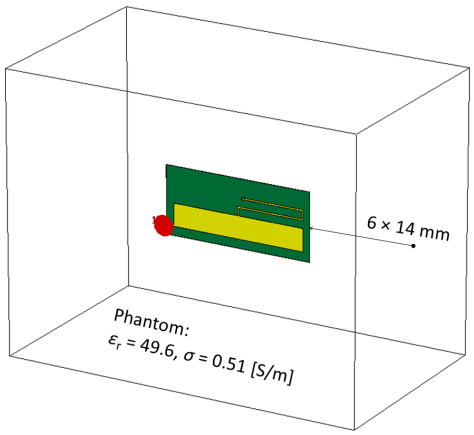

Fig. 4.7: Computational domain within the CST Microwave Studio using the rectangular homogeneous lossy phantom.

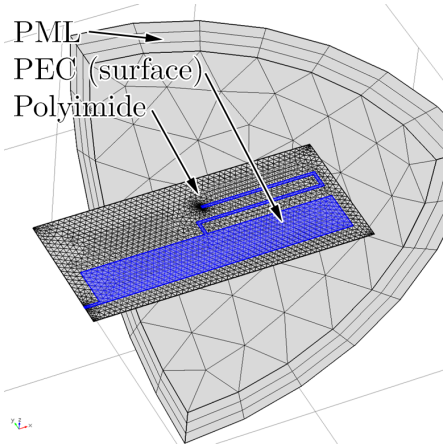

Fig. 4.8: COMSOL model. The mesh contains 56 347 elements (54 433 tetrahedral and 1 914 prismatic ⇒ 1 096 983 DoF).

substrate dielectric properties are from the DuPont™ Pyralux® AP datasheet: $\varepsilon_r = 3.4$, $\tan\delta = 0.003$ (frequency invariant).

Volumetric copper layers are the reference solution for the plating type; all other results are compared with it.

Plating type and material approximations affect all parameters of the model (Table 4.1): the thinner is the substrate, the stronger is the effect of plating approximation. While surface PEC provides a small error in f_{res} for (2 to 3) mil substrates, the bandwidth is affected significantly for all thicknesses. Both types of PEC plating (surface and volumetric) strongly increase the antenna impedance $\Re(Z_{\text{ANT}})$ (Figure 4.9). However, the PEC–Cu impedance difference reduces with the substrate thickening (Table 4.1), but stays still unacceptable for the thickest substrate (3 mil) that could be practically used for a miniature capsule antenna. As a result, we cannot use PEC to model the antenna when $h_{\text{sub}} \sim h_{\text{met}}$.

Different plating types do not affect the radiation pattern (Figure 4.10), which is consistent with the fundamental limitations on the directivity of electrically small antennas [23].

The optimal solution for the plating is to use the copper surface ground layer and the copper volumetric antenna. It considers both resistance losses in the plating and the fringing effects on the antenna edges. The resulted error is negligibly small.

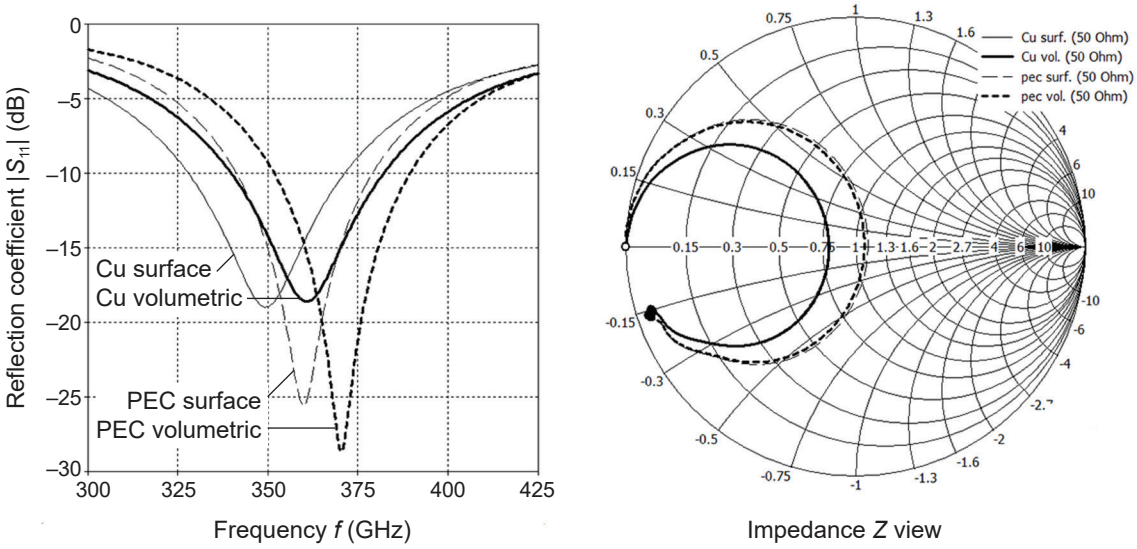

Fig. 4.9: S_{11} magnitude and Z Smith chart for 2 mil (50.8 µm) substrate.

As it could be seen from the Table 4.1 and the Figure 4.9, the resonant frequency f_{res} of the antenna is far from the desired 434 MHz. This is due to the absence of the insulation layer (superstrate), which is considered in the theoretical model (4.2) as the effective relative permittivity $\varepsilon_r^{\text{eff}}$ affecting the value of the phase constant β.

Impact of 50 MHz Coil

In order to simplify the model, I evaluated the effect of the 50 MHz coil in the vicinity of the antenna by modeling it in pure water. Figure 4.11 shows the model setup and the reflection coefficient $|S_{11}|$. The influence of the coil can be neglected during the parametric analysis and optimization procedure. However, it should be considered for the fine-tuning.

Table 4.1: Plating approximation. Resonant frequency f_{res}, bandwidth at $S_{11} < -10$ dB and the antenna real impedance $\Re(Z_{\text{ANT}})$ at f_{res}

Sub. thickness, (mil)*:		f_{res}, (MHz)			$\text{BW}_{-10\text{dB}}$,(MHz)			$\Re(Z_{\text{ANT}})$, (Ω)		
		1	**2**	**3**	**1**	**2**	**3**	**1**	**2**	**3**
Cu	surface	336.6	348.2	353.7	0	43	54	22.8	39.3	48.7
	volumetric	346.5	*360.3*	366.9	0	*42*	53	23.0	*39.2*	48.1
PEC	surface	358.1	359.7	361.9	25	38	47	45.1	54.1	59.6
	volumetric	365.8	369.6	374.0	25	39	47	43.3	52.4	57.5
Cu vol. ANT / surf. GND			359.2			41			39.2	

* 1 mil = 25.4 µm

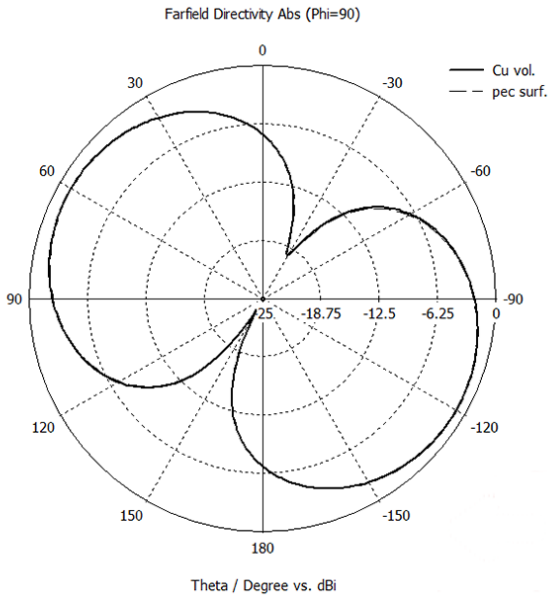

Fig. 4.10: Radiation pattern for surface PEC *vs.* volumetric copper platings.

Influence of the Capsule

I use the full-wave planar antenna model to study how PVC and epoxy affect the antenna impedance characteristics. Figure 4.12 shows the model geometry. The set up of the computational domain is the same as before. Figure 4.13 shows the results: it is obvious that the shell along with the filling affect significantly the antenna parameters. It increases the resonance frequency f_{res} and $\Re(Z_{\text{ANT}})$ at f_{res} because $\varepsilon_{\text{PVC}} < \varepsilon_{\text{phantom}} \Rightarrow \varepsilon_r^{\text{eff}}$ decreases. The shell and epoxy filling must be considered during the antenna optimization process.

Feed Point

The input impedance Z_{ANT} of a microstrip antenna depends on the feeding point [24]. As the present antenna has a quarter-wave length, the maximum Z_{ANT} will be at the bottom edge of the Z_{C1} (Figure 4.4) reducing to zero at the via location. As it is impractical to feed the antenna at the Z_{C2} element, I analyze the effect of the feed position along the Z_{C1} element. The results show that the input impedance Z_{ANT} and the efficiency η of the antenna are independent on the feeding position.

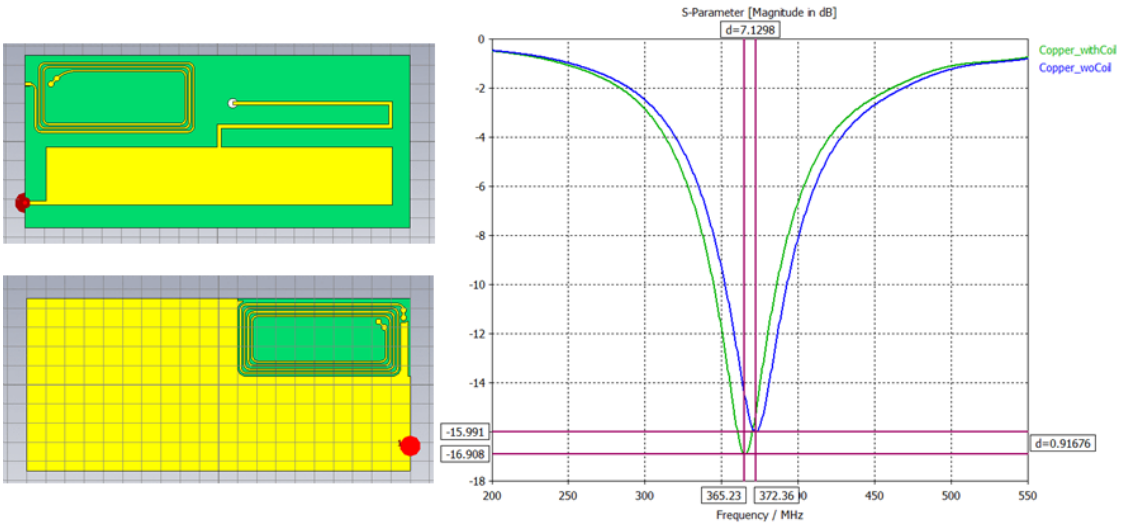

Fig. 4.11: Influence of the 50 MHz coil on the impedance of the antenna.

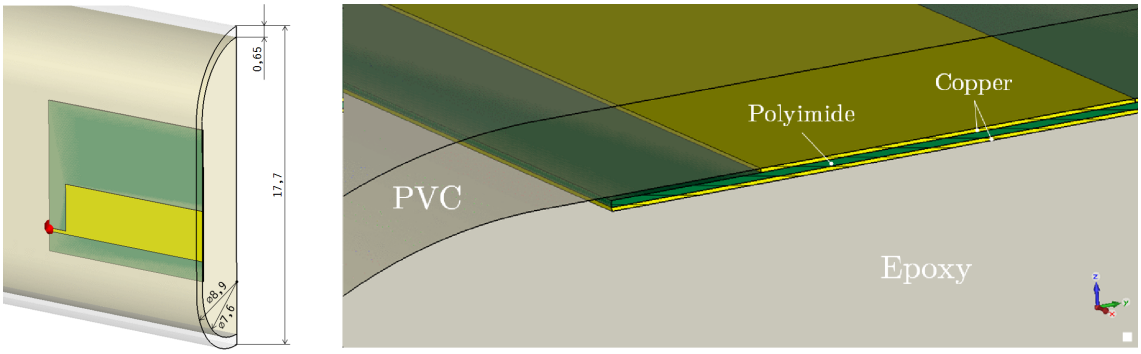

Fig. 4.12: Model slice of the planar antenna considering the effects of the PVC shell and the epoxy capsule-filling.

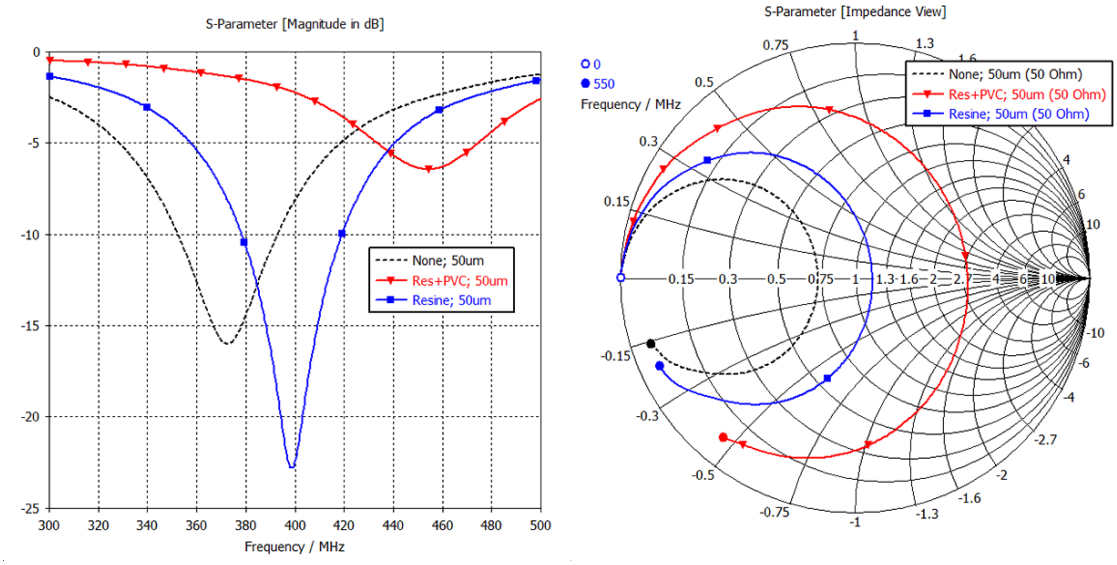

Fig. 4.13: The influence of the PVC shell and the epoxy filling on the resonant frequency f_{res} and the impedance Z_{ANT} of the antenna on a 50.8 µm substrate.

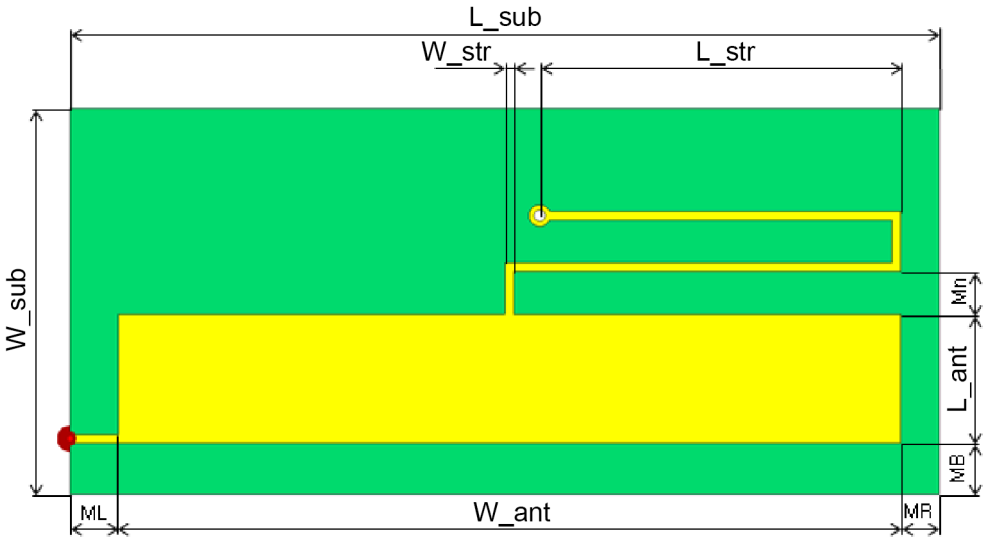

Fig. 4.14: Antenna geometry and parametric dimensions.

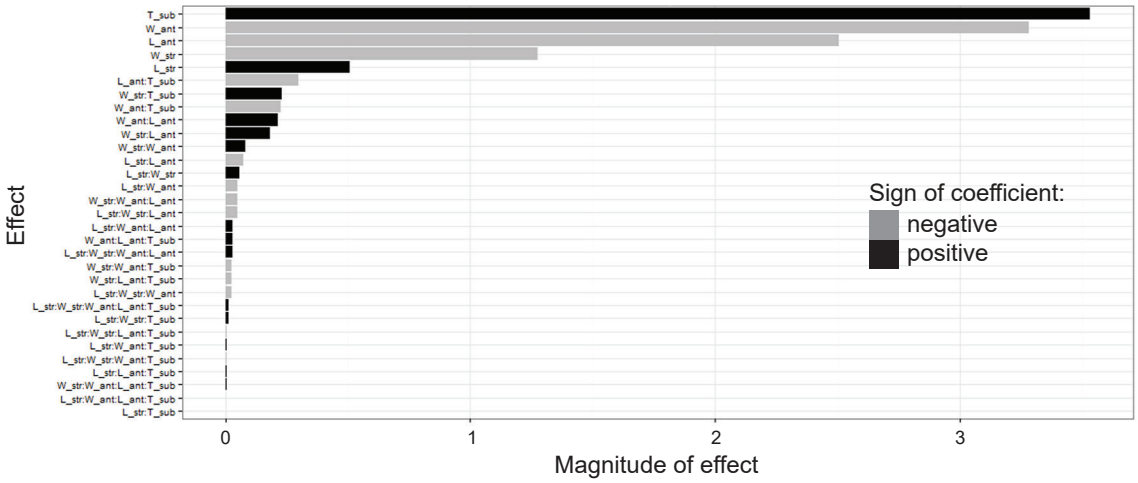

Fig. 4.15: The Pareto chart of effects of the antenna parametric dimensions on the input impedance Z_{ANT}.

Parametric Study of the Antenna

Figure 4.14 shows the parametric dimensions of the antenna (the substrate thickness T_sub is now shown). The effect of the dimensions on the f_{res} can be easily derived from the Eq. 4.2. However, analyzing the effect on the antenna impedance requires the numerical solution. To study these effects, I perform the full factorial numerical study of the antenna parameters. The Pareto chart on Figure 4.15 shows how the antenna parametric dimensions affect the input impedance Z_{ANT}. Clearly, the most prominent parameter is the substrate thickness: the thicker is the substrate, the higher is the antenna impedance. Increasing the width of the antenna elements leads to the decrease of the overall impedance.

In addition, the substrate thickness is directly proportional to the radiation efficiency η of the antenna. To accurately estimate the absolute values of the efficiency, I analyze the conformal antenna.

4.5.2 Conformal Model

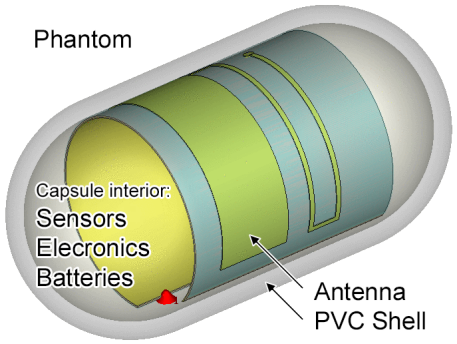

Fig. 4.16: The model of conformal capsule antenna inside a ⌀100 mm homogeneous phantom considering the PVC shell and epoxy filling.

Figure 4.16 shows the model geometry of the capsule. The conformal antenna model uses a homogeneous spherical phantom with a diameter of ⌀100 mm with various EM properties depending on the stage of analysis. The antenna is centered inside the phantom. This approach is more appropriate for estimating the radiation performance of in-body antennas with an undefined position within the body (e.g. ingestible). The spherical phantom preserves the intrinsic radiation pattern of the antenna whereas other shapes (e.g. cylindrical or cubic) may mislead about the antenna performance in terms of directivity D.

Because of the high contrast boundary between the phantom and the free space, any simple geometry phantom (as sphere, cuboid, cylinder, etc.) may act as a dielectric resonator, thus affecting the radiation performance [25], [26]. One way to alleviate the effect is to choose an appropriate non-resonant phantom size; however, this approach will work only for a narrow frequency band. A more general approach—that we propose and use here—consists in reducing the contrast on the phantom boundary by matching the permittivity ε_r of the free space (and so the PML) with the phantom. Still, the conductivity of the free space must remain zero ($\sigma = 0$ S·m^{-1}) to enable gain and efficiency evaluations. This approach allows comparing more accurately the antenna radiation performance within an optimization routine.

The conformal antenna study using the CST Microwave Studio® 2014 TD solver is impractical as it produces about 7×10^8 mesh cells for the converging result. I use CST Microwave Studio® 2014 FD for the future analysis of the conformal antenna.

Antenna bending to conform to the capsule shell interior with the diameter ⌀7.6 mm slightly reduces the f_{res} (7.6%) and the $\Re\,(Z_{\text{ANT}})$ at f_{res} (2.5%). The results are in agreement with the theoretical study on a cylindrical-rectangular microtrip antennas [27], [28]. The IEEE gain of the antenna in muscle-equivalent phantom is $G = -39$ dBi and the input impedance is $Z_{\text{ANT}} = 150\ \Omega$. Increasing the substrate thickness to 50 µm rises the gain to $G = -34$ dBi and the impedance to 200 Ω. Clearly, what is happening here is that the thicker substrate increases the radiation resistance R_r as the dielectric losses (and thus loss resistance R_l) stay constant. This mechanism substantially contributes to the increased gain [29].

Finally, the antenna prototype measurements have to be performed in order to validate the model.

4.6 Antenna Feeding and Measurements

To measure the antenna impedance, the antenna connects to the one end of a semi-rigid 50 Ω coaxial cable (Micro-Coax UT-085-M17, Figure 4.17: left); the opposite cable end has a SMA male connector (Radiall R125.052.000). I use the Agilent PNA–X network analyzer to measure the complex impedance within the 10 MHz to 1 GHz range. The measurement reference plane is at the end of the connector. The effect of the cable—the attenuation (0.49 dB·m^{-1}) and phase shift—are de-embedded during the post-processing using the CST Design Studio® 2014.

In total, nine antennas are manufactured to assess the measurement reproducibility. The planar antennas are measured in air and in pure water. The water temperature is measured and the EM properties are modeled accordingly using the Debye model [30, p. 96]. The conformal antenna is fixed in a Rohacell IG 51 foam with $\varepsilon_r = 1.05$, $\tan\delta = 0.0003$ (Figure 4.20); the dielectric properties of the latter are close to air.

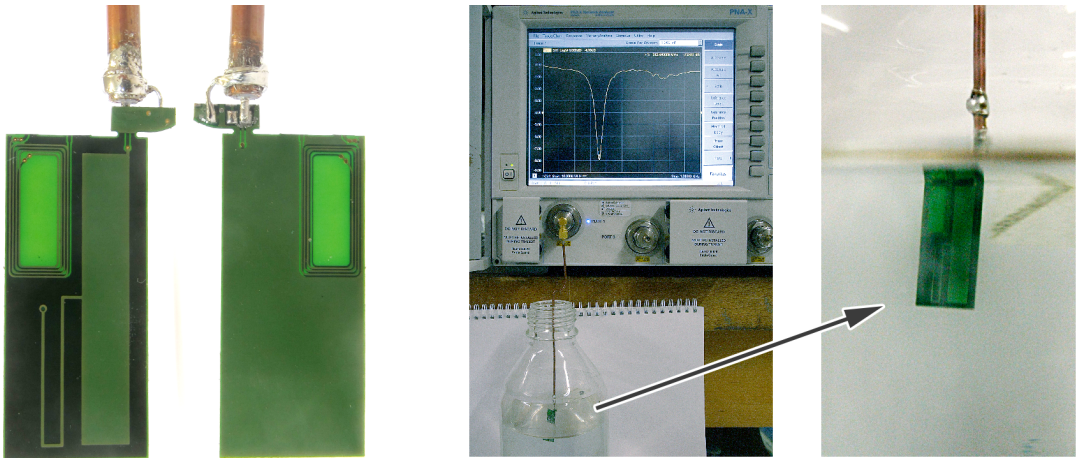

Fig. 4.17: Left: antenna on 50.4 µm polyimide substrate connected to 50 Ω semi-rigid coaxial cable. Right: Measurement set up using the Agilent PNA–X network analyzer (antenna in pure water).

4.6.1 Planar Antenna

In Air

Figure 4.18 shows the de-embedded measurement result of nine antennas in air compared to the simulation. The results agree with the simulation with less than 1% deviation of f_{res}, which is below the numerical precision. The ≈ 1 dB difference in $|S_{11}|$ shall be further investigated, the effect might be due to the cable.

In Water

Figure 4.19 shows the de-embedded measurement result of two antennas in pure water compared to the simulation (the model on the Figure 4.19: left). The results are in perfect agreement both on f_{res} and $|S_{11}|$. As water imposes a high contrast interface normal to the cable and separating it from the antenna, the previous suggestion of the cable effect on impedance seems plausible. In addition, Merli *et al.* [31]

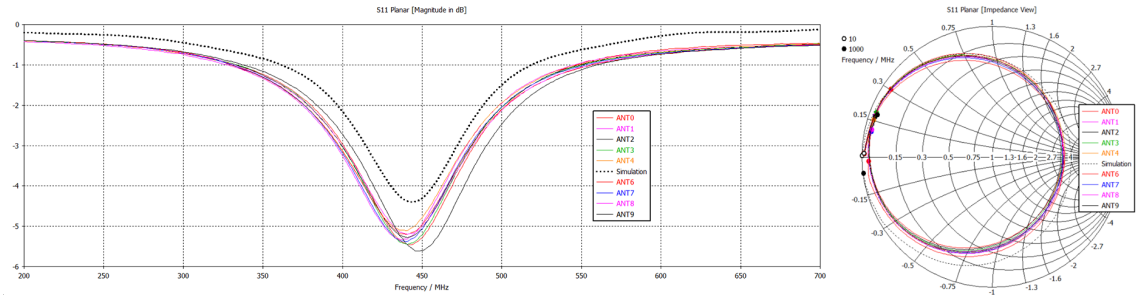

Fig. 4.18: Measurements for nine planar antennas in air *vs.* the numerical model: S_{11} and Z-Smith chart.

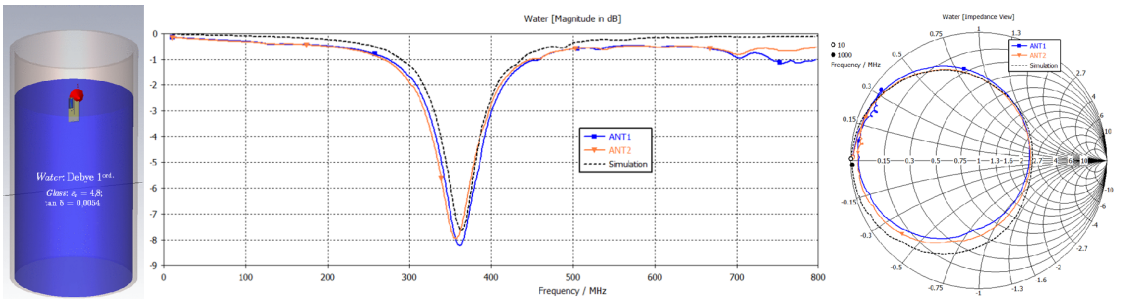

Fig. 4.19: Two planar antennas in water *vs.* the model: the model, S_{11} and Z Smith chart.

suggested using high contrast technique for decoupling electrically small antennas from the feeding cable.

4.6.2 Conformal Antenna

To study the conformal antenna eliminating the capsule effects, I use the Rohacell IG 51 foam ($\varepsilon_r = 1.05$, $\tan\delta = 0.0003$) to fix the antenna (Figure 4.20). The results show the 1.5% f_{res} reduction compared to the same planar antenna in air, which is about 6% less than the simulation results for the antenna in the phantom. The conformal antenna in the foam needs to be modeled to compare the results.

4.7 Influence of Capsule

As the antenna is intended to be used within a capsule that may significantly change the antenna performances (see Section 4.5.1), we measure the conformal antenna in the PVC shell as well as in the epoxy-filled capsule. Figure 4.21 describes the manufacturing process. The third step is necessary to mechanically reinforce the fragile cable-to-antenna connection. The measurement shows no significant difference $[\Delta(f_{\text{res}}) \ll 1\%]$ for the impedance during the steps 2) and 3).

4.7.1 Capsule Measurements in Air, Water, and Phantoms

We use two types of phantoms: the first has an average human GI tract properties ($\varepsilon_r = 64.1$, $\sigma = 1.12$ S·m^{-1}, see Section 2.1.2) and the second has its maximal ($\varepsilon_r = 68.7$, $\sigma = 2.11$ S·m^{-1}). The tissue EM properties are from Gabriel *et al.* [32].

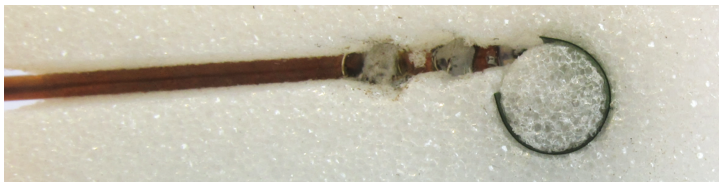

Fig. 4.20: Conformal antenna in the Rohacell IG 51 foam ($\varepsilon_r = 1.05$, $\tan\delta = 0.0003$).

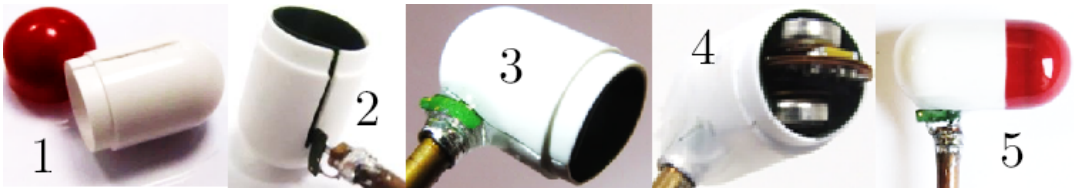

Fig. 4.21: Capsule preparation process for the impedance measurement: 1) to cut the PVC shell; 2) to insert the antenna and to measure the impedance; 3) to fix the connection with the epoxy resin for the mechanical rigidity and to re-measure the impedance; 4) to insert the capsule circuitry and to fill the capsule with the epoxy; 5) to measure the capsule impedance after 24 h (epoxy curing time).

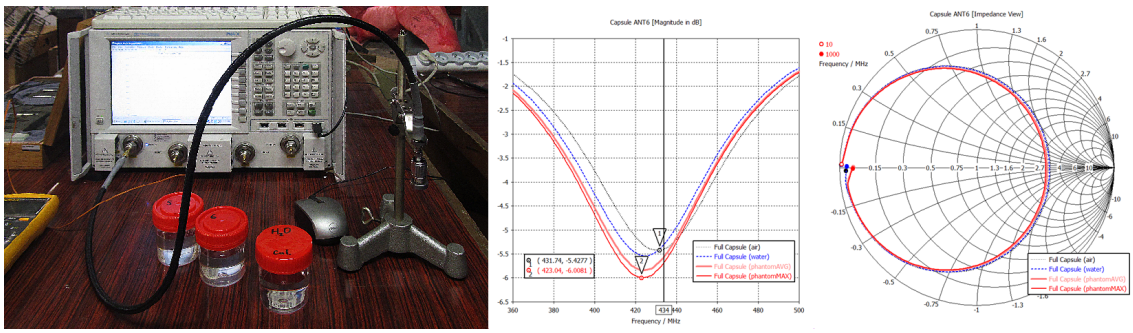

Fig. 4.22: Impedance characterization in phantoms. *left*: Phantom characterization using Agilent 85070C kit. *right*: $|S_{11}|$ and Z Smith chart measurement results of the antenna in the capsule in four environments (air, water, avg, and max. phantoms).

The phantoms are prepared using the recipe from containing pure water, sucrose, and NaCl. Section 2.3.2 gives detailed overview of the methodology. Exact EM properties were determined using the full factorial design methodology [33] and the resulting EM properties are verified using the Agilent 85070C dielectric measurement kit (Figure 4.22: left).

The results (Figure 4.22: right) show the antenna impedance $\Re\left(Z_{\mathrm{ANT}}\right)$ variation from 150 Ω (max phantom) to 165 Ω (air). Considering the e-Celsius® capsule using the "standard" matching circuit for a 50 Ω antenna from the application note AN 463 [6], a significant improvement of realized gain G_{tot} can be achieved.

4.8 Antenna Optimization

Taking into account the antenna operating frequency 434 MHz, the material, integration, and layout constraints (Section 4.2), no other state-of-the-art designs approaches (Table 1.2) are applicable to the e-Celsius® capsule design except for the one reported by Mahe *et al.* [3], [8]. The SiR miniaturization approach (see

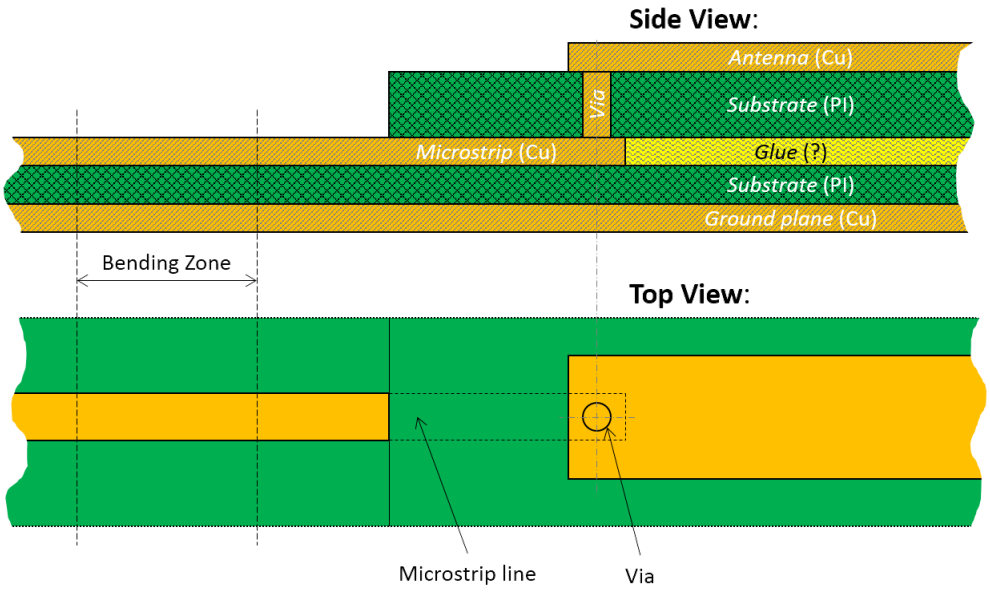

Fig. 4.23: PCB stack-up with the variable substrate thickness.

Section 4.3) allows us reducing the $\Lambda/4$ microstrip antenna to the physical size of $\Lambda/20$ [3].

It follows from all the foregoing chapters that in order to optimize the antenna in terms of radiation efficiency η, several options exist:

1. increase the thickness of the substrate according to the parametric studies of the existing antenna;
2. maximize the electrical size of the antenna ka (3.7) according to Section 3.2.3;
3. reduce its bandwidth according to Eq. 3.10 by decoupling the antenna from tissue (the bandwidth should be sufficiently large to prevent the impedance detuning);
4. avoid the meandering to maximize the polarization purity.

Concerning the thickness of the substrate, DuPont Pyralux® AP is proposed in thicknesses from 25.4 µm to 152.4 µm with 25.4 µm increment. According to the numerical analysis, the thickest substrate gives the highest radiation efficiency: $G = 31$ dBi for 152.4 µm. From the mechanical point of view—the PCB requires sharp bending—the substrate thickness is limited to 50.8 µm. An initial option is to use the variable thickness, as the one depicted in the Figure 4.23. However, due to the significant increase in manufacturing costs, this option was neglected and 50.8 µm thickness was chosen (final stack-up in Figure 4.24).

As the capsule materials must remain the same, and dielectric loading of the antenna is impossible, the electrical size of the antenna can be increased only by enlarging the Chu sphere radius a (Figure 3.2). So, the SiR elements Z_{C_1} and Z_{C_2} (Figure 4.4) can be extended in their total length $(L_1 + L_2)$ to the maximum length of the substrate (10 mm).

To avoid meandering of the line, $L_1 + L_2$ must be minimized. According to Eq. 4.2, the minimum length can be achieved by minimizing Z_{C_1} and maximizing Z_{C_2}. Extending the width of Z_{C_1} section to the whole length of the substrate

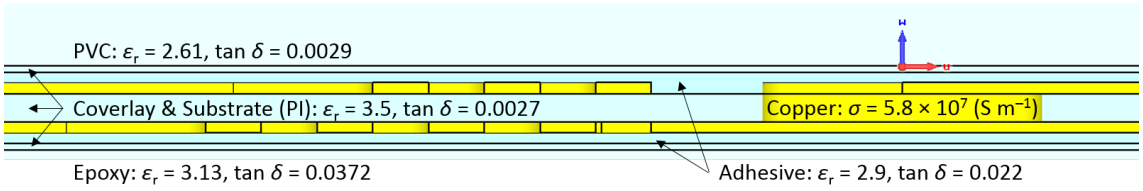

Fig. 4.24: Final PCB stack-up of the antenna PCB.

maximizes its impedance. As for the Z_{C_2}, the microstrip line of reasonable width ($w > 75\,\mu\text{m}$) does not give enough high impedance. Much higher impedance of the section can be achieved with co-planar lines. In addition, the co-planar line contributes to decoupling of the antenna from tissues that results in more efficient and robust antenna. Comparing to the meandered microstrip line, the improved decoupling of the co-planar antenna section is due to the effective permittivity ε_r of its environment being less perturbed by tissues. Hence, the EM-field propagating along the line concentrates more in the substrate, epoxy, and capsule shell.

4.8.1 Optimized Design

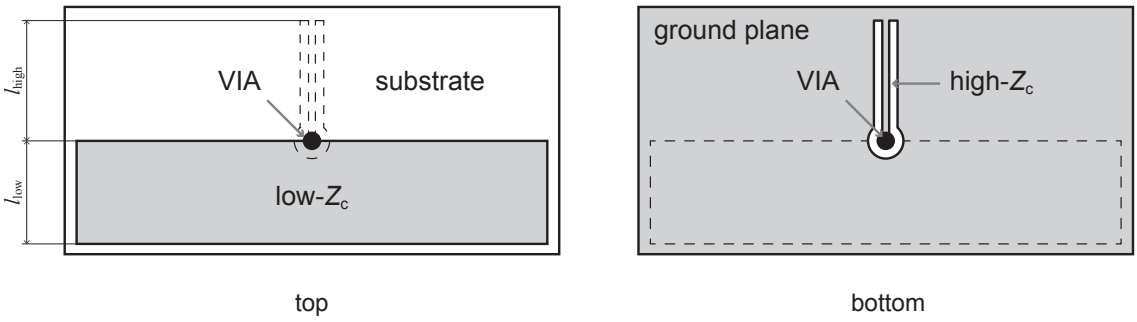

Fig. 4.25: Geometry of the optimized hybrid microstrip-coplanar antenna.

The hybrid microstrip–coplanar antenna design involves a quarter-wave stepped impedance resonator (SiR) as a main miniaturization technique [9], [10]. Figure 4.25 shows the antenna design and geometry. The dimensioning follows the same procedure described in Section 4.3. The low characteristic impedance element (low-Z_c) couples with the high impedance element (high-Z_c) by a VIA. The low-Z_c is a microstrip realized on a top layer of the substrate (closer to body tissue) and the high-Z_c is a coplanar line in a bottom layer. In this way, the fringing EM fields of the high-Z_c are moved away from lossy and dispersive body tissues with uncertain EM properties into a substrate and device environment with controllable dielectric properties. The antenna substrate is made of either a flexible material (e.g. to be rolled and conform to the inner surface of a capsule) or a rigid one for planar devices. A feed may connect to the low-Z_c element in an arbitrary place.

To fine-tune the operating frequency of the design to $f_0 = 434$ MHz , I perform the optimization of, at first, the planar antenna (setup similar to the one on Figure 4.12) in terms of the co-planar conductor and gap widths with the objective $\Im\left(Z_{\text{ANT}}\right) = 0$ at f_0. Second, for the obtained co-planar line geometry, I fine-tune the antenna using the full conformal model of the capsule (Figure 4.26) solved using the

FD solver. For both models, the phantom properties are defined as GI time-averaged ($\varepsilon_r = 63.0$ and $\sigma = 1.02$ S·m^{-1}, see Section 2.1.2).

4.8.2 Performance

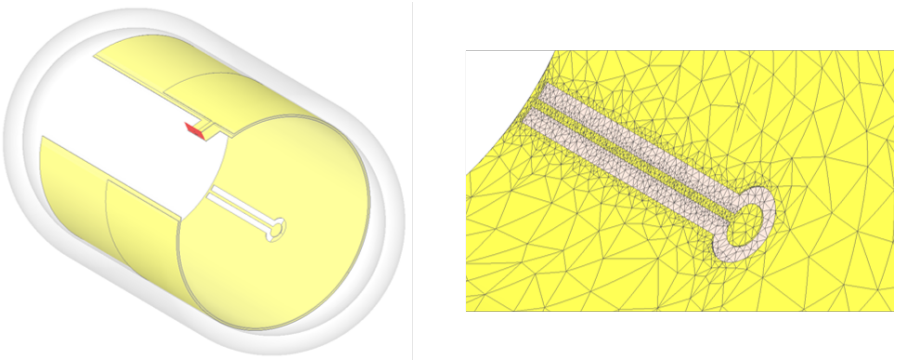

Fig. 4.26: Conformal model of the optimized antenna taking into account the PCB stack-up, PVC shell and epoxy filling. *left*: Full capsule. *right*: Final mesh of the co-planar line.

The optimized antenna performance is estimated in ⌀100 mm spherical homogeneous muscle-equivalent phantom as the reference one (Section 4.5.2). The IEEE gain of the antenna is $G = 27$ dBi that is 11 dBi higher than the reference antenna. The simulated input impedance is $Z_{\text{ant}} \approx 100\ \Omega$. The antenna is tuned to resonate [$\Im(Z_{\text{ANT}}) = 0$ at 434MHz] in averaged GI phantom ($\varepsilon_r = 63.0$ and $\sigma = 1.02$ S·m^{-1}). The bandwidth is $\text{BW}_{-10\text{ MHz}} = 11$ MHz ($\text{FBW}_{-10\text{ MHz}} = 2.5\%$) that is 24 MHz less than for the reference design in the same phantom. The bandwidth reduction—considering the increased thickness of the substrate—confirms the improved decoupling from the tissue and thus the increased radiation efficiency [*cf.* Figure 3.1(d)]. A cautionary remark: one must pay attention with such a narrow bandwidth to the impedance robustness to varying EM properties of biological environment. For the given indigestible application, the antenna is robust to the GI tissues ($\Delta f_{\text{res}} = 1.3\%$) and stays perfectly matched in muscle as well ($|S_{11}| = -25$ dBi) considering the antenna impedance $Z_{\text{ANT}} = 100\ \Omega$.

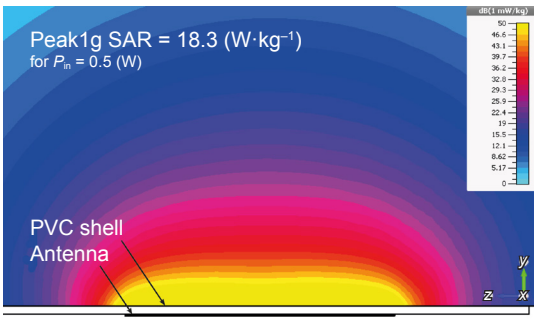

Fig. 4.27: y–z plane slice of the local SAR for an optimized antenna planar approximation.

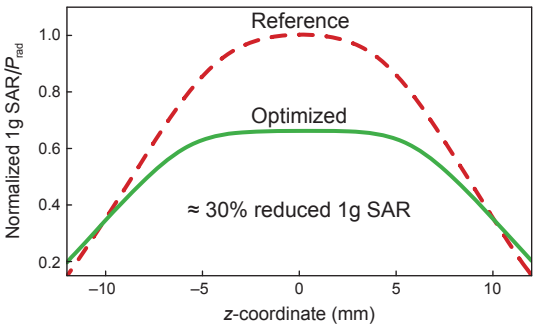

Fig. 4.28: Simulated 1g SAR (normalized by the radiated power P_{rad}) over the line in y–z plane 1 mm on top of the shell.

To further quantify the improvement of decoupling from tissue, I analyze the specific absorption rate (SAR) normalized to the power radiated by the antenna.

Figure 4.27 shows the SAR distribution and Figure 4.28 the normalized 1g SAR over a line in y–z plane 1 mm on top of antenna superstrate. About 30% reduction of the normalized SAR is achieved.

4.8.3 Prototyping and Measurements

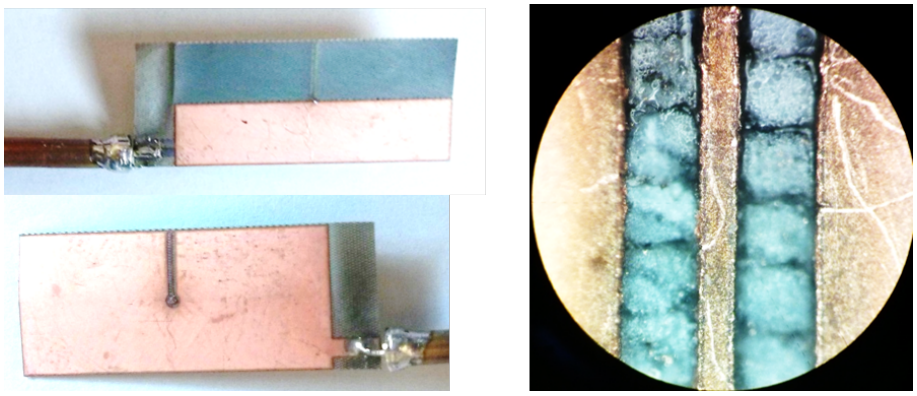

Fig. 4.29: Initial proof-of-concept prototype of the optimized antenna on Rogers XT/duroid® 8000 substrate. *left*: Top and bottom views of the antenna connected to a 50 Ω semi-rigid coaxial cable. *right*: Magnified view of the co-planar line.

To validate the design, I print the planar antenna prototype using laser ablation (LPKF ProtoLaser S) on 50.4 µm Rogers XT/duroid® 8000 ($\varepsilon_r = 3.23$, $\tan\delta = 0.0035$) with 17.5 µm copper plating. A 100 mm semi-rigid 50 Ω coaxial cable connects the antenna to a VNA (Agilent PNA-X). Figure 4.29 shows the top and bottom views of the prototype as well as the magnified view of the co-planar line depicting the uneven edges due to manufacturing imprecision.

The antenna is characterized in free space and in pure water. The results in water agree well with the simulation (within the variation $\Delta f_0 = 2\%$). The agreement in air is $\Delta f_0 = 5\%$. Better agreement can be achieved using more precise prototyping methods. However, this validates the model in terms of impedance, and the prototypes using photo-lithography can now be manufactured to evaluate the antenna input impedance with on-board circuitry .

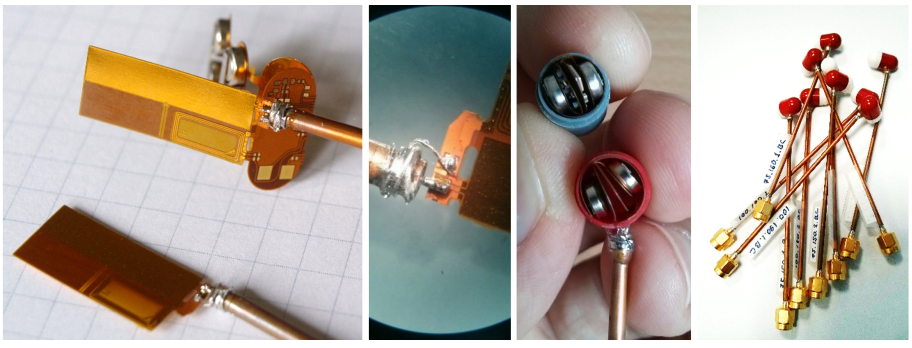

Fig. 4.30: Final prototype of the optimized antenna on polyimide substrate. *left to right*: Connected antenna with and without circuitry, soldering connection, folding of the antenna inside of the capsule, and nine fully assembled antennas.

The assembly procedure is similar to the one depicted in Figure 4.21. Figure 4.30 shows the final prototypes of the optimized antenna on polyimide substrate. The

antennas were characterized in terms of impedance in muscle-equivalent, GI time-averaged, and maximum EM properties phantoms. The results are in perfect agreement with simulations. The circuitry increases the f_{res} by 1.8%. In GI time-averaged phantom, the antenna input impedance is 80 Ω. Now, a matching circuit and balun must be designed to match the antenna impedance to Rx and Tx pins of SI 1014 MCU [4]. Appendix C overviews the matching procedure.

4.9 Summary

In this chapter, we modeled, characterized, and optimized the antenna of the BodyCap e-Celsius® capsule. Prior to the optimization, I studied the ways on achieving fast and accurate model of the antenna taking into account the capsule materials and biological tissue. The capsule shell and epoxy filling required dielectric characterization as their dielectric properties were unknown. We measured the properties using a transmission/reflection method via APC7 coaxial line.

The theoretical model allows understanding the antenna operation principle and defining the antenna dimensions for a given resonance frequency. In this way, the subsequent numerical optimization could be carried out for only one antenna parameter. Full wave antenna modeling is necessary to finely tune the antenna and define the optimal layout in terms of the gain G or the radiation efficiency η. We chose the FI-TD solver of the CST Microwave Studio® 2014 to analyze and optimize the planar antenna, and the CST Microwave Studio FD (FEM) solver to validate the conformal design. For the initial validation, I used FEM solver of another software—COMSOL—to check for erroneous results due to model building errors. The planar FI-TD antenna model is in perfect agreement with the FEM models. The model requires the volumetric lossy layers to represent the plating layer as the surface and PEC approximations give incorrect results due to the substrate thickness comparable to the plating one. The influence of the capsule materials is significant and must be taken into account from initial steps. Antenna bending, however, affects impedance insignificantly. Considering the conformal antenna computational effort, bending effect could be neglected for the optimization.

To validate the model, I fed the antenna by a semi-rigid coaxial cable and characterized its impedance. The measurements are in perfect agreement with the theory and the full wave model. They show good repeatability of the antenna S_{11} characteristics. The established antenna measurement procedure permits one to analyze the impedance and its detuning effects due to the EM parameters variation of the environment. In addition, it validates the numerical models used for the subsequent parametric studies and optimization.

We found that the microstrip antenna with the superstrate has the potential robustness to the detuning effects, which is important for the gastrointestinal capsule application, as the EM parameters of the environment vary. To optimize the existing design in terms of efficiency under the material and geometry constraints, we 1) increased the thickness of the substrate, 2) maximized the electrical size ka of the antenna, 3) decoupled it from the tissue by implementing its high-impedance element as a co-planar line in the ground plane, and 4) increased polarization purity by avoiding meandering. The antenna was fine-tuned to be perfectly matched in the averaged GI phantom ($\varepsilon_r = 63.0$ and $\sigma = 1.02$ S·m^{-1}). The gain of the antenna is 27 dBi that is 11 dBi higher than the reference design. To achieve such

improvement, in particular, the bandwidth needed to be sacrificed (see Figure 3.1 and Section 3.2.3). The new bandwidth is $BW_{-10\ MHz} = 11$ MHz that is 24 MHz less than the reference design. The antenna stays, however, robust to the variation of EM properties of GI tract tissues.

We characterized the antenna in two stages. First, I manufactured a proof-of-concept prototype using laser ablation of the Rogers XT/duroid 8000 substrate and it measured in air and water. Second, using the final designs on the polyimide substrate, I characterized full capsule containing the circuitry in muscle-equivalent, GI time-averaged, and maximum EM properties phantoms. For the obtained impedance of 80 Ω at f_{res}, an appropriate matching circuit and balun has to be e designed to transform the antenna impedance to RX (differential) and TX pins of SI 1014 MCU [4]. The standard circuit given in the application note AN436 [6] does not account for non-50Ω impedance and is not adapted for miniature devices. Appendix C overviews the matching procedure.

Bibliography

[1] BodyCap Medical, *E-Celsius*. [Online]. Available: http://www.bodycap-medical.com/.

[2] A. Kiourti and K. Nikita, "Implantable antennas: A tutorial on design, fabrication, and in vitro/in vivo testing," *IEEE Microwave Magazine*, vol. 15, no. 4, pp. 77–91, Jun. 2014.

[3] Y. Mahe, A. Chousseaud, M. Brunet, and B. Froppier, "New flexible medical compact antenna: Design and analysis," *International Journal of Antennas and Propagation*, vol. 2012, May 2012.

[4] Silicon Labs, *Si10xx Sub-GHz Wireless MCUs*. [Online]. Available: http://www.silabs.com/products/wireless/proprietary/si10xx-sub-ghz (visited on 08/06/2016).

[5] Silicon Labs. (2009). AN427: EZRadioPRO^{TM} Si433x & Si443x RX LNA matching, [Online]. Available: https://www.silabs.com/documents/public/application-notes/AN427.pdf (visited on 02/13/2017).

[6] Silicon Labs. (2011). AN436: Si4030/4031/4430/4431 PA matching, [Online]. Available: https://www.silabs.com/documents/public/application-notes/AN436.pdf (visited on 02/13/2017).

[7] L. F. Chen, C. K. Ong, C. P. Neo, V. V. Varadan, and V. K. Varadan, *Microwave Electronics: Measurement and Materials Characterization*. West Sussex, England: John Wiley & Sons, Apr. 2004.

[8] Y. Mahe, A. Chousseaud, and M. Brunet, "Antenne radioélectrique, procédé de dimensionnement d'un corps plat de l'antenne, et procédé de fabrication d'une telle antenne," WO2010119207 A1, Oct. 2010.

[9] M. Sagawa, M. Makimoto, and S. Yamashita, "Geometrical structures and fundamental characteristics of microwave stepped-impedance resonators," *IEEE Transactions on Microwave Theory and Techniques*, vol. 45, no. 7, pp. 1078–1085, Jul. 1997.

[10] M. Makimoto and S. Yamashita, "Bandpass filters using parallel coupled stripline stepped impedance resonators," *IEEE Transactions on Microwave Theory and Techniques*, vol. 28, no. 12, pp. 1413–1417, Dec. 1980.

[11] D. M. Pozar, *Microwave engineering*, 4th ed. Hoboken, NJ: Wiley, 2012.

[12] C. A. Balanis, *Advanced engineering electromagnetics*, 2nd ed. Hoboken, NJ: John Wiley & Sons, 2012.

[13] S. M. Musa and M. N. O. Sadiku, "Using finite element method to calculate capacitance, inductance, characteristic impedance of open microstrip lines," en, *Microwave and Optical Technology Letters*, vol. 50, no. 3, pp. 611–614, Mar. 2008. (visited on 04/25/2014).

[14] P. Solin, K. Segeth, and I. Dolezel, *Higher-Order Finite Element Methods*. London: Chapman and Hall/CRC, 2003.

[15] P. Karban, F. Mach, P. Kus, D. Panek, and I. Dolezel, "Numerical solution of coupled problems using code Agros2D," *Computing*, vol. 95, no. 1, pp. 381–408, 2013.

[16] "ISO 11452-5:2002: Road vehicles – Component test methods for electrical disturbances from narrowband radiated electromagnetic energy – Part 5: Stripline," International Organization for Standardization, Geneva, CH, Standard, Apr. 2002.

[17] ANSYS, Inc., *Ansys HFSS*. [Online]. Available: `http://www.ansys.com/products/electronics/ansys-hfss` (visited on 08/06/2016).

[18] COMSOL Inc., *COMSOL Multiphysics*. [Online]. Available: `https://www.comsol.com/` (visited on 03/28/2017).

[19] Computer Simulation Technology AG, *CST Microwave Studio*. [Online]. Available: `https://www.cst.com/Products/CSTMWS` (visited on 08/06/2016).

[20] Altair Engineering, Inc., *FEKO*. [Online]. Available: `https://www.feko.info/` (visited on 03/28/2017).

[21] Schmid & Partner Engineering AG, *SEMCAD X*. [Online]. Available: `https://www.speag.com/products/semcad/` (visited on 03/28/2017).

[22] M. Clemens and T. Weiland, "Discrete electromagnetism with the finite integration technique," *Progress In Electromagnetics Research*, vol. 32, pp. 65–87, 2001.

[23] J. Volakis, C.-C. Chen, and K. Fujimoto, *Small Antennas: Miniaturization Techniques & Applications*. McGraw Hill Professional, Jun. 2010.

[24] C. A. Balanis, *Antenna theory: analysis and design*, 4th ed. Hoboken, NJ: John Wiley & Sons, 2016.

[25] A. Shapiro, R. Lutomirski, and H. Yura, "Induced fields and heating within a cranial structure irradiated by an electromagnetic plane wave," *IEEE Transactions on Microwave Theory and Techniques*, vol. 16, no. 2, pp. 187–196, 1968.

[26] H. N. Kritikos and H. P. Schwan, "Formation of hot spots in multilayer spheres," *IEEE Transactions on Biomedical Engineering*, vol. BME-23, pp. 168–172, 1976, 2.

[27] C. Krowne, "Cylindrical-rectangular microstrip antenna," *IEEE Transactions on Antennas and Propagation*, vol. 31, no. 1, pp. 194–199, Jan. 1983.

[28] M. Abbaspour and H. Hassani, "Wideband planar patch antenna array on cylindrical surface," *IEEE Antennas and Wireless Propagation Letters*, vol. 8, pp. 394–397, 2009.

[29] R. Moore, "Effects of a surrounding conducting medium on antenna analysis," *IEEE Transactions on Antennas and Propagation*, vol. 11, no. 3, pp. 216–225, May 1963.

[30] J. Patterson and B. Bailey, *Solid-State Physics: Introduction to the Theory*, 2nd ed. Heidelberg: Springer, Dec. 2010.

[31] F. Merli, L. Bolomey, J. Zurcher, G. Corradini, E. Meurville, and A. Skrivervik, "Design, realization and measurements of a miniature antenna for implantable wireless communication systems," *IEEE Transactions on Antennas and Propagation*, vol. 59, no. 10, pp. 3544–3555, Oct. 2011.

[32] S. Gabriel, R. W. Lau, and C. Gabriel, "The dielectric properties of biological tissues: II. Measurements in the frequency range 10 Hz to 20 GHz," *Physics in Medicine and Biology*, vol. 41, pp. 2251–2269, Nov. 1996.

[33] G. E. P. Box, J. S. Hunter, and W. G. Hunter, *Statistics for Experimenters: Design, Innovation, and Discovery*, Second. Hoboken, N.J: Wiley-Interscience, May 2005.

Chapter 5

Miniature and Robust Antenna for In-Body Capsules

Contents

5.1 Introduction 104
5.2 In-Body Antenna Environment 104
5.2.1 Range of Tissue EM Properties 105
5.3 Antenna Design 106
5.3.1 Theoretical Considerations 106
5.3.2 Approach Validation: Proof-of-Concept Antenna 107
5.3.3 Final Antenna Synthesis and Miniaturization 111
5.3.4 Material Choice and Capsule Weight Estimation 113
5.3.5 Capsule Size Constraints 113
5.4 Full-Wave Numerical Analysis and Optimization 114
5.4.1 Numerical Model 114
5.4.2 Phantoms 115
5.5 Fine-Tuning and Performance in Simplified Phantoms . 116
5.6 Antenna Performance in Realistic Environment 117
5.6.1 Robustness: Variation of Tissue EM Properties 117
5.6.2 Influence of Capsule Circuitry 118
5.6.3 Application to Endoscopy 119
5.6.4 Interference with Neighboring Devices 120
5.6.5 Performance in Realistic Phantom 121
5.6.6 Link Budget Calculation 121
5.7 Prototyping and Measurements 122
5.7.1 Prototype Manufacturing 122
5.7.2 Phantoms 123
5.7.3 Antenna Reflection Coefficient 124
5.7.4 Radiation Performance 124
5.8 Summary 126

5.1 Introduction

IMPROVING the transmission range of miniature in-body devices remains a major challenge. For the time being they are able to operate only up to a few meters. Among the main issues to face are low radiation efficiencies ($\eta < 0.1\%$), antenna impedance detuning, and strong coupling to lossy and dispersive biological tissues.

The radiation efficiency is mostly constrained by attenuation and reflection losses in tissues [1], as well as by the required miniaturization of antennas that imposes fundamental limits on the maximum achievable radiation efficiency [2] (see Chapter 3). Detuning occurs since the antenna impedance depends strongly on EM properties of a surrounding environment that, in case of biological tissues, vary both in terms of permittivity and conductivity [3]. Ingestible antennas are more susceptive to impedance detuning than implantable ones as they must operate in a dynamically changing environment, i.e. through different gastrointestinal (GI) tract tissues. A straightforward approach is to design a wideband antenna with a bandwidth covering the expected detuning range, as reported in [4]–[6]. However, extending the bandwidth often implies sacrificing the radiation efficiency η, especially for electrically small antennas (ESA) [7] (see Chapter 3).

Merli *et al.* [1] and Skrivervik [8] studied the effect of implantable device encapsulation on radiation efficiency and found that it improves with increasing permittivity of encapsulation. In addition, high permittivity and low loss superstrate contributes to the decoupling of the antenna from lossy tissues with varying EM properties [9].

Here, I introduce a new approach to increase the operating range and matching stability as well as design a low-profile conformal microstrip antenna suitable for a wide range of in-body capsule applications. Ultra-miniature dimensions, enhanced robustness and efficiency (compared to counterparts) allow to employ it for implantable and ingestible applications (e.g. BodyCAP e-Celsius® capsule [10]). The gain of the capsule exceeds its counterparts by about 3 dBi whereas it is more miniature and robust. In addition, I propose: 1) a hybrid analytical–numerical approach to in-body capsule design involving a narrowband microstrip antenna combined with a high permittivity shell; 2) an experimental protocol to determine the antenna gain using spherical phantoms and an analog fiber optic link. The antenna operation frequency is $f_0 = 434$ MHz; it can also be tuned for MedRadio (401 to 406) MHz band by modifying only two geometrical parameters.

5.2 In-Body Antenna Environment

An in-body device must transmit efficiently from within a biological tissue. The antenna performance—in particular, the impedance matching—strongly depends on EM properties of the surrounding tissues. Thus, the antenna must be optimized to perform within a specified range of the tissue EM properties. This range typically depends on the location of the device inside the body, i.e. on the application scenario.

By designing a universal in-body antenna that is robust against varying EM properties of the in-body environment, one can use it—hypothetically—within any body tissue. Namely, other device specifications (such as its size, mechanical constraints, etc.) must be considered for a given application.

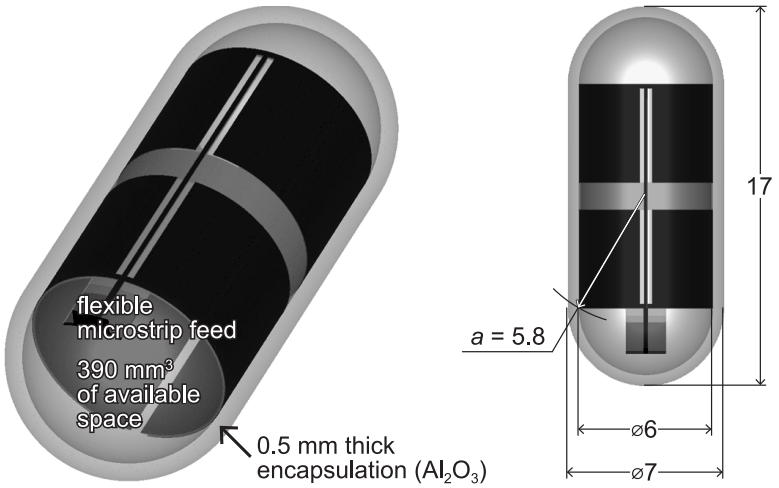

Fig. 5.1: Proposed in-body capsule antenna. (a) Antenna within an alumina (Al_2O_3) capsule. (b) Capsule dimensions (mm) and antenna circumradius a.

5.2.1 Range of Tissue EM Properties

Table 5.1: Electromagnetic Properties of Biological Tissues at 434 MHz For Some Implantable (Top) and Ingestible (Bottom) Cases

Tissue	ε_r	σ (S·m^{-1})
Fat (*lowest overall values*)	**11.6**	**0.08**
Grey matter	56.8	0.75
White matter	41.7	0.46
Muscle	56.9	0.81
Lung (inflated)	23.6	0.38
*Highest overall values**	**77.3**	**2.26**
Stomach	67.2	1.01
Small intestine	65.3	1.92
Large intestine	62.0	0.87
GI average (see Sec. 2.1.2)	**63.0**	**1.02**

* ε_r of salivary gland, σ of cerebrospinal fluid

Capsule antennas can be used for two classes of in-body applications: implantable and ingestible. For implantable applications, the capsule remains stationary inside the body, and the antenna needs to be designed taking into account the expected range of EM properties at the operating site. Ingestible capsule antennas must efficiently transmit from any point of the GI tract, hence be immune to the impedance detuning caused by varying EM properties of the biological environment. Table 5.1 lists the EM properties of human tissues reported by Gabriel *et al.* [3]: overall maximum, overall minimum, examples of tissues at potential implantation sites, and average GI tract values (see Section 2.1.2).

Within a real anatomical environment, the antenna couples not only to the ad-

jacent tissue: the effective EM properties of the surrounding media should be also accounted for. Moreover, the effective EM properties may also vary depending on the subject, age, capsule position, etc. At $f_0 = 434$ MHz, the estimate range of EM properties is $\varepsilon_r \in [11.6, 77.3]$ and $\sigma \in [0.08, 2.26]$ S·m^{-1} (Table 5.1). The relative permittivity ε_r of most body tissues tend to the upper limits of the specified range, and the conductivity σ is about in the middle [3]. Therefore, a universal in-body capsule antenna must remain operable in the whole specified range. As the majority of existing in-body applications—especially ingestible—require operation within an environment with higher EM properties ($\varepsilon_r \sim$ 50–70, $\sigma \sim 1$ S·m^{-1}), we have prioritized ensuring perfect matching for the highest overall EM properties. The acceptable matching must though be maintained for the overall minimum case (fat tissue). When implanted in fat, the antenna is close to the surface of a body and surrounded by the environment with lower loss ($\sigma = 0.08$ S·m^{-1} at 434 MHz) compared to muscle for instance ($\sigma = 0.81$ S·m^{-1}). In this way, the reduced attenuation in the tissue compensates the increased antenna mismatch loss. However, low relative permittivity ε_r of fat reduces dielectric loading that may decrease the maximum achievable efficiency (Fig. 5.2).

Therefore, we have specified the following impedance robustness constraints: $|S_{11}| \leqslant -10$ dB for the overall maximum EM properties, and $|S_{11}| \leqslant -3$ dB for the overall minimum. In addition, the $|S_{11}| \leqslant -10$ dB levels must be ensured for the remaining EM properties listed in the Table 5.1.

5.3 Antenna Design

5.3.1 Theoretical Considerations

Considering studies on the optimal operational frequency for in-body devices (see Chapter 3), I have chosen MedRadio (medical device radiocommunications service) (401 to 406) MHz and mid-ISM (the industrial, scientific and medical) (433 to 434.8) MHz as the most suitable, unlicensed, and globally available frequency bands.

Taking into account the antenna size constraints discussed in Section 5.3.5 (circumradius $a = 5.8$ mm, Figure 5.1b), at these frequencies we deal with ESA limitations [2], as $ka < 0.5$. This implies that a theoretical maximum limit exists for the radiation efficiency $\eta_{\max}$ for a given bandwidth BW (at a given voltage standing wave ratio [VSWR] level) (see Eq. 3.10 and Section 3.2.3). The derivation of (3.10) is accurate for an antenna in free space. To apply it to the antenna radiating into lossy media, two assumptions have to be made. First, the currents induced in a lossy tissue reradiate negligible power. Second, assuming the antenna can be modeled by a Thevenin's equivalent circuit, the loss resistance R_L accounts for the power dissipation in tissue. Because of these assumptions, Eq. (3.10) is a too rough approximation to obtain an accurate limit on the achievable radiation efficiency for a given bandwidth. However, it gives a qualitative insight: the narrower is the bandwidth, the higher is the achievable radiation efficiency.

Figure 5.2 shows the approximate maximum achievable radiation efficiencies for a 434-MHz antenna with circumradius $a = 5.8$ mm (as the one reported in this paper). To increase the theoretically achievable radiation efficiency $\eta_{\max}$, we may reduce the BW by designing a narrowband antenna (e.g. microstrip). In addition, high permittivity of the surrounding tissue enhances the theoretically achievable

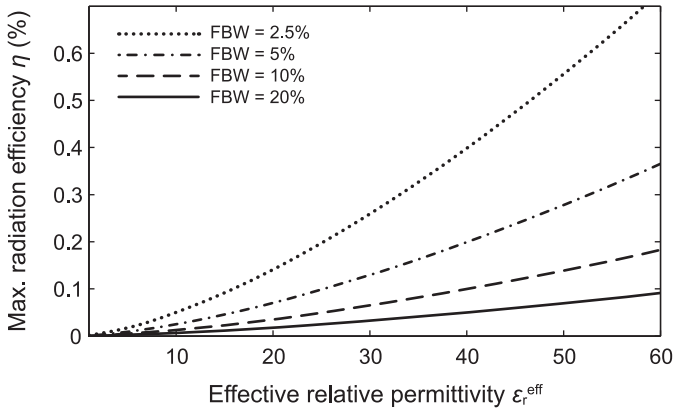

Fig. 5.2: Maximum achievable radiation efficiency of an arbitrary dielectric-loaded electrically small antenna with circumradius $a = 5.8$ mm operating at $f_0 = 434$ MHz with 2.5%, 5%, 10%, and 20% fractional bandwidths (FBW).

radiation efficiency $\eta_{\max}$ by increasing the electrical size of the antenna. However, considerable tissue conductivity induces losses that deteriorate the efficiency. We can partially reduce the losses in the near field by using a low loss shell acting as an antenna superstrate [1]. Reducing losses in the near field also further narrows the BW.

By designing a narrowband in-body antenna, one must ensure detuning immunity (or robustness) to varying EM properties of the surrounding tissues. We consider the antenna as robust when it remains adequately matched in the whole operating frequency band within the range of given EM properties of the biological environment (see Section 5.2.1).

The microstrip designs are of choice here, as f_{res} is defined mostly by the antenna design (substrate geometry and dielectric properties) and less affected by the environment, compared to antennas without or with a reduced ground plane. Superstrate further increases the microstrip antenna detuning immunity. An appropriate thickness and permittivity ε_r must be chosen to ensure the robustness within the desired EM properties range of the biological environment.

5.3.2 Approach Validation: Proof-of-Concept Antenna

To demonstrate the practical feasibility of the proposed approach, at first, I design a 434 MHz low-profile conformal microstrip antenna for a pill-shaped in-body device with the dimensions of ($18 \times \varnothing 8$) mm; the size allows both ingestible and implantable applications. The antenna conforms to the inner surface of the capsule with the diameter of $\varnothing 6$ mm (Figure 5.3, left). The capsule shell is 1 mm thick.

To fit the antenna within the capsule, I use the half wave stepped impedance resonator (SIR) as a major miniaturization technique (Figure 5.7). The SIR consists of two low-impedance elements connected by a high-impedance microstrip line containing loops in order to increase the antenna impedance $Z_{\text{ant}}\,(f\text{res})$ up to 50 Ω. Two ground plane slots lengthen the current path, and were used to finely tune the antenna resonant frequency f_{res} (Figure 5.3, right).

The antenna is designed to be printed on a flexible 50 µm-thick (2 mil) Rogers

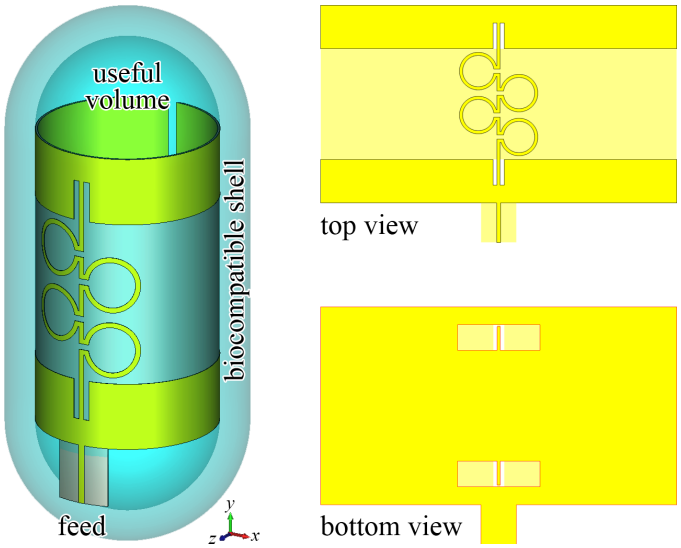

Fig. 5.3: Proof-of-concept capsule antenna: (left) conformal design within the (18 × ⌀8) mm capsule; (right) top and bottom views of the planar antenna geometry.

ULTRALAM® 3850HT substrate (liquid crystalline polymer (LCP), $\varepsilon_r = 2.9$, $\tan\delta = 0.002$) with 17.5 µm copper plating thickness. The total thickness is 85 µm. Other common flexible substrates can be used instead, such as polyimide (PI) or polyether ether ketone (PEEK).

As for the capsule shell (superstrate), we designed the antenna for the 1 mm thick biocompatible ceramics $MgTa_{1.5}Nb_{0.5}O_6$ ($\varepsilon_r = 27.9$, $\tan\delta < 0.001$), as was suggested by Chien *et al.* [11]. Better efficiencies and stronger antenna–body decoupling could be achieved with higher permittivity materials, as Figure 5.2 shows.

To further improve the dielectric loading, the capsule may be filled with a high permittivity material, as was suggested by Dissanayake et al. [12]. I use pure water for this purpose ($\varepsilon_r = 78.4$, $\tan\delta = 0.022$ at 434 MHz). If required, a poly-saccharide material, as TX-151, can be used to increase the liquid viscosity.

Numerical Analysis

To design, optimize, and evaluate the antenna performance, we used the finite element method (FEM) implemented in the CST Microwave Studio® 2015 [13] frequency domain (FD) solver. The finite integration technique (time domain solver) was used in order to validate the FD results. The models were set up with an automatic adaptive mesh refinement with a convergence criterion $|S_{11}| < 1\%$ at f_{res} for three consecutive checks. The initial FD mesh step was set below 0.2 mm for the antenna elements and below 0.5 mm for the superstrate. The distance from the antenna to model boundaries (terminated with PML) was at least $\lambda/4$ for both solvers.

To analyze the in-body performance of the antenna in terms of the reflection coefficient S_{11}, gain G and radiation efficiency η, we used the ⌀100 mm spherical homogenous phantom with muscle-equivalent EM properties: $\varepsilon_r = 56.9$ and $\sigma = 0.8$ S·m^{-1} at 434 MHz, according to Gabriel *et al.* [3].

When simulated in a ⌀100 mm spherical homogeneous phantom with muscle-equivalent EM properties, the antenna is optimized to resonate at $f_{\text{res}} = 433.9$ MHz that isthe center frequency of mid-ISM (433 to 434.8) MHz band (Figure 4). The

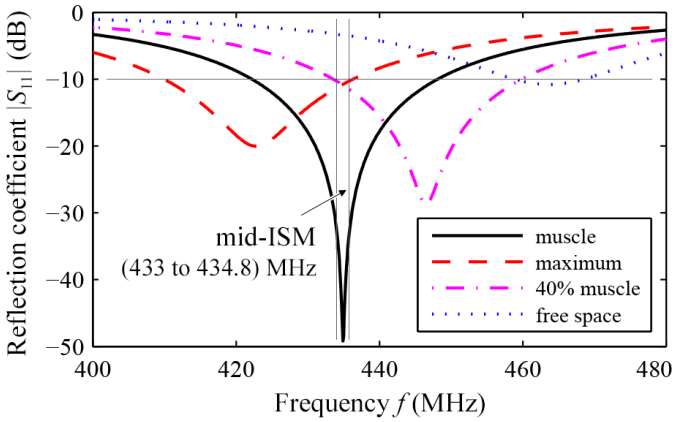

Fig. 5.4: Reflection coefficient of the proof-of-concept antenna simulated in following environments: muscle-equivalent phantom, maximum phantom, 40% muscle phantom, and free space.

bandwidth is 26 MHz (or fractional $\text{FBW}_{-10\text{dB}} = 6\%$). The IEEE gain $G = -20.4$ dBi and the realized gain is $G_{tot} = -21.4$ dBi. The radiation efficiency η reaches 0.6%.

Figure 5.4 shows the reflection coefficient of the antenna in the ⌀100 mm spherical homogenous phantom with various EM properties as well as in free space. The antenna remains matched below $|S_{11}| < -10$ dB level within the mid-ISM (433 to 434.8) MHz band from 40% muscle properties and up to the maximum EM properties of human tissue. In free space, the antenna is matched below $|S_{11}| < -3$ dB, while the resonant frequency differs from f_{res} in muscle only about 7%, which is comparable to the bandwidth. The radiation pattern is dipole-like in agreement with the ESA fundamental limitations.

Experimental Validation

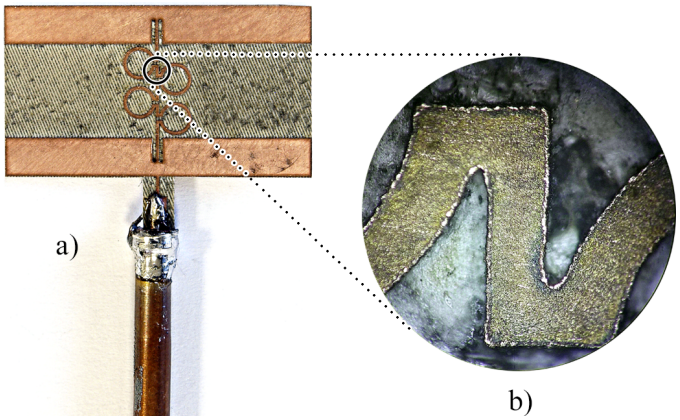

Fig. 5.5: Proof-of-concept antenna prototype. (a) Photograph of the antenna printed on the 18 mm × 10 mm × 50 µm flexible substrate (Rogers ULTRALAM® 3850HT) and connected to a 50 Ω coaxial cable; (b) magnified view of the 0.2 mm microstrip line.

To validate the numerical model, I simulate and measure the reflection coefficient $|S_{11}|$ in pure deionized water of a planar antenna without the superstrate. Three prototypes were manufactured and measured to verify the reproducibility.

The antennas were shaped on a Rogers ULTRALAM® 3850HT substrate using the laser ablation technique, then soldered to 100 mm 50 Ω semi-rigid coaxial cables terminated with SMA connectors (Figure 5.5a). The Agilent PNA-X network analyzer was used to characterize the antennas. The cable and connector influence were de-embedded in post-processing using the CST Design Studio®.

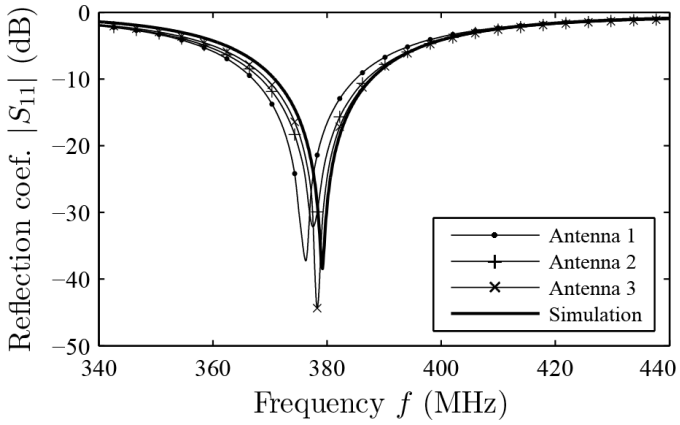

Fig. 5.6: Measured and simulated reflection coefficients of three antenna prototypes in pure deionized water.

The measured results shown on Figure 5.6 agree well with the numerical data. The maximum f_{res} deviation is below 1% (prototype No. 1) and can be further reduced by employing more accurate manufacturing methods, e.g. photolithography; Figure 5.5b demonstrates the inaccuracies of laser ablation technique (uneven edges, burned substrate).

The proposed approach substantially increases the achievable radiation efficiency and robustness of in-body capsule antennas by using the narrowband microstrip designs loaded with a high permittivity superstrate. The approach allows designing low profile conformal antennas, thus minimizing the volume occupied by the antenna within an in-body capsule.

As the maximum achievable radiation efficiency depends on the antenna electrical size, we can distinguish two ways to rise radiation performance: 1) increasing the physical size of an antenna, e.g. by effectively using the surface of an in-body device; 2) via dielectric loading. Both methods were applied to the proof-of-concept antenna.

We used $MgTa_{1.5}Nb_{0.5}O_6$ ceramics ($\varepsilon_r = 27.9$)—a biocompatible material reported previously for similar applications [11]. However, as Figure 5.2 suggests, higher radiation efficiency could be achieved by using a capsule shell with higher permittivity than for the proof-of-concept design. A comprehensive overview of such dielectric materials is given in [14]. For instance, low loss composite ceramics can be manufactured using barium titanates ($Ba_2Ti_9O_{20}$ plus TiO_2, $\varepsilon_r \in [40..100]$) or magnesium titanates ($MgTiO_3$ plus $CaTiO_3$, $\varepsilon_r \in [13..150]$).

However, such designs are cumbersome and require a thick ($\geqslant 1$ mm) and costly shell, limiting their scope of applications. For this reason, below I propose a low-profile conformal microstrip antenna suitable for a wide range of in-body capsule applications using a thin 0.5 mm and cost-effective Al_2O3 (alumina) shell.

5.3.3 Final Antenna Synthesis and Miniaturization

Miniaturization is required to fit the 434 MHz ($\lambda/2 \approx 34$ cm) microstrip antenna within the 17 mm×⌀7 mm capsule. Again, I usee the half-wave stepped impedance resonator (SiR) technique [15], [16] with two impedance steps—low-to-high and high-to-low—in order to reduce the antenna size and match the antenna input impedance to $Z_{\text{in}} = 50\,\Omega$. This structure may be further miniaturized by short circuiting the high-Z element in the middle (results in quarter-wave SiR). However, this approach relies on metallized via in order to establish a through-substrate connection. As it requires an additional plating step that increases the overall plating thickness, we decided to neglect this option.

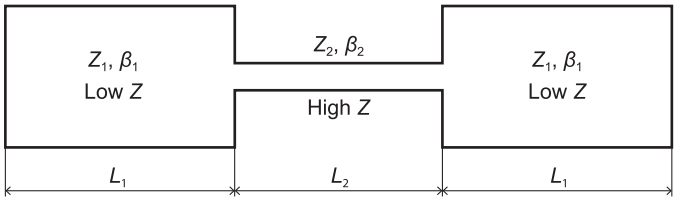

Fig. 5.7: H-type half-wave microstrip stepped impedance resonator.

Half-wave SiR microstrip antennas could be modeled using the transmission line impedance equation [17, p. 59] as the three section transmission line with identical first and third elements (Figure 5.7)

$$Z_1 \left[Z_1 \tan\left(\beta_2 L_2\right) + 2 Z_2 \tan\left(\beta_1 L_1\right) \right] - Z_2^2 \tan^2\left(\beta_1 L_1\right) \tan\left(\beta_2 L_2\right) = 0 \tag{5.1}$$

where Z_n are the impedances of each section, β_n denote the phase constants, and L_n stand for the section lengths.

Eq. (5.1) relates the high-Z and low-Z element lengths L_n and impedances Z_n to the resonant frequency f_{res} (when $\mathbb{I}\text{m}\left(Z_{\text{in}}\right) = 0$). The phase constants β_n are defined as

$$\beta_n = \frac{2\pi}{c} f_{\text{res}} \sqrt{\varepsilon_{r_n}^{\text{eff}}} \tag{5.2}$$

where $c = 3 \times 10^8$ m·s^{-1} is the speed of light in vacuum and $\varepsilon_{r_n}^{\text{eff}}$ are the effective relative permittivity of each line section.

The impedances Z_n and the effective relative permittivities $\varepsilon_{r_n}^{\text{eff}}$ can be evaluated using numerical modeling of the appropriate line cross-sections. To do so, I enhance the method reported in Section 4.4 and based on the *hp*-adaptive solution of 2D electrostatic formulation. Here, I consider the 2D cross-sections of the antenna already folded to conform within a capsule (Figure 5.8). In this way, not only the effect of the phantom, but also the one of antenna bending was already taken into account before continuing to the full-wave analysis. In addition, curvilinear elements implemented in Agros 2D [18] accurately represent the circular geometry of the model.

Further size reduction of the antenna is achieved by the inset of the high-Z section into low-Z sections and by slots in the ground plane to lengthen the current path. Bending the final microstrip design to conform inside a ⌀6 mm cylinder slightly reduces f_{res} too (by about 1%). This is consistent with previous studies on cylindrical microstrip antennas [19]. Figure 5.9 shows the final antenna dimensions after performing numerical optimization for the ISM 434 MHz band (as developed

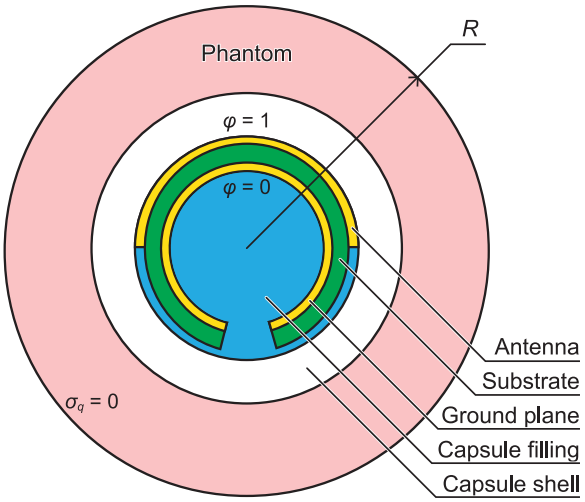

Fig. 5.8: 2D cross-section (not in scale) of the folded antenna inside the capsule within a circular phantom of radius R.

originally), as well as retuned for the MedRadio (401 to 406) MHz. Only two parameters need to be changed to adjust the operating frequency. The MedRadio antenna performance is similar in terms of matching levels, robustness, gain G, and radiation efficiency η. In this chapter, the sake of brevity I report only the main results for the MedRadio band.

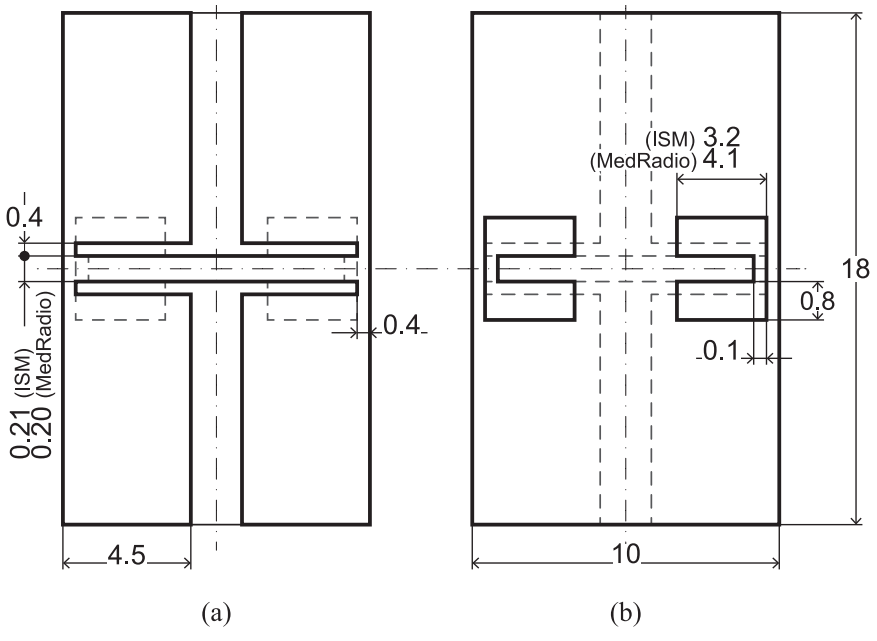

Fig. 5.9: (a) Top and (b) bottom views of the antenna PCB and its dimensions (not in scale, mm) for ISM (433 to 434.8) MHz and MedRadio (401 to 406) MHz bands.

A flexible microstrip line integrated in its substrate feeds the antenna (Figure 5.1). This allows printing the antenna on the same substrate as the capsule circuitry as the one reported for the e-Celsius® capsule (Chapter 4).

5.3.4 Material Choice and Capsule Weight Estimation

5.3.5 Capsule Size Constraints

An in-body device suitable for confortable ingestion and implantation sould be pill-sized. The minimal capsule dimensions are limited, as it may contain sensors, a microcontroller, and a power source. The smallest microcontrollers equipped with RF transceiver are about 4 mm wide. A power source could be a conventional battery (button cell, $\geqslant \varnothing 4.8$ mm) or an ultra-miniature wireless powering scheme, as, for instance, the 3.5 mm$\times\varnothing$2 mm device reported by Ho *et al.* [20].

Considering the necessary wiring of the components and an optional folding of the printed circuit board (PCB) (e.g. as for the e-Celsius capsule, see Chapter 4), I restricted the capsule inner diameter to $\varnothing$6 mm (Figure 5.1) that allows accommodating button cell batteries. The length depends on the size constraints of on-board components and can vary typically from mm to cm depending on the application scenarios. As the proposed antenna can be used for a wide range of applications (both ingestible and implantable), I looked for the sizes of existing miniature in-body capsules (summarized in Section 1.4), averaged the smallest ones, and rounded to the whole number resulting in 17 mm. The capsule size—17 mm$\times\varnothing$7 mm—is comparable to a pill and within the reasonable limits for both implantation and ingestion.

Printed Circuit Board

The antenna was designed for a 50 µm (2 mil) flexible substrate that conforms to the inner surface of the capsule. In this way, the extension of the same printed circuit board (PCB) may contain the device circuitry, as, for instance, the e-Celsius® capsule. We considered three substrate materials that could be used interchangeably with minor changes to the antenna geometry due to the slightly varying dielectric properties: 1) Rogers ULTRALAM® 3850HT (liquid crystal polymer, $\varepsilon_r = 2.9$, $\tan\delta = 0.002$); 2) Rogers XT/duroid® 8000 (polyether ether ketone, $\varepsilon_r = 3.23$, $\tan\delta = 0.0035$); 3) DuPont Pyralux® AP (polyimide, $\varepsilon_r = 3.4$, $\tan\delta = 0.002$).

In this study, I report the results for the antenna on the Rogers ULTRALAM® 3850HT substrate with a 9 µm-thick copper plating as it can be conveniently manufactured using laser ablation technique.

Encapsulation

The biocompatible encapsulation acts as a superstrate that may help decouple the antenna from the surrounding tissue. Concerning its EM properties, an ideal superstrate should have high permittivity ε_r and low loss, [1]. Only a few such materials have been reported for implantable applications so far: e.g. $MgTa_{1.5}Nb_{0.5}O_6$ ($\varepsilon_r \approx 28$) [11] and Al_2O_3 ($\varepsilon_r \approx 10$) [21]. Koulouridis *et al.* have also proposed polymer–ceramic biocompatible composites [22].

We choose 99.7% Al_2O_3 (Degussit® AL23, $\varepsilon_r = 9.9$, $\tan\delta = 0.0001$) as practically lossless, biocompatible, and widely available commercially in various shapes and sizes. As mentioned above, the minimal capsule inner diameter is limited to $\varnothing$6 mm. We choose a 0.5 mm thick capsule shell ($\varnothing$7 mm outer capsule diameter, Figure 5.1) as sufficient to ensure the robust operation for implantable and ingestible scenarios.

Capsule Filling

As Figure 5.2 suggests, increasing the relative permittivity of the antenna environment improves the maximum achievable radiation efficiency. Filling an in-body capsule with a high permittivity substance (glycerol) was first proposed by Dissanayake *et al.* [12]; however, glycerol has relatively low permittivity ($\varepsilon_r \approx 12$) and considerable losses ($\tan\delta \approx 1$) at 434 MHz (EM properties are measured using SPEAG DAK-12 probe [23]). Pure water, on the other hand, has high permittivity ($\varepsilon_r = 78.4$) and lower losses ($\tan\delta = 0.022$) at 434 MHz. For the industrial implementation, though, solid high-permittivity (and low loss) materials may be preferred: for instance, a ceramic-powder-loaded polymer [22] or epoxy [24].

Capsule Weight Estimation

The volume of a capsule with half-spherical endings is $V = \pi R^2 h + (4/3)\pi R^3$, where R is the radius of the capsule and h stands for the height of its cylindrical part (10 mm in our case). For the 17 mm×⌀7 mm capsule with 0.5 mm thick shell, the mass of the inner filling (water, $V_{\text{in}} = 395.8$ mm^3, $\rho = 997$ kg·m^{-3}) is $m = \rho V = 3.9$ g. The mass of the shell (alumina, $\rho \approx 3800$ kg·m^{-3}) is $\rho(V_{\text{total}} - V_{\text{in}}) = 0.64$ g. The total mass is thus $m_{\text{total}} = 4.5$ g. Considering that the density of the circuitry (especially batteries) might be higher than that of water, we can estimate the maximum total mass of the device to be roughly 5 g. This is comparable to the mass of existing ingestible and implantable capsules (see Chapter 1).

5.4 Full-Wave Numerical Analysis and Optimization

Eqns (5.1) and (5.2) determine the antenna geometry. However, numerical modeling is required to optimize and finely tune the antenna for the robustness constraints defined in Section 5.2.1.

5.4.1 Numerical Model

I used CST Microwave Studio® 2016 [13] to model and optimize the antenna. Figure 5.10 shows a flowchart of the numerical modeling process. At first, a planar antenna approximation was solved and optimized (in terms of $|S_{11}|$) using the CST time domain solver (finite integration technique, FIT), then validated using the frequency domain solver (finite element method, FEM). Both methods used an automatic adaptive mesh refinement with $< 1\%$ $|S_{11}|$ error tolerance at 434 MHz for three consecutive iterations as a convergence criterion. FIT models used hardware acceleration (2 × NVIDIA Tesla K20c GPUs) that reduced significantly the simulation time and, therefore, the whole optimization routine.

The metalization layers (top and ground) were modeled as volumetric copper ($\sigma = 5.96 \times 10^7$ S·m^{-1}), as the thin sheet perfect electric conductor (PEC) approximation introduced a significant error in the antenna impedance. The effect is due to comparable thicknesses of the plating and substrate layers.

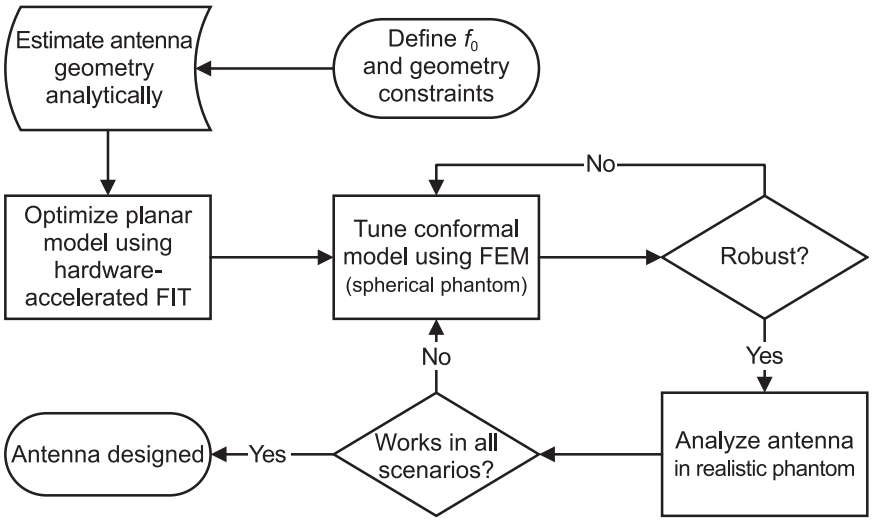

Fig. 5.10: Antenna numerical analysis flowchart.

The optimized parameters of the planar antenna approximation initialized the conformal antenna analysis and the tuning in a spherical phantom using the FEM solver. The automatic adaptive mesh refinement settings were set as reported above; however, the model was pre-meshed constraining the maximum element size to reduce the formation of low quality elements during the adaptivity process. The metallization layers were pre-meshed with 0.2 mm max step width, the substrate with 0.1 mm, the shell with 0.5 mm, and the phantom with $\lambda/10$ (e.g. 9 mm for muscle). For the anatomically realistic phantom, the ⌀100 mm spherical area around the antenna was pre-meshed with $\lambda/10$ max. step. The polynomial order was set as variable and up to the third order with automatic curved element attribution (10° curvature tolerance). We used the iterative solver (10^{-9} accuracy threshold) as the mesh is well defined for an initial adaptivity step (it resulted in faster solution than for direct solver in our case). The open boundaries were modeled as the perfectly matched layers (PML), and the distance to the model was at least $\lambda/2$ (a distance equal to λ was used for an accurate gain estimation).

5.4.2 Phantoms

The theoretical estimation and the planar antenna FIT analysis used phantoms with muscle-equivalent EM properties ($\varepsilon_r = 56.9$, $\sigma = 0.81$ S·m^{-1} at 434 MHz). A homogeneous rectangular cuboid phantom ($100 \times 100 \times 50$ mm^3) accounted for the tissue in the planar FIT model.

The conformal antenna models used a homogeneous spherical phantom with a diameter of ⌀100 mm with various EM properties depending on the stage of analysis (Figure 5.10 and Table 5.1). The antenna is centered inside the phantom. This approach is more appropriate for estimating the radiation performance of in-body antennas with an undefined position within the body (e.g. ingestible). The spherical phantom preserves the intrinsic radiation pattern of the antenna whereas other shapes (e.g. cylindrical or cubic) may mislead about the antenna performance in terms of directivity D.

Because of the high contrast boundary between the phantom and the free space, any simple geometry phantom (as sphere, cuboid, cylinder, etc.) may act as a di-

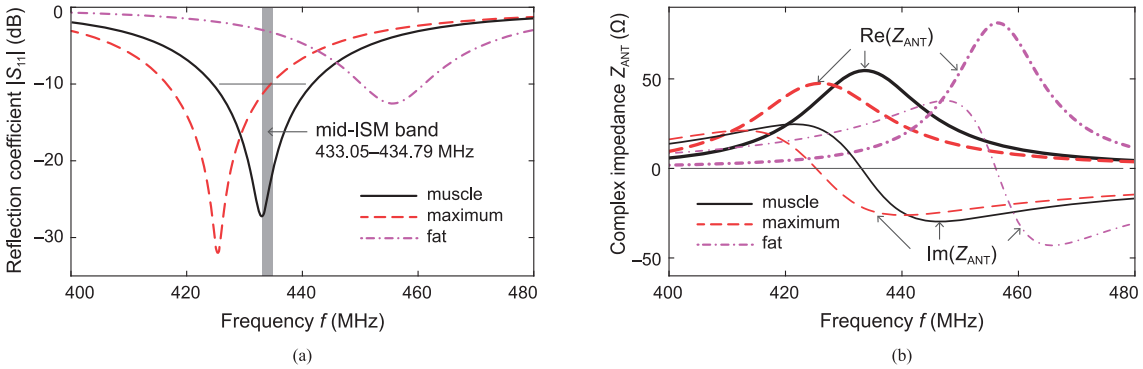

Fig. 5.11: Impedance characteristics of the capsule antenna simulated in the homogeneous ⌀100 mm spherical phantom with muscle-equivalent ($\varepsilon = 56.9$, $\sigma = 0.81$ S·m^{-1}), highest ($\varepsilon = 77.3$, $\sigma = 2.26$ S·m^{-1}), and lowest (fat-equivalent, $\varepsilon = 11.6$, $\sigma = 0.08$ S·m^{-1}) EM properties. (a) Reflection coefficient $|S_{11}|$ and (b) antenna complex impedance Z_{ANT}.

electric resonator [25], [26], affecting thus the radiation performance. One way to alleviate the effect is to choose an appropriate non-resonant phantom size; however, this approach will work only for a narrow frequency band. A more general approach—that we propose and use here—consists in reducing the contrast on the phantom boundary by matching the permittivity ε_r of the free space (and so the PML) with the phantom. Still, the conductivity of the free space must remain zero ($\sigma = 0$ S·m^{-1}) to enable gain and efficiency evaluations.

This approach allows comparing more accurately not only the antenna radiation performance within an optimization routine, but also with various counterparts. However, this method does not provide an accurate estimate of the antenna radiation performance for realistic in-body scenarios. For this purpose, we suggest working with an anatomically realistic phantom. In this study, we used the CST Female Visible Human model "Nelly" (optimized for tetrahedral mesh) in order to evaluate the capsule radiation performance in different application scenarios (Section 5.2.1).

5.5 Fine-Tuning and Performance in Simplified Phantoms

To maximize the robustness, we tuned the antenna numerically to resonate below mid-ISM band so that $|S_{11}| = -10$ dB at 434.79 MHz (upper bound of mid-ISM band, Figure 5.11a) in the phantom with the highest overall values of tissue EM properties (Table 5.1). The alumina shell thickness then was minimized iteratively (and rounded to the tenth of millimeter) to ensure a $|S_{11}| < -3$ dB matching level (Figure 5.11a) in fat (lowest overall values of tissue EM properties, $\varepsilon_r = 11.6$, $\sigma = 0.08$ S·m^{-1} at 434 MHz). We used the same methodology to retune the antenna for the MedRadio (401 to 406) MHz band; the dispersive EM properties of the phantoms were adjusted accordingly.

Figure 5.11 shows the antenna performance in terms of impedance. In the phantom with the highest overall EM properties, the antenna resonant frequency ($\mathbb{I}\mathrm{m}\,(Z_{\mathrm{in}}) = 0$) is $f_{\mathrm{res}} = 425$ MHz. In the phantom with muscle-equivalent EM

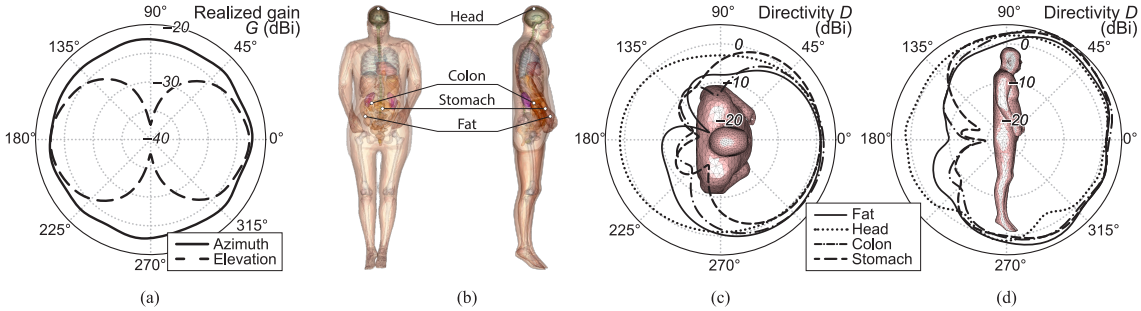

Fig. 5.12: (a) Simulated radiation pattern of the antenna at 434 MHz in ⌀100 mm spherical phantom with muscle-equivalent EM properties. (b) Locations of the capsule for the radiation performance evaluation in realistic phantom. (c) Azimuth and (d) elevation plane radiation patterns of the capsule simulated in the realistic phantom for four application scenarios.

properties, $|S_{11}| = -24.4$ dB at the mid-ISM center frequency $f_0 = 434$ MHz; $f_{\text{res}} = 433$ MHz. The -10 dB bandwidth ($\text{BW}_{-10\text{dB}}$) is 17 MHz (or the fractional bandwidth $\text{FBW}_{-10\text{dB}} = 4\%$). In fat, the antenna matching is $|S_{11}| = -3.2$ dB at f_0, and $f_{\text{res}} = 456$ MHz. In free space, the antenna shows poor matching; however, the resonant frequency is 470 MHz that is only 8% higher than f_0.

As for the antenna retuned for the (401 to 406) MHz MedRadio band, it resonates in the phantom with muscle-equivalent EM properties at $f_{\text{res}} = 400$ MHz and matched at $|S_{11}| = -15$ dB level at the center frequency $f_0 = 403.5$ MHz. The bandwidth $\text{BW}_{-10\text{dB}} = 16$ MHz (or $\text{FBW}_{-10\text{dB}} = 4\%$, the same as for the 434 MHz design).

Figure 5.12a shows the radiation pattern of the antenna at 434 MHz inside the ⌀100 mm spherical phantom with muscle-equivalent EM properties. The radiation pattern is dipole-like that is consistent with the ESA fundamental limitations on directivity. The realized gain is -22.4 dBi and the radiation efficiency reaches 0.4%.

5.6 Antenna Performance in Realistic Environment

In practical applications, the antenna couples to active and passive components inside the capsule and to various biological tissues outside. The radiation pattern depend on the application scenario, i.e. where a capsule locates in a body.

5.6.1 Robustness: Variation of Tissue EM Properties

To analyze the antenna impedance detuning immunity to the variation of surrounding tissue EM properties, we analyzed antenna matching levels at 434 MHz in a ⌀100 mm spherical phantom with $\varepsilon_r \in [10, 80]$ and $\sigma \in [0, 2.3]$ S·m^{-1}. This range covers all biological tissues at 434 MHz [3].

Figure 5.13 demonstrates the area of detuning immunity of the antenna. It remains well matched ($|S_{11}| < -10$ dB) for most in-body scenarios and deteriorates to -3.2 dB in fat. Even though reduced attenuation in fat compensates for the increased antenna mismatch, low effective relative permittivity decreases the antenna electrical size ka and thus affects radiation efficiency (see Section 5.2.1 and

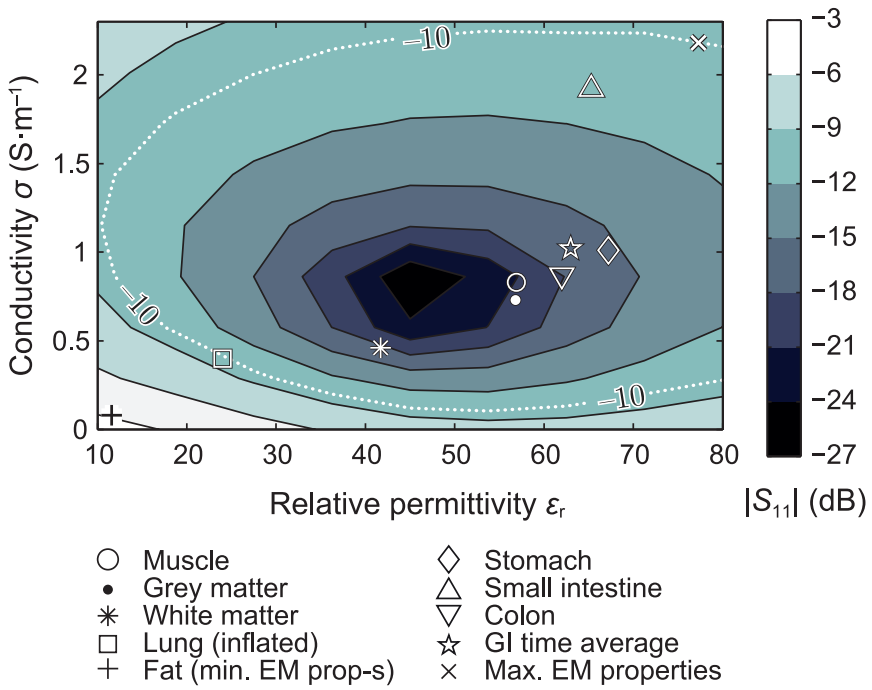

Fig. 5.13: Detuning immunity: reflection coefficient $|S_{11}|$ at $f_0 = 434$ MHz within the homogenous spheric phantom ⌀100 mm with $\varepsilon_r \in [10, 80]$ and $\sigma \in [0, 2.3]$ S·m^{-1}. White dotted contour denotes the $|S_{11}| = -10$ dB level.

??). The 0.5 mm thick alumina superstrate provides sufficient decoupling from the surrounding tissues in most cases. To improve both matching and dielectric loading in fat, one may consider implanting antenna closer to muscle.

5.6.2 Influence of Capsule Circuitry

Various solutions have been proposed in literature to decouple an antenna from circuitry and batteries. The common approach to verify the robustness against the components consist in introducing a PEC cylinder to the capsule model. Merli *et al.* [21] designed a dedicated volume shielded by a ground plane to house the components; the resulting design is fully robust. Liu *et al.* [27] studied the robustness by modeling transceiver, battery pack, and other electrical components as a 12.6 mm×⌀11 mm PEC cylinder; the $|S_{11}|$ variation is insignificant. Alrawashdeh *et al.* [4] optimized the antenna to operate with an internal battery resembled by a copper cylinder of 7.5 mm×⌀6 mm, but the robustness to other components has not been verified. Izdebski *et al.* [28] simulated the presence of batteries by 8 mm-long cylinder with variable radii; the antenna requires retuning accordingly to the battery radius. Xu *et al.* [6] have used a similar approach by placing an unspecified PEC shape (apparently a cylinder) to model the battery and varying the distance to the antenna. As the antenna has no ground plane, the effect on the impedance is noticeable and inversely proportional to the distance. The design by Psathas *et al.* [29] also requires retuning the antenna when the components are present.

We would like to propose a versatile antenna that is applicable "as is" for a wide range of in-body applications. This implies that it may be used in conjunction with a microcontroller, a power source, and RF circuits. Hence, there is an endless variety of possible capsule circuitry arrangements. To validate such a design, the worst-case

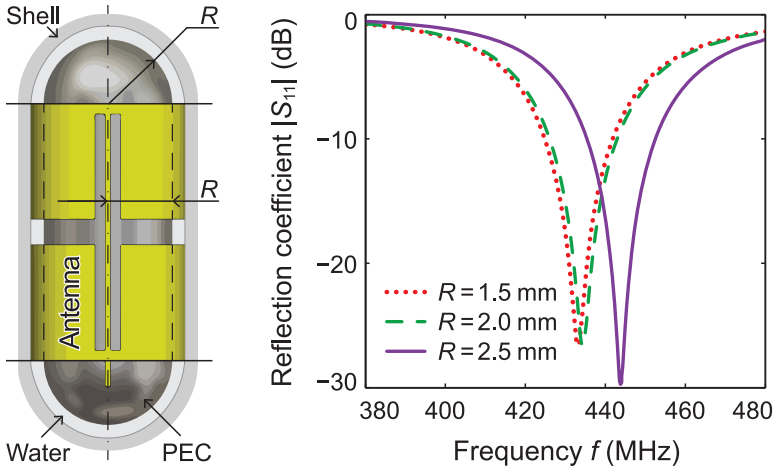

(a) (b)

Fig. 5.14: Effect of capsule components on the antenna performance. (a) Perfect electric conductor capsule of the radius R modeling the device circuitry to analyze its effect on the antenna impedance. (b) Reflection coefficients $|S_{11}|$ of the antenna (muscle phantom) for the various radii R of the PEC capsule.

scenario should be determined: if the components entirely fill all available volume, how close could they be to the antenna to detune it? We searched for the safe distance by: (1) introducing a perfect electric conductor capsule of a radius R and a length $2R \times 10$ mm inside the model (Figure 5.14a); (2) performing the parametric sweep over the radii R to determine the maximum safe distance to the antenna.

Figure 5.14b shows how the circuitry may affect the reflection coefficient $|S_{11}|$. The matching level remains unaffected for $R \lessapprox 2$ mm and below $|S_{11}| < -10$ dB for up to 2.5 mm PEC capsule radius that represents 432 µm distance from the ground plane to the PEC capsule. Generally, it means that if capsule components will be in direct contact with the antenna, there might be a negative effect on its performance. To avoid it, a general guideline is to keep a safe distance of about 400 µm to the antenna, especially near the slots in its ground plane. This can be achieved, for instance, by using small ceramic spacers with the permittivity roughly close to the filling material (pure water with $\varepsilon_r = 78.4$).

Robustness of the antenna to the circuitry is reduced compared to the one proposed in [21]. However, the latter takes about 24% of the capsule volume whereas our design requires less than 4%.

5.6.3 Application to Endoscopy

For applications to endoscopy , at least one ending of a capsule must be transparent to house a camera and LEDs. The influence of the camera itself on the antenna impedance is negligible according to Section 5.6.2. To analyze the effect of replacing one alumina half-sphere of the capsule by a transparent cap, we have modeled the cap as made of biocompatible polyvinyl chloride (PVC, $\varepsilon_r = 2.6$, $\tan\delta = 0.003$, Figure 5.15a). The inner space is filled with either air or pure water. As endoscopy capsules are intended to be swallowed, the phantom EM properties are the GI average (Table 5.1).

Figure 5.15b shows the reflection coefficients of the capsule with one transparent

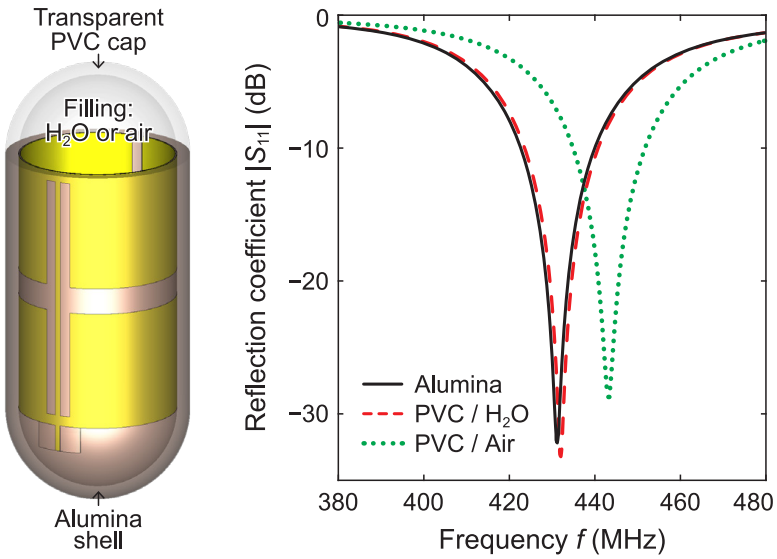

(a) (b)

Fig. 5.15: Application of the antenna to endoscopy. (a) Capsule antenna with a transparent cap. The PVC cap may be filled with either air or water. (b) Reflection coefficients $|S_{11}|$ of the antenna (average GI phantom) in the full alumina shell, with the cap filled with air or with water.

ending. If the half-sphere is filled with pure water (as for the reference design), the effect on impedance is insignificant. Filling the half-sphere with air raises the resonance frequency. However, the matching level at the operating band remains about −10 dB.

5.6.4 Interference with Neighboring Devices

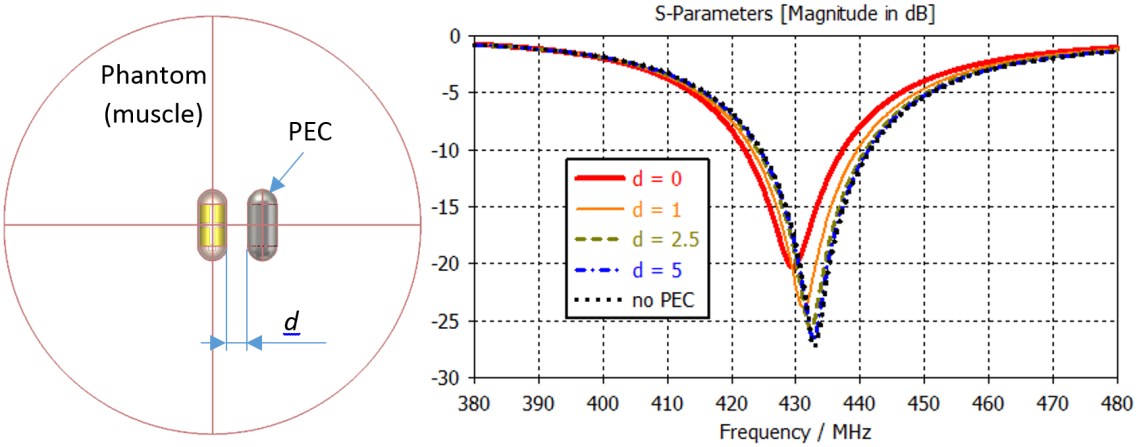

Fig. 5.16: Influence of Other Devices in Proximity. (a) Numerical model. (b) Reflection coefficients $|S_{11}|$ of the antenna (muscle-equivalent phantom) for the various distances d to the PEC capsule.

For some applications, two or more in-body devices may operate in close proximity. The metallic components contained in these devices (e.g. other antennas) can affect the impedance of the antenna.

We have modeled the proximity of a conductive object by putting a PEC capsule of the same dimensions (17 mm $\times \varnothing$7 mm) next to the antenna. Then, we performed a parametric sweep over the distance d between the two. The matching remains below $|S_{11}| < -10$ dB even for the PEC in direct contact with the capsule ($d = 0$).

5.6.5 Performance in Realistic Phantom

To evaluate the antenna radiation performance in various application scenarios, we simulated the antenna in the anatomically-realistic CST Female Visible Human model "Nelly". Four different locations have been studied (Figure 5.12b): 1) head—implanted in the highest permittivity and highest loss environment, the capsule close to the body surface; 2) colon—ingested with the capsule deep in the body; 3) stomach—ingested, at medium depth and close to the muscle layer; and 4) fat layer in the abdominal region—implanted in the lowest permittivity tissue and close to the body surface.

The maximum realized gains are the following: −22.6 dBi (head), −24.7 dBi (colon), −26.3 dBi (stomach), and −30 dBi (fat). Even though close to the body surface (less attenuation in the tissue), the lowest gain in fat is due to the poorer matching (Figure 5.11a) and reduced dielectric loading (Fig. 5.2). Figs. 5.12c and 5.12d show the directivity patterns of the capsule in the phantom. The radiation pattern strongly depends on the capsule position in the body. The closer the implantation is to the surface, the more the antenna is omnidirectional. As the deep in-body location is concerned—for instance in the colon—the maximum radiation intensity is directed to the closest boundary of the body, and the minimum faces opposite. The front-to-back ratio is about –10 dB to –15 dB.

5.6.6 Link Budget Calculation

Radiation of in-body antennas strongly depends on the capsule position inside a body [30]. In other words, the antenna and the body forms together a radiative system. Therefore, the Tx antenna total gain G_t includes losses in a human body, and the operating distance d is evaluated from the surface of the body to exterior equipment. Under far-field conditions, we can calculate the link-budget, or, equivalently, the signal-to-noise ratio SNR at Rx of exterior equipment using the Friis formula [31]–[33] as

$$\mathrm{SNR}_\mathrm{dBm} = P_{\mathrm{r,\,dBm}} - P_{\mathrm{noise,\,dBm}} \tag{5.3a}$$

$$P_{\mathrm{r,\,dBm}} = P_{\mathrm{t,\,dBm}} + G_{\mathrm{t,\,dBi}} + G_{\mathrm{r,\,dBi}} - \mathrm{loss}_\mathrm{dBm} \tag{5.3b}$$

$$\mathrm{loss}_\mathrm{dBm} = e_{\mathrm{p,\,dB}} + \mathrm{PL}_\mathrm{dBm} \tag{5.3c}$$

$$\mathrm{PL}_\mathrm{dBm} = 10n \log\left(\frac{d}{d_0}\right) + 10 \log\left(\frac{4\pi d}{\lambda_0}\right)^2 + X_\mathrm{dBm} \tag{5.3d}$$

where P_r is the power received by Rx, $P_\mathrm{noise} = -100$ dBm is the total power of background noise [33], P_t is the power available at Tx, $G_\mathrm{r} = 2$ dBi is the Rx antenna total gain (a typical well-matched dipole antenna), e_p is the polarization mismatch factor, PL is the path loss, n is the path loss exponent, $d_0 = 1$ m is the reference distance [34], $\lambda_0 = 0.69$ m is the free space wavelength, and X is the shadowing factor: a zero-mean Gaussian variable with standard deviation s.

Table 5.2: Signal-to-Noise Ratios in Four in-Body Sites at 10 m Operating Distance for Free-Space, LOS, and NLOS Propagation

SNR (dBm)	**Head**	**Colon**	**Stomach**	**Fat**
Optimal case ($G_{\mathrm{t,max}}, n = 2$)	18.3	16.2	14.6	10.9
Worst case ($G_{\mathrm{t,min}}, n = 2$)	14.1	0.7	−1.8	−9.3
Indoor LOS ($G_{\mathrm{t,avg}}, n = 1.5$)	22.6	19.4	17.7	9.1
Indoor NLOS ($G_{\mathrm{t,avg}}, n = 3$)	7.6	4.4	2.7	−5.9

Due to the presence of human tissues, the intrinsic omnidirectional radiation pattern of the antenna (Fig. 5.12a) becomes a directive one (Figs. 5.12c and 5.12d). Therefore, the SNR in communication links strongly depends on the orientation of a human subject with respect to the receiver. It requires analyzing both optimal- and worst-case radiation scenarios for four capsule locations from Section **??**.

The maximum allowable P_{t} is limited by the safety guidelines and the equivalent isotropically radiated power (EIRP) restrictions to mitigate EM interference with other devices. The $\mathrm{EIRP}_{\max}\,(434\,\mathrm{MHz}) = 12.1$ dBm [35]. However, the low gain of in-body antennas ($G \lesssim -15$ dBi) along with maximum Tx power of miniature button-cell-powered microcontrollers (for instance, $P_{\mathrm{t}} = 13$ dBm for SI 1084 MCU) results in the EIRP $\lesssim 0$ dBi. In addition, extremely low power Tx power ensure small specific absorption rates (SAR) and so the patient's safety. In this study, $P_{\mathrm{t}} = 10$ dBm.

We consider four communication scenarios [33], [36]: 1) optimal free-space propagation ($G_{\mathrm{t,\,max}}, n = 2$), 2) worst-case free-space ($G_{\mathrm{t,\,min}}, n = 2$), 3) line-of-sight (LOS) indoor ($G_{\mathrm{t,\,avg}}, n = 1.5$), and 4) non-line-of-sight (NLOS, $G_{\mathrm{t,\,avg}}, n = 3$). The polarization mismatch e_{p} and shadowing X factors are considered zero is this study.

Table 5.2 lists the SNRs at $d = 10$ m for the aforementioned scenarios. The antenna ensures 10 m operating distance when transmitting from a head or colon for all considered scenarios. In stomach, SNR ≈ 0 in the back of a body for free-space propagation (Fig. 5.12c). In fat, SNR < 0 for this scenario; in addition, SNR < 0 for NLOS case. At 7 m distance, SNR > 0 for all scenarios and tissues. LOS transmission holds up to 14 m for all tissues.

5.7 Prototyping and Measurements

Following the numerical analysis and optimization, we have built a prototype to evaluate the antenna performance experimentally for the 434 MHz mid-ISM band.

5.7.1 Prototype Manufacturing

We shaped the antenna prototype with laser ablation (LPKF ProtoLaser S) of 9 µm copper cladding on a 50 µm Rogers ULTRALAM® 3850HT substrate (Figure 5.17a). The printed design was soldered to a 100 mm 50 Ω semi-rigid coaxial cable terminated with an SMA connector. Then, the antenna was bent and inserted into a 17 mm×⌀7 mm Degussit® AL23 cylinder (Figure 5.17b). The opening on the cable side was sealed with Araldite® 2011 epoxy paste. Next, the capsule was filled with

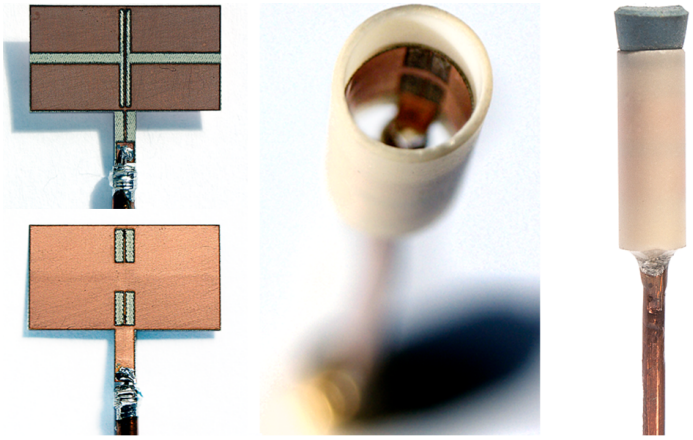

(a) (b) (c)

Fig. 5.17: Capsule antenna prototype. (a) Top and bottom views of the planar antenna soldered to a 50 Ω coaxial cable. (b) Antenna in the 0.5 mm thick alumina encapsulation. (c) Final assembly filled with pure water and sealed at both ends.

pure water, outgassed, and sealed at the other end with a rubber plug (Figure 5.17c).

To characterize the radiation performance, a silicone-sealed ⌀10 mm polyamide tube was fitted between the capsule and the connector to insulate the cable from the phantoms.

5.7.2 Phantoms

Table 5.3: Phantoms Used for Measurements: EM Properties at 434 MHz and Concentrations for Water–Sucrose–NaCl Solutions

	Muscle	**Avg GI**	**Max**
Relative permittivity ε_r	56.9	63.0	77.3
Conductivity σ (S·m^{-1})	0.8	1.0	2.3
Concentration of Sugar (%)	51.3	44.6	40.7
Concentration of NaCl (%)	1.53	1.44	2.56

To experimentally validate the antenna performance in terms of impedance, robustness, and radiation, we prepared three liquid phantoms with muscle-equivalent, maximum, and time-averaged GI EM properties (see Section 2.1.2). We used pure deionized water as a base component, sucrose to reduce the permittivity ε_r, and pure NaCl to increase the conductivity σ. To define the concentration of each ingredient, we used a full factorial experiment design along with the response surface optimization methodology (see Section 2.3.2). Table 5.3 lists the final concentrations. The EM properties of the phantoms were measured using the SPEAG DAK kit with DAK-12 probe [23].

To evaluate the radiation performance, we used a ⌀100 mm spherical glass container filled with muscle-equivalent liquid, sealed with a rubber plug, and fixed using a Rohacell® IG foam ($\varepsilon_r = 1.05$, $\tan\delta = 0.0017$). The SMA connector locates outside of the sealed container easing the connection to measurement equipment. Section 2.4 gives the detailed description of the phantom set-up.

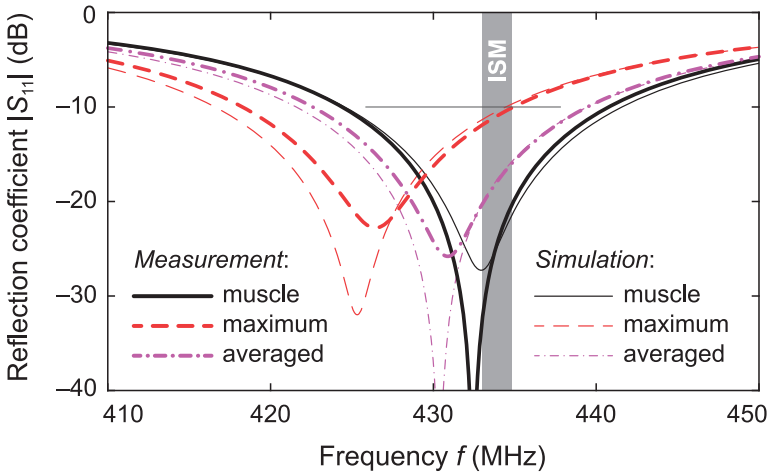

Fig. 5.18: Measured and computed reflection coefficients of the antenna in phantoms with muscle-equivalent, maximum, and averaged GI EM properties.

5.7.3 Antenna Reflection Coefficient

We used the Agilent PNA-X vector network analyzer (VNA) to measure the antenna reflection coefficient. As the VNA was calibrated in the reference plane of the SMA connector, the cable influence on the impedance was de-embedded during the post-processing using CST Design Studio®. The capsule model (Figure 5.1) is in perfect agreement with the prototype model that takes into account the rubber plug ($\varepsilon_r = 3$) and the cylindrical-shaped alumina shell.

Figure 5.18 shows the measured reflection coefficients for three liquid phantoms with properties listed in Table 5.3. The experimental results agree fairly well with the simulations. As the substrate laser ablation provides lower precision than photolithography, better agreement can be achieved using more precise manufacturing methods.

5.7.4 Radiation Performance

Characterization of both electrically and physically small antennas remains a major challenge. The antenna under test (AuT) couples strongly to a feeding cable that leads to impaired measured data [37]. The current induced on the cable affects the radiation pattern and matching, making difficult, if not impossible, to separate the antenna radiation from the one of the cable. Different approaches allow minimizing this effect using a balun [38], an electro-optical converter [39], [40], or performing measurements using a monostatic scattering characterization of the antenna connected to standard terminations [41]. For in-body antennas, the problem gets more complicated as, in addition to these sources of corruption, the antenna has to be measured in a lossy phantom.

We characterized the antenna using the direct illumination far-field technique. Section 2.4 overviews our approach and Figure 5.19(a) depicts the measurement setup. The AuT is located inside a glass spherical container filled with a reference material (liquid phantom). The vertically positioned AuT and its container constitute the device under test (DuT). The DuT localizes at a distance from the measurement horn fulfilling the far-field criteria. An electro-optical converter (enprobe LFA-3 [42]) feeds the DuT. So, an optical fiber replaces the RF cable inside

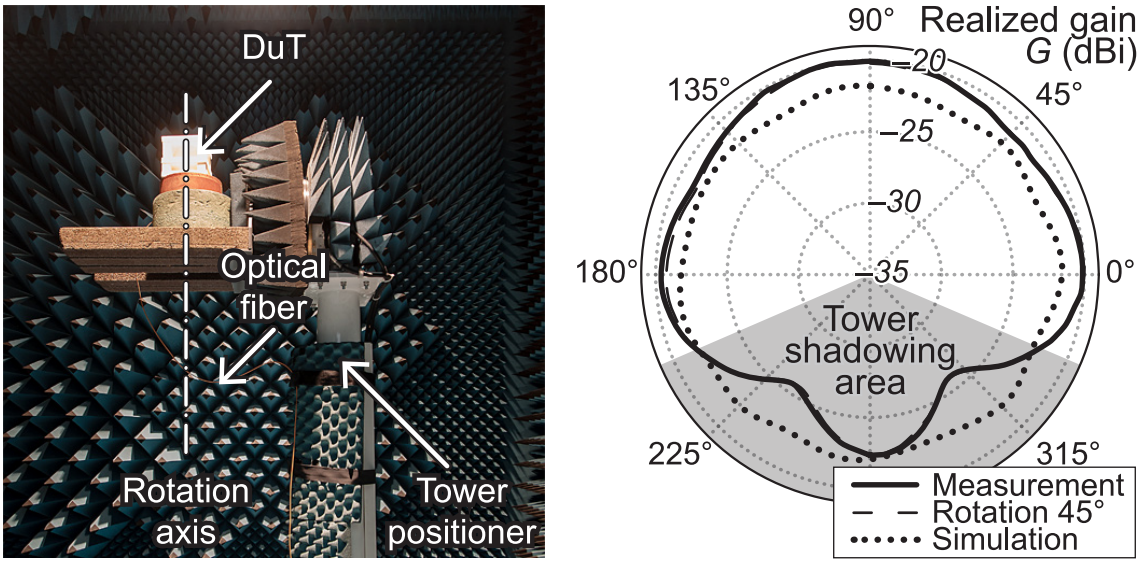

(a) (b)

Fig. 5.19: Far-field characterization of the antenna. (a) The AuT mounted on the tower positioner and fed using an optical fiber. (b) Measured co-pol (vertical) radiation patterns of the AuT contained in the ⌀100 mm sphere filled the liquid with muscle-equivalent EM properties.

the anechoic chamber and minimizes the main source of signal corruption.

The DuT was mounted on the positioner using an L-shape foam block attached to the tower (Figure 5.19a). A white foam frame (Rohacell® IG) ensured the vertical alignment of the AuT within the DuT. Additional foam cylinders elevated the DuT in order to reduce the shadowing effect of the tower during the measurement process.

We measured the radiation pattern in the azimuth plane, for both co-polarization and cross-polarization components. The frequency sweep was set up from 300 MHz to 600 MHz in order to ensure that the maximum radiation occurs at the f_{res}. The estimation of the DuT realized gain used the gain substitution technique employing a reference antenna of known gain (ETS-Lindgren 3164-06 [43]).

Figure 5.19b shows the far-field characterization results. The realized gain is −19.6 dBi (vertical polarization), and −33.4 dBi in X-pol. The radiation pattern is consistent with the simulated one. Nevertheless, one can notice the backward radiation distortion due to the shadowing effect of the tower positioner for an angular range. Moreover, the magnitude is decreasing for two specific azimuth angle values. To verify whether this effect is indeed due to the shadowing and not the intrinsic pattern of the DuT, we have taken into account the axial symmetry of the DuT and measured the radiation pattern at the original azimuthal position of the DuT as well as rotated 45°. The same defective angular range appears for both positions (Figure 5.19b) proving that the diffraction and shadowing effects of the tower affect backward radiation.

Table 5.4: Design, Operating Frequency, Capsule Size, and Radiation Performance in the Given Phantom of Capsule Antennas Reported in Literature

Ref.	Antenna type	f_0 (MHz)	Size (mm)	G (dBi)	Phantom: tissue, shape, size (cm)
—	Microstrip	434	$17 \times \varnothing 7$	-22	Muscle, sphere, $\varnothing 10$
[21]	Stacked spiral	*dual-band*	$32 \times \varnothing 10$	-29^*	Muscle, cylinder†, $11 \times \varnothing 80$
[27]	Stacked helical	2450	$26 \times \varnothing 11$	-32	Muscle, cube, 100^3
[4]	Loop w/ CSRR	*multi-band*	$25 \times \varnothing 10$	$-25^\ddagger$	Mus., ellip. cyl., $\varnothing 18 \times \varnothing 10 \times 5$
[28]	Assym. dipole	1400	$26 \times \varnothing 11$	-26	Muscle, box§, $20 \times 30 \times 35$
[6]	Assym. dipole	402	$24 \times \varnothing 11$	-37	Skin, cube¶, 18^3
[44]	Microstrip	434	$17 \times \varnothing 7$	-33	$\varepsilon_r = 49.6$ $\sigma = 0.51$, cyl., $\varnothing 20$
[29]	Microstrip	402	$24 \times \varnothing 10$	-30	Muscle, cube, 10^3

* The antenna operates in MedRadio 403 MHz and ISM 2.45 GHz bands. The gain is for 403 MHz.
† The capsule is off-centered, distance to a surface ≈ 10 mm.
‡ The bandwidth covers from MedRadio 403 MHz to ISM 2.45 GHz bands. The gain is for 434 MHz.
§ The capsule is off-centered, distance to a surface is not given.
¶ The capsule is off-centered, distance to a surface is 3 mm.

5.8 Summary

In this chapter, we designed and characterized a low-profile conformal microstrip antenna suitable for a wide range of in-body capsule applications. Ultra-miniature dimensions, enhanced robustness and efficiency (compared to counterparts) allow to employ it for both implantable and ingestible applications. This capsule antenna may also be considered for animal biotelemetry since the EM properties of some animal tissues may differ from those of humans, and the high robustness of the antenna reduces partially the impedance detuning.

In addition, we proposed and experimentally validated the new design involving an in-body narrowband microstrip antenna combined with a high permittivity capsule shell. In this way, it is no longer necessary to increase the antenna bandwidth to cover the detuning range at the expense of radiation efficiency. We have chosen alumina (Al_2O_3) as encapsulation layer material since it is widely available and biocompatible. By choosing a higher permittivity material, one can further increase the radiation efficiency, improve robustness, or decrease the capsule shell thickness. The antenna, of course, has to be optimized to operate within the modified encapsulation. However, the proposed approach comes at a price. The design requires using ceramic capsule shell and a high permittivity filling that increase the cost.

The realized gain of the capsule exceeds the existing counterparts by about 3 dBi (Table 5.4) whereas it is more miniature and robust. It should be noted, however, that an accurate comparison of the radiation performance requires all counterparts to be evaluated within the same environment: specifically, using a phantom with identical geometry and EM properties. Spherical shapes are of choice, as they do not affect the intrinsic radiation pattern of the antenna (see Section 5.4.2). The phantom diameter should be large enough not to perturb the antenna impedance; however, a too big phantom will strongly attenuate a signal reducing the signal-to-noise ratio affecting the measurement accuracy. Hence, in this study we have chosen to work with a $\varnothing 100$ mm phantom.

Initial antenna synthesis used the hybrid analytical–numerical methodology. This

approach accelerates the design by reducing the optimization routine (to reach a given f_{res}) complexity down to one degree of freedom. The subsequent parametric studies and optimization require full-wave numerical modeling. Adaptive-FEM tetrahedral mesh allowed evaluating the antenna performance in realistic scenarios using an anatomical heterogeneous phantom and avoiding the staircase effect—one of the major drawbacks of voxelized phantoms. In such manner, one can adequately estimate the antenna realized gain and hence the link budget for a specific application.

The proposed antenna remains well-matched for the whole range of human tissue EM properties and is robust to the presence of integrated components too. This allows using the antenna "as is" for a given in-body application in conjunction with a microcontroller or an RF circuit of choice. The antenna is well matched for a standard input impedance of 50 Ω for both mid-ISM and MedRadio band versions. It contributes thus to the further development of a new generation of miniature in-body devices that involves a complex and dense integration of sensors, logic, and power sources.

Bibliography

[1] F. Merli, B. Fuchs, J. R. Mosig, and A. K. Skrivervik, "The effect of insulating layers on the performance of implanted antennas," *IEEE Transactions on Antennas and Propagation*, vol. 59, no. 1, pp. 21–31, 2011.

[2] J. Volakis, C.-C. Chen, and K. Fujimoto, *Small Antennas: Miniaturization Techniques & Applications*. McGraw Hill Professional, Jun. 2010.

[3] S. Gabriel, R. W. Lau, and C. Gabriel, "The dielectric properties of biological tissues: II. Measurements in the frequency range 10 Hz to 20 GHz," *Physics in Medicine and Biology*, vol. 41, pp. 2251–2269, Nov. 1996.

[4] R. Alrawashdeh, Y. Huang, M. Kod, and A. Sajak, "A broadband flexible implantable loop antenna with complementary split ring resonators," *IEEE Antennas and Wireless Propagation Letters*, vol. 14, pp. 1506–1509, 2015.

[5] M. M. Suzan, K. Haneda, C. Icheln, A. Khatun, and K. Takizawa, "An ultra-wideband conformal loop antenna for ingestible capsule endoscope system," in *10^{th} European Conference on Antennas and Propagation (EuCAP 2016)*, Davos, Switzerland, Apr. 2016, pp. 1–5.

[6] L.-J. Xu, Y.-X. Guo, and W. Wu, "Bandwidth enhancement of an implantable antenna," *IEEE Antennas and Wireless Propagation Letters*, vol. 14, pp. 1510–1513, 2015.

[7] S. Best, "Bandwidth and the lower bound on Q for small wideband antennas," in *IEEE Antennas and Propagation Society International Symposium 2006*, Albuquerque, NM USA, Jul. 2006, pp. 647–650.

[8] A. K. Skrivervik, "Implantable antennas: The challenge of efficiency," in *7^{th} European Conference on Antennas and Propagation (EuCAP 2013)*, Gothenburg, Sweden, Apr. 2013, pp. 3627–3631.

[9] A. Kiourti, J. Costa, C. Fernandes, and K. Nikita, "A broadband implantable and a dual-band on-body repeater antenna: Design and transmission performance," *IEEE Transactions on Antennas and Propagation*, vol. 62, no. 6, pp. 2899–2908, Jun. 2014.

[10] BodyCap Medical, *E-Celsius*. [Online]. Available: `http://www.bodycap-medical.com/`.

[11] T.-F. Chien, C.-M. Cheng, H.-C. Yang, J.-W. Jiang, and C.-H. Luo, "Development of Nonsuperstrate Implantable Low-Profile CPW-Fed Ceramic Antennas," *IEEE Antennas and Wireless Propagation Letters*, vol. 9, pp. 599–602, 2010.

[12] T. Dissanayake, K. Esselle, and M. Yuce, "Dielectric Loaded Impedance Matching for Wideband Implanted Antennas," *IEEE Transactions on Microwave Theory and Techniques*, vol. 57, no. 10, pp. 2480–2487, Oct. 2009.

[13] Computer Simulation Technology AG, *CST Microwave Studio*. [Online]. Available: `https://www.cst.com/Products/CSTMWS` (visited on 08/06/2016).

[14] M. T. Sebastian, *Dielectric Materials for Wireless Communication*. Elsevier, Jul. 2010.

[15] M. Makimoto and S. Yamashita, "Bandpass filters using parallel coupled stripline stepped impedance resonators," *IEEE Transactions on Microwave Theory and Techniques*, vol. 28, no. 12, pp. 1413–1417, Dec. 1980.

[16] M. Sagawa, M. Makimoto, and S. Yamashita, "Geometrical structures and fundamental characteristics of microwave stepped-impedance resonators," *IEEE Transactions on Microwave Theory and Techniques*, vol. 45, no. 7, pp. 1078–1085, Jul. 1997.

[17] D. M. Pozar, *Microwave engineering*, 4th ed. Hoboken, NJ: Wiley, 2012.

[18] P. Karban, F. Mach, P. Kus, D. Panek, and I. Dolezel, "Numerical solution of coupled problems using code Agros2D," *Computing*, vol. 95, no. 1, pp. 381–408, 2013.

[19] J. Dahele, R. Mitchell, K. Luk, and K. Lee, "Effect of curvature on characteristics of rectangular patch antenna," *Electronics Letters*, vol. 23, no. 14, pp. 748–749, Jul. 1987.

[20] J. S. Ho, A. J. Yeh, E. Neofytou, S. Kim, Y. Tanabe, B. Patlolla, R. E. Beygui, and A. S. Y. Poon, "Wireless power transfer to deep-tissue microimplants," *PNAS*, vol. 111, pp. 7974–7979, 2014.

[21] F. Merli, L. Bolomey, J. Zurcher, G. Corradini, E. Meurville, and A. Skrivervik, "Design, realization and measurements of a miniature antenna for implantable wireless communication systems," *IEEE Transactions on Antennas and Propagation*, vol. 59, no. 10, pp. 3544–3555, Oct. 2011.

[22] S. Koulouridis, G. Kiziltas, Y. Zhou, D. Hansford, and J. Volakis, "Polymer–ceramic composites for microwave applications: Fabrication and performance assessment," *IEEE Transactions on Microwave Theory and Techniques*, vol. 54, no. 12, pp. 4202–4208, Dec. 2006.

[23] Schmid & Partner Engineering AG, *Dielectric Assessment Kit*. [Online]. Available: `http://www.speag.com/products/dak/dielectric-measurements/` (visited on 08/06/2016).

[24] S. Lee, J. G. Hyun, H. Kim, and K. W. Paik, "A study on dielectric constants of epoxy/SrTiO3 composite for embedded capacitor films (ECFs)," *IEEE Transactions on Advanced Packaging*, vol. 30, no. 3, pp. 428–433, Aug. 2007.

[25] A. Shapiro, R. Lutomirski, and H. Yura, "Induced fields and heating within a cranial structure irradiated by an electromagnetic plane wave," *IEEE Transactions on Microwave Theory and Techniques*, vol. 16, no. 2, pp. 187–196, 1968.

[26] D. Nikolayev, "Radio frequency resonances inside a human head," *Computational Problems of Electrical Engineering*, vol. 3, no. 1, pp. 73–78, 2013.

[27] C. Liu, Y.-X. Guo, and S. Xiao, "Circularly polarized helical antenna for ISM-band ingestible capsule endoscope systems," *IEEE Transactions on Antennas and Propagation*, vol. 62, no. 12, pp. 6027–6039, Dec. 2014.

[28] P. Izdebski, H. Rajagopalan, and Y. Rahmat-Samii, "Conformal ingestible capsule antenna: A novel chandelier meandered design," *IEEE Transactions on Antennas and Propagation*, vol. 57, no. 4, pp. 900–909, Apr. 2009.

[29] K. A. Psathas, A. Kiourti, and K. S. Nikita, "A novel conformal antenna for ingestible capsule endoscopy in the MedRadio band," in *34th Progress in Electromagnetics Research Symposium (PIERS 2013)*, Stockholm, Sweden, Aug. 2013.

[30] L. Xu, M.-H. Meng, H. Ren, and Y. Chan, "Radiation characteristics of ingestible wireless devices in human intestine following radio frequency exposure at 430, 800, 1200, and 2400 MHz," *IEEE Transactions on Antennas and Propagation*, vol. 57, no. 8, pp. 2418–2428, Aug. 2009.

[31] A. Kiourti, K. A. Psathas, and K. S. Nikita, "Implantable and ingestible medical devices with wireless telemetry functionalities: A review of current status and challenges," *Bioelectromagnetics*, vol. 35, no. 1, pp. 1–15, Jan. 2014.

[32] H. Rajagopalan and Y. Rahmat-Samii, "Wireless medical telemetry characterization for ingestible capsule antenna designs," *IEEE Antennas and Wireless Propagation Letters*, vol. 11, pp. 1679–1682, 2012.

[33] A. Sani, A. Alomainy, and H. Yang, "Numerical characterization and link budget evaluation of wireless implants considering different digital human phantoms," *IEEE Transactions on Microwave Theory and Techniques*, vol. 57, pp. 2605–2613, Sep. 2009.

[34] A. Alomainy and Y. Hao, "Modeling and characterization of biotelemetric radio channel from ingested implants considering organ contents," *IEEE Transactions on Antennas and Propagation*, vol. 57, no. 4, pp. 999–1005, Apr. 2009.

[35] "Short Range Devices (SRD) operating in the frequency range 25 MHz to 1000 MHz," ETSI EN 300 220, Standard, Nov. 2016.

[36] A. Kiourti and K. Nikita, "Miniature scalp-implantable antennas for telemetry in the MICS and ISM Bands: Design, safety considerations and link budget analysis," *IEEE Transactions on Antennas and Propagation*, vol. 60, no. 8, pp. 3568–3575, Aug. 2012.

[37] L. Huitema, C. Delaveaud, and R. D'Errico, "Impedance and radiation measurement methodology for ultra miniature antennas," *IEEE Transactions on Antennas and Propagation*, vol. 62, no. 7, pp. 3463–3473, Jul. 2014.

[38] S. Pivnenko, J. Zhang, A. Khatun, T. Laitinen, and J. Carlsson, "Characterization of small antennas for hearing aids by several measurement techniques," in *Proceedings of the Fourth European Conference on Antennas and Propagation*, Barcelona, Spain, Apr. 2010, pp. 1–5.

[39] T. H. Loh, D. Cheadle, and L. Rosenfeld, "Radiation pattern measurement of a low-profile wearable antenna using an optical fibre and a solid anthropomorphic phantom," *Electronics*, vol. 3, no. 3, pp. 462–473, Aug. 2014.

[40] M. Alexander, T. H. Loh, and A. L. Betancort, "Measurement of electrically small antennas via optical fibre," in *Antennas and Propagation Conference (LAPC 2009)*, Loughborough, UK, Nov. 2009, pp. 653–656.

[41] W. Wiesbeck and E. Heidrich, "Wide-band multiport antenna characterization by polarimetric RCS measurements," *IEEE Transactions on Antennas and Propagation*, vol. 46, no. 3, pp. 341–350, Mar. 1998.

[42] enprobe GmbH, *LFA-3 Analog fiber optic link*. [Online]. Available: `http://www.enprobe.de/products_FO-Links.htm` (visited on 07/02/2016).

[43] ETS-Lindgren, *3164-06 Open boundary quad-ridged horn*. [Online]. Available: `http://www.ets-lindgren.com/3164-06` (visited on 07/14/2016).

[44] Y. Mahe, A. Chousseaud, M. Brunet, and B. Froppier, "New flexible medical compact antenna: Design and analysis," *International Journal of Antennas and Propagation*, vol. 2012, May 2012.

Chapter 6

Dual-Band Capsule Antenna and *In Vivo* Sensing of EM Properties

Contents

6.1 Introduction 134

6.2 Antenna Design 134

6.2.1 Biological Tissue Environment 134

6.2.2 Theoretical Considerations 135

6.2.3 Antenna Synthesis 135

6.2.4 Material Choice and Capsule Weight Estimation 137

6.3 Dual-Band Capsule Antenna 139

6.3.1 Numerical Modeling and Optimization 139

6.3.2 Antenna Performance 139

6.3.3 Prototyping and Measurements 142

6.4 *In Vivo* Sensing of EM Properties 144

6.4.1 Introduction 144

6.4.2 Methodology Description 145

6.4.3 Sensing Electromagnetic Properties via the Variation of Antenna Impedance 146

6.5 Summary 146

6.1 Introduction

Typically, an in-body device has a wireless link functionality to transmit biotelemetry data or to receive or modify operational and treatment instructions. As is shown in Chapter 3, RF transmission in VHF–SHF bands yields the longest range and highest data transfer rates for in-body wireless devices [1]–[7].

As for the power source, the straightforward approach is to use the batteries or percutaneous (i.e. through the skin) wires. However, any battery has a limited energy storage and life span, and percutaneous links are susceptible to infection and reliability problems [8]. Wireless power transfer (WPT), on the other hand, provides the energy for indefinite periods without the risk of infection and need to replace the device for recharging. Alternative means of powering have been proposed as well, including optical, ultrasound, or harvesting from biological sources. Nevertheless, WPT through RF is the most established one [9]. A dual-band RF antenna can integrate both data transmission and WPT functionality increasing the available space inside an in-body device. A robust capsule dual-band antenna is presented in [6]. Several planar double-band designs are reported for implantable applications, for instance [10]–[13].

The antenna performance—for both data and power transfer—strongly depends on EM properties of the surrounding tissues. Thus, antennas must be optimized to perform optimally (i.e. remain efficient and well matched) within a specified range of tissue EM properties. This range typically depends on the location of the device inside the body and therefore on the application scenario.

Here, I introduce a dual-band low-profile conformal microstrip antenna suitable for a wide range of in-body capsule applications. Increased robustness and high efficiency (compared to counterparts) allow to employ it for implantable and ingestible applications (e.g. BodyCAP e-Celsius® capsule [14]). The gain of the capsule exceeds its counterparts by about 9 dBi. In addition, I propose an approach to in-body sensing of physiological parameters via EM properties of tissue adjacent to the capsule. The novelty of this approach consists in realizing a wireless miniature in-body device with the capability of simultaneous EM properties sensing and trough-body data transmission.

6.2 Antenna Design

6.2.1 Biological Tissue Environment

The biological environment considered for this antenna is identical to the one reported in the previous chapter (see Section 5.2.1) except now we have to account for different tissue EM properties for the ISM 2.45 GHz band.

A universal dual-band in-body capsule antenna must remain operable in the whole specified range of tissue EM properties for both frequency ranges. Same as before, we have prioritized ensuring perfect matching for the highest overall EM properties. The acceptable matching must though be maintained for the overall minimum case (fat tissue). When implanted in fat, the antenna is close to the surface of a body and surrounded by the environment with lower loss ($\sigma = 0.08$ S·m^{-1} at 434 MHz and $\sigma = 0.27$ S·m^{-1} at 2.45 GHz) compared to muscle, for instance ($\sigma = 0.81$ S·m^{-1} at 434 MHz and $\sigma = 1.74$ S·m^{-1} at 2.45 GHz) [15]. In this way, the

reduced attenuation loss in the tissue would compensate for the increased antenna mismatch loss.

6.2.2 Theoretical Considerations

Taking into account the theoretical studies on in-body antenna radiation efficiency (Chapter 3), the following is necessary to further improve the radiation efficiency η.

- Increase the electrical size of the antenna ka by maximizing the surface area (physical size) of the antenna within a capsule. It may require increasing the length of the capsule.
- Increase the electrical size of the antenna ka by loading it with low loss high permittivity material (Figure 5.2).
- Decouple the antenna from tissue (results in higher Q).
- Increase the substrate thickness of a microstrip antenna to compensate for the reduced bandwidth due to the decoupling (see Section 4.8).
- Improve robustness to avoid impedance detuning.
- Design a dual- or multi-band antenna. It enables frequency hopping to maximize the efficiency if the depth of implantation varies (see Chapter 3).

With these in mind, we proceed to the synthesis of the antenna.

6.2.3 Antenna Synthesis

Miniaturization is required to fit the 434 MHz ($\lambda/2 \approx 34$ cm) microstrip antenna section within the 28 mm$\times\varnothing$9 mm capsule. Again, I use the quater-wave stepped impedance resonator (SiR, Figure 4.4) technique [16], [17] with one impedance step—low-to-high—in order to reduce the antenna size and match the antenna input impedance to $Z_{\text{in}} = 50\,\Omega$. Section 4.3 gives the synthesis and dimensionless procedure for 434 MHz section with the exception of the modeling procedure of characteristic impedance Z_c. The model uses 2D cross-section of the already folded antenna inside a capsule within a circular phantom of radius R (Figure 5.8). In this way, not only the effect of the phantom, but also the one of antenna bending was already taken into account before continuing to the full-wave analysis and optimization.

The 2.45 GHz antenna section radiates as a half-wave patch and can be coupled to the 434 MHz section by, for instance, a microstrip line. The approximate length L_{Z_3} of the section for the $f_0 = 2.45$ GHz operating frequency can be estimated using [18, p. 37]

$$L \approx \frac{1}{2f_0\sqrt{\varepsilon_0\varepsilon_r^{\text{eff}}}}, \tag{6.1}$$

where $\varepsilon_r^{\text{eff}}$ is the effective relative permittivity of the antenna environment.

Larger ground plane (compared to the 434 MHz section) allows us controlling the input impedance and the radiation pattern at 2.45 GHz via the section width W_{Z_3}. The wider the patch becomes the lower the input impedance is.

Description of the Design

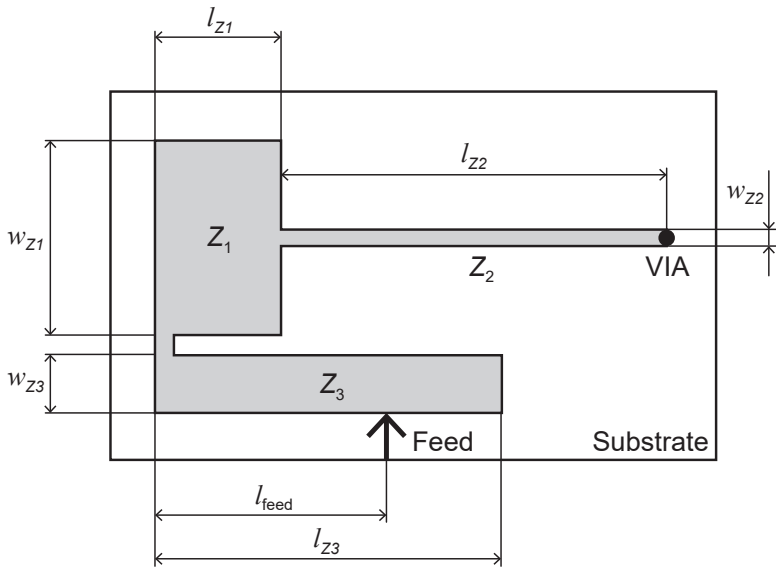

Fig. 6.1: Antenna element geometry and parametric dimensions.

The antenna is realized on a thin substrate with a full ground plane. The substrate is made of either a flexible material (e.g. to be rolled and conform to the inner surface of a capsule) or a rigid one for planar devices. Figure 6.1 shows the geometry of the antenna. The rectangular element Z_1 of length l_{Z_1} and width w_{Z_1} is connected to both Z_2 and Z_3 microstrip elements. The Z_2 element of length l_{Z_2} and width w_{Z_2} is connected to Z_1 on one side and is short-circuited to the ground plane by means of a VIA on the other. The element Z_2 may be realized as a straight, serpentine, zigzag, or meander line in order to achieve the necessary electric length. The element Z_2 may also be realized as a co-planar line for further miniaturization and robustness, as in Chapter 4. The element Z_3 of length l_{Z_3} and width w_{Z_3} connects to Z_1 by means of a microstrip transition. The feed connects to the longer (non-radiating) edge of the element Z_3 at the distance l_{feed} from the origin of the antenna (on the left side on Figure 6.1).

The resonance frequencies are dependent on dimension ratios of the antenna elements Z_1, Z_2, and Z_3. The elements Z_1 and Z_2 operate as a quarter-wave stepped impedance resonator antenna and form the lower frequency resonance (434 MHz). By varying the widths w_{Z_1} and w_{Z_2} and their length ratio (w_{Z_2}/w_{Z_2}) while keeping the overall antenna length ($l_{Z_1} + l_{Z_2}$), one can tune the first resonant frequency f_{res} as well as match the antenna to given impedance at f_{res} (e.g. 50 Ω).

The Z_3 element radiate as a loaded half-wave patch for the higher operating frequencies (2.45 GHz). The resonance frequency is defined mostly by the length l_{Z_3}. The input impedance at f_{res} depends on the width w_{Z_3} and the feed location l_{feed}.

The substrate thickness affects mostly the impedance bandwidth as for patch antennas, especially at the lower resonance frequency.

The location of the feed point allows us forming an array of two or more antennas (identical or slightly different to increase the bandwidth). Whereas used as conformal antenna inside a capsule, the array configuration improves omnidirectionality for the higher resonance frequencies (at lower frequency the reported antenna

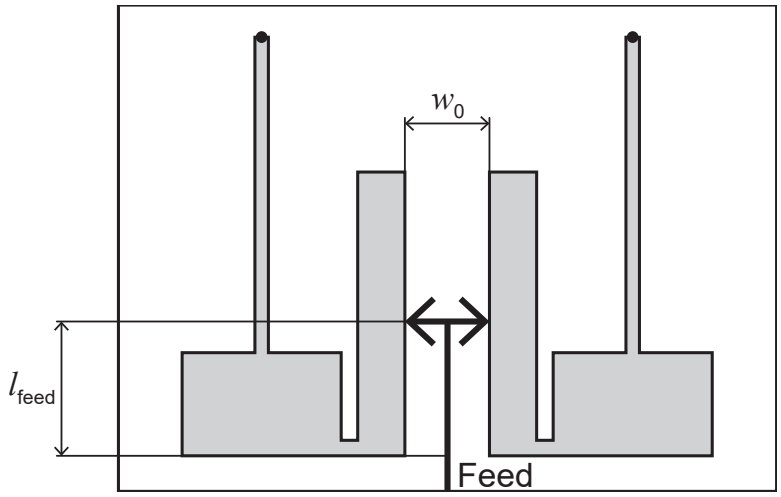

Fig. 6.2: Array of two mirrored elements.

is electrically small, hence omnidirectional). The impedance matching is achieved by adjusting the separation between elements w_0 and the feed position l_{feed}.

6.2.4 Material Choice and Capsule Weight Estimation

Capsule Size

An in-body device suitable for confortable ingestion and implantation sould be pill-sized. The minimal capsule dimensions are limited, as it may contain sensors, a microcontroller, and a power source. The smallest microcontrollers equipped with RF transceiver are about 4 mm wide. A power source could be a conventional battery (button cell, $\geqslant \varnothing 4.8$ mm) or an ultra-miniature wireless powering scheme, as, for instance, the 3.5 mm$\times\varnothing$2 mm device reported by Ho *et al.* [9].

Considering the necessary wiring of the components, an optional folding of the printed circuit board (PCB), and an eventual implementation of wireless powering scheme, I restricted the capsule inner diameter to $\varnothing$7 mm (Figure 5.1)—1 mm more than in previous chapter. The length defines the radius of the Chu sphere and thus the maximum achievable radiation efficiency. In contrary to the antenna reported in previous chapter (where the miniaturization was a key objective), I looked for the sizes of existing miniature in-body capsules (summarized in Section 1.4), averaged the largest ones, and rounded to the whole number resulting in 28 mm. The capsule size—28 mm$\times\varnothing$9 mm—is comparable to a pill and within the reasonable limits for both implantation and ingestion.

Printed Circuit Board

The antenna is designed for a 100 µm (4 mil) flexible substrate that conforms to the inner surface of the capsule. In this way, the extension of the same printed circuit board (PCB) may contain the device circuitry, as, for instance, the e-Celsius® capsule. As in the previous chapter, we considered three substrate materials that could be used interchangeably with minor changes to the antenna geometry: 1) Rogers ULTRALAM® 3850HT (liquid crystal polymer, $\varepsilon_r = 2.9$, $\tan\delta = 0.002$); 2) Rogers XT/duroid® 8000 (polyether ether ketone, $\varepsilon_r = 3.23$, $\tan\delta = 0.0035$); 3) DuPont

Pyralux® AP (polyimide, $\varepsilon_r = 3.4$, $\tan\delta = 0.002$).

Here, I report the results for the antenna on the Rogers ULTRALAM® 3850HT substrate with a 9 µm-thick copper plating as it can be conveniently prototyped using laser ablation technique.

Encapsulation and Filling

The biocompatible encapsulation acts as a superstrate that help decoupling the antenna from the surrounding tissue. Concerning its EM properties, an ideal superstrate should have high permittivity ε_r and low loss, [19]. Only a few such materials have been reported for implantable applications so far: e.g. $MgTa_{1.5}Nb_{0.5}O_6$ ($\varepsilon_r \approx 28$) [20] and Al_2O_3 ($\varepsilon_r \approx 10$) [6]. Koulouridis *et al.* have also proposed polymer–ceramic biocompatible composites [21].

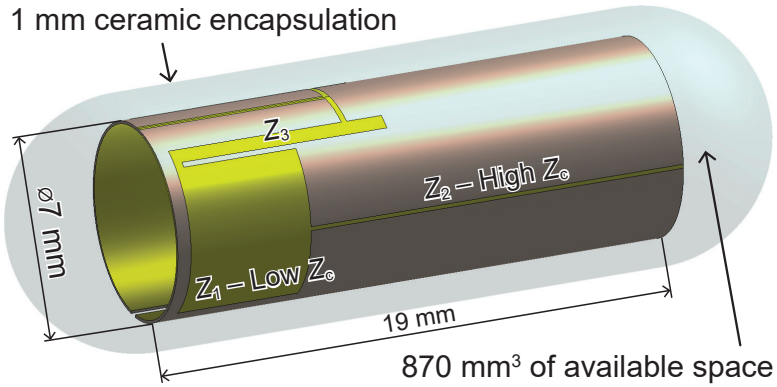

Fig. 6.3: Proof-of-concept two-element antenna array prototype inside a (28 × ⌀9) mm capsule

To maximize the electrical size of the antenna and decouple it from tissue, we choose a superstrate material with $\varepsilon_r = 80$, $\tan\delta = 0.0001$). As mentioned above, the minimal capsule inner diameter has been limited to ⌀7 mm. According to the Section 5.3.2, a 1 mm thick capsule shell (⌀9 mm outer capsule diameter, Figure 5.1) is sufficient to ensure the robust operation for implantable and ingestible scenarios.

Increasing the relative permittivity of the antenna environment improves the maximum achievable radiation efficiency. As in the previous chapter, pure water fills the capsule ($\varepsilon_r = 78.4$, $\tan\delta = 0.022$ at 434 MHz). For the industrial implementation, though, solid high-permittivity (and low loss) materials may be preferred: for instance, a ceramic-powder-loaded polymer [21] or epoxy [22].

Weight Estimation

The volume of a capsule with half-spherical endings is $V = \pi R^2 h + (4/3)\pi R^3$, where R is the radius of the capsule and h stands for the height of its cylindrical part (19 mm in our case). For the 28 mm×⌀9 mm capsule with 1 mm thick shell, the mass of the inner filling (water, $V_{\text{in}} \approx 910$ mm^3, $\rho = 997$ kg·m^{-3}) is $m = \rho V = 9.1$ g. The mass of the shell ($\rho \approx 2700$ kg·m^{-3}) is $\rho(V_{\text{total}} - V_{\text{in}}) \approx 15$ g. The total mass is thus $m_{\text{total}} \approx 25$ g. Considering that the density of the circuitry (especially batteries) might be higher than that of water, we can estimate the maximum total mass of the device to be roughly 30 g. A cautionary remark, this is higher than the mass of

existing ingestible and implantable capsules (see Chapter 1). It limits the scope of applications: for instance, the capsule may be too heavy for endoscopy.

6.3 Dual-Band Capsule Antenna

Following the synthesis, we have designed and built a prototype to evaluate performance experimentally. The antenna conforms to the inner surface of a capsule (Figure 6.3). The capsule size is ($28 \times \varnothing 9$) mm, the ceramic shell thickness is 1 mm and the permittivity is $\varepsilon_r = 80$. The shell material is K-80 provided by TCI ceramics [23]. The antenna consists of the array of two elements (mirrored configuration, as on Figure 6.2).

6.3.1 Numerical Modeling and Optimization

I used CST Microwave Studio® 2016 [24] to model and optimize the antenna. Figure 5.10 shows a flowchart of the numerical modeling process. At first, a planar antenna approximation was solved and optimized (in terms of $|S_{11}|$) using the CST time domain solver (finite integration technique, FIT), then validated using the frequency domain solver (finite element method, FEM). Both methods used an automatic adaptive mesh refinement with $< 1\%$ $|S_{11}|$ error tolerance at 434 MHz for three consecutive iterations as a convergence criterion. The plating layers (top and ground) were modeled as thin sheet copper ($\sigma = 5.96 \times 10^7$ S·m^{-1}) as, on the contrary to the previous case (Section 5.4.1), this approximation gives accurate results since the substrate is two times thicker.

FIT models used hardware acceleration (NVIDIA Tesla K20c GPUs) that reduced significantly the simulation time and, therefore, the whole optimization routine. High interaction between the antenna parameters require fully-dimensional optimization to satisfy two optimization criteria $|S_{11}| \leq -20$ dB at 434 MHz and 2.45 GHz simultaneously. Seven geometrical parameters require tuning: these on Fig 6.1 taking into account that $l_{Z1} + l_{Z2} = \text{const}$ and the separation between two antenna elements w_0 (Fig 6.2). Considering high dimensionality of the optimization routine, it needs to be parallelized to achieve the result over a reasonable time. I distribute the Trusted Region Framework [25] algorithm over seven nodes (each equipped with NVIDIA Tesla K20c GPUs).

6.3.2 Antenna Performance

The operating frequencies are ISM 434 MHz for the first resonance and a double resonance around ISM 2.45 GHz band (Figure 6.4) when simulated in $\varnothing 100$ muscle-equivalent phantom (dispersive EM properties according to [26]–[28]). The results between FEM and FIT solvers are in good agreement both in terms of reflection coefficient $|S_{11}|$ and realized gain G_{tot}. The max. realized gains G_{tot} are -16.1 dBi and -14.4 dBi and the radiation efficiencies η are 2.03% and 1.02% for 434 MHz and 2.45 GHz, respectively. Seeing this, we should not be surprised to find that the eightfold increase in superstrate permittivity and twofold increase of Chu sphere radius R (compared to the antenna reported in Chapter 4) together give almost five dBi increase in gain at 434 MHz. The gain of the capsule therefore exceeds the other counterparts reported in the literature by about 9 dBi. Figures 6.6 and 6.7 show the

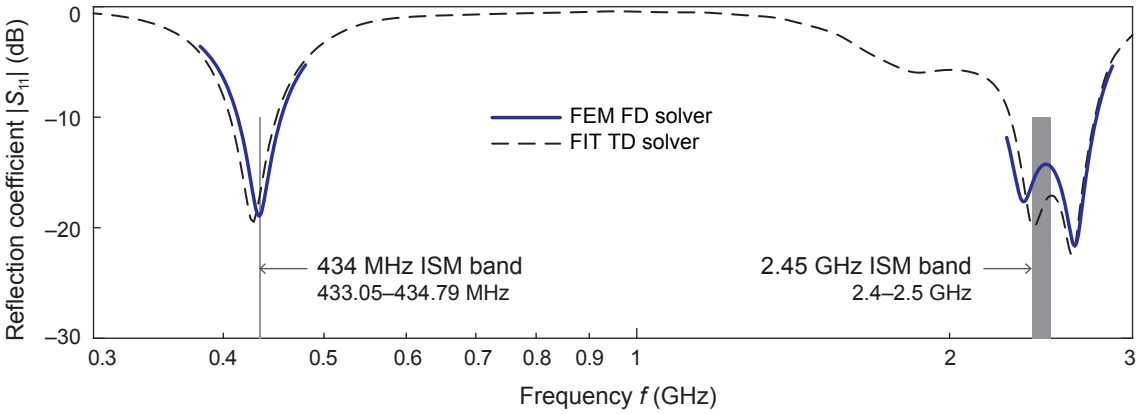

Fig. 6.4: Reflection coefficient $|S_{11}|$ of the antenna simulated in a ⌀100 mm spherical muscle-equivalent phantom using both time- (FIT) and frequency-domain (FEM) solvers of CST Microwave Studio® 2016.

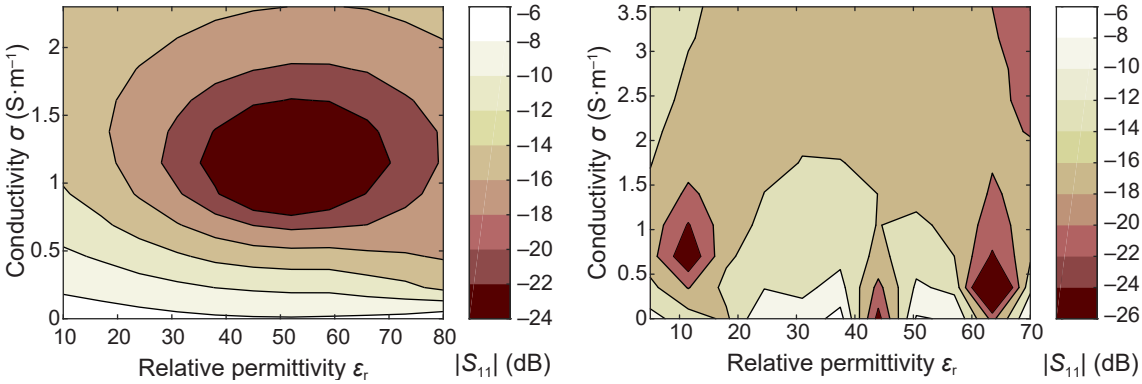

Fig. 6.5: Detuning immunity within the homogenous spheric phantom ⌀100 mm. *left:* Reflection coefficient $|S_{11}|$ at $f_0 = 434$ MHz with $\varepsilon_r \in [10, 80]$ and $\sigma \in [0, 2.3]$ S·m^{-1}. *right:* Reflection coefficient $|S_{11}|$ at $f_0 = 2.45$ GHz with $\varepsilon_r \in [5.5, 70]$ and $\sigma \in [0, 3.5]$ S·m^{-1}.

radiation patterns of the antenna at 434 MHz and 2.45 GHz, respectively. We can notice that, even though the radiation efficiency η at 434 MHz in two times better than the one at 2.45 GHz, the realized gain G_{tot} at 2.45 GHz is 1.7 dBi higher. This is due to the higher directivity $D = 5.94$ dBi at 2.45 GHz compared to the $D = 2.2$ dBi at 434 MHz.

Owing to the twofold increase in substrate thickness, the $\text{BW}_{-10\text{ dB}} = 42.4$ MHz bandwidth ($\text{FBW}_{-10\text{ dB}} = 10\%$) in the muscle-equivalent phantom at 434 MHz is 25.4 MHz wider that the one for the antenna reported in the previous chapter (Section 5.5). This further contributes to the robustness of the antenna to the variation of the tissue EM properties.

Robustness: Variation of Tissue EM Properties

To analyze the antenna impedance detuning immunity to the variation of surrounding tissue EM properties, I analyze antenna matching levels at 434 MHz and 2.45 GHz in a ⌀100 mm spherical phantom using the FEM solver. The range of the phantom EM properties is $\varepsilon_r \in [10, 80]$ and $\sigma \in [0, 2.3]$ S·m^{-1} at 434 MHz and $\varepsilon_r \in [5.5, 70]$ and $\sigma \in [0, 3.5]$ S·m^{-1} at 2.45 GHz. These ranges cover all biological

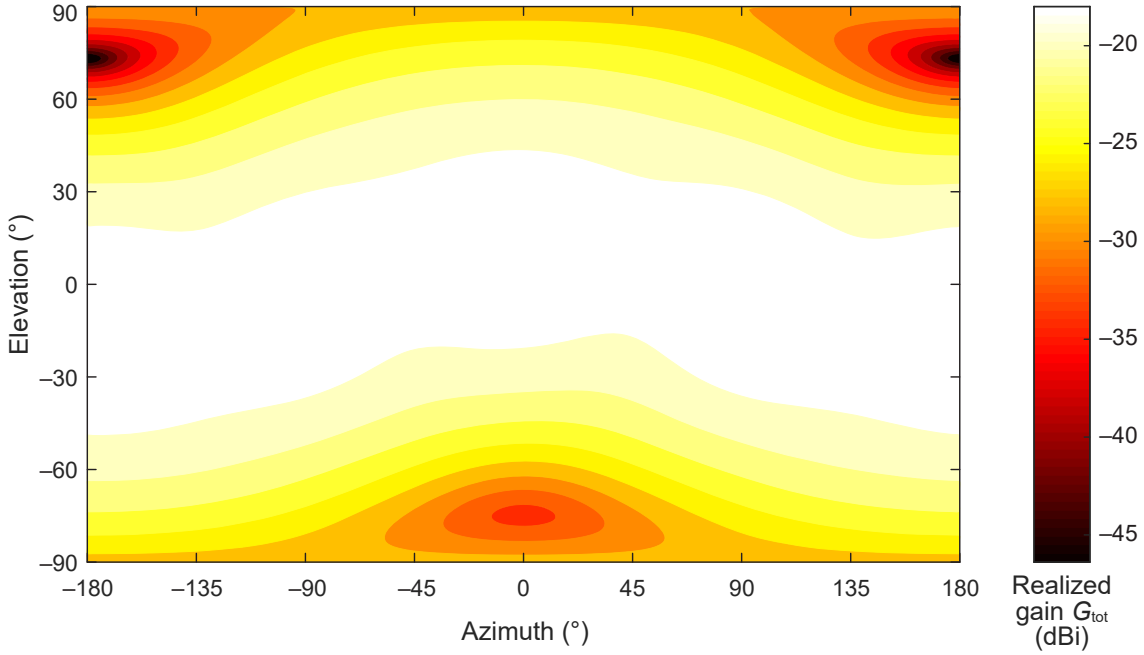

Fig. 6.6: Co-pol (vertical polarization) radiation pattern of the antenna at 434 MHz simulated in the ⌀100 mm spherical muscle-equivalent phantom.

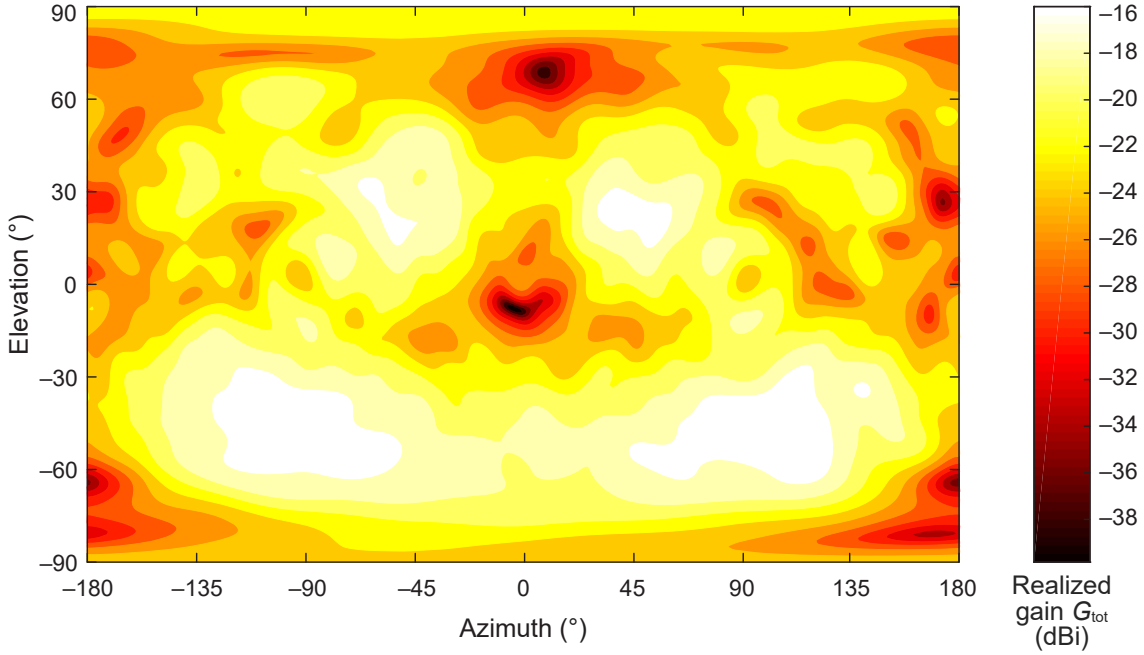

Fig. 6.7: Co-pol (vertical polarization) radiation pattern of the antenna at 2.45 GHz simulated in the ⌀100 mm spherical muscle-equivalent phantom.

Table 6.1: Water–Sucrose–NaCl Phantoms Used for Measurements: EM Properties and Concentrations at 434 MHz and 2.45 MHz

	434 MHz	**2.45 GHz**
Relative permittivity ε_r	56.9	52.7
Conductivity σ (S·m^{-1})	0.8	1.7
Concentration of Sugar (%)	51.3	41.8
Concentration of NaCl (%)	1.53	0

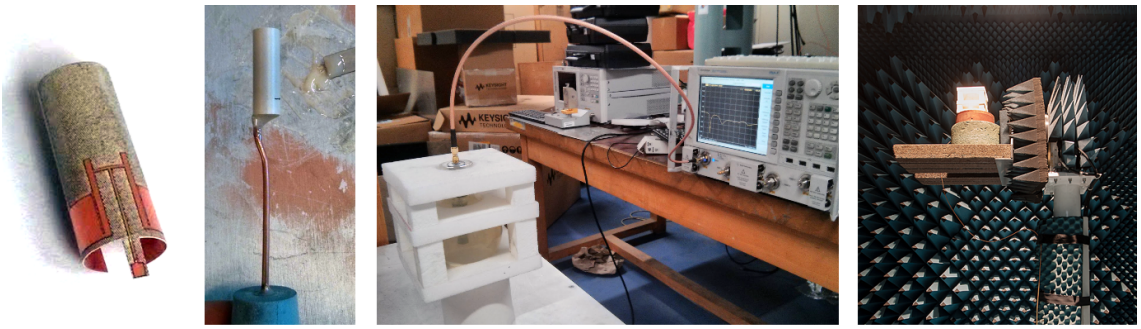

(a) (b) (c) (d)

Fig. 6.8: Antenna prototyping. (a) Printed and folded antenna with a microstrip feed. (b) Antenna inside a ⌀9 mm ceramic shell soldered to a semi-rigid coaxial cable and sealed at the bottom with epoxy. (c) Impedance characterization setup using spherical muscle-equivalent phantom. (d) Far-field characterization: the antenna in spherical muscle-equivalent phantom mounted on the tower positioner in an anechoic chamber.

tissues at corresponding frequencies [27].

Figure 6.5 demonstrates the area of detuning immunity of the antenna for both frequencies. It remains well matched ($|S_{11}| < -10$ dB) for most in-body scenarios and deteriorates to −6.8 dB in fat at 434 MHz. The reduced attenuation in fat compensates the increased antenna mismatch loss at this frequency (see Section 5.2.1). A 1 mm thick ceramic superstrate decouples well the antenna from the surrounding tissues providing additional 3.6 dB improvement in matching for fat compared to the antenna reported in the previous chapter (Section 5.6.1).

6.3.3 Prototyping and Measurements

Following the design and optimization, the antenna prototype is printed using the laser ablation technique (LPKF Proto-Laser S) on a 100 µm flexible substrate (Figure 6.8a, Rogers ULTRALAM® 3850HT, liquid crystal polymer, $\varepsilon_r = 2.9$, $\tan\delta = 0.002$) conforming to the inner surface of a (28 × ⌀9) mm ceramic (TCI Ceramics "K-80" [23] tube ($\varepsilon_r \approx 80$ for both frequency bands). A semi-rigid 50 Ω coaxial cable connects to a microstrip feed of the antenna allowing characterizing the antenna in terms of impedance and radiation (Figure 6.8b). The bottom end of the tube was sealed using Araldite 2011 epoxy (Figure 6.8b) and the top end with a rubber plug identical to one in Figure 5.17. Both materials do not affect antenna impedance characteristics according to simulations and impedance measurements.

I use muscle-equivalent liquid phantoms to evaluate experimentally the antenna

performance in-body. Table 6.1 shows the mixture concentrations. The 434 MHz phantom is based on full factorial experiment results reported in Section 2.3.2 whereas the 2.45 GHz phantom bases on results obtained by Karacolak *et al.* [10]. The phantoms were characterized in terms of EM properties using the SPEAG DAK kit [29] with DAK-12 probe.

Figure 6.8(c) shows the impedance measurement setup. The antenna under test (AuT) is centered inside a spherical ⌀100 mm jar filled with one of tissue-simulating liquids according to the frequency band (see Table 6.1). As for the radiation performances evaluation, I characterize the antenna using a direct illumination far-field technique. Section 2.4 overviews the characterization approach and Figure 6.8(d) depicts the measurement setup. The AuT and the spherical jar containing the phantom constitute the device under test (DuT). The DuT localizes at a distance from the measurement horn fulfilling the far-field criteria [30]. An electro-optical converter (enprobe LFA-3 [31]) feeds the DuT in order to avoid the signal degradation due to currents induced on a feeding cable.

As in the previous chapter, we measured the radiation pattern in the azimuth plane, for both co-polarization and cross-polarization components. The frequency sweep was set from 300 MHz to 600 MHz and from 2 GHz to 3 GHz in order to ensure that the maximum radiation occurs at the f_{res}. The estimation of the DuT realized gain used the gain substitution technique employing a reference antenna of known gain (ETS-Lindgren 3164-06 [32]).

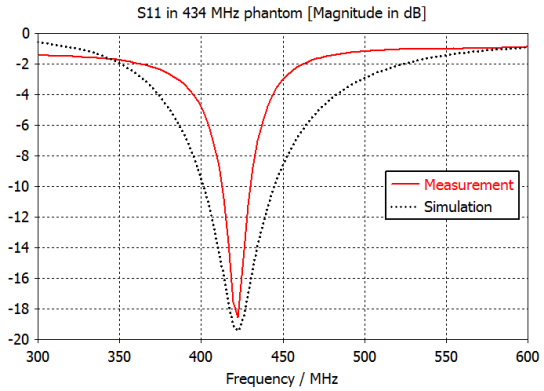

Fig. 6.9: $|S_{11}|$ of the antenna prototype in 434 MHz muscle-equivalent phantom.

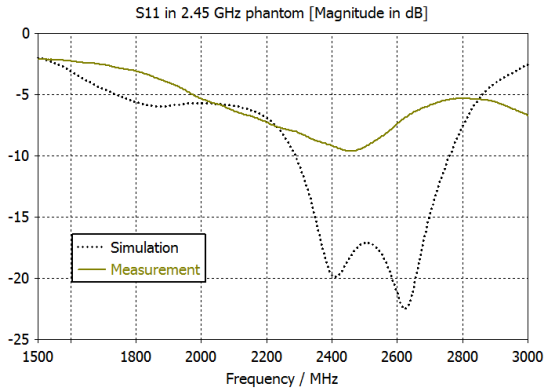

Fig. 6.10: $|S_{11}|$ of the antenna prototype in 2.45 GHz muscle-equivalent phantom.

Figs. 6.9 and 6.10 show the antenna performance in terms of impedance. The results agree well with the experiment for 434 MHz band and satisfactorily for the 2.45 GHz band. Precise manufacturing method (e.g. photolithography instead of laser ablation) can further improve the S_{11} result for both bands band. As for 2.45 GHz band, better decoupling from the feeding cable can improve the agreement too. A balaced feed (as in [33]) or a balun [34] can help suppress unbalanced current on the capsule. Moreover, using electromagnetic simulation can help extrapolate the isolated antenna impedance from altered measurement with "infinite" feeding cable [35].

The measured max. realized gains are –15.8 dBi at 434 MHz and –19.7 dBi at 2.45 GHz that agrees good with the simulations considering the introduced mismatch loss at 2.45 GHz (Figure 6.10).

6.4 *In Vivo* Sensing of EM Properties

6.4.1 Introduction

The electromagnetic (EM) properties of biological tissue determine the antenna–tissue coupling and absorption of EM fields into that tissue. Knowledge of these properties allows one to employ successfully the EM fields for biomedical applications, such as: imaging, sensing, and optimization of through-body wireless transmission performances [36], [37]. Various methods and implementations of measuring EM properties *in vivo* were reported [36], [38], [39]. Mostly, an open-ended coaxial probe connected to a network analyzer is used to measure the reflection coefficient (e.g. Keysight N1501A [40] or Speag DAK [29]). However, these devices do not allow autonomous measurements in-body.

The capsule antenna impedance Z_{ANT} is affected by varying properties of surrounding biological tissue (e.g. while the gastrointestinal (GI) transit). One can exploit further this principle to use a specifically designed antenna that will be measurably detuned by the variation of tissue EM properties, but still maintain an acceptable level of matching (for instance, $|S_{11}| < -6$ dB) at the operating frequency f_0. The complex antenna impedance at operating frequency $Z_{\mathrm{ANT}}(f_0)$ then can be measured via reflection from antenna terminals using RF circuit. Variation of EM properties of surrounding media thus can be detected and, if necessary, quantified (depending on application).

Potential Applications

Existing technologies and devices do not allow to measure or to detect variations of EM properties *in vivo* inside a body. The implantable glucose and pH systems require special sensors. Non-invasive on-body glucose sensor (for instance, Glucowise [41]) uses EM properties to evaluate glucose levels (do not transmit data using the same antenna), but requires an active actions from user, whereas implantable sensor can be completely autonomous (e.g. by automatically measuring, transmitting data, and alerting the patient as well as the physician). EM characterization probes require connection to the vector network analyzer, therefore they are inapplicable for wireless *in vivo* measurements.

GI transition time analysis and pH levels time provide an important diagnostic information for various disorders. The variable EM properties of GI tract tissues (Figure 2.1) could be used to sense the ingestible capsule position (down to the organ) within the GI tract. Currently, a GI pH profile is used as a measure of the GI transition time. In addition, pH levels are used to monitor the acid reflux in esophagus (e.g. Bravo pH capsule [42]). The pH sensing sensors (glass electrodes) are bulky, costly, and energy consuming. Using the proposed invention instead can be a more efficient alternative, avoiding the use of dedicated pH sensor and thus saving space within the in-body device or reducing its size. Also, the methodology may be used to measure the EM properties of GI tract filling (such *in vivo* measurements have never been performed before). The obtained data are significant for biomedical use to diagnose various GI disorders that manifest in specific EM properties patterns (similar methods are used nowadays for food monitoring to detect bacterial or mold induced rotting). In addition, knowing the typical EM properties of GI tract filling, we may optimize the ingestible device transmission performance by minimizing the

antenna detuning due to the variation of these properties.

As for the implantable biotelemetry, it relies on capsule sensing capabilities to monitor the deviations of physiological parameters. Variation of some of these parameters—as e.g. pH, glucose, lactate, cholesterol levels—may affect the EM properties of body tissues or fluids under analysis. The proposed invention could be used to sense in-body and transmit wirelessly the variation of parameters unaffecting the patient mobility and quality of life. As for the capsule endoscopy, if an endoscopy capsule needs to film a specific section of gastrointestinal tract (e.g. small bowel), the activation of a camera only when the capsule reaches this section will save the battery and so potentially extend the achievable frame-per-second rate, improving diagnostic functionality.

The same counts for the drug delivery (site-specific delivery capsule) and therapeutic functionality (both ingestible and implantable)—the medication could be released automatically when the environment matches the given EM properties.

6.4.2 Methodology Description

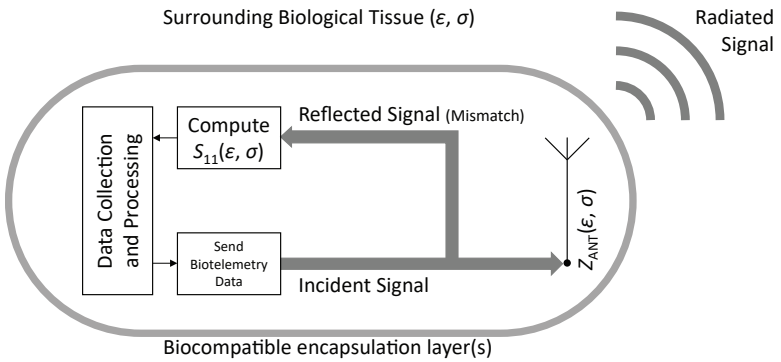

Fig. 6.11: Operation principle of the *in vivo* sensing of EM properties.

Figure 6.11 shows the operation principle. An in-body device uses the same antenna for data communication and for environment sensing. A fraction of the signal delivered to the antenna will be reflected due to mismatch $S_{11}(\varepsilon, \sigma)$ that depends on surrounding tissue EM properties. The RF circuit separates the reflected signal from incident and measures the reflection coefficient at operating frequency f_0. Figure 6.12 shows examples of possible implementations of the RF circuit. The measured reflection $S_{11}(\varepsilon, \sigma)$ amplitude and phase could be either transmitted to be processed further externally (off-body), or handled on-board within the capsule. The relative shift in the measured S_{11} can be used to sense the tissue transition (stomach $\rightarrow$ small intestine $\rightarrow$ colon) without computing the EM properties of surrounding media.

If it is necessary to determine the EM properties, an expression relating the complex antenna impedance in free space to *in vivo* could be used. This expression require a model of antenna impedance in arbitrary media (ε, σ). Analytical models exist for simple radiators as short monopole probes [36] or coaxial probes [43]. For our complex radiator case, an accurate analytical model is unrealizable. However, as the sensing is required at operation frequency only, both the antenna impedance in free space and in medium with given variation of EM properties at f_0 could be

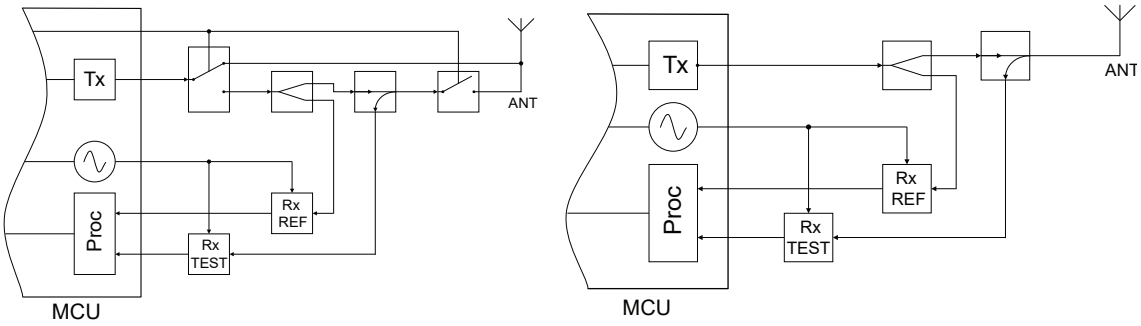

Fig. 6.12: RF circuit implementation examples. *left*: Direct connection. *right*: A realization containing switches.

modeled numerically and interpolated into an accurate analytical expression (e.g. using full factorial methodology along with surface response optimization [44]).

6.4.3 Sensing Electromagnetic Properties via the Variation of Antenna Impedance

Antenna impedance $Z_{ANT} = R + jX$ depends on complex permittivity of the adjacent biological tissue $\hat{\varepsilon}(\omega) = \varepsilon'(\omega) - j\varepsilon''(\omega)$.

This dependence was firstly quantified by Deschamps in 1962 [45]; it is widely used nowadays for wideband EM characterization using coaxial probes (e.g. Keysight N1501A [40] or Speag DAK [29]). Considering the nonmagnetic properties of biological tissue ($\mu \approx \mu_0$), the antenna complex impedance Z_{ANT} in free space could be related to its impedance *in vivo* as [36]

$$\frac{Z_{ANT}(\omega, \hat{\varepsilon})}{Z_i} = \frac{Z_{ANT}(n\omega, \hat{\varepsilon_0})}{Z_0} \tag{6.2}$$

where Z_i is the complex intrinsic impedance of the medium, Z_0 stands for the intrinsic impedance of free space, and n denotes the complex index of refraction of the medium relative to that of air.

This equation is applicable for any antenna type provided an expression could be found for the antenna impedance both in free space and in the dielectric medium.

6.5 Summary

This chapter begun with the description of design and characterization of a dual-band conformal microstrip antenna. Such antenna can integrate both data transmission and wireless power transfer functionality increasing the available space inside of an in-body device. The proposed design occupies only 2.6% of the available volume inside of the 28 mm $\times\varnothing$ 9 mm capsule. This ultra-miniature footprint, along with enhanced robustness and efficiency (compared to counterparts), allow employing it for both implantable and ingestible applications. As for the antenna reported in the previous chapter, this one may also be considered for animal biotelemetry since the EM properties of some animal tissues may differ from those of humans, and the high robustness of the antenna reduces the impedance detuning.

To maximize the efficiency of the antenna, we 1) increased the electrical size ka by physically elongating the antenna and by loading it with high-permittivity

superstrate ($\varepsilon_r = 80$) and 2) decoupled it from the tissue by the dielectric loading as well as by implementing its high-impedance element as a straight microstrip line. To synthesize the initial antenna, we proposed wieldy dimensioning techniques comprising of analytic–numerical approach described in Section 4.3 coupled to a $\lambda/2$ patch. However, high interaction between the antenna geometrical parameters require fully dimensional optimization for all the seven parameters to achieve 50 Ω matching for both 434 MHz and 2.45 GHz bands.

The realized gain of the capsule exceeds the existing 434 MHz counterparts by about 9 dBi and the 2.45 GHz-ones by about 3 dBi (Tables 1.2 and 5.4). At the same time, the antenna is more robust. It should be noted, however, that an accurate comparison of the radiation performance requires all counterparts to be evaluated within the same environment: using a phantom with identical geometry and EM properties. The proposed approach comes, however, at a price. The design requires using ceramic capsule shell and a high permittivity filling that increase the cost.

The proof-of-concept antenna is perfectly matched for the whole range of human tissue EM properties and is robust to the presence of integrated components as well thanks to its continuous ground plane. This allows one using the antenna "as is" for a given in-body application in conjunction with a microcontroller, RF circuit, and power source of choice. The antenna is well matched for a standard input impedance of 50 Ω for both 434 MHz and 2.45 GHz bands.

The chapter concluded with the application of developed antennas (with reservation, all in-body antennas) to *in vivo* sensing of EM properties. Knowledge of these properties allows one to employ successfully the EM fields for biomedical applications, such as imaging, sensing, and optimization of through-body wireless transmission performance. With the proposed methodology, an in-body device uses the same antenna for data communication and for environment sensing. The method is based on measurements of the reflected signal due to antenna mismatch, which depends on surrounding tissues. In addition to the sensing, the method can be used to adjust the adaptive matching of the in-body device significantly increasing its robustness.

As a minor limitation of the proposed approach, we can mention the reduced sensitivity of the system if the robust antenna is required for the device (thus thicker encapsulation); however, the possible wide area of application of the system alleviates this limitation.

Bibliography

[1] L. Chirwa, P. Hammond, S. Roy, and D. Cumming, "Radiation from ingested wireless devices in biomedical telemetry bands," *Electronics Letters*, vol. 39, no. 2, pp. 178–179, Jan. 2003.

[2] L. Chirwa, P. Hammond, S. Roy, and D. Cumming, "Electromagnetic radiation from ingested sources in the human intestine between 150 MHz and 1.2 GHz," *IEEE Transactions on Biomedical Engineering*, vol. 50, no. 4, pp. 484–492, Apr. 2003.

[3] L. Xu, M.-H. Meng, H. Ren, and Y. Chan, "Radiation characteristics of ingestible wireless devices in human intestine following radio frequency exposure at 430, 800, 1200, and 2400 MHz," *IEEE Transactions on Antennas and Propagation*, vol. 57, no. 8, pp. 2418–2428, Aug. 2009.

[4] L. Xu, M.-H. Meng, and C. Hu, "Effects of dielectric values of human body on specific absorption rate following 430, 800, and 1200 MHz RF exposure to ingestible wireless device," *IEEE Transactions on Information Technology in Biomedicine*, vol. 14, no. 1, pp. 52–59, Jan. 2010.

[5] A. S. Y. Poon, S. O'Driscoll, and T. H. Meng, "Optimal frequency for wireless power transmission into dispersive tissue," *IEEE Transactions on Antennas and Propagation*, vol. 58, no. 5, pp. 1739–1750, 2010.

[6] F. Merli, L. Bolomey, J. Zurcher, G. Corradini, E. Meurville, and A. Skrivervik, "Design, realization and measurements of a miniature antenna for implantable wireless communication systems," *IEEE Transactions on Antennas and Propagation*, vol. 59, no. 10, pp. 3544–3555, Oct. 2011.

[7] A. K. Skrivervik, M. Bosiljevac, and Z. Sipus, "Propagation considerations for implantable antennas," in *11th European Conference on Antennas and Propagation (EuCAP 2017)*, Paris, France, Mar. 2017.

[8] P. Si, A. P. Hu, S. Malpas, and D. Budgett, "A frequency control method for regulating wireless power to implantable devices," *IEEE Transactions on Biomedical Circuits and Systems*, vol. 2, no. 1, pp. 22–29, Mar. 2008.

[9] J. S. Ho, A. J. Yeh, E. Neofytou, S. Kim, Y. Tanabe, B. Patlolla, R. E. Beygui, and A. S. Y. Poon, "Wireless power transfer to deep-tissue microimplants," *PNAS*, vol. 111, pp. 7974–7979, 2014.

[10] T. Karacolak, A. Hood, and E. Topsakal, "Design of a dual-band implantable antenna and development of skin mimicking gels for continuous glucose monitoring," *IEEE Transactions on Microwave Theory and Techniques*, vol. 56, no. 4, pp. 1001–1008, Apr. 2008.

[11] L.-J. Xu, Y.-X. Guo, and W. Wu, "Miniaturized dual-band antenna for implantable wireless communications," *IEEE Antennas and Wireless Propagation Letters*, vol. 13, pp. 1160–1163, 2014.

[12] W. Lei and Y.-X. Guo, "Miniaturized differentially fed dual-band implantable antenna: Design, realization, and in vitro test," *Radio Science*, vol. 50, no. 10, 2014RS005640, Oct. 2015.

[13] X. Q. Zhu, Y. X. Guo, and W. Wu, "A compact dual-band antenna for wireless body-area network applications," *IEEE Antennas and Wireless Propagation Letters*, vol. 15, pp. 98–101, 2016.

[14] BodyCap Medical, *E-Celsius*. [Online]. Available: `http://www.bodycap-medical.com/`.

[15] C. Gabriel, "Dielectric properties of biological materials," in *Handbook of biological effects of electromagnetic fields. Bioengineering and biophysical aspects of electromagnetic fields*, F. S. Barnes and B. Greenebaum, Eds., 3rd ed., Boca Raton, FL: CRC Press, 2007, pp. 51–100.

[16] M. Makimoto and S. Yamashita, "Bandpass filters using parallel coupled stripline stepped impedance resonators," *IEEE Transactions on Microwave Theory and Techniques*, vol. 28, no. 12, pp. 1413–1417, Dec. 1980.

[17] M. Sagawa, M. Makimoto, and S. Yamashita, "Geometrical structures and fundamental characteristics of microwave stepped-impedance resonators," *IEEE Transactions on Microwave Theory and Techniques*, vol. 45, no. 7, pp. 1078–1085, Jul. 1997.

[18] R. Waterhouse, *Microstrip Patch Antennas: A Designer's Guide*. New York, NY: Springer Science & Business Media, Feb. 2003.

[19] F. Merli, B. Fuchs, J. R. Mosig, and A. K. Skrivervik, "The effect of insulating layers on the performance of implanted antennas," *IEEE Transactions on Antennas and Propagation*, vol. 59, no. 1, pp. 21–31, 2011.

[20] T.-F. Chien, C.-M. Cheng, H.-C. Yang, J.-W. Jiang, and C.-H. Luo, "Development of Nonsuperstrate Implantable Low-Profile CPW-Fed Ceramic Antennas," *IEEE Antennas and Wireless Propagation Letters*, vol. 9, pp. 599–602, 2010.

[21] S. Koulouridis, G. Kiziltas, Y. Zhou, D. Hansford, and J. Volakis, "Polymer–ceramic composites for microwave applications: Fabrication and performance assessment," *IEEE Transactions on Microwave Theory and Techniques*, vol. 54, no. 12, pp. 4202–4208, Dec. 2006.

[22] S. Lee, J. G. Hyun, H. Kim, and K. W. Paik, "A study on dielectric constants of epoxy/SrTiO3 composite for embedded capacitor films (ECFs)," *IEEE Transactions on Advanced Packaging*, vol. 30, no. 3, pp. 428–433, Aug. 2007.

[23] TCI Ceramics, *K-80*. [Online]. Available: `http://www.magneticsgroup.com/m_dielec.htm`.

[24] Computer Simulation Technology AG, *CST Microwave Studio*. [Online]. Available: `https://www.cst.com/Products/CSTMWS` (visited on 08/06/2016).

[25] R. Byrd, R. Schnabel, and G. Shultz, "A trust region algorithm for nonlinearly constrained optimization," *SIAM Journal on Numerical Analysis*, vol. 24, no. 5, pp. 1152–1170, Oct. 1987.

[26] C. Gabriel, S. Gabriel, and E. Corthout, "The dielectric properties of biological tissues: I. Literature survey," *Physics in Medicine and Biology*, vol. 41, pp. 2231–2249, Nov. 1996, 11.

[27] S. Gabriel, R. W. Lau, and C. Gabriel, "The dielectric properties of biological tissues: II. Measurements in the frequency range 10 Hz to 20 GHz," *Physics in Medicine and Biology*, vol. 41, pp. 2251–2269, Nov. 1996.

[28] S. Gabriel, R. W. Lau, and C. Gabriel, "The dielectric properties of biological tissues: III. Parametric models for the dielectric spectrum of tissues," *Physics in Medicine and Biology*, vol. 41, pp. 2271–2293, Nov. 1996.

[29] Schmid & Partner Engineering AG, *Dielectric Assessment Kit*. [Online]. Available: `http://www.speag.com/products/dak/dielectric-measurements/` (visited on 08/06/2016).

[30] R. Moore, "Effects of a surrounding conducting medium on antenna analysis," *IEEE Transactions on Antennas and Propagation*, vol. 11, no. 3, pp. 216–225, May 1963.

[31] enprobe GmbH, *LFA-3 Analog fiber optic link*. [Online]. Available: `http://www.enprobe.de/products_FO-Links.htm` (visited on 07/02/2016).

[32] ETS-Lindgren, *3164-06 Open boundary quad-ridged horn*. [Online]. Available: `http://www.ets-lindgren.com/3164-06` (visited on 07/14/2016).

[33] M. M. Suzan, K. Haneda, C. Icheln, A. Khatun, and K. Takizawa, "An ultra-wideband conformal loop antenna for ingestible capsule endoscope system," in *10th European Conference on Antennas and Propagation (EuCAP 2016)*, Davos, Switzerland, Apr. 2016, pp. 1–5.

[34] S. Pivnenko, J. Zhang, A. Khatun, T. Laitinen, and J. Carlsson, "Characterization of small antennas for hearing aids by several measurement techniques," in *Proceedings of the Fourth European Conference on Antennas and Propagation*, Barcelona, Spain, Apr. 2010, pp. 1–5.

[35] L. Huitema, C. Delaveaud, and R. D'Errico, "Impedance and radiation measurement methodology for ultra miniature antennas," *IEEE Transactions on Antennas and Propagation*, vol. 62, no. 7, pp. 3463–3473, Jul. 2014.

[36] E. Burdette, F. Cain, and J. Seals, "In vivo probe measurement technique for determining dielectric properties at VHF through microwave frequencies," *IEEE Transactions on Microwave Theory and Techniques*, vol. 28, no. 4, pp. 414–427, Apr. 1980.

[37] K. Entesari, A. A. Helmy, and M. Moslehi-Bajestan, "Integrated systems for biomedical applications: Silicon-based RF/microwave dielectric spectroscopy and sensing," *IEEE Microwave Magazine*, vol. 18, no. 5, pp. 57–72, Jul. 2017.

[38] M. Stuchly and S. Stuchly, "Coaxial line reflection methods for measuring dielectric properties of biological substances at radio and microwave frequencies – a review," *IEEE Transactions on Instrumentation and Measurement*, vol. 29, no. 3, pp. 176–183, Sep. 1980.

[39] J.-M. Kim, D. Oh, J. Yoon, S. Cho, N. Kim, J. Cho, Y. Kwon, C. Cheon, and Y.-K. Kim, "In vitro and in vivo measurement for biological applications using micromachined probe," *IEEE Transactions on Microwave Theory and Techniques*, vol. 53, no. 11, pp. 3415–3421, Nov. 2005.

[40] Keysight Technologies, *N1501a Dielectric Probe Kit*. [Online]. Available: `http://www.keysight.com/en/pd-2492144-pn-N1501A/` (visited on 08/06/2016).

[41] MediWise, *Glucowise*. [Online]. Available: `http://www.gluco-wise.com/`.

[42] Given Imaging, *Bravo pH*. [Online]. Available: `http://www.givenimaging.com/en-int/Innovative-Solutions/Reflux-Monitoring/Bravo-pH/`.

[43] D. Blackham and R. D. Pollard, "An improved technique for permittivity measurements using a coaxial probe," *IEEE Transactions on Instrumentation and Measurement*, vol. 46, no. 5, pp. 1093–1099, Oct. 1997.

[44] G. E. P. Box, J. S. Hunter, and W. G. Hunter, *Statistics for Experimenters: Design, Innovation, and Discovery*, Second. Hoboken, N.J: Wiley-Interscience, May 2005.

[45] G. Deschamps, "Impedance of an antenna in a conducting medium," *IRE Transactions on Antennas and Propagation*, vol. 10, no. 5, pp. 648–650, Sep. 1962.

General Conclusion

To wrap-up this Ph.D. dissertation, I summarize the main conclusions and novel contributions of this work. Moreover, I highlight some topics that can be further developed and outline possible directions for future research.

Summary and Contributions

The main objective of this dissertation was to investigate and propose miniature antennas that could achieve improved operating range and robustness for biotelemetry, therapeutic and neural interfacing in-body devices. Wireless biotelemetry enables continuous monitoring of physiological parameters unaffecting the mobility of a patient: it allows one efficiently preventing, monitoring, and treating a disease timely. Apart from telemetering various diagnostic data, modern in-body applications include brain–machine interfaces and visual prosthesis, pacemakers and defibrillators, drug delivery and hyperthermia. Emerging neural interfacing allows us studying the brain, restoring sensory function, and assisting in the rehabilitation of amputees, survivors of paralysis, and patients with neurodegenerative diseases.

Wireless in-body biotelemetry relies on an efficient and steady communication with an external monitor via a radio frequency link. Although many alternatives exist to radio frequency transmission for in-body devices, they are limited in both operational range and throughput. Wireless transmission in VHF–SHF bands yields the longest range and highest data transfer rates for ingestible wireless devices.

Modern VHF–SHF in-body capsule antennas can be divided into wire, printed planar, and printed conformal. Wire and printed planar antennas are either bulky and poorly integrable into a capsule design or non-technological. Flexible substrates permit to minimize an antenna footprint within a capsule by conforming it to the shell. In this way, we can increase the physical size of the antenna by using all available capsule surface, thus increasing the maximum achievable radiation efficiency. Moreover, printed conformal antennas are technological and could be fully integrated into a circuit design. For instance, the antenna could be printed on the same flexible PCB with electronics and rolled to fit into the capsule.

Improving the transmission range of miniature in-body devices remains a major challenge (for the time being they are able to operate only up to a few meters). Among the main issues to face are low radiation efficiencies ($\eta < 0.1\%$), antenna impedance detuning, and strong coupling to lossy and dispersive biological tissues.

The radiation efficiency is mostly constrained by attenuation and reflection losses in tissues, as well as by the required miniaturization of antennas that imposes fundamental limits on the maximum achievable radiation efficiency (see Chapter 3). Detuning occurs since the antenna impedance depends strongly on electromagnetic

(EM) properties of a surrounding environment that, in case of biological tissues, vary both in terms of permittivity and conductivity.

Human Body Modeling

Body tissues are heterogeneous and highly dispersive medium. The effective EM properties $\hat{\varepsilon}(\omega)$ of each individual tissue are characterized by four relaxation regions that can be accurately modeled using the multiple Cole–Cole dispersion. One must account for these properties while designing antennas for in-body applications. In particular, for ingestible applications—where the surrounding tissues vary in time—an averaging of the tissue EM properties is necessary. Therefore, in Chapter 2 we proposed a time-averaging scheme based on the standard GI transition time reported in the literature.

Two-dimensional (2D) approximation of realistic heterogeneous phantom geometry allows one significantly reducing the computation time of full-wave simulations and at the same time preserving the anatomical accuracy of the model. In Chapter 2, we developed two 2D boundary representation phantoms: a normal human brain (used only for algorithm testing in this dissertation) and a human abdominal region (torso) phantom employed in Chapter 3 to study in-body propagation within realistic biological environment.

Liquid physical phantoms are ubiquitous for the in-body antenna experimental characterization of impedance and radiation. In Chapter 2, we developed a prediction model for the water–sucrose–salt liquid phantoms to achieve given EM properties at a given frequency in 200 MHz to 1 GHz range. The model is based on a full-factorial design considering the first order interactions and gives accurate predictions for impedance and radiation characterization of in-body antennas.

Chapter 2 describes also the approach to far-field characterization of in-body antennas. It improves the measurement accuracy in two ways: (1) the spherical phantom preserve the intrinsic radiation pattern of an antenna; (2) replacing the majority of a feeding cable with an optical fiber as well as insulating the remaining part with air allow suppressing currents induced on the cable.

Radiation Efficiency of In-Body Antennas

In Chapter 3, we evaluated the radiation efficiency dependence on the frequency and on implantation depth of the source. Maximizing the efficiency for a given depth is negotiating between the attenuation due to dielectric losses and reflection (mismatch) losses caused by high contrast between media. The optimal frequency of operation for deep implantation (for instance, ingestible; $d \gtrsim 3$) lies in 10^8–10^9 Hz range for all four model formulations and can be conveniently approximated as $f = 2.2 \times 10^7/d$. MedRadio 401 MHz and mid-ISM 434 MHz frequency bands belong to this range.

For subcutaneous applications ($d \lesssim 3$ cm), the interference effects induced by a standing surface wave play an important role. Within the optimal frequency range, the local max/min efficiency ratio reaches 6.5 times for the realistic case (torso phantom). The exact location of local minima and maxima depends on the implantation depth d as well as on skin and subcutaneous fat layers thickness. It is, however, invariant on the source formulation and thus on the polarization.

Therefore, for a given subcutaneous device, it is important to consider that the optimal frequency strongly depends on a subject and an implantation site.

Full p-polarization of TM_z mode reduces the effect of reflection losses at the sub-10^8 Hz part of the spectrum. Hence, the radiation efficiency increases compared to TE_z mode. However, such efficiency is unrealizable in this frequency range as it implies the source must operate with inapplicably narrow bandwidth. Minimum realistic bandwidth $FBW_2 \approx 1\%$ imposes the limitations on achievable efficiency within the lower part of the optimal frequency range. Yet, the estimate of achievable efficiency for a given bandwidth using Eq. (3.10) gives a conservative value due to the assumptions made (see Section 3.2.3). The real-world values would be less strict due to re-radiation of energy by currents induced in tissue.

Optimized Antenna of BodyCap e-Celsius® Capsule

In Chapter 4, we modeled, characterized, and optimized the antenna of the BodyCap e-Celsius® capsule. Prior to the optimization, I studied the ways on achieving fast and accurate model of the antenna taking into account the capsule materials and biological tissue.

The proposed hybrid analytic–numerical model allows understanding the antenna operation principle and defining the antenna dimensions for a given resonance frequency. In this way, the subsequent numerical optimization could be carried out for only one antenna parameter.

To optimize the existing design in terms of efficiency under the material and geometry constraints, we 1) increased the thickness of the substrate, 2) maximized the electrical size ka of the antenna, 3) decoupled it from the tissue by implementing its high-impedance element as a co-planar line in the ground plane, and 4) increased polarization purity by avoiding meandering. The novel antenna was fine-tuned to be perfectly matched in the averaged GI phantom ($\varepsilon_r = 63.0$ and $\sigma = 1.02$ S·m^{-1}). The gain of the antenna is 27 dBi that is 11 dBi higher than the reference design. To achieve such improvement, in particular, the bandwidth needed to be sacrificed (see Figure 3.1 and Section 3.2.3). The new bandwidth is $BW_{-10\text{ dB}} = 11$ MHz that is 24 MHz less than the reference design. The antenna stays, however, robust to the variation of EM properties of GI tract tissues and remains perfectly matched in muscle. An optimizing matching circuit was developed to maximize the antenna total efficiency and reduce the number of components. A software tool embedding the proposed matching procedure was developed for BodyCap Company. It allows one defining the component values to match an arbitrary impedance antenna to the SI 1014 MCU.

Miniature Versatile Antenna for In-Body Capsules

Going beyond strict constraints imposed on antenna design in Chapter 4, in the following Chapter 5 we designed and characterized a low-profile conformal microstrip antenna suitable for a wide range of in-body capsule applications. Ultra-miniature dimensions, enhanced robustness and efficiency (compared to counterparts) allow employing it for both implantable and ingestible applications. This capsule antenna may also be considered for animal biotelemetry since the EM properties of some animal tissues may differ from those of humans, and the high robustness of the antenna reduces partially the impedance detuning.

In addition, we proposed and experimentally validated the new design involving an in-body narrowband microstrip antenna combined with a high permittivity capsule shell. In this way, it is no longer necessary to increase the antenna bandwidth to cover the detuning range at the expense of radiation efficiency. We have chosen alumina (Al_2O_3) as encapsulation layer material since it is widely available and biocompatible. By choosing a higher permittivity material, one can further increase the radiation efficiency, improve robustness, or decrease the capsule shell thickness. The antenna, of course, has to be optimized to operate within the modified encapsulation. However, the proposed approach comes at a price. The design requires using ceramic capsule shell and a high permittivity filling that increase the cost.

The realized gain of the capsule exceeds the existing counterparts by about 3 dBi whereas it is more miniature and robust. It should be noted, however, that an accurate comparison of the radiation performance requires all counterparts to be evaluated within the same environment: specifically, using a phantom with identical geometry and EM properties.

The proposed antenna remains well matched for the whole range of human tissue EM properties and is robust to the presence of integrated components too. This allows using the antenna "as is" for a given in-body application in conjunction with a microcontroller or an RF circuit of choice. The antenna is well matched for a standard input impedance of 50 Ω for both mid-ISM and MedRadio band versions.

Dual-band Versatile Antenna for In-Body Capsules

In Chapter 6 we designed and characterized of a dual-band conformal microstrip antenna. Such antenna can integrate both data transmission and wireless power transfer functionality increasing the available space inside of an in-body device. The proposed design occupies only 2.6% of the available volume inside of a 28 mm $\times\varnothing$ 9 mm capsule. This ultra-miniature footprint, along with enhanced robustness and efficiency (compared to counterparts), allow employing it for implantable and ingestible applications as well as for animal biotelemetry.

To maximize the efficiency of the antenna, we increased the electrical size ka by 1) physically elongating the antenna and 2) loading it with a high-permittivity superstrate ($\varepsilon_r = 80$). In addition, dielectric loading decouples the antenna from tissues. To synthesize the initial antenna, we used a stepped impedance resonator (SiR) modeled by the analytic–numerical approach described in Section 4.3. The SiR is coupled to a $\lambda/2$ patch. Finally, we optimized the antenna to achieve 50 Ω matching for both 434 MHz and 2.45 GHz bands. The realized gain of the capsule exceeds the existing 434 MHz counterparts by about 9 dBi and the 2.45 GHz-ones by about 3 dBi (Tables 1.2 and 5.4). At the same time, the antenna is more robust.

In Vivo Sensing of Tissue EM Properties

Finally, in the second part of Chapter 6, we talked about the application of in-body antennas for *in vivo* sensing of EM properties. With the proposed methodology, an in-body device can use the same antenna for data communication and for environment sensing. The method is based on the measurement of the reflected signal due to antenna mismatch, which depends on surrounding tissues. From the measured amplitude and phase of the reflected signal, one can retrieve the complex impedance of the antenna and, if necessary, the EM properties of surrounding environment. In

addition to the sensing, the method can be used for adaptive matching of an in-body device increasing its robustness.

Future Work and Perspectives

Here, we discuss some aspects of this dissertation that could be strengthened, extended, or further developed.

The liquid phantom prediction model described in Chapter 2 has sufficient accuracy for impedance and radiation characterization of robust in-body antennas. However, more precision may be required for calibration purposes. One can achieve higher prediction accuracy by refitting the model with new data points (to begin with, the EM properties for the phantom with 1.5% of NaCl of 45% of $C_{12}H_{22}O_{11}$) and introducing higher degree polynomial approximation. In addition, the prediction frequency range may be extended as well to allow phantom designs with given EM properties under 200 MHz as well as over 2.45 GHz. It would be also convenient to study of the bactericide effect on EM properties (for long-term storage), ambient temperature, and temperature-dependent evaporation dynamics.

The far-field characterization approach proposed in Chapter 2 gives accurate results at 434 MHz; however, the antenna reported in Chapter 6 is still coupled to the feeding cable at 2.45 GHz. A balanced feed or balun can help to suppress unbalanced current on the capsule. Moreover, using EM simulation with "infinite" feeding cable can help to extrapolate the isolated antenna impedance from altered measurement.

In Chapter 3, the established optimal frequency ranges relay on 2D problem formulations. Going beyond this approximation brings us up against more conditions to consider. Namely: 1) standing surface-wave interference behavior is more complex affecting the local minima and maxima of the radiation efficiency for shallow sources ($d \lesssim 3$ cm); 2) impure p-polarization of the TM_z mode incident on the air–body interface; and 3) depending on application, slightly reduced attenuation losses due to finite z-dimensionality. These additional conditions do not influence the main findings of this study in terms of optimal frequency range. Nevertheless, they provide the opening point for further investigations on maximum achievable radiation efficiency.

To evaluate the optimized antenna for Chapter 4 BodyCap e-Celsius® in realistic conditions and compare the operating range with the reference antenna, we will perform measurements in phantom as well as *in vivo*. This comparison will quantify the total gain improvement comparing to the reference design, as we do not have data yet about reference matching circuit performance.

The approach presented in Chapter 5 on increasing robustness and efficiency of in-body antennas along with the maximum achievable radiation efficiency predictions given in Chapter 3 together suggest that there is still room for improvement. We would like to investigate more low loss materials for substrates and superstrates as well as additional microstrip designs. The first step would be to implement the co-planar SiR section presented in Chapter 4 with the 434 MHz part of the antenna presented in Chapter 6.

Finally, the circuitry prototype of the *in vivo* sensing methodology should be manufactured and implemented, for instance, within the capsule presented in Chapter 6.

Further research directions include also wireless power transfer using near-field shaping and cutaneous antennas for augmenting the biotelemetry capabilities and, if necessary, relaying the signal of in-body devices.

Appendix A

Automatic *hp*-Adaptivity

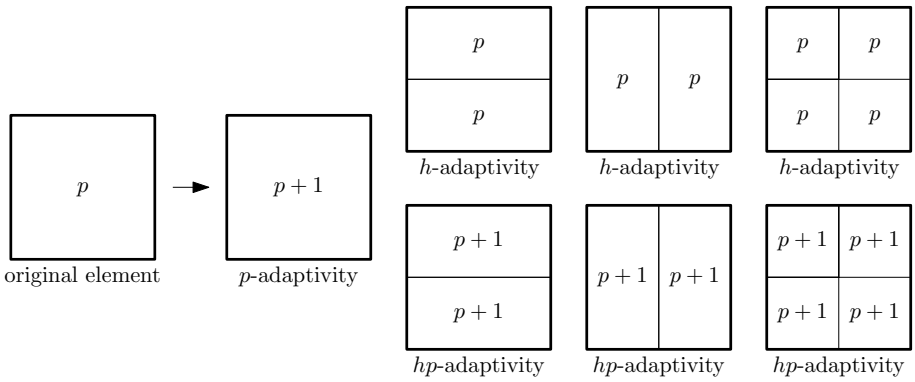

Fig. A.1: Possible types of automatic adaptivity implemented in Agros 2D.

Agros2D combines both the adaptive spatial subdivision of the elements (h-adaptivity) and polynomial order increment (p-adaptivity). The algorithm starts when the local solution error exceeds the desired tolerance. Considering the equation

$$Lf = 0, \tag{A.1}$$

where L is a differential operator and f stands for the function over the domain Ω, the error is defined as

$$\delta = f_{\text{ref}} - f', \tag{A.2}$$

where f_{ref} is the reference solution (realized on globally refined mesh) and f' is the approximate solution of (A.1). The elements to refine could be estimated using these three norms [1]:

- basic energetic norm

$$\|e\| = \left| \int_\Omega \delta \left(L\delta\right) \mathrm{d}\Omega \right|^{1/2}, \tag{A.3}$$

- L^2 norm

$$\|e\|_{L^2} = \left| \int_\Omega \delta^2 \mathrm{d}\Omega \right|^{1/2}, \tag{A.4}$$

- and H^1 norm

$$\|e\|_{H^1} = \left| \int_\Omega \left(\delta^2 + \nabla\delta \cdot \nabla\delta\right) \mathrm{d}\Omega \right|^{1/2}. \tag{A.5}$$

When the solution error expressed by an appropriate norm is higher than a given threshold, the adaptation process is started. The algorithm weights the local error of the elements to be refined with respect to the adaptivity type. The weight w is selected with respect to the kind of adaptivity that is *planned* to be used: 1) $w = 2$ for the h-adaptivity, 2) $w = 1$ for the p-adaptivity, and 3) $w = \sqrt{2}$ for the hp-adaptivity.

After, it is necessary to evaluate the score s of the candidate for refinement [2]:

$$s = \frac{\log_{10}\left(\frac{\epsilon}{\epsilon_0}\right)}{(d - d_0)^{\xi}}\,, \tag{A.6}$$

where ϵ is the estimated error in the candidate, d denotes its number of DoF while ϵ_0 and d_0 represent the error and number of DOFs of the original element, respectively. Finally, the symbol ξ stands for the convergence exponent. Now, the elements are ordered by the score s, and suitable adaptivity is chosen according to Fig. A.1.

The common h-adaptivity refinement process, implemented in some commercial FEM solvers (e.g. Ansys® HFSS™ or CST Microwave Studio® FD solver), leads to the creation of hanging nodes, which are removed by a forced refinement of relevant neighbor elements. It results in a considerable increase of the number of DoF and decrease of quality of elements (sharp edges appear).

Agros2D implements higher-order elements that allow allocating arbitrary level hanging nodes (k-irregularity rule) without any need of an additional refinement of the elements neighboring with the refined one.

In this way, the required numerical accuracy may be reached iteratively in a fully automated manner; furthermore, the hp-adaptivity improves the convergence in terms of speed and robustness [1], [3].

Appendix B

Impedance Analysis of Transmission Line Cross-Sections: Model Validation

To validate the method proposed in Section 4.4, we simulate in Agros2D [1] a 50 Ω standard stripline with the dimensions according to the ISO 11452-5:2002 [4]. Fig. B.1 shows the geometry of the stripline cross-section model. An arbitrary TEM transmission line geometry could be modeled this way, including both elements of the antenna on Fig. 4.14. The model parameters in this case will be the widths W_L1, W_L2, the substrate thickness and ε_r, the plating thickness, and eventually the phantom and superstrate layer cross-section geometries as in Fig. 5.8.

The FEM model must be truncated by a perfectly matching layer (PML). Spherical or rectangular study domains can be used according to the cross section geometry. We choose a spherical computational domain to demonstrate the relation of relative error to domain size. In most cases, a spherical computational domain is preferable for transmission line configurations with Width $\sim$ Height, and a rectangular domain with Width $\gg$ Height. Fully shielded transmission lines do not require the domain extension with zero charge boundary condition. For this case, the boundary condition would be not a zero charge (4.11) but a zero potential $\varphi = 0$ as in (4.10) for the ground plane.

Fig. B.2 shows the fragment of the model discretization with the initial and the *hp*-adapted solution mesh (see Appendix A). The automatic adaptivity was set up to maintain the relative error $\leq 1\%$. Fig. B.3 shows the scalar potential and the electric field distribution for the testing model (Fig. B.1) created using the Agros2D postprocessor.

Finally, Fig. B.4 depicts the relation of the relative error to the radius of the computational domain for the unshielded case. For the demonstration 50 Ω microstrip model, the result converge to a 50.5Ω that represents the 1% error, which corresponds to the tolerance set for the automatic *hp*-adaptivity. The shielded transmission lines do not require the computational domain extension, so this error type is eliminated.

The solution time on a notebook computer (Intel i5 2520M with 16GB PC3-10600 RAM) is 2.4 sec. It permits to use the algorithm for a multi-factor and multi-objective optimization tasks. Optimization routine could be conveniently written in Agros2D built-in scripting environment PythonLab.

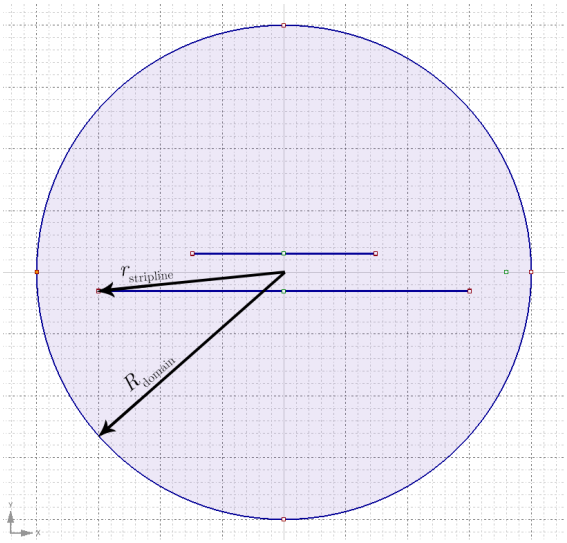

Fig. B.1: Model geometry for 50Ω ISO 11452-5:2002 stripline for validation of the methodology.

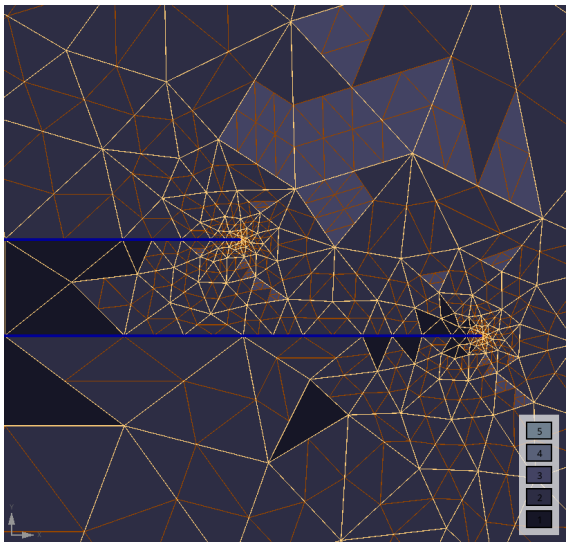

Fig. B.2: Initial and solution meshes using *hp*-adaptivity.

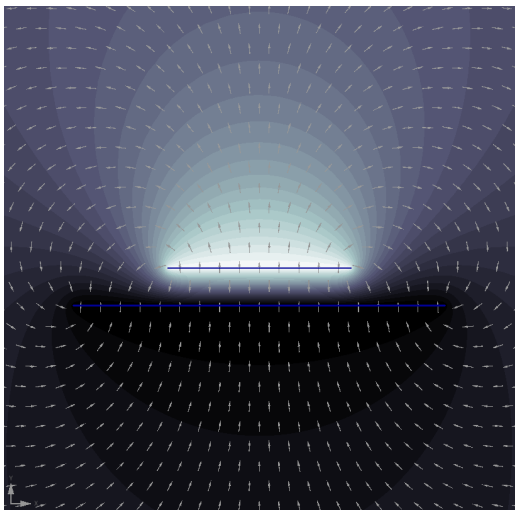

Fig. B.3: Scalar potential and electric field distributions.

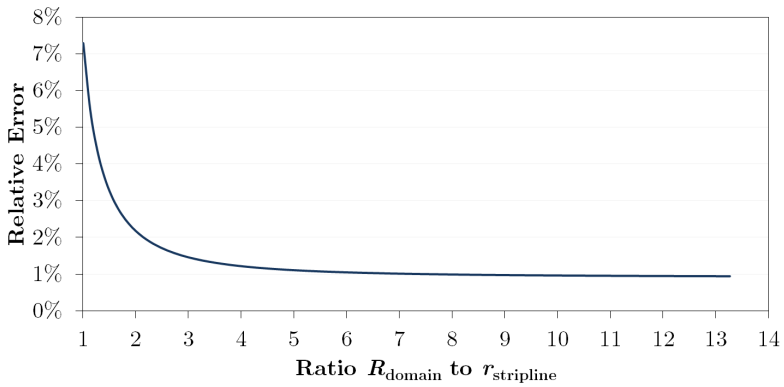

Fig. B.4: Error depends on the radius of computational domain for unshielded transmission lines.

Appendix C

Matching Circuit of e-Celsius® Antenna

The optimized antenna for the e-Celsius capsule (Section 4.8) has an input impedance of 80 Ω. A matching circuit and balun must be designed to transform the antenna impedance to Rx (differential) and Tx pins of SI 1014 MCU [5]. The standard circuit given in the application note AN436 [6] does not account for non-50 Ω impedance and is not adapted for miniature devices.

The goal of this study is to optimize the matching circuit achieving simultaneously several goals:

1. maximize RF output power (with the priority given to TX);
2. minimize number of elements;
3. minimize power consumption (i.e. maximize efficiency);
4. comply with ETSI and FCC specifications for spurious emissions;
5. if necessary, constrain the peak voltage at the drain.

The matching procedure outlined here allows achieving for the above-listed goals. As single antenna operates for both TX and RX, I optimize the direct tie configuration as outlined in AN436 [6] (Figure C.1). We begin by evaluating the ideal values for optimum Tx performance, then—taking into account real-world elements—define their realistic values using optimization.

At first, the value of L_{choke} must be determined. According to AN436 [6, p. 12], the value should be approximately equal 270 nH for 434 MHz operation. Then, we determine the inductance and capacitance of the resonant tank L_0–C_0. AN436 recommends choosing the values with high L-to-C ratio. The equation for the resonant frequency of LC-series resonator is $\omega = 1/\sqrt{LC}$. For the $L_0 = 30.7$ nH, the corresponding capacitor should be $C_0 = 5.9$ pF.

Z_{load} is the impedance to be presented from antenna to the output of the L_0–C_0 resonant tank at the 434 MHz. It can be estimated as [6]: and equals $Z_{\text{load}} = 27.0617 + j31.1884$.

Next, one needs to estimate the peak drain voltage. It should not exceed 6.5V; however, the MCU could operate properly for up to 8 V [6, p. 10]. To find the theoretical value of peak drain voltage limiting resistor, we use the equations 4–10

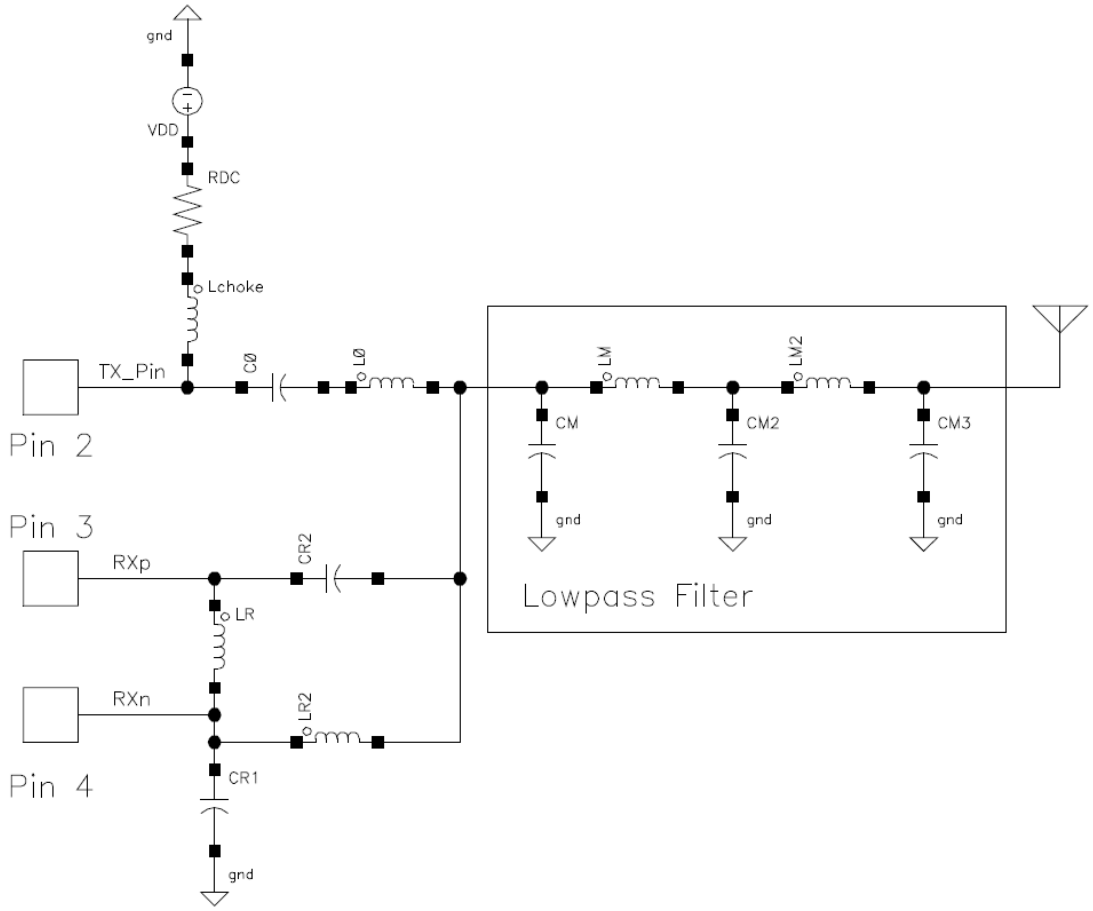

Fig. C.1: Matching topology for direct tie configuration (reprinted from AN436 [6]).

of the AN436. I determined the value $R_{\mathrm{DC}} = 98\Omega$ using the following equations (MATLAB):

```
f_res = 4.34e8;          % Antenna resonant frequecy
omega = 2*pi*f_res;
V_in = 3;                % input voltage (VDD)
C_shunt = 2.5e-12;       % PA shunt capacitance from datasheet
P_out = 0.02;            % Max output power: 20 mW = +13 dBm

V_DD = sqrt(P_out / (pi * omega * C_shunt));
I_DD = pi * omega * C_shunt * V_DD;
R_DC = (V_in - V_DD) / I_DD % Peak drain voltage limiting resistance
```

Hoverer, considering the voltage drop during the TX mode, the V_{in} would be significantly lower than 3 V. Therefore, after measuring the peak drain voltage, we decide to omit the R_{DC}.

TX Matching

Z_{load} must be transformed to the Z_{ANT} in order to maximize the power delivered to antenna. We can build two types of matching circuits: with high pass or low

pass behavior. As higher harmonics should be filtered out, we choose to design the circuit with low pass behavior.

Using the Smith chart, we, at first, define the value of L_M to be 25.3 nH (from $27.1+j31.2\Omega$ to $27.1-j31.2\Omega$) and, second, the C_M to be 6.4 pF (from $27.1-j31.2\Omega$ to 80Ω).

Low Pass Filter

Considering the Figure 25 of the AN436 [6, p. 39], the second harmonic at maximum achievable output power (13 dBm) is –41.4 dBm. The aforementioned C_M–L_M low pass matching circuit provide further 6.2 dB attenuation.

It reduces the second harmonic to -47.6 dBm at the antenna input (P_{in}). The capsule antenna efficiency is $\eta < 0.1\%$, which implies that the max radiated power (considering the perfect matching) for the second harmonic will be less than -77 dBm, which is much less than -49 dBm required in FCC Part 15.205 and Part 15.209. Therefore, we do not need to integrate the low pass filter. Thus, we reduce the matching circuit footprint, diminish the losses due to the element tolerances, and cut the cost.

RX Matching

The low-noise amplifier (LNA) [7] on the SI 1014 MCU [5] is designed as a differential amplifier and therefore has two input pins (RXp and RXn) on the RFIC. It is necessary to design a network that not only provides a conjugate match to the input impedance of the LNA but also provides a balanced-to-unbalanced conversion function (i.e., a balun). The RXp and RXn inputs of the RX LNA are internally capacitively-coupled; there is no need to provide external coupling capacitors to act as DC blocks.

According to the application note AN 427 [7], the RX matching network can be realized either with three or four elements. The advantage of using the 3-element network is reducing of parasitic effects and footprint and cutting the price. The disadvantage is the RX performance reduction by 0.5 dB: the waveforms obtained at the RXp and RXn inputs to the RFIC will not be exactly 180° out of phase. The result is a slight loss in conversion gain in the LNA and a small drop in overall sensitivity of the RFIC. As the transmission performance is a priority for biomedical telemetry, we choose to proceed with 3-element circuit. Figure C.2 shows the final matching circuit (RX + TX) topology for the 3-element RX and low-pass C_M–L_M matching.

Here I provide the calculation for 3-element network at 434 MHz computed using the equations 1–7 from AN427 [7]. MATLAB code:

```
R_LNA = 227;            % LNA equivalent resistance @ f_res [Ohm]
C_LNA = 2.01e-12;       % LNA equivalent capacitance @ f_res [F]

C_PAOFF = imag(1 / ...  % Tx pin impedance in Rx mode (AN436 p.34)
       (1i * omega * -192.24))

% STEP 1: Compute Z_in
Z_in = (R_LNA * (1/(1i*omega*C_LNA))) / ...
```

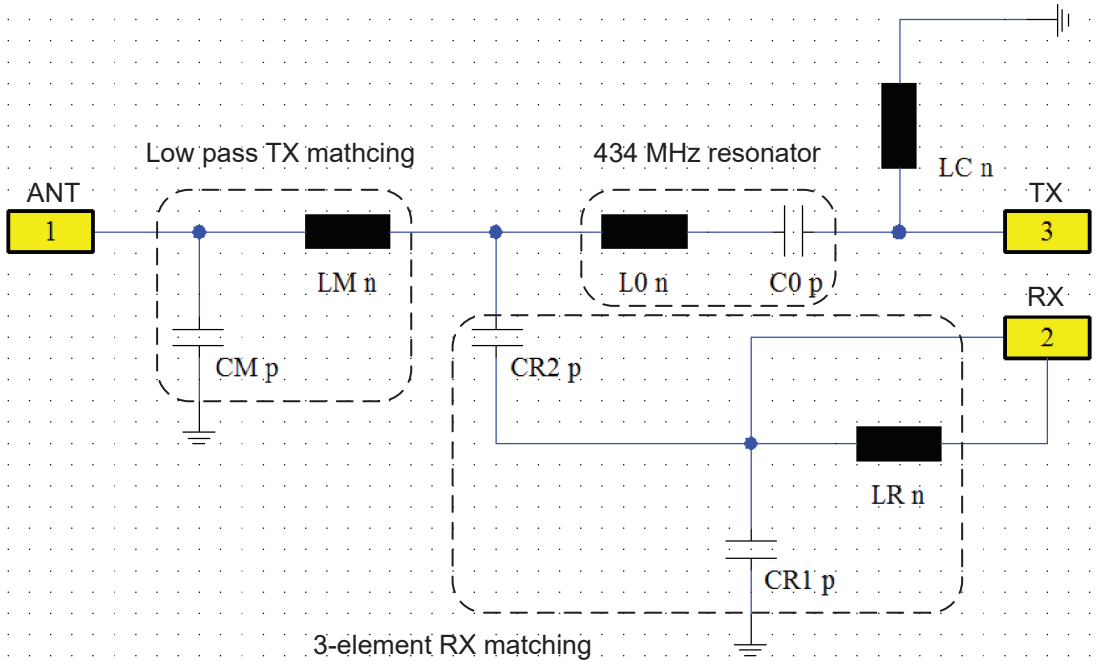

Fig. C.2: Optimized matching circuit topology for direct tie configuration.

```
    (R_LNA + (1/(1i*omega*C_LNA)))

% STEP 2: Compute shunt L_LNA to compensate C_LNA
L_LNA = 1 / (omega^2 * C_LNA);

% STEP 3: Compute L_M to match to the Re(Z_Load) circle
L_M = 1 / (omega * sqrt((1/(real(Z_load)*R_LNA))-(1/R_LNA)^2));

% STEP 3(a): Compute combined L (shunt)
L = (L_LNA*L_M) / (L_LNA + L_M)

% STEP 4: Compute C (series) to match
%   to Z_load (CONJUGATE) using Smith chart

% STEP 5: Split total C to CR1 (series) and CR2 (shunt)
%   to balance RXp/RXn
CR_2 = (2 * sqrt((R_LNA/Z_load) - 1)) / (omega * R_LNA)
CR_1 = 1 / ((1/C_total) - (1/C_2))
```

The ideal computed value of $L_R = 21$ nH (matching from $89.1 - j110.8\Omega$ to $27.1 + j73\Omega$). Using the Smith chart, $C_{R_{\text{total}}} = 3.5$ pF (from $27.1 + j73\Omega$ to $27.1 + j31.2\Omega$). The final step is to properly allocate this total required series capacitive reactance between C_{R_1} and C_{R_2}. There are an infinite number of possible matching networks which achieve a perfect match to 80 Ω. However, only one of these solutions also achieves the best possible equal-amplitude-with-180°-phase relationship between the waveforms at the RXp / RXn inputs [7]. C_{R_2} was found to be 5.8 pF and C_{R_1} 8.8 pF, accordingly.

Figure C.3 shows the S-parameters of the antenna in RX mode taking into

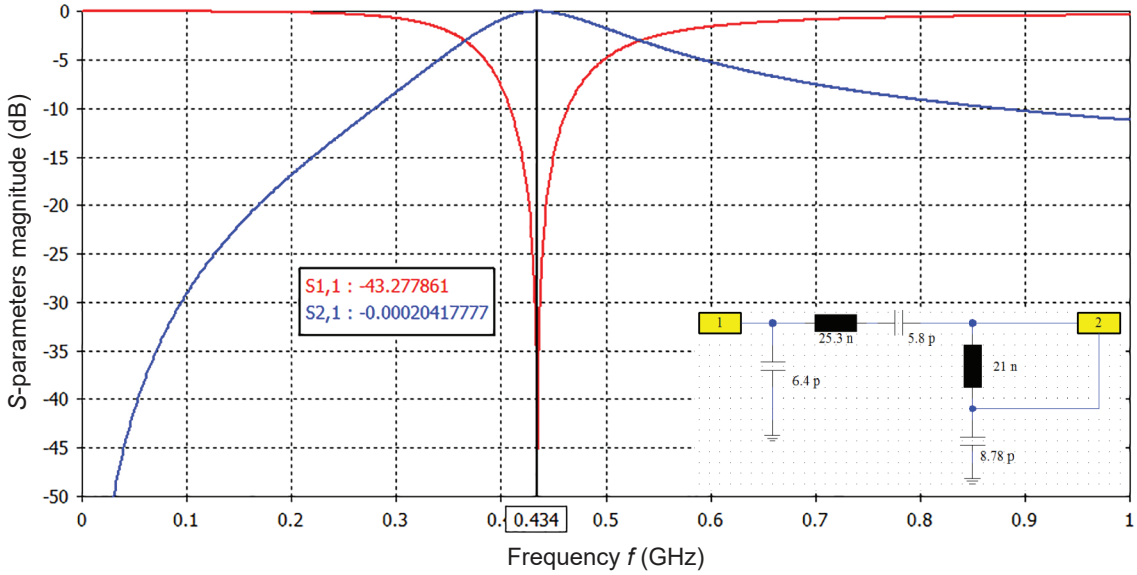

Fig. C.3: *S*-parameters of the circuit for the MCU in RX mode taking into account the TX.

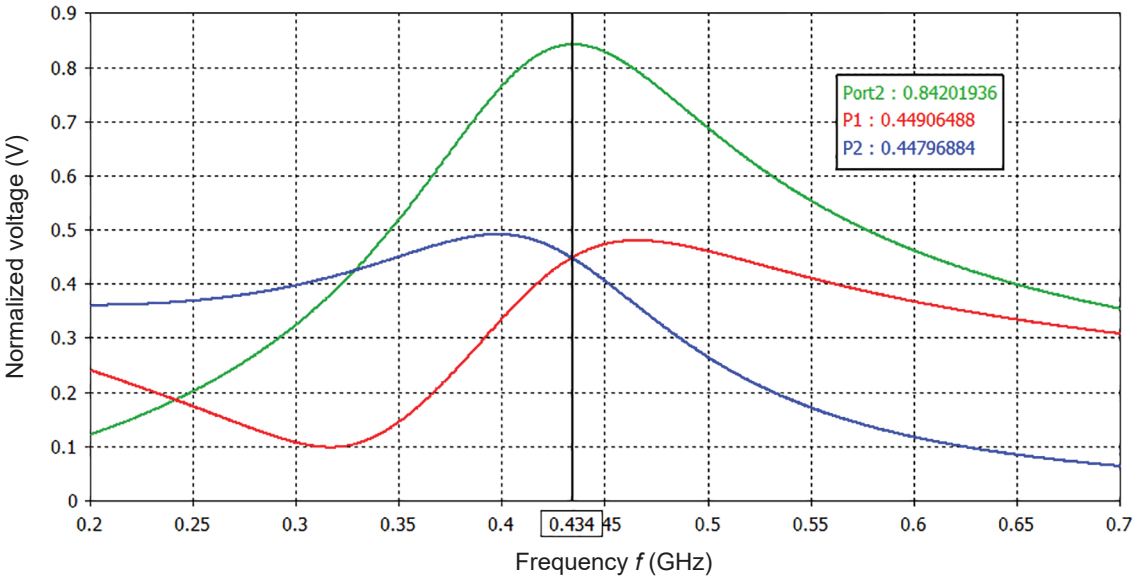

Fig. C.4: Voltages at the RXp (P1) and RXn (P2) pins. The circuit takes into account TX as in previous Figure.

account the TX circuit as well. Figure C.4 depicts the voltages at the RXp and RXn pins that are equal at 434 MHz.

In TX mode, RX pins are short-circuited by the MCU and connected to the ground plane. The 0.7 dB mismatch (Figure C.5) is due to the shunt capacitor of the RX circuit.

In RX mode, the PA of TX is in OFF mode and its impedance depend on the capacitance of the transistors. This output capacitance is effectively in series with matching capacitor C_0 and will result in series-resonance with inductor L_0 at some frequency. It is necessary to choose L_0 and C_0 to ensure that this resonance does not excessively degrade RX performance at the desired operating frequency. It is necessary to alter the value of L_0 slightly away from their calculated optimum values in order to accomplish this goal, thus slightly degrading TX performance [7]. To achieve the optimal performance of both RX and TX, we perform the optimization.

Optimization

The aforementioned coupling between TX and RX reduces the performances of both. TX performance can be improved by varying CM and LM. RX performance would be less affected if the L_0–C_0 resonance will be slightly out of tune (however, too big change will deteriorate the TX).

To find the optimal parameters, I perform the simultaneous optimization of TX and RX in terms of S_{21}. The parameters to optimize are L_0, L_M, and C_M. I use the algorithm "Trusted Region Framework" of CST Design Studio [8]. The goals are defined as $S_{21}^{\mathrm{TX}} = 0$ and $S_{21}^{\mathrm{RX}} = 0$ with a priority given to TX (weight = 2). Figure C.6 show the optimized S-parameters for both RX and TX modes. The results show good matching both for TX and RX.

In the final stage, the bill of materials (BoM) is compiled for the closest optimum values and the parasitic are included into the model. The optimization is re-run with the new values, and the BoM is finalized.

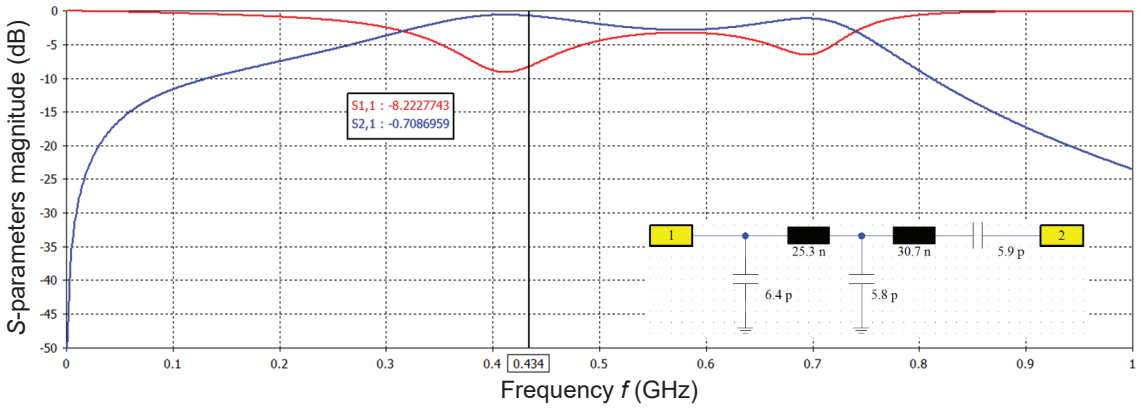

Fig. C.5: *S*-parameters of the non-optimized circuit for the MCU in TX mode taking into account the RX.

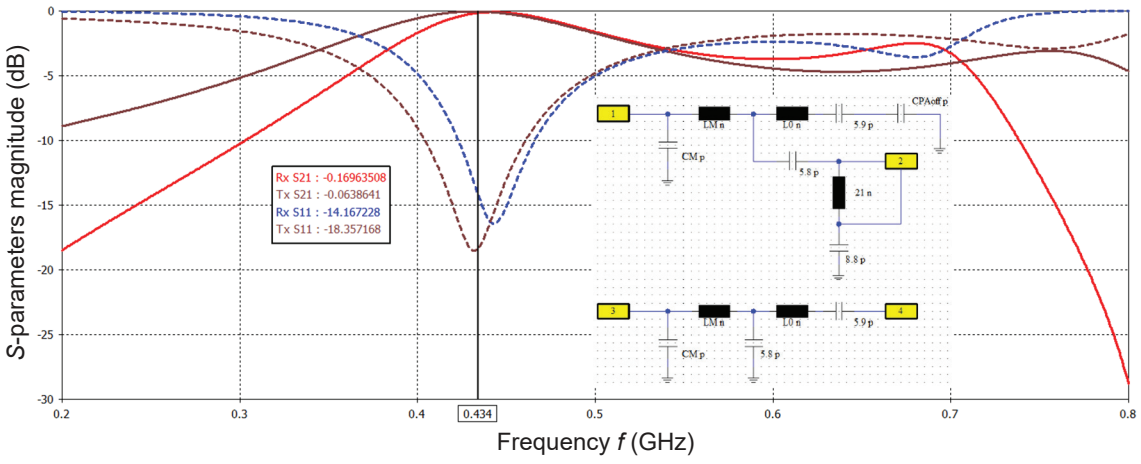

Fig. C.6: *S*-parameters of the optimized matching circuit for the MCU both in TX and RX modes.

Bibliography

[1] P. Karban, F. Mach, P. Kus, D. Panek, and I. Dolezel, "Numerical solution of coupled problems using code Agros2D," *Computing*, vol. 95, no. 1, pp. 381–408, 2013.

[2] P. Solin, L. Korous, and P. Kus, "Hermes2d, a C++ library for rapid development of adaptive -FEM and -DG solvers," *Journal of Computational and Applied Mathematics*, Fourth International Conference on Finite Element Methods in Engineering and Sciences (FEMTEC 2013), vol. 270, pp. 152–165, Nov. 2014.

[3] P. Solin, K. Segeth, and I. Dolezel, *Higher-Order Finite Element Methods*. London: Chapman and Hall/CRC, 2003.

[4] "ISO 11452-5:2002: Road vehicles – Component test methods for electrical disturbances from narrowband radiated electromagnetic energy – Part 5: Stripline," International Organization for Standardization, Geneva, CH, Standard, Apr. 2002.

[5] Silicon Labs, *Si10xx Sub-GHz Wireless MCUs*. [Online]. Available: `http://www.silabs.com/products/wireless/proprietary/si10xx-sub-ghz` (visited on 08/06/2016).

[6] Silicon Labs. (2011). AN436: Si4030/4031/4430/4431 PA matching, [Online]. Available: `https://www.silabs.com/documents/public/application-notes/AN436.pdf` (visited on 02/13/2017).

[7] Silicon Labs. (2009). AN427: EZRadioPRO™ Si433x & Si443x RX LNA matching, [Online]. Available: `https://www.silabs.com/documents/public/application-notes/AN427.pdf` (visited on 02/13/2017).

[8] Computer Simulation Technology AG, *CST Microwave Studio*. [Online]. Available: `https://www.cst.com/Products/CSTMWS` (visited on 08/06/2016).

About the Author

Denys Nikolayev received the B.Sc. (*cum laude*) and M.Sc. (*summa cum laude*) degrees in electronics and telecommunications from the Lviv Polytechnic National University, Lviv, Ukraine, in 2008. In 2012, he started working toward his Ph.D. degree in electrical engineering at the University of West Bohemia in Pilsen, Czechia, and in 2014, the joint supervision Ph.D. in electronics with the Institute of Electronics and Telecommunication of Rennes (IETR), France in collaboration with the BodyCap Company, France.

His research interests include antennas and propagation for body-centric networks, bioelectromagnetics, and numerical methods in electromagnetics. He authored one book chapter, six journal papers, and nine publications in international conference proceedings. Mr. Nikolayev is a member of the Institute of Electrical and Electronics Engineers (IEEE), the Bioelectromagnetics Society (BEMS), and the European Bioelectromagnetics Association (EBEA). He is a laureate of the Eiffel Excellence Doctoral Grant (2015/2016). He received the Best Paper Award at the URSI-France 2017 Workshop, the Poster Award at the international conference BioEM'2015, and seven Ukrainian national awards for student papers and conference presentations.

List of Publications

Book Chapter

1. D. Nikolayev, M. Zhadobov, R. Sauleau, and P. Karban, "Antennas for ingestible capsule telemetry," in *Advances in Body-Centric Wireless Communication: Applications and State-of-the-Art*, London, UK: IET, 2016, pp. 143–186.

Journal Papers

1. D. Nikolayev, M. Zhadobov, L. Le Coq, P. Karban, and R. Sauleau "Robust ultra-miniature capsule antenna for ingestible and implantable applications," accepted to *IEEE Trans. Antennas Propag.*

2. D. Nikolayev, M. Zhadobov, P. Karban, and R. Sauleau "Electromagnetic radiation efficiency of body-implanted devices," submitted to *Phys. Rev. Applied.*

3. D. Nikolayev, Z. Kubík, P. Karban, and J. Skála, "Impedance analysis of transmission line cells for EMC applications using Agros2D," *Appl. Math. Comput.*, vol. 289, pp. 381–387, 2016.

4. Z. Kubík, D. Nikolayev, P. Karban, J. Skála, and M. Hromádka, "Optimization of electrical properties of parallel plate antenna for EMC testing," *J. Comput. Appl. Math.*, vol. 270, pp. 283–293, 2014.

5. D. Nikolayev, "An anatomically realistic boundary representation phantom for studying VHF–UHF radiation effects," *Comput. Probl. Electr. Eng.*, vol. 3, no. 2, pp. 77–82, 2013.

6. D. Nikolayev, "Radio frequency resonances inside a human head," *Comput. Probl. Electr. Eng.*, vol. 3, no. 1, pp. 73–78, 2013.

Patents

1. D. Nikolayev, M. Zhadobov, and R. Sauleau, "Biological environment sensing in vivo for ingestible and implantable wireless devices" submitted to *SPV CNRS 06/09/2016.*

2. D. Nikolayev, M. Zhadobov, and R. Sauleau, "Miniature low-profile antenna with ultra-robust impedance characteristics," submitted to *SPV CNRS 02/11/16.*

3. D. Nikolayev, M. Zhadobov, and R. Sauleau, "Implantable or ingestible device with low-profile multi-band antenna," submitted to *SPV CNRS 03/03/2017.*

International Conference Papers

1. D. Nikolayev, M. Zhadobov, P. Karban, and R. Sauleau, "Long-range antenna systems for in-body biotelemetry: design methodology and characterization approach" in *EMBEC'17 & NBC'17 Joint Conference*, Tampere, Finland, 2017. — **best paper award finalist**

2. D. Nikolayev, M. Zhadobov, P. Karban, and R. Sauleau, "434 MHz ISM band antenna for in-body biotelemetry capsules," in *11th European Conference on Antennas and Propagation (EuCAP 2017)*, Paris, France, 2017.

3. D. Nikolayev, M. Zhadobov, P. Karban, and R. Sauleau, "Increasing the radiation efficiency and matching stability of in-body capsule antennas," in *10th European Conference on Antennas and Propagation (EuCAP 2016)*, Davos, Switzerland, 2016.

4. D. Nikolayev, M. Zhadobov, R. Sauleau, P.-A. Chapon, E. Blond, and P. Karban, "Decreasing SAR and enhancing transmission of an in-body biotelemetry capsule by reducing the near-field coupling with surrounding tissues," in *BioEM 2015*, Monterey, CA, 2015. — **poster and paper award**

5. Z. Kubík, J. Skála, and D. Nikolayev, "3D FEM simulation of small stripline for EMC testing," in *International Conference on Applied Electronics (AE 2014)*, Pilsen, Czechia, 2014.

6. D. Nikolayev, "SAR variation in a human head due to intrinsic resonances," in *4th European Seminar on Computing (ESCO 2014)*, Pilsen, Czechia, 2014.

7. D. Nikolayev, Z. Kubík, P. Karban, and J. Skála, "Modelling and simulation of an unshielded stripline," in *4th European Seminar on Computing (ESCO 2014)*, Pilsen, Czechia, 2014.

8. J. Kacerovsky, F. Mach, D. Nikolayev, P. Karban, and I. Dolezel, "Estimation of charges and critical velocity of plastic particles in triboelectric separator," in *10th International Conference ELEKTRO 2014*, Rajecke Teplice, Slovak Republic, 2014.

9. Z. Kubík, D. Nikolayev, M. Hromádka, P. Karban, and J. Skála, "Optimization of electrical properties of parallel plate antenna for EMC testing," in *4th International Congress on Computational Engineering and Sciences*, Las Vegas, NV, 2013.

National Conference Papers

1. D. Nikolayev, M. Zhadobov, P. Karban, and R. Sauleau, "Antenne miniature à 434 MHz pour dispositifs biotélémétriques in-body," in *20^{émes} Journées Nationales Micro-ondes*, Saint-Malo, France, 2017.

2. D. Nikolayev, P. Karban, M. Zhadobov, and R. Sauleau, "Antenne in-body pour capsules biotélémétriques miniatures : augmentation de la robustesse et

de l'efficacité de rayonnement," in *Les journées Scientifiques 2017 de l'URSI-France "Radiosciences au service de l'humanité,"* Sophia Antipolis, France, 2017. — **best paper presented by a PhD student award**

3. D. Nikolayev, "Electromagnetic Eigenfrequency Analysis of a Human Head," in *Elektrotechnika a informatika 2013*, Nečtiny, Czechia, 2013.

4. D. Nikolayev, "Assessing multisource exposure from mobile telecommunication electromagnetic field," in *Elektrotechnika a informatika 2012*, Nečtiny, Czechia, 2012.

VU :

Le Directeur de Thèse
Ronan SAULEAU

VU :

Le Responsable de l'École Doctorale
Jean-Marie LION

VU pour autorisation de soutenance :

Rennes, le ___ /___ / 2017

Le Président de l'Université de Rennes 1
David ALIS

VU après soutenance pour autorisation de publication :

Le Président de Jury
Anja SKRIVERVIK